Three-dimensional Electron Diffraction for Crystal Structure Solution of Complex Natural Silicates

Fachbereich Material- und Geowissenschaften der Technischen Universität Darmstadt

Zur Erlangung des Grades Doctor rerum naturalium (Dr.rer.nat.)

Dissertation von Emilia Buchsteiner

Erstgutachterin: Prof. Dr. Ute Kolb
Zweitgutachter: Prof. Dr. Christoph Schüth

Darmstadt, 2024

TECHNISCHE
UNIVERSITÄT
DARMSTADT

Buchsteiner, Emilia: Three-dimensional Electron Diffraction for Crystal Structure Solution of Complex Natural Silicates

Darmstadt, Technische Universität Darmstadt

Jahr der Veröffentlichung auf TUprints: 2024

Tag der mündlichen Prüfung: 15.10.2024

Veröffentlicht unter CC BY 4.0 International

https://creativecommons.org/licenses/

Erklärung gemäß §8 Abs. 1 lit. c, d und § 9 Abs. 1, 2 der Promotionsordnung der TU Darmstadt

Hiermit versichere ich, Emilia Buchsteiner, die vorliegende Dissertation ohne Hilfe Dritter und nur mit den angegebenen Quellen und Hilfsmitteln angefertigt zu haben. Alle Stellen, die Quellen entnommen wurden, habe ich eindeutig als solche kenntlich gemacht. Ich versichere, dass zu einem vorherigen Zeitpunkt noch keine Promotion versucht wurde und dass die vorliegende Dissertation in gleicher oder ähnlicher Form noch keiner Prüfungsbehörde vorgelegen hat. Ich versichere, dass die schriftlichen und elektronischen Kopien der eingereichten Dissertation identisch sind.

Ort, Datum: Unterschrift:

Darmstadt, 21.11.2024 _____

Emilia Buchsteiner

© 2024. This work is openly licensed via CC BY 4.0.

Three-dimensional Electron Diffraction for Crystal Structure Solution of Complex Natural Silicates

The characterization and hence the understanding of complex silicates pose a significant challenge due to their intricate structures and diverse chemical compositions. Conventional crystallographic techniques often fall short in providing comprehensive and accurate crystal structure information for these structures. However, recent advances in electron diffraction techniques offer promising avenues for overcoming these limitations. This thesis explores the application of three-dimensional electron diffraction (3D ED) as a powerful tool for solving the crystal structures of complex natural silicates. Three minerals were chosen for their exceptional and challenging structural characteristics, which have previously complicated or even hindered successful structure determination through conventional methods such as X-ray powder diffraction (XRPD).

In the first part of the study, a structure solution on a single crystal of illite is demonstrated, where prior attempts using XRPD failed due to inherent limitations in dealing with its impurity and disorder. Additionally, a new form of disorder is identified and characterized, providing valuable insights into fluid-dependent structure alterations and rendering a new model for XRPD data refinement. With labradorite, the research showcases 3D ED's ability to handle materials with incommensurate modulations and low symmetry, offering a possibility for direct comparison of data taken from different length scales. Moreover, a complete hierarchical structure description is provided. Finally, the structure of one of the most intricate minerals known, eveslogite, is solved despite its twinning on a nanoscale demonstrating the advantage of an accessibility to single crystalline nano domains.

Throughout this thesis, the advantages of 3D ED as a promising alternative to traditional methods are highlighted, especially in dealing with complex silicate minerals. The successes achieved in unraveling the atomic structures of illite, labradorite and eveslogite, which constitutes the largest mineral structure ever solved by 3D ED methods, demonstrate the power and versatility of 3D ED as a cutting-edge technique for structure analysis in the realm of mineralogical research. These findings pave the way for further advancements and open new avenues in the field of crystallography.

Dreidimensionale Elektronenbeugung zur Lösung der Kristallstruktur von komplexen natürlichen Silikaten

Die Charakterisierung und das Verständnis komplexer Silikatminerale stellen aufgrund ihrer komplizierten Strukturen und vielfältigen chemischen Zusammensetzungen eine große Herausforderung dar. Für eine genaue und umfassende Beschreibung dieser Kristallstrukturen, erweisen sich herkömmliche kristallographische Techniken oft als unzureichend. Aktuelle Fortschritte in den Elektronenbeugungstechniken bieten jedoch vielversprechende Möglichkeiten, um diese Einschränkungen zu überwinden. Diese Dissertation zeigt die Anwendung der dreidimensionalen Elektronenbeugung (3D ED) als leistungsfähiges Werkzeug zur Lösung der Kristallstrukturen komplexer natürlicher Silikate. Aufgrund ihrer außergewöhnlichen und herausfordernden strukturellen Eigenschaften wurden drei Minerale ausgewählt, bei denen zuvor eine erfolgreiche Strukturbestimmung durch konventionelle Methoden wie die Röntgenpulverdiffraktometrie (XRPD) stark verkompliziert oder nicht möglich war.

Im ersten Teil der Studie wird eine Strukturlösung an einem Illit Einkristall demonstriert, bei welchem bisherige Versuche mittels XRPD aufgrund großer Einschränkungen durch Verunreinigungen und Unordnungsphänomenen gescheitert waren. Zusätzlich wird eine neue Form der Unordnung im Illit identifiziert und charakterisiert, was wertvolle Einblicke in Fluid-abhängige Alterationen der Struktur liefert und ein neues Model für XRPD Verfeinerungen erbringt. Anhand von Labradorit wird gezeigt, dass 3D ED Materialien mit inkommensurablen Modulationen und niedrigen Symmetrien bewältigen kann und eine Möglichkeit zum Vergleich von Daten aus verschiedenen Größenskalen bietet. Darüber hinaus wird eine vollständige hierarchische Strukturbeschreibung präsentiert. Abschließend wird die Struktur eines der komplexesten bekannten Minerale, Eveslogit, trotz starker Verzwilligung auf der Nanoskala analysiert, was den Vorteil von auflösbaren einkristallinen Nanodomänen zeigt.

Im Verlauf dieser Dissertation werden die Vorteile von 3D ED als vielversprechende Alternative zu herkömmlichen Methoden hervorgehoben, insbesondere im Umgang mit komplexen Silikatmineralen. Die erzielten Erfolge bei der Aufklärung der Kristallstrukturen von Illit, Labradorit und Eveslogit, welches die größte je mit 3D ED gelöste Mineralstruktur darstellt, demonstrieren die Vielseitigkeit von 3D ED als innovative Technik für die Strukturanalyse im Bereich der mineralogischen Forschung. Diese Erkenntnisse ebnen den Weg für weitere Fortschritte und eröffnen neue Möglichkeiten auf dem Gebiet der Kristallographie.

Content

List of publications

Journal articles

- **Götz, E.**, Klementová, M., Depmeier, W., Krivovichev, S.V., Czank, M., Schowalter, M., Palatinus, L., Kolb, U. (2024): A binary nanotubular titanosilicate mineral with sharply diverging structural and compositional features of the nanotubules: The structure of eveslogite revealed by electron diffraction techniques. Science Advances (in preparation)

- Schäffer R., Osman R., **Götz E.**, Kandler K., Banning A. (2024): Mineral precipitation and aerosol release from natural brine in graduation towers, Hesse, Germany. Environmental Processes (in preparation)

- Plana-Ruiz, S., **Götz, E.**, Neumann, T., Schwesig, P., Kolb, U. (2024): 3D electron diffraction on clinkers: The incommensurate modulated structure of belite α'_H. Acta Crystallographica Section B, 80(2), 105-116.

- **Götz, E.**, Neder, R.B., Kolb, U., Kleebe, H.-J. (2023): The Alteration of Illite by Bad Nauheim and Gerolstein Brine; Implications on Fluid Permeability in Geothermal Systems. Applied Clay Science, 243, 107082.

- Stubenrauch, K., **Götz, E.**, Thomas, R., Rericha, A. (2023): Rätselhafte Onyx-Achate (Chalcedonyx) aus den miozänen Ablagerungen vom Jakobsberg (Rheinland-Pfalz) – ein Chalcedonproblem. Mainzer Naturwissenschaftliches Archiv, 60, 5-34.

- **Götz, E.**, Kleebe, H.-J., Kolb, U. (2022): The Hierarchical Internal Structure of Labradorite. European Journal of Mineralogy, 34, 393-410.

- Schäffer, R., **Götz, E.**, Schlatter, N., Schubert, G., Weinert, S., Schmidt, S., Kolb, U., Sass, I. (2022): Fluid-Rock Interactions in Geothermal Reservoirs, Germany: Thermal Autoclave Experiments Using Sandstones and Natural Hydrothermal Brines. Aquatic Geochemistry, 28, 63-110.

Conference contributions

- **Götz, E.**, Klementová, M., Depmeier, W., Krivovichev, S., Czank, M., Schowalter, M., Palatinus, L., Kolb, U. (2023): Eveslogite – Decoding the complexity of eveslogite through three-dimensional electron diffraction. MinWien2023, Vienna, Austria.

- **Götz, E.**, Kleebe, H.-J., Kolb, U. (2023): Alteration of Illite by Bad Nauheimer and Gerolsteiner Brine: Implications on Fluid Permeability in Geothermal Projects. Microscopy Conference, Darmstadt, Germany.

- **Götz, E.**, Kleebe, H.-J., Kolb, U. (2021): Analysis of Illites in Remlinger Sandstones. Der Geothermie Kongress, Essen, Germany.

- **Götz, E.**, Kleebe, H.-J., Kolb, U. (2020): Application of electron diffraction tomography on incommensurate crystal structure. Joint Polish-German Crystallographic Meeting, Wroclaw, Poland.

- Zuber, P., Frank, S., **Götz, E.**, Schreuer, J., Wohnlich, S. (2019): Crystal Nucleation and Filter Processes in Geothermal Systems. Der Geothermie Kongress, Munich, Germany.

- Koch, T.E., Brenker, F.E., **Götz, E.**, Kolb, U., Prior, D.J., Lilly, K., Krot, A.N., Schreiber, A., Bizzarro, M. (2019): Shock history of the metal-rich CB chondrite Quebrada Chimborazo (QC) 001. GeoMünster, Munster, Germany.

List of figures

List of tables

List of abbreviations

ABF	Annular bright-field
3D ED	Three-dimensional electron diffraction
(HOH)	Bafertisite-like heterophyllosilicates
$(HOH)_A$	Astrophyllite-like heterophyllosilicates
Ab	Albite
ABF	Annular bright-field
ADF	Annular dark-field
ADT	Automated diffraction tomography
AFM	Atomic force microscopy
AIPEA	Association Internationale pour l'Étude des Argiles
An	Anorthite
Arg	Aragonite
At%	Atomic %
BF	Bright-field
BSE	Back scattered electron
C1	Condenser lens 1
C2	Condenser lens 2
C-S	Chlorite-smectite
CA	Condenser aperture
Cal	Calcite
CBED	Convergent beam electron diffraction
C_C	Chromatic aberration
CCD	Charge coupled device
CEC	Cation exchange capacity
CL	Cathodoluminescence
C_S	Spherical aberration
CTF	Contrast transfer function
cv	Cis-vacant
DF	Dark-field
DL	Diffraction lens
DTPMP	Diethylentriaminepentamethyleneposphonic acid
EDS	Energy dispersive X-ray spectroscopy
ESEM	Environmental scanning electron microscope/microscopy
FEG	Field emission gun
FIB	Focused ion beam microscope/microscopy
FWHM	Full width at half maximum
GOF	Goodness of fit
HAADF	High-angle annular dark-field
Hem	Hematite
Hl	Halite
HRTEM	High-resolution transmission electron microscopy
I-S	Illite-smectite
IC	Illite crystallinity index, Kübler index
Ilt	Illite
IMA	International Mineralogical Association
KAP	Kola alkaline province
LSD	Lithium drifted silicon detector
MDO	Maximum degreee of order
NBD	Nanobeam diffraction
occ	Occupancy
OL	Objective lens

Or	Orthoclase, K-feldspar
PED	Precession electron diffraction
Qz	Quartz
RED	Rotation electron diffraction
ROI	Region of interest
SAED	Selected area electron diffraction
SE	Secondary electron
SEM	Scanning electron microscope/microscopy
SRO	Short range order
SSD	Silicon drifted detector
STEM	Scanning transmission electron microscope/microscopy
TDS	Total dissolved solids
TEM	Transmission electron microscope/microscopy
TOT	Tetrahedra-octahedra-tetrahedra
tv	Trans-vacant
U(iso)/(aniso)	Isotropic/anisotropic atomic displacement factor
UC	Unit cell
Wt%	Weight %
XRF	X-ray fluorescence
XRPD	X-ray powder diffraction

1. Introduction

Complex silicate minerals are of significant interest in various scientific disciplines, including materials science, geoscience and environmental science. These minerals possess intricate atomic structures that are closely linked to their unique properties and behaviors. Nevertheless, unraveling their atomic structures poses a huge challenge due to factors like disorder, incommensurate structures, large unit cells or twinning at the nanoscale.

Enhancing the understanding of the processes in the Earth's crust, which consists of approximately 95% silicate minerals, holds great importance, for example in light of the increasing utilization of geothermal energy. The global community committed to the Paris Agreement in 2015, aiming to limit global warming to under 2°C. Germany, aligned with this objective, seeks to achieve greenhouse gas neutrality and reduce emissions by 2050, necessitating a transition away from fossil fuels. Geothermal energy emerges as a promising renewable energy source capable of generating electricity as well as heat/cooling energy [1]. Within Germany, there exist several hydrothermal reservoirs suitable for geothermal energy production, including the Jurassic limestones in the Molasse Basin [2], as well as the Permian and Triassic sandstones located in the North German Basin [3] and the Upper Rhine Graben [4]. While the Jurassic limestones in the Munich region have been successfully utilized, the vast potential of the Permian and Triassic sandstones remains largely untapped in terms of geothermal power generation [5]. Unfortunately, both commercial and research projects have faced significant challenges related to scaling, primarily caused by the production of hot brines and the subsequent reservoir clogging. This phenomenon occurs due to the notable reduction in permeability resulting from the reinjection of cooled fluids [6,7]. Minerals such as barite, calcite, illite, kaolinite, amorphous phases and others have been identified as contributing to these issues [8–12].

Furthermore, the field of materials science continually benefits from the exploration of minerals and the development of synthetic counterparts. Minerals have long acted as templates for novel materials designed for specific purposes, as their properties are typically determined by their crystal structure. Opal, for instance, owes its unique appearance to the diffraction of visible light by a highly ordered periodic three-dimensional array of monodisperse spheres of amorphous silica, with a lattice constant comparable to the wavelength of visible light. Because of this structure opals can potentially be used as photonic crystals [13]. Another intriguing example is zorite, a microporous titanosilicate originating from the Kola Peninsula in Russia [14]. Interestingly, zorite exhibits nearly identical properties to synthetic zeolites patented as ETS [15]. Zeolites are currently applied in fields such as gas separation, catalysis, energy storage, optoelectronics and radioactive waste management [16–19].

Unraveling the intricate relationships among the structure, properties and performance of materials is a critical task [20]. Most minerals, whether they occur naturally or are synthetic, exist as crystalline phases [21]. The arrangement of atoms within these materials greatly influences their properties. To gain insights into the three-dimensional structure and fundamental constituents of the material, numerous techniques utilizing modern instrumentations have been applied.

Traditional methods of characterization, such as single crystal X-ray diffraction, have played a pivotal role in revealing crystal structures [22]. However, they are limited to crystals of at least one micrometer in size. Since not all crystals reach this size, X-ray powder diffraction (XRPD)

has emerged as a valuable technique for obtaining atomic-level structural information for smaller crystals [23]. XRPD has been used over the years to determine many crystal structures of various materials [24,25]. However, when dealing with complex structures as mentioned above, these techniques encounter limitations. Challenges such as low symmetry, large unit cells, diffuse scattering, low-quality diffraction patterns, preferred orientation or difficulties in phase determination for polyphase materials often impede the accurate characterization of these materials.

Advances in electron optics have enabled the use of electron-based microscopic techniques, such as scanning electron microscopy (SEM) and transmission electron microscopy (TEM), for both chemical and structural characterizations [26,27]. TEM has emerged as a powerful tool for studying materials at the atomic scale benefiting from inventions like aberration correctors and direct electron detectors [28,29]. Both conventional TEM and scanning TEM (STEM), especially when aberration corrected, allow for the resolution of atom columns, enabling the observation of defects and modulations [30,31]. Due to temperature and strongly ionizing effects of the high-energy electron beam interacting with the specimen, achieving resolutions below 1 nm usually requires beam stable specimens. To obtain three-dimensional structural information, tomographic (S)TEM methods can be employed. In imaging mode, these methods have for example been successfully applied to Au and particles embedded in a matrix [32]. However, interpreting more complex structures remains challenging. In general, TEM imaging with atomic resolution necessitates excellent instrument stability and meticulous sample preparation. Electron diffraction is less sensitive to instabilities, i.e., relatively invariant with respect to small beam shifts on the crystal and demands a significantly lower electron dose. Selected area electron diffraction (SAED) has been utilized to determine the structure of complex inorganic and organic nanostructures with atomic resolution [33], although it does not match the quality achieved by single crystal X-ray diffraction for structure analysis.

In 2007, Dr. Ute Kolb's research group at the Johannes-Gutenberg-University of Mainz introduced a method for tomographic data acquisition of diffraction images called automated diffraction tomography (ADT). This technique enables crystal structure analysis solely from electron diffraction data, significantly reducing the experimental effort required [34–36]. Electrons, due to their stronger interaction with matter compared to X-rays, allow for the analysis of crystal structures in nanocrystalline materials [27]. The ADT method has been successfully applied to a wide range of materials with complex features, including low crystallinity, multiple phases, twinning, disorder and large unit cells [37–41]. Subsequently, similar acquisition methods have emerged, such as rotation electron diffraction (RED), which combines beam tilt and crystal tilt [42]. More recently, new techniques like fast electron diffraction tomography [43] and ultra-fast electron diffraction tomography [44] have been developed, enabling continuous specimen tilting and fast data collection using high-speed detection cameras. These advances are particularly crucial for determining the structure of beam-sensitive materials [44,45]. Collectively, these methods are referred to under the umbrella term three-dimensional electron diffraction (3D ED) [46]. 3D ED methods have proven successful in characterizing complex crystal structures, making them efficient tools for structure analysis [38,40,47,48]. These methods significantly reduce dynamical effects during data acquisition, which can be further minimized by employing electron beam precession [49,50]. By using low-dose conditions, 3D ED also allows for the characterization of electron beam-sensitive materials, like organic compounds or metal-organic frameworks [51]. With continuous advancements in acquisition methods [43,52,53] and data processing tools [54–

56], along with the recent automation of the ADT method (Fast-ADT) [57], the routine use of 3D ED is on the horizon. This cutting-edge technique holds the potential to overcome the limitations of traditional techniques and already yielded valuable insights into the atomic structures of complex materials.

The objective of this thesis is to investigate the applicability of 3D ED for the structure determination of three complex silicate minerals: partially disordered illite, incommensurately modulated labradorite and eveslogite, a previously unknown structure that may be further complicated by twinning. The structure determination relies on the application of Fast-ADT. However, when the materials exhibit disorder, additional simulations are needed. To support the analysis and achieve an unbiased structural characterization, the results of the electron diffraction experiments are complemented by SEM and (S)TEM analyses, including energy dispersive X-ray spectroscopy (EDS) and high-resolution TEM (HRTEM), as well as XRPD data. This comprehensive approach enhances the understanding of the respective structures and supports the clarification of their genesis, opening up avenues for advancements in geoscience, materials science and other related disciplines.

The research in this thesis encompasses three areas:

1. Illite: The crystal structure of illite has only been refined on multiphase data based on the structure of muscovite [58]. Up until this day, no reliable refined structure data exist [59] and structure solution of illite has not been achieved based on single crystal data. This study aims to solve the structure of illite using 3D ED with Fast-ADT data collected on a single illite fiber. Both kinematical and dynamical refinements will be employed in the structure determination. Additionally, the change in the structure and stacking of the illite when exposed to different brines commonly found in geothermal systems is explored since the illitic cementation of the sandstones is the major component that comes into contact with the brines. Illite samples from controlled experiments with various brines and conditions will be examined. The diffuse scattering produced by the alteration is compared to the simulations of the newly created disorder model. Furthermore, the implications of changes in the illite structure induced by brines on the long-term operation of geothermal plants will be discussed.
2. Labradorite: Labradorite exhibits complex structures at various scales. The objective is to analyze all these structures within a single labradorite sample. The detailed electron microscopy analysis will begin by identifying and characterizing twinning, lamellae and domains. In addition to these crystallographic features, labradorite also possesses an incommensurately modulated structure. First, the average structure of labradorite will be solved on a single lamella. Based on this structure model, the incommensurately modulated structure will be analyzed. Both structures will be compared to each other as well as the structure solved by X-ray diffraction techniques [60]. The underlying causes of the incommensurability will be explored and the advantages of the structure solution with 3D ED data compared to X-ray data will be highlighted.
3. Eveslogite: The crystal structure solution of eveslogite presents challenges for traditional methods due to its complexity, large unit cell and nanoscale twinning. In this thesis, 3D ED will be applied to characterize the structure. Previous assumptions [61–64] about the structure will be reviewed and the structure solution will be compared with high resolution high-angle annular dark field (HAADF) STEM imaging. Additionally, the twin matrix will be determined and visualized within the atomic structure. For a comprehensive understanding, the structure of eveslogite will be compared to minerals

with related characteristics, identifying similarities and differences. Finally, potential order-disorder phenomena, as well as possible applications and limitations of similar structures, will be discussed.

The materials selected for this research consist of a diverse group of silicate minerals, each presenting its own complexities. Illite is a 2:1 dioctahedral clay mineral with the interlayer occupied by potassium. In comparison to muscovite, which shares a similar structure, illite exhibits a higher occurrence of isomorphous substitutions, resulting in a wide range of compositions [65]. Fibrous or lath-shaped crystals are a special morphology of illite, which are most often found in pores and pore throats of hydrothermally altered sandstones [66–69]. The quality of sandstones intended for use as geothermal reservoirs heavily relies on the quantity and type of cementation [70,71], with illitic cement being the most restricting one [72]. By their growth within pore spaces, illite fibers significantly increase tortuosity [73] and reduce the number of available flow paths in the initial pore system [68]. The fragile nature of these fibers makes them susceptible to tangling and breakage, potentially leading to their migration and blockage of pore throats through fluid movement [72,74,75]. In sandstone reservoirs, fibrous illite is commonly found as a $1M_{tv}$ polymorph [76]. Illite can also occur as a $1M_d$ polymorph, characterized by disordered layers of 1M illite [77]. Within reservoir sandstones, disordered illite has been identified as an alteration product of feldspar grains [68]. Crystal structure solution of clay minerals in general has always been hindered by obstacles [78]. On the one hand, the small particle size poses a major problem; on the other hand, they rarely occur as a pure phase but as a mixture of several clay minerals. Additionally, many of them have at least some degree of disorder [59]. Their low symmetry, possibility for cation substitution in the tetrahedra, octahedra or interlayer and the possibility to contain variable amounts of water, further complicate structure solution. Only a couple of structure refinements have been achieved, namely, a single crystal refinement of clinochlore [79], kaolinite [80] and few Rietveld refinements of well-ordered kaolinites [81–83]. Because illite is seen as structurally isomorphous to muscovite, Gualtieri et al. [58] attempted the refinement of the crystallographic structure based on the structure of muscovite for the first time but their refinement still left a lot of questions unanswered. Up until this day, no reliable refined structure data exists [59] and structure solution of illite has not been achieved with single crystal illite data.

Labradorite belongs to the plagioclase series, which includes the endmembers albite and anorthite and it exists within the composition range of 50% to 70% anorthite [84]. It is commonly twinned and exhibits various structural features, such as a modulated superstructure, domain textures and lamellae that give rise to the well-known phenomenon of labradorescence [85]. Labradorescence resembles the color creation in opals but with crystalline lamellae instead of amorphous spheres. The lamellae differ in Ca and Na content [86] and are likely formed through spinodal segregation [87]. Most compositions within the plagioclase series crystallize in a $C\bar{1}$ structure. However, in compositions rich in anorthite, the structure changes to $I\bar{1}$ due to an increasing Al:Si ratio. In the compositional range between albite and anorthite, neither of these ordering schemes is possible. Deviations from the 1:3 and 1:1 Al:Si ratios of the endmembers create an energetically unfavorable situation [88]. To minimize the energy of the solid solutions, the structure undergoes reorganization and ordering. Since the distribution of Al^{3+} and Si^{4+} is coupled with the distribution of Na^{+} and Ca^{2+} and the Al-Si ordering schemes differ between albite and anorthite, an incommensurate structure is formed causing satellite reflections of varying periodicity imposed on the main

reciprocal lattice [89–91]. Previous scientific studies have addressed the solution of incommensurate structures with 3D ED. The charge flipping algorithm was employed to solve the hexagonal incommensurate structure of η'-$Cu_{3|x}$(Si,Ge) using 3D ED data [92]. Other works demonstrate the application of 3D ED for solving orthorhombic materials with modulation along a main axis [93–95] and one monoclinic material with a modulation vector exhibiting components from two axes was determined [96]. In comparison, labradorite also has a monoclinic symmetry but a modulation vector with components from all three axes, which has not been solved before with 3D ED. The modulated structure can subsequently be compared to results from single-crystal X-ray diffraction [60].

Eveslogite is a mineral found exclusively on the Kola Peninsula, Russia. Its discovery and initial description were only made in 2003 by Men'shikov et al. and up to this day, limited knowledge exists about this mineral [64]. Initially, it was thought to be a heterophyllosilicate similar to astrophyllite [63,64]. However, doubts emerged when a comparable mineral called yuksporite was successfully structurally characterized and did not align with the previous description [61,62,97]. All attempts to solve the structure of eveslogite by conventional diffraction methods did not succeed. Intermediate successes in structure determination of similarly complex silicate structures grown under closely related geochemical conditions using 3D ED were encouragement to attempt structure solution of eveslogite using similar approaches [98–101].

The following chapter of this thesis will offer a comprehensive review of the crystallographic basics, encompassing a detailed exploration of disorder and superspace. Subsequently, the methodology utilized, including a comprehensive background of electron diffraction techniques, will be presented. In chapter 3, the above-mentioned materials will be discussed in detail. The experimental procedures will be explained, followed by the presentation and discussion of the research questions and results. Ultimately, the final chapter will outline the conclusions drawn from this study and discuss the future prospects.

2. Crystallographic background and methods

2.1. Crystallographic basics

2.1.1. Basic concepts

Crystallography encompasses the study of crystal habits, their underlying crystal structures and their physical properties. Crystallographic techniques have been used to develop new materials with specific properties, to understand the structure and functions of molecules and proteins, and to study the geological history of the Earth and other planets. Thus, crystallography has been instrumental in advancing our understanding of properties and behavior of materials, as well as in the study of biological and geological systems [102].

What is a crystal?

A crystal is a three-dimensional arrangement of atoms, ions or molecules. Crystals have long-range order, meaning that the arrangement of the atoms is repeated periodically in space [103]. The ideal crystal structure is described by the smallest repeating motif, the so-called base, and the length and direction of the translation vector

$$R = n_1 a_1 + n_2 a_2 + n_3 a_3, \quad n_i \in Z \tag{1}$$

where the base vectors a_i (i = 1,2,3) are linearly independent, which makes the crystal structure correspond to itself. The chosen vectors represent the axes a, b and c in the so-called unit cell (UC), which is the smallest repeating unit of the lattice. The unit cell is defined by its lattice parameters, which include the length of the edges a, b and c and the angles α, β and γ between them. The position of an atom j in the crystal structure is defined by

$$r_j = x_j a + y_j b + z_j c \tag{2}$$

given in terms of fractional coordinates x_j,y_j,z_j and starting from the origin of the unit cell [104]. The periodic repetition of the base vectors creates a point lattice, also called translation lattice because of its translational symmetry.

Crystals can be classified according to their symmetry and lattice parameters. There are seven crystal systems (triclinic, monoclinic, orthorhombic, tetragonal, trigonal/rhombohedral, hexagonal, cubic) defined by three cell parameters and three angles. In addition to translational symmetry, a crystal can have other symmetry elements. If a primitive unit cell cannot describe the highest symmetry of a crystal, a centered base has to be chosen, which increases the volume of the unit cell. Adding seven centered lattice types to the primitive ones, there are 14 so-called Bravais lattices, which are based on the crystal systems.

There are a set of symmetry operations that, when applied to the unit cell, produce new atomic positions finally pointing back to the original positions. These operations are inversion, mirroring, rotation, translation and combinations thereof [105]. This leads to 32 possible combinations without a translation component, which are called point groups.

By adding translation to the possible symmetry operations, 230 space groups are created. Hence, for the description of a crystal structure only the space group and positions of the symmetrically independent atom positions in the unit cell are necessary. This is called asymmetric unit.

The symmetry of a crystal can affect its properties, e.g. electrical, optical or mechanical. For example, in some materials with a high degree of symmetry, like diamond, the strong covalent bonding between atoms can lead to a very low density of free charge carriers, resulting in poor electrical conductivity [106]. In contrast, in materials with lower symmetry, such as graphite, the weak interlayer bonding can result in a high density of free charge carriers and good electrical conductivity [107]. The symmetry of a crystal can also affect its optical properties by influencing its response to light. For example, in materials with a high degree of symmetry, like quartz, the optical properties can show strong anisotropy [108]. This can lead to the birefringence of light, making the crystal useful in polarization filters and optical devices. The arrangement of atoms in a crystal can also affect its chemical properties. For example, layered crystals can have swelling properties if the sheets have a low charge.

2.1.2. Diffraction

When a flat wave front interacts with an object, it generates multiple spherical waves that interfere with each other. As these waves propagate, their radius increases and they become flatter, appearing planar when detected from infinity. Near-field diffraction, or Fresnel diffraction, occurs close to the source, while far-field diffraction, or Fraunhofer diffraction, occurs far from the source. The latter is used in the TEM to record diffraction images.

Diffraction was first observed in 1665 by Francesco Maria Grimaldi, who noticed that light waves passing through a small hole or slit produced a pattern of bright and dark spots in a screen behind it [109]. With the discovery of the diffraction of X-rays by crystals by Max von Laue in 1912 [110], William Henry Bragg and his son William Lawrence Bragg were able to analyze a special kind of diffraction in the same year [111]. They conducted a series of experiments with sodium chloride crystals and a beam of X-rays to study the diffraction pattern that resulted when the X-rays passed through the crystal. In the sample, incident electron waves are diffracted at the crystal lattice, creating secondary waves that interfere either destructively or constructively depending on their path difference (see Figure 1). This results in the primary beam containing several orders of coherent beams after passing through the sample. The Bragg equation

$$2dsin\theta = n\lambda \tag{3}$$

with λ = wavelength, θ = angle of incidence and reflection, d = distance between the atomic planes and n = order of diffraction, determines the direction of these beams.

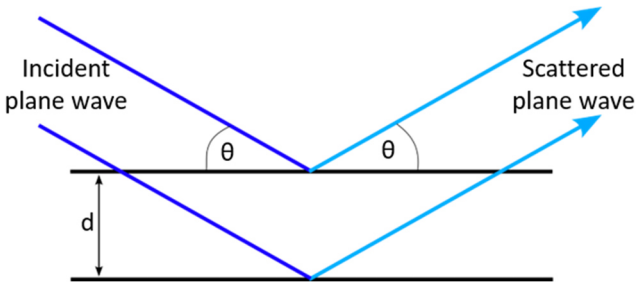

Figure 1: Visualization of the Bragg equation with the incident plane wave being scattered at an angle θ on a lattice plane. The distance between two lattice planes is d.

In diffraction, k_I represents the normal of the incident wave front, while k_D represents the normal of the diffracted wave front. The change of k due to diffraction is represented by the vector K (see Ewald construction Figure 2A)), which can be described by

$$K = k_D - k_I \quad (4)$$

or

$$|K| = \frac{2sin\theta}{\lambda} = \frac{n}{d} \quad (5)$$

If θ corresponds to the Bragg angle, then

$$|K| = 1/d \quad (6)$$

This vector is defined as g, such that

$$K = g \quad (7)$$

Thus, constructive interference of k_I and k_D occurs when this equation is satisfied. Kinematical diffraction is based on Bragg's law and refers to the theoretical analysis of scattering of waves by a crystal lattice without taking into account the interaction between the wave and the atoms in the crystal. This type of diffraction assumes that the crystal has a perfect periodic structure and that the wave passes through without any distortion or absorption. The intensity of the scattered wave is determined by the constructive interference between the waves scattered by the atoms in the crystal lattice.

Reciprocal space

A reciprocal lattice can be established in which all lattice points correspond to the possible g vectors because K is reciprocally related to d. The vector g_{hkl} is described by

$$g_{hkl} = ha^* + kb^* + lc^* \quad (8)$$

where h, k and l intersect the a^*-, b^*- and c^*-axis at 1/h, 1/k and 1/l, respectively. The intensity of the maximum occurring as a reflection (hkl) depends on the scattering potential in direct space present on the plane (hkl) [27]. If the translation lattice of a crystal is known in direct space, the reciprocal lattice is defined uniquely. The basis vectors of the reciprocal lattice, often referred to as a^*, b^* and c^* are can then be calculated by [112]:

$$a^* = 2\pi \frac{b \times c}{a * (b \times c)} = 2\pi \frac{b \times c}{V_{UC}} \quad (9)$$

$$b^* = 2\pi \frac{c \times a}{a * (b \times c)} = 2\pi \frac{c \times a}{V_{UC}} \quad (10)$$

$$c^* = 2\pi \frac{a \times b}{a * (b \times c)} = 2\pi \frac{a \times b}{V_{UC}} \quad (11)$$

where V_{UC} is the volume of the unit cell.

Ewald construction

Alternatively, a geometric construction can be used to describe diffraction and to derive the real space lattice from reciprocal space. It illustrates the dependence of the crystal orientation to the incident beam for satisfying the diffraction condition (see Figure 2B)). It is named after the German physicist Paul Peter Ewald, who introduced the concept in 1913 [113]. In reciprocal space, the Ewald sphere has a radius of $1/\lambda$ and determines whether the Bragg condition is fulfilled for a diffraction spot. If the sphere intersects a spot, it is displayed in the diffraction pattern. The origin of the reciprocal lattice is O. The incident beam is described by

$$k_I = \overline{CO} \tag{12}$$

O lies on the Ewald sphere because it describes the primary beam, which is always visible in the diffraction image. Since k_D is normal to the scattered wave front, it starts from the center of the sphere C and ends at a point on the sphere. For a given wavelength, only certain diffraction spots will be observed. For long wavelengths, the Ewald sphere can only intersect a small number of diffraction spots because of its small radius. This is the case for X-ray diffraction with a wavelength of around 0.2 nm, leading to a need for rotational movement of the crystal. Electron diffraction, however, uses very small wavelengths (0.00197 nm in case of a 300 kV acceleration voltage). This causes the Ewald sphere to be almost flat and cut through a large number of diffraction spots [27].

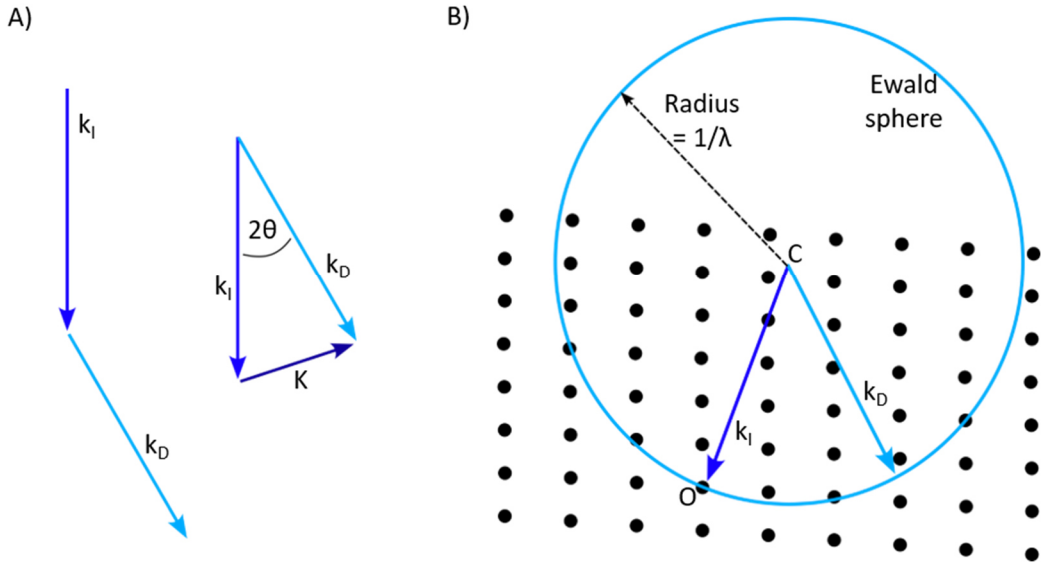

Figure 2: A) The scattering vectors can be defined as the incident wavefront normal k_I and the diffracted wavefront normal k_D. K is the difference vector of them. B) The Ewald sphere has a radius of $1/\lambda$. All points that are intersected by the Ewald sphere appear in the diffraction pattern. For X-rays the sphere can only intersect a few points, as shown. For electron radiation the radius is much larger, leading to more points in the diffraction pattern. (changed after Williams and Carter[27]).

The zone equation

$$uh + vk + wl = 0 \tag{13}$$

can be used to find the zone [uvw] in which several (hkl) are located. In the case of electron diffraction, the reciprocal lattice consists of rods rather than points, which allows reflections to be imaged in the diffraction pattern even if they are not in the exact Bragg condition (see

Figure 3). The intensity of the reflection decreases with increasing distance from the Bragg condition. This distance is called excitation error s with

$$K = g + s \tag{14}$$

If s = 0, then the sphere intersects the diffraction spot at the center of the rod [27].

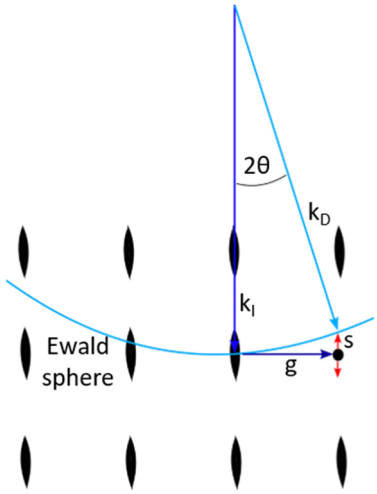

Figure 3: The excitation error s causes reflections that are not in the exact Bragg condition to appear in the electron diffraction pattern.

2.1.3. Structure factor

Structure factor

In kinematical diffraction, the structure factor describes a single scattering of rays by the crystal in terms of amplitude and phase of the scattered waves. The amplitude of the scattered wave is described by

$$F(K) = \sum_{h,k,l} \rho_{hkl} \int_{V_{UC}} e^{i(g-K)*r} dV \tag{15}$$

where ρ_{hkl} is the Fourier coefficient of the scattering density distribution ρ(r). Since there is a coherent addition of the waves, the maximum amplitude is reached for $\exp(i(g-K)*r) = 1$. Thus, there can only be constructive interference when equation (7) is fulfilled [27].

The scattering density distribution can be depicted as the overlapping of the values of N atoms in the unit cell, which is described by the equation [114]

$$\rho(r) = \sum_{j=1}^{N} \rho_j(r - r_j) \tag{16}$$

where r_j is the position of atom j in the unit cell. The amplitude of the scattered wave can then also be described by

$$F(g) = \sum_{j=1}^{N} \int_{V_{UC}} \rho_j(\sigma) e^{ig*(\sigma+r_j)} dV \tag{17}$$

$$F(g) = \int_{V_{UC}} \rho_j(\sigma) e^{ig*\sigma} dV \sum_{j=1}^{N} e^{ig*r_j} \tag{18}$$

$$F(g) = \sum_{j=1}^{N} f_j * e^{ig*r_j} \tag{19}$$

where $\sigma = r - r_j$ and f_j is the atomic structure factor for the different atom types j. The structure factor is then defined as

$$F_{hkl} = \sum_{j=1}^{N} f_j e^{2\pi i(hx_j + ky_j + lz_j)} \tag{20}$$

where F(hkl) is the structure factor for a particular set of Miller indices and x_j,y_j,z_j are the fractional coordinates of atom j in the unit cell. The calculation of the structure factor requires the determination of the electron density at each point in the crystal. This is typically done using Fourier transformation, which involves transforming the electron density distribution from real space into reciprocal space.

Atomic structure factor

The atomic structure factor is the Fourier transform of the form of the scattering potential of one atom j and thus depends mainly on the type of electromagnetic radiation used

$$f_j(K) = \int_j \rho_j(r) e^{iK*r} dr \tag{21}$$

Since the scattering potential of the atoms does not depend on the crystal structure, translational symmetry can be disregarded. This means that K and r can replace g and σ, respectively [112].

The scattering density distribution for X-rays is the electron density distribution. Due to the extended electron shell of an atom in relation to the nucleus, the atomic structure factor for X-rays f_j^X is also called atomic form factor.

For electron radiation the scattering takes place elastically attractive with the nucleus and inelastically repulsive with the electrons. Therefore, the inverse Fourier transform of the atomic structure factor represents the Coulomb potential of an atomic nucleus shielded by the electron shell. The nucleus is treated as a scattering point, whereas the charge distribution of the electrons is assumed to be spherically symmetric. The direct relationship with the atomic form factor for X-rays and the atomic number Z is described by the Moth-Bethe formula [115]

$$f_j^{el}(K) = \left(\frac{\lambda}{2sin\theta}\right)^2 (Z - f_j^X(K)) \tag{22}$$

All atomic structure factors for electron and X-ray radiation are tabulated in the International Tables for Crystallography, Vol C [116].

2.1.4. Interaction of electrons with matter

Electron as wave/particle

Electrons are known to exhibit properties of both waves and particles, a concept known as wave-particle duality. This idea was first proposed by Louis de Broglie in 1924 and later confirmed by experiments such as the double-slit experiment [117]. The wave-like behavior of electrons can be described using the de Broglie equation

$$\lambda = \frac{h}{p} \tag{23}$$

where λ is the wavelength of the electron, h is Planck's constant and p is the momentum of the electron. In the field of electron diffraction this duality is important. The description of an electron as a wave allows the explanation of diffraction phenomena in which an incident electron wave, through interaction with atoms, generates secondary waves that interfere with each other, producing a diffraction pattern. The particle-like behavior is important to image the surface of a sample at high resolution.

Interaction with an atom

When the incident electron beam hits the sample, it interacts with the electric field of the sample's atoms producing various primary and secondary signals that contain information about the materials' structural and chemical properties (see Figure 4). Scattering of the electrons can occur in any direction, but it is strongest in forward direction. The thickness of the sample affects the area where an interaction can take place and more electrons are backscattered with thicker samples. Although an electron can scatter multiple times, single scattering is usually assumed due to the difficulty of interpreting results when the primary beam is scattered multiple times (see chapter 2.1.5).

Fast electrons are scattered with little or no energy loss, interacting with the electron cloud of the atom and scattering at an angle of less than 10°. This so-called elastic scattering is usually coherent in thin crystalline samples, i.e., the scattered beam retains the phase relationship of the primary beam. However, some elastically scattered electrons are attracted by Coulomb forces from the atomic nucleus and scattered at a higher angle, which is called Rutherford scattering. The probability of Rutherford scattering is described by the following equation

$$\sigma_R(\theta) = \frac{e^4 Z^2}{16(4\pi\varepsilon_0 E_0)} \frac{d\Omega}{\sin\left(\frac{\theta}{2}\right)^4} \tag{24}$$

with Z = atomic number, ε = electrical constant ~ 8.85*10^{-12} F/m, E_0 = primary energy, θ = scattering angle and dΩ/dσ = the probability of particle scattering.

Contrary to this, during inelastic scattering electrons lose energy as they interact with the atom. It is always incoherent. In this process, the total energy and momentum of the electrons are not conserved. This can result in excitation or ionization of atoms or the emission of secondary electrons or photons.

Scattering is dependent on the primary energy, atomic number of the scattering atom, as well as the thickness, density, crystallinity and the angle of the sample to the incident beam. The effective cross section σ describes the likelihood of the incident beam interacting with an atom

with each interaction having its own cross section of action σ. The mean free path is the average distance between scattering events and is described by

$$\lambda = \frac{1}{\sigma_{total}} \tag{25}$$

with typical values for λ in the range of tens of nanometers for single scattering. σ_{total} decreases with increasing accelerating voltage and increases with increasing sample density, requiring thinner samples for single scattering in higher density samples. The distribution of scattered beams can be visualized in two ways in a transmission electron microscope (TEM): spatially resolved in imaging mode as contrast and directionally resolved in diffraction mode as diffraction spots [27].

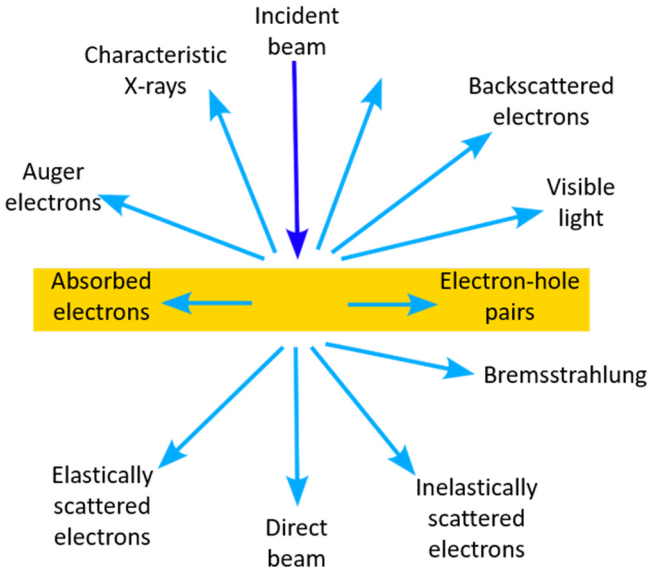

Figure 4: Interactions of the incident beam with the sample (changed after Williams and Carter [27]).

2.1.5. Dynamical effects

Dynamical diffraction is a more complete and sophisticated theory of wave scattering by a crystal lattice compared to kinematical diffraction. In dynamical diffraction the wave is scattered and transmitted by the crystal and undergoes further scattering by the atoms in the crystal (see Figure 5). Unlike kinematical diffraction, it takes into account the interactions between the wave and the atoms in the crystal and considers the wave as a propagating field rather than a simple plane wave. Incident electron waves can be scattered by the atomic potential. Atom columns with high atomic potentials act as electrostatic lenses, leading to an increased occurrence of dynamic effects. The effects increase with the height of the scattering potential, i.e. along atom columns in oriented zones, when atom columns contain strong scatterers and with increasing sample thickness. Dynamical diffraction leads to changes in the intensities of the diffraction image and possibly breaking reflection conditions [27].

Dynamic effects can be described using different theories. For imaging purposes, the multislice method is commonly employed, which is used to simulate the propagation of electron waves through a crystalline sample. This approach considers the interactions of the electron beam with the crystal as discrete slices or layers.

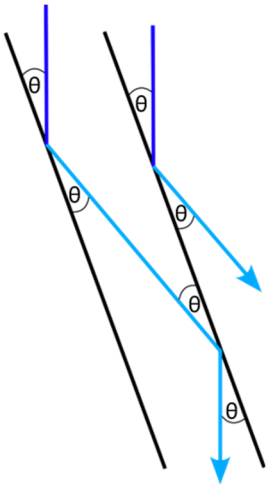

Figure 5: Dynamical scattering. If the incident beam is scattered according to the Bragg equation it has the perfect orientation to be scattered again multiple times.

For diffraction studies, the use of Bloch waves is the dominant approach. The electron wave function is described as a Bloch wave, which is a solution to the Schrödinger equation with a periodic potential. The Bloch wave function at position r in the crystal for the wave vector k can be expressed as

$$\Psi(k,r) = u(k,r) * e^{ik*r} \tag{26}$$

where Ψ is the wavefront, u(k,r) is the periodic part of the Bloch wave, which is typically the lattice potential and e^{ik*r} is the plane wave part representing the wave's propagation in space. Since the crystal lattice's periodicity is explicitly included in the Bloch wave function, it provides a natural framework to analyze how waves are affected by the lattice potential as they propagate though the crystal. Unlike the kinematic scattering approximation, the Bloch wave approach fully accounts for multiple scattering events, providing a more accurate description of the diffraction process.

2.2. Disorder

As described in chapter 2.1.2, perfectly ordered crystals show discrete reflections in their diffraction patterns. In addition to the vibrational motion of the atoms, there is a large number of dynamic and static structural defects (disorder) in real crystals, which can violate the translational symmetry and have an effect on the material's behavior and properties. The transition from a 3D long-range order to an amorphous crystal is fluent and described by the crystallinity, which can be difficult to quantify. Disorder can arise from a variety of defects, including vacancies in the crystal lattice, the presence of impurities or foreign atoms or variations in the atomic arrangement. Depending on the type and amount of defects in the crystal lattice, the reflections become more diffuse.

Defects

Point defects occur at individual lattice sites and can further be divided into two categories: vacancies and interstitial defects. A vacancy occurs when an atom is missing from its lattice site, leaving behind an empty space. An interstitial defect occurs when an atom occupies a site that

is not normally part of the lattice. Additionally, one atom type can be substituted with another of similar size and charge.

Line defects, also known as dislocations, occur when there is a deviation in the regular pattern of atoms along a line within the crystal lattice. This can be caused by a variety of factors, such as plastic deformation or thermal stress. They can be classified into two types: edge dislocations (step-like distortion) and screw dislocations (helical distortion).

Planar defects occur at interfaces. If the interface is between two crystals with different orientations, they are called grain boundaries. Layered structures in particular often tend to have stacking sequences, which do not follow a strict periodicity. A so-called stacking fault is created if a layer is arranged in a position contradicting the stacking order. In layered structures this happens when several orientations of the layers to each other are possible with similar energy during growth.

There are various distributions of stacking faults possible, which can be classified into groups. For twinning, the stacking sequence is reversed (see Figure 6A)). In this case, there is only one stacking fault and the periodicity is continued from the layer that is shifted. A displacement is caused by a shift of an individual in relation the other another individual (see Figure 6B)) [118]. If these types of stacking faults occur often and in short distances an intergrowth is created (see Figure 6C)).

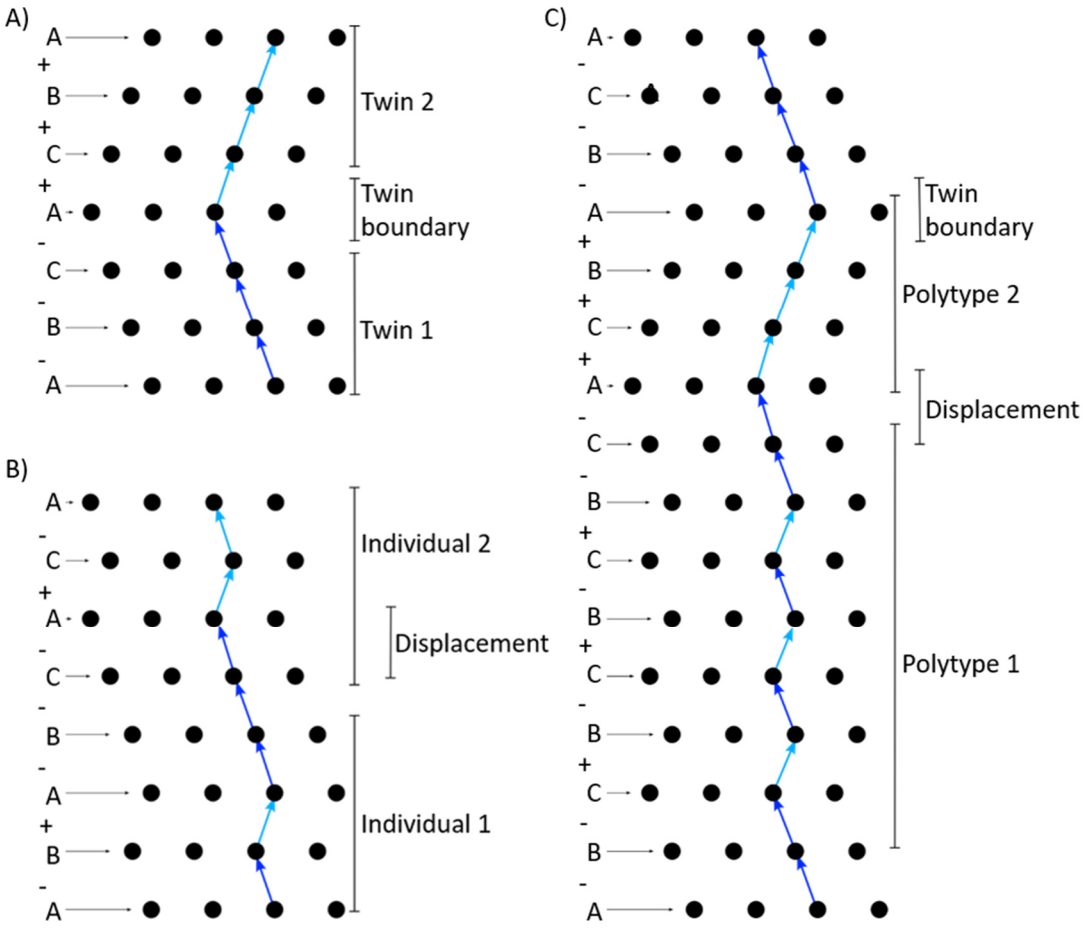

Figure 6: Three different types of stacking faults. A) twinning, B) displacement and C) intergrowth (Illustration adapted after Krysiak [119]).

The presence of crystal defects can have a significant impact on the physical properties of materials. For example, the presence of impurities as point defects can alter the properties of materials, while dislocations can affect mechanical properties like ductility and strength. Grain boundaries can affect properties like electrical conductivity and corrosion resistance. While some forms of disorder may be undesirable, others can be intentionally introduced or manipulated to achieve specific functions. For example, defects also play an important role in many industrial processes, such as the strengthening of metals through heat treatment or the production of semiconductor devices through the introduction of impurities[120].

Diffuse scattering

Crystal defects often result in measurable interference in diffraction experiments, which can be observed as shifted positions with reduced intensity in the diffraction pattern compared to the Bragg reflections of ideal crystals. This additional interference is called diffuse scattering and can provide valuable information about the type of disorder present in a crystal. Table 1 provides a general overview of these relationships.

Table 1: Relationship of the dimension of the defect in real space to the dimension of diffuse scattering in reciprocal space.

Type of defect	Type of diffuse scattering
0D, point defect	3D, anisotropic and disordered
1D, line defect	2D, planes perpendicular to the line defect in real space
2D, planar defect	1D, streaks perpendicular to the planar defect in real space
3D, volume defect	0D, additional intensity

The intensity distribution in reciprocal space can be calculated as

$$I(hkl) \sim \left(\sum_{j}^{N} f_j e^{2\pi i(hx_j+ky_j+lz_j)}\right)^2 \tag{27}$$

with each layer contributing

$$I(hkl) \sim \left(\sum_{j}^{N} f_j e^{2\pi i(h(x_j+\Delta x)+k(y_j+\Delta y)+l(z_j+\Delta z))}\right)^2 \tag{28}$$

$$I(hkl) \sim \left(\sum_{j}^{N} f_j e^{2\pi i(hx_j+ky_j+lz_j)} * e^{2\pi i(h\Delta x+k\Delta y+l\Delta z)}\right)^2 \tag{29}$$

The position of each layer is described by Δx, Δy and Δz. For an ideal crystal, these displacement terms are zero for all layers, making them identical. This factorized expression can be useful in qualitatively analyzing diffraction patterns, as the systematic occurrence of diffuse scattering for certain classes of reflections can provide information about the shift vectors of the layers.

By analyzing the extinct diffuse scattering in a diffraction pattern, it is possible to determine the shift vector. To illustrate this, a 2D structure is considered where layers can be shifted by *½b* (see Figure 7A)). For a constant layer distance, the diffraction patterns of the (0kl) reflections will show different patterns of diffuse scattering depending on the shift vector. In the case of *½b* every other line is diffuse ($k = 2n$) (see Figure 7B)). The expression

$h\Delta x + k\Delta y + l\Delta z = n$ can be simplified to $k\Delta y = n$. Since $k = 2n$, the displacement must be $\Delta y = ½$.

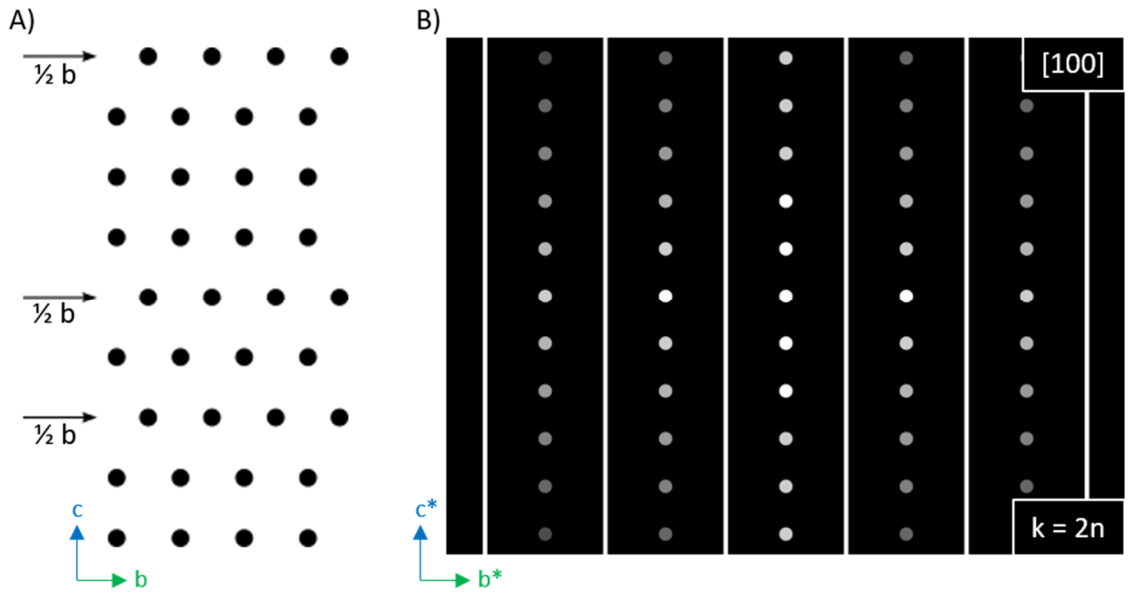

Figure 7: A) Sketch of an atomic lattice with the shift vector ½*b*. B) Sketch of a diffraction pattern of the zone [100] consistent with the structure from A) containing diffuse scattering caused by the disorder in the structure. Every second line of diffraction spots along *b** is smeared (*k = 2n*) leading to a shift vector of ½*b*.

Simulation

If diffuse streaks appear in the diffraction pattern of a layered structure, it may be possible to simulate them using generated structure models. Successfully modeling aperiodic layer structures depends on having chemical and structural knowledge of the layers that make up the structure, thus, the average structure should be solved beforehand. Alternatively, a model based on a similar structure can be used.

For periodic structures, equation (20) can be used to calculate the structure factor and the resulting intensity distribution (see equation(27)). In case of a macroscopic ideal crystal, the total scattering amplitude is then calculated with

$$A(K) = \sum_{N=1}^{N_{UC}} F_N e^{iK*R_N} \qquad (30)$$

using

$$F_N = \sum_{j=1}^{N_A} f_j e^{iK*r} \qquad (31)$$

where F_N is the structure factor of the n^{th} unit cell expressed with the scattering vector K and the number of atoms N_A. R_N represents the position vector of the n^{th} cell and N_{UC} is the number of unit cells in the ideal crystal. The relative intensity is given by the squared magnitude of the amplitude (* = conjugate complex)

$$I(K) \sim A(K)A^*(K) \qquad (32)$$

$$I(K) \sim \sum_{N} \sum_{N'} F_N F_{N'} e^{iK*(R_N - R_{N'})} \tag{33}$$

For structures in which layers of atoms remain as a perfect unit, the summation should be over the atoms of the layers. F_N would thus be a layer form factor and the summation over N would imply an interdimensional arrangement of points defining the origin of each of the layers. For an equidistant stacking, the points have a layer spacing of a_3 such that $R_N = N * a_3$. Thus, a layered structure can be generated by a convolution product of the atomic positions within a single layer type with the list of layer positions. Using the convolution theorem, the diffraction pattern is the Fourier transform of the convolution product

$$\mathcal{F}(g \otimes h) = \mathcal{F}(g) \cdot \mathcal{F}(h) \tag{34}$$

which is the product of the individual Fourier transforms. Thus, it is sufficient to simulate the atomic positions within a single layer as well as the list of layer positions. These individual Fourier transforms require much less computing time than the Fourier transform of the full crystal.

In systems with N layers, a certain amount m_A can be assigned to layer A and to layer B with $m_B = 1 - m_A$. Sorting the summation equation (33) by pairs of layers in the direction of the third dimension a_3, with the distance $R_N - R_{N'} = |n_3|a_3 = na_3$, for two types of layers there are four pairs of layers of order n whose probabilities are expressed by P_n^{AA}, P_n^{BA}, P_n^{AB} and P_n^{BB} and whose sum must be one. The order n represents the distance between two layers of a layer pair and is a crucial parameter for determining the short-range order (SRO). The ratio of the layers m_A and m_B equals the probabilities of the mixed layer pairs $m_A = P_n^{AB} + P_n^{AA} = P_n^{BA} + P_n^{AA}$ and $m_B = P_n^{AB} + P_n^{BB} = P_n^{BA} + P_n^{BB}$. The correlation coefficient C_n is defined in relation to P_n^{AA}

$$C_n = \frac{(P_n^{AA} - m_A^2)}{m_A * m_B} \tag{35}$$

and can be used to express the probability of the layer pairs dependent on

$$P_n^{AA} = m_A^2 + C_n m_A m_B$$

$$P_n^{AB} = P_n^{BA} = m_A m_B + C_n m_A m_B$$

$$P_n^{BB} = m_B^2 + C_n m_A m_B$$

After sorting, the intensity can be expressed independent from C_n with

$$I(K) \sim (m_A F_A + m_B F_B)(m_A F_A^* + m_B F_B^*) \sum_{n=-(N-1)}^{N-1} e^{iK*na_3} \tag{36}$$

$$+ m_A m_B (F_A - F_B)(F_A^* - F_B^*) \sum_{n=-(N-1)}^{N-1} C_n e^{iK*na_3}$$

The intensity fraction of the ideal crystal is described by the first term $F = m_A F_A + m_B F_B$, which is the average layer form factor, while the second term describes the diffuse intensity and is defined by the difference of the two layer form factors [121,122].

C_n indicates the strength and direction of a linear relationship between layer pairs of order n = 1. Positive correlations have values between 0 and 1, while negative correlations have values between 0 and -1. If $C_n = 0$ there is no linear relationship between the pairs of layers. When two layer types are stacked, $C_n = 0$ at a given m_A results in a random layer sequence (see Figure 8A)). Positive correlation occurs independently of the layer ratio (see Figure 8B)), whereas negative correlation depends on the layer ratio. The correlation between pairs of layers can only be in the range of $-m_A/m_B < C_n > 1 + m_A/m_A$ or $-m_B/m_A < C_n > 1 + m_B/m_B$, respectively [122]. For example, a perfect …ABAB… sequence requires an equal ratio of $m_A/m_B = 1$ in addition to C_n = -1 (see Figure 8C)).

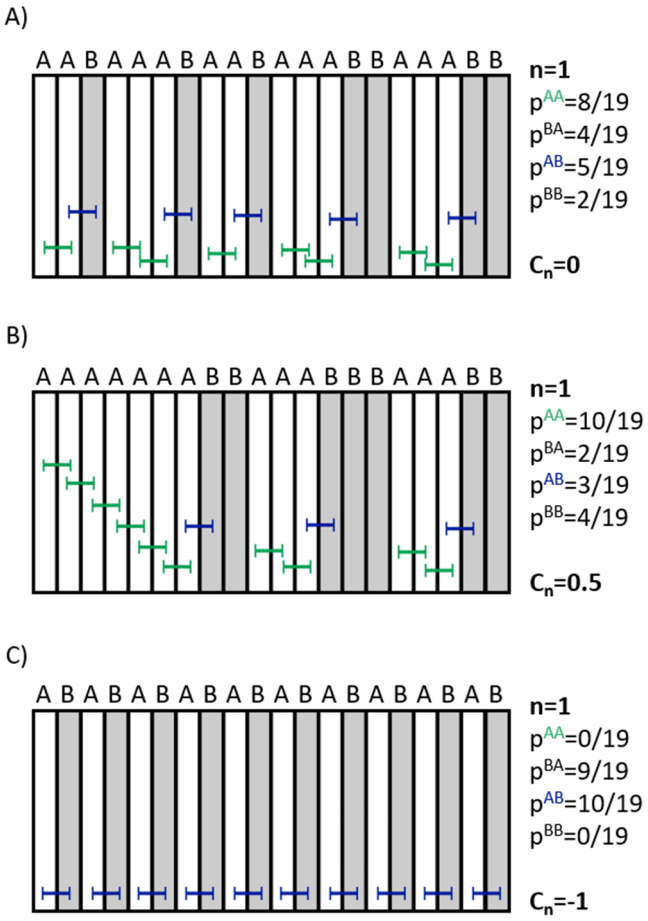

Figure 8: Layer sequences with identical number of layers N = 20. A) and B) have the same layer A and layer B ratio with m_A = 13/20 and m_B = 7/20; C) has an equal amount of layer A and B. The probabilities are different for layer pairs of the first order n = 1 for A), B) and C). The correlation coefficient C_n is 0 for A), 0.5 for B) and -1 for C), respectively. (Illustration adapted after Krysiak [119])

In order to create stacking sequences utilizing two or more types of layers with specific parameters m_A and C_n, simulations are required. The Monte Carlo method, for example, has been widely adopted [123].

The functions needed for disorder simulation are contained in the program DISCUS (Diffuse Scattering and Defects in Crystalline Materials Using X-Rays) [124]. The program is capable of extracting information on defects, distortions and other non-periodic features from the diffuse scattering data. It works by modeling the crystal structure as a perfect lattice and then introducing deviations to account for the observed diffuse scattering. The program allows for the incorporation of different types of disorder, such as stacking faults, vacancies and local

distortions. The program uses different types of simulation approaches to model the crystal structure, allowing for the calculation of the expected diffuse scattering pattern of the model. This pattern can then be compared to the experimental data to refine the model parameters. The program has been used in a wide range of applications, including the study of disordered materials, defects in metals and semiconductors and the investigation of proteins structures.

Disorder in sheet silicates

Disorder in sheet silicates can present itself in a number of ways, including positional disorder, faulting and stacking disorder [125]: Positional disorder can occur due to the replacement of one atom by another in the crystal structure. For example, in biotite, Fe^{3+} can substitute for Mg^{2+} [126]. Faulting can arise due to a disruption of the crystal structure along certain planes, resulting in a change in the layer stacking sequence. This can happen because of defects in the crystal structure or due to the presence of impurities. For example, in chlorite faulting can occur due to the presence of Mg^{2+}, resulting in a change of the stacking sequence of the layers [127]. Disorder in the arrangement of the layers within the crystal structure leads to a stacking disorder. For example, in montmorillonite stacking disorder arises from the presence of different types of layers with different orientations [128]. The disorder can affect the mineral's chemical reactivity and its ability to interact with other substances.

2.3. Superspace

Disorder is not the only example of a crystal losing its 3D translational symmetry. Aperiodic crystals are another exception, as they lack translational symmetry but still produce distinct reflections in their diffraction patterns. These structures can arise due to various factors, such as temperature changes, pressure changes or the presence of impurities. However, indexing the reflections with only three integer indices can pose a challenge.

Different types of aperiodic crystals

Aperiodic crystals can be classified into three different types: quasicrystals, incommensurate composite crystals and incommensurately modulated crystals [129].

Quasicrystals are solid materials that require the use of non-crystallographic point symmetries, such as five-fold or eight-fold. As a result, a space of more than three dimensions is necessary to accurately describe the positions of the reflections [130].

Incommensurate composite crystals result from the intergrowth of two periodic crystal structures. When the sub-systems share a common periodicity along the stacking direction, one direction parallel to the layer is incommensurate with respect to the other layer, requiring an irrational number of unit cells to retrieve periodicity along this direction. Consequently, the atomic arrangement of these crystals results in diffraction patterns containing strong main reflections surrounded by weaker reflections that cannot be indexed using the three Miller indices of the two sub-systems. These reflections are known as satellites [131].

Incommensurately modulated structures are characterized by a translational periodic average structure that can be established by disregarding the satellites. However, the true atomic positions in the crystal are defined by modulation functions. Consequently, the averaged structure and atomic positions modulated by special functions recover a perfect long-range order without 3D translational symmetry.

Incommensurately modulated structures

To properly fit all observed reflections and recover the translational symmetry in diffraction patterns that exhibit satellite reflections, the concept of superspace is needed, which involves a (3+d)D space [132]. To achieve this, a new reciprocal base vector, called modulation vector q, is introduced, which connects the main reflection to its corresponding satellite reflection. It is defined as the difference between the wave vector of the satellite reflection and that of the main reflection

$$q = \delta h a^* + \delta k b^* + \delta l c^* \tag{37}$$

where δh, δk and δl are coefficients that define the modulation vector. At least one of them must be irrational to fulfill the property of incommensurability. If not, a supercell can be selected to index all reflections and the structure would be commensurately modulated. Because the intrinsic nature of an experiment cannot distinguish between rational and irrational numbers, a structure is considered incommensurate if the denominator of the rational approximation of at least one of the coefficients of the modulation vector is large enough [133]. The magnitude of the modulation vector is given by the distance between the main reflection and the satellite reflections. The satellites are located at ±mq distance from the main reflections and there is no limit to the number of modulated wave vectors required to index all reflections. The integer number m defines the order of the satellites for a given q and its maximum m_{max} is set according to the observable satellite intensities in the diffraction pattern. In exceptional cases, satellites up to the 9th order have been found [134].

After defining the modulation vectors, any reciprocal lattice vector in the constructed superspace can be represented as

$$g_s = \sum_{k=1}^{3+d} h_{s,k} a^*_{s,k} \tag{38}$$

The parameter d indicates the additional numbers of dimensions required to index all reflections, and $a^*_{s,k}$ refers to the reciprocal base vectors of the reciprocal superspace Σ*. These vectors can be described as

$$\Sigma^* = \begin{cases} a^*_{s,i} \equiv (a^*_i, 0) & i = 1,2,3 \\ a^*_{s,3+j} \equiv (q_j, b^*_j) & j = 1, \dots, d \end{cases} \tag{39}$$

where $a^*_{s,i}$ represents the reciprocal lattice base in the 3D space, $a^*_{s,3+j}$ denotes the additional base defined from the 3D space and the extra components b^*_j of the reciprocal superspace, which are perpendicular to the 3D space. Figure 9 illustrates Σ* for a 3+1D incommensurately modulated structure. As it is not possible to depict a 4D space in a 2D plane or 3D volume, the 3D diffraction space is folded in a line while the extra dimension is shown perpendicular to this line. The position of each reflection is projected into the 3D space along the directions defined by b^*_j in the reciprocal superspace. The equation (42) can be extended to include the possible modulation of a crystal structure as

$$g = \sum_{k=1}^{3+d} h_k a^*_k \tag{40}$$

, where a^*_k are a^*, b^*, c^*, q_1, …, q_d. To obtain the superspace in real space, the reflection intensities and the positions are first brought from 3D reciprocal space to the reciprocal superspace. Then, the inverse Fourier transform is applied to retrieve the electrostatic potential or electron density in the real super space.

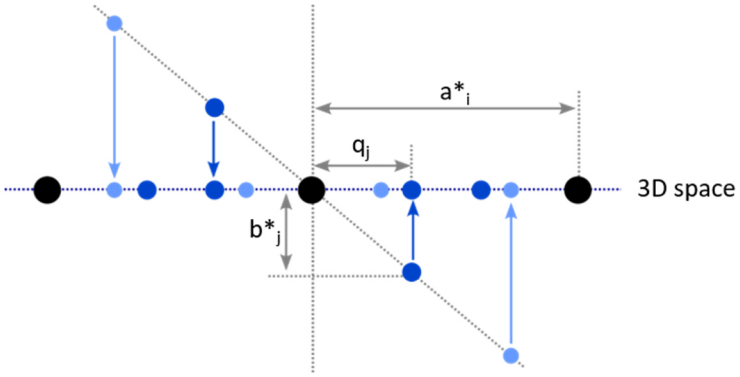

Figure 9: Depiction of the reciprocal superspace of a 3+1D incommensurately modulated structure. The main reflections are displayed in black, the satellite reflections of the first order in dark blue and of the second order in light blue. The blue dashed line shows the projection of the 3D reciprocal space onto a line. The vertical dashed line is the extra dimension, which represents the reciprocal superspace. The diffraction patterns of such structures are the projection of the reciprocal super space into the 3D reciprocal space along b^*_j. q_j is the modulus of the modulation vector along a^*_i in the 3D reciprocal space.

To visualize the obtained potential, a similar approach to Figure 9 needs to be followed, as shown in Figure 10. First, the positions of the base vectors *a1*, *a2* and *a3* have to be identified in real superspace with respect to *q*. The modulation vector defines the orientation of the real 3D space inside the real superspace with the extra dimension being defined perpendicular to the entire 3D reciprocal space. The concept of superspace implies that atomic positions are not fixed positions but are domains expanded along the extra dimensions, known as atomic domains [135].

Types of modulations

The modulation of atomic positions is the most commonly observed type, known as displacive modulation. However, occupational and thermal modulation can also occur, where atomic occupancies and displacement parameters are modulated, respectively. Structural modulations are generally continuous and described by a finite number of parameters, often using a truncated Fourier series to accurately depict all the satellite intensities [136]. In stronger modulated structures, discontinuous functions such as crenel and saw tooth functions are necessary to properly fit the electrostatic potential [137]. Figure 10 shows an example of an atomic domain following a harmonic function along the extra dimension $a_{s,4}$ in a ($x_{s,1}$, $x_{s,4}$) section of the superspace, also known as de Wolff section. Each 3D section of the superspace at different modulation phases t between 0 and 1 corresponds to a possible aperiodic 3D unit cell. The translational symmetry is recovered in superspace, hence the resulting potential is periodic as well and a superspace symmetry can be derived.

The symmetry of aperiodic crystals cannot be described by using traditional point groups. Van Smaalen introduced the concept of a superspace group. It includes the space group symmetry of the underlying crystal structure, as well as the symmetry of the modulation itself [129]. These additional operations include fractional translations and rotations that are not present in conventional space groups. For example, in the space group $X\bar{1}(\alpha\beta\gamma)0$, X denotes a non-standard centering, $\bar{1}$ refers to a triclinic point group and (αβγ) indicates that the modulation

vector has components along all main directions (δh, δk, δl). The 0 denotes the absence of any further translations. These operations can be identified using guidelines from Sander van Smaalen [129] or tables from the International Tables for Crystallography Vol. C [116].

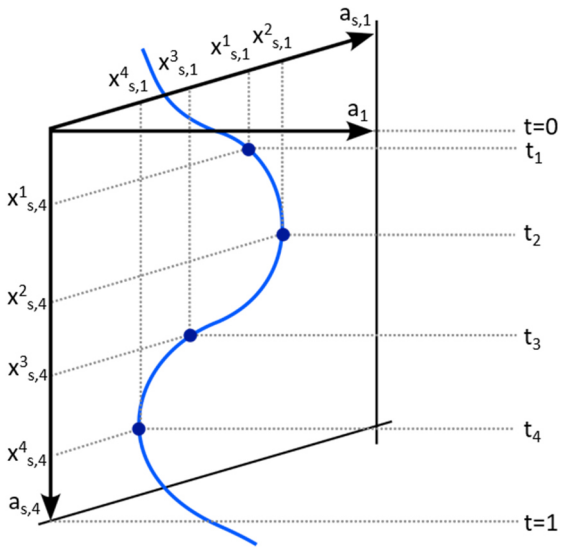

Figure 10: A ($x_{s,1}$,$x_{s,4}$) de Wolff section of an atomic domain, which is represented by the blue line. a_1 is the basis vector a of the 3D unit cell. $a_{s,1}$ and $a_{s,4}$ are two basis vectors of the superspace unit cell. The dashed lines labeled as t_i represent the different 3D sections of the superspace, which retrieve the aperiodic 3D representation of the atom domain with their coordinates ($x^i_{s,1}$,$x^i_{s,4}$).

2.4. Scanning electron microscopy

Scanning electron microscopy (SEM) is a type of electron microscopy that uses a focused beam of electrons to create surface images point by point. In SEM, a beam of high-energy electrons is focused onto the surface of a sample, which causes several different types of signals. Some of the primary electrons are scattered back by the atoms in the sample, producing back scattered electron (BSE) signals. These are sensitive to the atomic number of the material and provide information about its composition and density (see Figure 11A)). The electron beam can knock secondary electrons (SE) out of the sample. They can be used to image the surface topography of the sample (see Figure 11B)). When the primary beam interacts with the sample, it can also excite the atoms, causing them to emit characteristic X-rays or Auger electrons (see chapter 2.7). These signals can be detected and used to identify the chemical composition of the sample. The electron beam can also cause certain materials to emit light. This so-called cathodoluminescence (CL) is useful for imaging optical and electronic properties (see Figure 4 in chapter 2.1.4).

One of the main advantages of the SEM is the ability to operate under a wide range of conditions, including high vacuum, low vacuum and even in the presence of a gas or liquid environment (Environmental SEM; ESEM). This allows researchers to study samples in conditions that more closely mimic real-world scenarios [138].

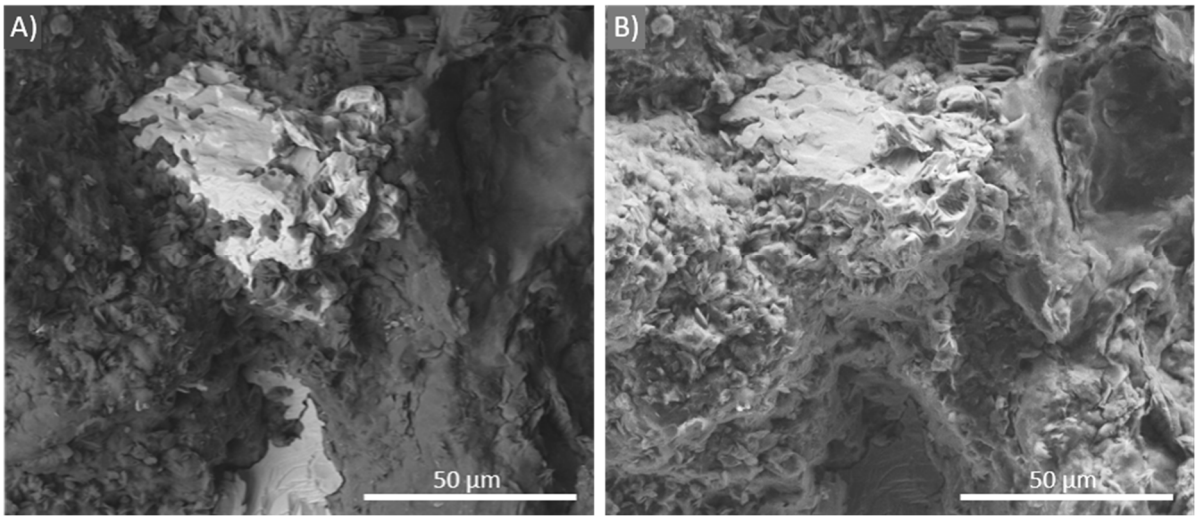

Figure 11: SEM images of the same position of a sandstone containing barite in a clay mineral matrix. A) The SEM-BSE image shows Z contrast, making the barite grain appear very bright compared to the clay mineral matrix. B) The SEM-SE image shows the surface topography of the sandstone. The barite grain cannot be distinguished from the clay mineral matrix.

2.5. Transmission electron mciroscopy

2.5.1. Introduction

Characterization on a nanometer scale plays a crucial role in understanding the properties and behaviors of various materials. Transmission electron microscopy (TEM) is one of the most powerful tools for analyzing the structure and properties of materials at said scale. It is a high-resolution imaging and diffraction technique that uses an electron beam to image and analyze samples with a thickness of a few tens of nanometers. It works on the same principle as conventional optical microscopy, but here an electron beam is transmitted through a thin sample and focused onto a fluorescent screen or detector to form an image. However, because electrons have much shorter wavelengths than light, TEM can provide much higher resolution than optical microscopy. It can provide information on the crystal structure, crystallographic orientation, defects and composition of materials. It can also be used to study mechanical, electrical, magnetic and optical properties, as well as the microstructure of materials, including grain size, morphology and texture [139].

2.5.2. Components

A TEM consists of a source, illumination unit, objective, magnification unit and detector. The illumination system in a TEM is responsible for producing a high-quality electron beam with a well-defined spatial coherence and a high degree of monochromaticity.

Gun

A key component of a TEM is the electron source, which generates an electron beam that is focused onto the sample. There are different types of electron sources, each with its own advantages and disadvantages. The most common type of electron source is a thermionic source, which uses heat to release electrons from a tungsten filament. When a high voltage is applied, electrons are emitted from the filament and accelerated towards the sample. Thermionic sources like tungsten carbide (WC) or lanthanum hexaboride (LaB_6) are reliable and produce a stable beam, but they have limited brightness and can suffer from contamination

of the filament. Field-emission sources use a sharp tungsten or carbon tip where a high electric field is applied. Electrons are emitted from the surface due to the quantum mechanical phenomenon of electron tunneling. Cold field-emission guns (FEGs) can produce a highly focused beam with high brightness. Thermally assisted Schottky FEGs facilitate the electron emission by heating a tungsten tip which is coated in zirconium oxide, thus, combining the benefits of thermoionic and field-emission sources. This creates a better stability and higher possible currents. However, compared to a cold FEG, they have a shorter lifetime and a slightly worse image quality. The choice of electron source depends on the specific application and requirements of the experiment. For high-resolution imaging and analysis, FEGs or cold FEGs are often used. For routine imaging, thermionic sources are sufficient. Specialized sources, such as photoelectron and plasma sources, are used in particular applications such as surface analysis and ion-beam milling.

Illumination system and objective lens

The condenser lens system is responsible for shaping the electron beam to provide optimal illumination of the sample. The first condenser lens (C1) creates a reduced image of the electron source. This so-called spot size determines the beam diameter when the second condenser lens (C2) is focused. The C2 lens creates an image of C1 and its aperture limits the beam's convergence, reducing the beam convergence angle α and the brightness. To achieve parallel irradiation of the sample, α should be minimized. The collection angle β is established when the scattering angle θ is limited by an aperture, resulting in an Airy disk as the aperture diameter decreases, resolution decreases (see Figure 12).

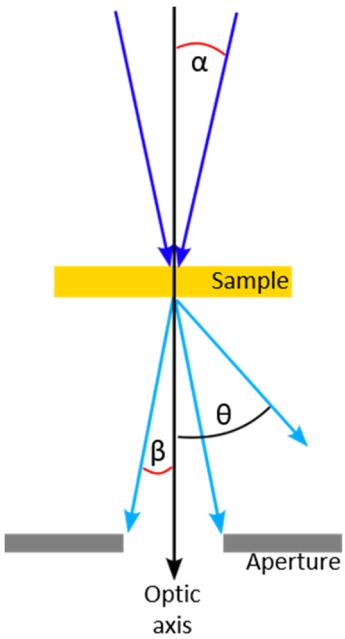

Figure 12: The beam-convergence angle α should be kept as small as possible. The scattering angle θ can be reduced to the collection angle β by an aperture (changed after Williams and Carter [27]).

Since the object distance u in the equation

$$M = \frac{v}{u} \tag{41}$$

where M is the magnification and v the image distance, is extremely small, the sample must be positioned as close to the center of the objective lens as possible. This issue is addressed by utilizing two lenses directly above and below the specimen as the objective lens, enabling the sample to be at the eucentric height, or the focal point of the objective lens, to prevent oscillation when tilted.

The selected area electron diffraction (SAED) aperture is located in the first image plane of the objective lens. It can be used to select specific areas for diffraction imaging. The nominal distance between the sample and the diffraction image plane is determined by the effective camera length, which is calculated from the lens' focal length and magnification. The intermediate lens switches between the diffraction and image planes, with the image forming in the image plane and the diffraction image forming in the back focal plane of the objective lens [27].

Aberrations and distortions

Due to the high resolving power of the TEM, it is susceptible to various types of aberrations that can affect image quality and limit resolution:

- Chromatic aberration (C_C): Occurs when electrons of different energies are focused on different points along the optical axis, resulting in a blurred image.
- Spherical aberration (C_S): Happens when electrons, which are scattered at high angles are not focused on the same point as electrons, which are scattered at low angles.
- Astigmatism: Arises when the focus of the electrons in the horizontal and vertical directions is different, resulting in an image that is elongated in one direction.
- Coma: Causes the image to appear distorted at the edges, forming a comet-like shape. This aberration arises due to the non-uniformity of the magnetic field across the aperture of the lens.
- Distortion: Occurs when the electron path varies throughout the sample.

To improve the resolution and image quality, various methods have been developed to correct aberrations. One such method is the use of aberration-corrected lenses, which can correct for both spherical and chromatic aberrations. Another approach is the use of image processing techniques, such as Fourier filtering, to reduce distortion and improve image contrast [27].

2.5.3. Imaging vs. diffraction

Imaging

Three types of contrast can be observed in the TEM: diffraction, thickness and mass contrast. One of the most commonly used imaging modes is bright-field (BF) imaging (see Figure 13A)). Here, diffraction contrast arises due to the fact that only the primary beam (and possibly some diffracted beams) is captured by the objective aperture. Locations within the specimen where diffraction occurs appear dark since this information is not contained in the selected beam. In contrast, in dark-field (DF) imaging only diffracted rays are selected within the objective aperture (see Figure 13B)), causing areas of the sample where diffraction occurs to appear bright.

Mass contrast can also be detected in bright-field mode, as atoms with higher atomic number scatter more and thus less information about them is contained in the primary beam. As a result, these areas appear darker [27].

Diffraction

In order to record diffraction in the TEM, the back focal plane of the objective lens can be imaged on the detector by adjusting the focal length of the intermediate lens (see Figure 13C)) [140]. There are three main types of diffraction modes: selected area electron diffraction (SAED), convergent beam electron diffraction (CBED) and nanobeam diffraction (NBD). SAED is produced by illuminating a larger area of the sample and selecting a specific area for diffraction with the help of the selected area aperture. For CBED the electron beam is focused to achieve a small convergence angle. This way, diffraction discs containing additional patterns are revealed, which can be used to gain structural information [141]. NBD involves using a highly focused electron beam to obtain diffraction patterns from nanometer-sized regions of the sample. This method is further explained in chapter 2.5.5.

Dynamical diffraction can have severe effects on a diffraction pattern. The effects depend on the crystal structure, thickness and orientation of the crystal as well as the energy and coherence of the electron beam. One of the most significant effects of dynamical diffraction is the appearance of extinction contours in the diffraction pattern. Extinction occurs when the diffracted wave is out of phase with the incident wave and interferes destructively, leading to a decrease in the intensity of the diffracted beam. Another effect is the broadening of the Bragg peaks in the diffraction pattern. This broadening arises from the multiple scattering of electrons by the crystal, which results in the redistribution of electron intensity between different Bragg reflections. Additionally, electrons can undergo absorption and inelastic scattering within the crystal, which can cause a reduction in the intensity of certain reflections and distort the diffraction pattern.

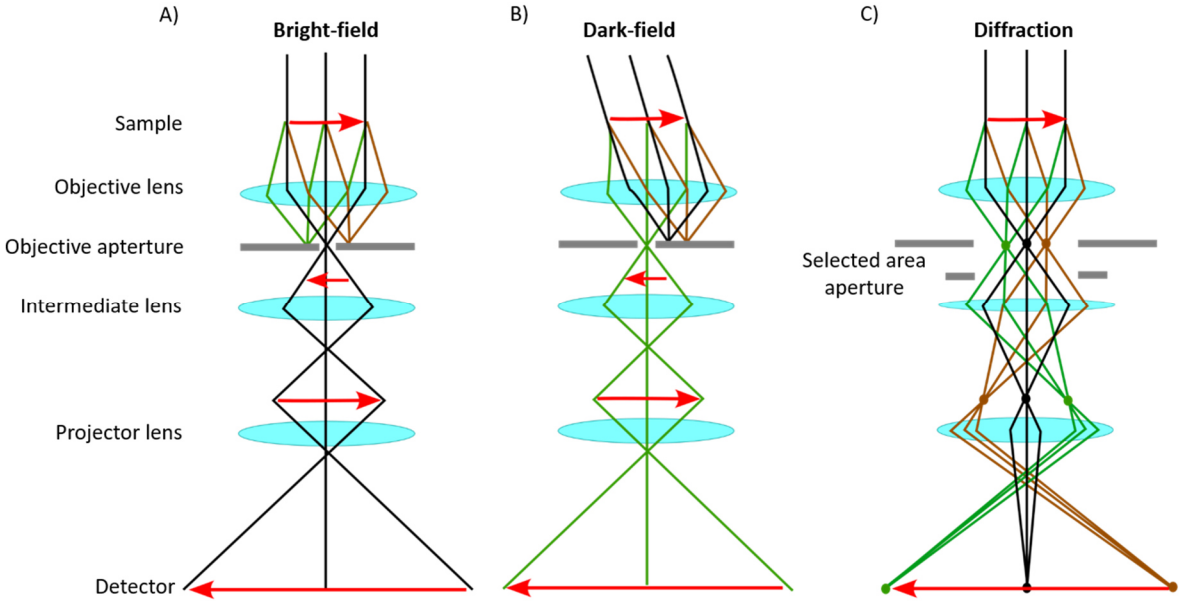

Figure 13: Ray path in the TEM for A) bright-field mode, B) dark-field mode and C) diffraction mode.

High-resolution imaging

To achieve high resolution, at least one diffracted beam containing information about the d-spacing of a material must be included in the detected signal. If the sample is oriented in a zone axis and the d-spacing is sufficiently large, the lattice planes can be imaged. For this, a large convergence angle is required. At high resolution, there is an additional phase contrast

caused by the spherical aberration C_S and defocus Δf of the objective lens. From this, a contrast transfer function (CTF; see Figure 14) can be derived

$$CTF(q) = sin\chi * e^{-\pi^2 C_C^2 (\frac{\Delta E}{E_0})^2 \lambda^2 q^4} \quad (42)$$

$$\chi(q) = \frac{\pi}{2}(C_S \lambda^3 q^4 - 2\Delta f \lambda q^2 \quad (43)$$

with $q = 1/d$ [140]. It determines the ultimate resolution that can be achieved in the TEM. The information limit is defined as the frequency of the CTF at $1/e^2$. The resolution limit is the first zero crossing of the CTF ($\sin \chi = 0$). Hence, the information limit surpasses the resolution limit. By adjusting the focus, the contrast can switch between negative and positive. The optimal focus up to the first zero crossing is known as the Scherzer focus $\Delta f_{Scherzer}$, which can be calculated using the equation

$$\Delta f_{Scherzer} = 1.2 * \sqrt{C_S \lambda} \quad (44)$$

When the electron beam is focused at the Scherzer focus, the size of the electron beam is minimized, resulting in the highest possible spatial resolution. However, the focus moving away from $\Delta f_{Scherzer}$ leads to changes in the CTF and the resulting image contrast [27].

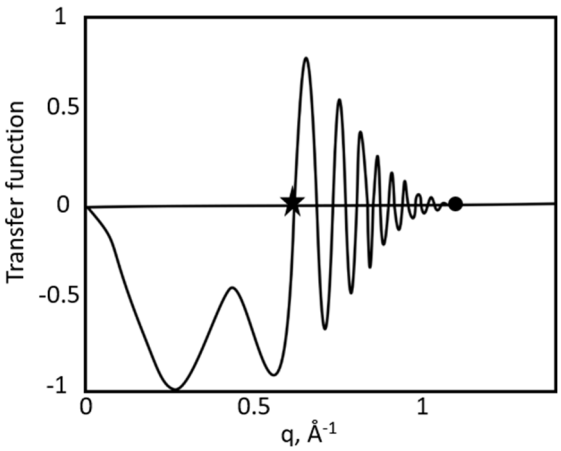

Figure 14: Typical trend of the contrast transfer function (CTF) in a TEM. The Scherzer focus is displayed as a star and the information limit is indicated by a black dot.

2.5.4. Precession electron diffraction

Precession electron diffraction (PED) is an electron diffraction technique that can be used to overcome dynamical scattering effects. This can be achieved by precessing the incident beam at a specific tilt angle with respect to the optical axis using the upper deflection coils. The resulting displacement of the electron beam is then compensated for the imaging system using the lower deflection coils [142]. This causes the Ewald sphere to follow the same motion in reciprocal space (see Figure 15). Diffraction intensities are then integrated via the Bragg condition during the acquisition of a diffraction pattern. With a large enough precession angle (3-4°), the position resembles a two-beam condition, effectively removing dynamical effects [27]. As a result, forbidden reflections are eliminated, the intensities of the reflections are normalized and intensity ordering occurs. This generates quasi-kinematic data that can be used for structure solution in direct methods [143,144].

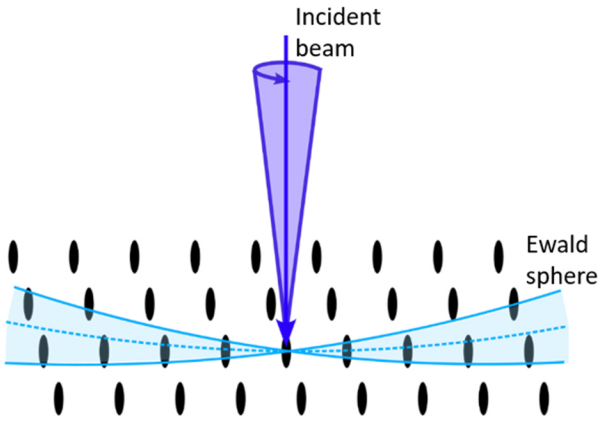

Figure 15: Precession of the incident beam causes the Ewald sphere to precess in the reciprocal space, leading to more intensities being reached and an integration of reflections.

2.5.5. Nano-beam diffraction

The nano-beam diffraction (NBD) mode enables the processing of crystallites or regions of interest in the nm range that cannot be achieved with X-ray diffraction [145]. A small condenser aperture (10 μm) is utilized to produce a quasi-parallel electron beam with a convergence angle of < 1 mrad [146,147]. The resulting diffraction patterns are similar to SAED patterns, but the diffraction volume is directly defined by the beam size, thereby enabling acquisition of diffraction images with a good signal-to-noise ratio from single nanoparticles [148].

2.5.6. Scanning transmission electron microscopy

Scanning transmission electron microscopy (STEM) works by scanning a focused beam of electrons across a specimen and detecting the electrons that are transmitted through the specimen. Similar to TEM, STEM also employs an electron-transparent sample and the detectors are placed underneath the specimen. The beam is focused on the sample through a lens system, which can reduce the beam to atomic resolution. Microprobe STEM can be used with slightly convergent sample illumination, resulting in a higher depth of field that benefits tomographic experiments because they are less dependent on the focus setting [149]. Additionally, it allows for NBD to be performed without exiting STEM mode [150], making measurement sequences easier to automate.

Diffraction of the convergent beam from the sample produces diffraction disks on the detector, which interfere with each other when they overlap, creating an incoherent image on the HAADF detector for sufficiently high detection angles and lower minimum detection angle. The transfer function is always positive, allowing for direct interpretation (see Figure 16). The intensity is proportional to Z^2 and the thickness of the sample.

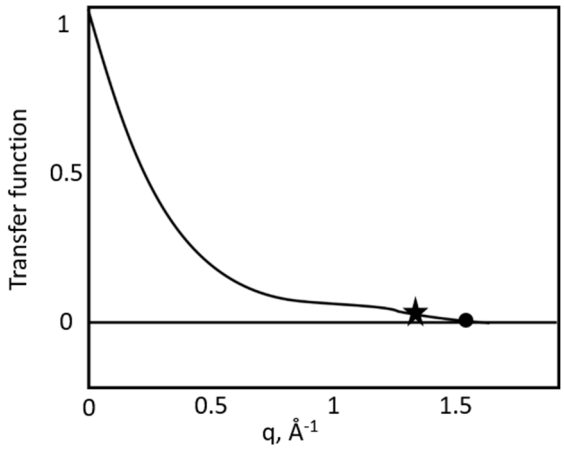

Figure 16: Typical trend of the transfer function in a STEM. The Scherzer focus is indicated by the star and the information limit by the black dot. The contrast remains positive.

Detectors

There are several imaging modes in STEM that use a combination of electron scattering and detector geometry to create contrast in the image: annular bright-field (ABF), annular dark-field (ADF) and high-angle annular dark-field (HAADF) imaging (see Figure 17). The bright-field (BF) detector collects electrons with low-angle scattering, mainly generated by the transmitted beam on the detector and contains diffraction contrast. It corresponds to the BF mode in TEM. The annual dark-field (ADF) detector, located around the BF detector mainly picks up Bragg diffracted and thermally diffuse scattered electrons due to its angle. It corresponds approximately to the hollow-cone dark-field mode in TEM. The outermost detector ring is the high-angle annular dark-field (HAADF) detector, which registers thermally diffuse scattered electrons (elastically coherent) and Rutherford scattering (elastically incoherent) [151]. HAADF STEM can provide atomic and subatomic resolution enabling chemical interpretation. However, an electron probe with a beam size smaller than atomic column distances is necessary, typically a few angstroms. To achieve this, the condenser system's dominant aberrations must be minimized with an aberration corrector [152].

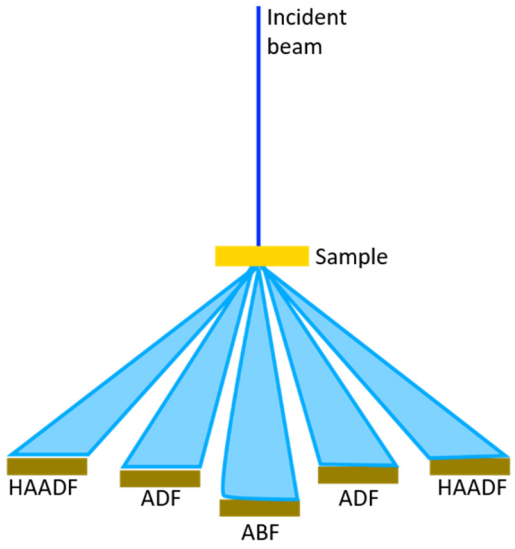

Figure 17: The various detectors used for imaging in STEM mode: annular bright-field (ABD), annular dark-field (ADF) and high-angle annular dark-field (HAADF).

2.6. Three-dimensional electron diffraction

In the 1950s, Pinsker and Vainshtein developed an electron diffraction camera, leading to the first successful results in solving structures from electron diffraction data sets [153,154]. With the structural characterization of individual nanocrystals [155], there was a renewed interest in electron diffraction and crystallography in the 1970s. For several decades both inorganic and organic structures were extensively studied by collecting data on very thin crystals in order to reduce dynamical effects to such an extent that kinematical scattering can be assumed as an approximation ($I_{hkl} \approx |F_{hkl}|^2$) for the structure solution [156,157]. The development of PED allowed the use of electron diffraction images of thicker crystals for structural characterization because of a decrease in dynamical effects [158,159]. Less than 20 years ago, Ute Kolb's group at the Johannes-Gutenberg-University of Mainz developed a method for tomographic data acquisition called automated electron diffraction tomography (ADT), allowing ab initio crystal structure analysis of nanoparticles purely from electron diffraction data [34,36,160]. With ADT applicable to a wide range of materials, improved data sets could be obtained, allowing structure analysis on nanocrystals in a reasonable time frame. For example, a structurally complicated silicate called charoite (see chapter 3.3.4) [100] or the extremely beam sensitive zeolite ITQ-43 [161] could be solved. More recently, the rotational method was developed, based on a similar principle [42]. Meanwhile, using ADT has become the standard for the electron crystallography community and beyond [162]. In 2021, both Rigaku and ELDICO presented the first dedicated electron diffractometers, thus making it possible to perform 3D ED without a TEM [163].

2.6.1. Principle

The best results are achieved on a small, thin single crystal in the range of about 100 nm. ADT is performed in NBD mode with the smallest spot size of 0.5 nm and the 10 μm C2 aperture, but the SAED mode could also be used [92,164]. α depends on the beam size, with larger beam sizes leading to a larger α setting. To be able to obtain three-dimensional diffraction data, a tilt series of diffraction patterns is needed. To ensure the crystal does not move off-axis during tilting, the eucentric height must first be mechanically adjusted. The residual movement can be corrected in imaging mode by hand or automated via cross-correlation [36].The tilting range is limited by the pole piece, thickness of the sample holder and position of the particle to be examined on the grid. To ensure the largest possible range, it is important to select a crystal that is not too close to a grid bar or another crystal and to use a tomography holder with a tilt range from -70° to +70° measured in one go in order to avoid hysteresis. Since it is never possible to tilt 90° in any direction, a so-called missing cone is created in the reciprocal space (see Figure 18).

Compared to static diffraction images limited to zones, ADT with fixed tilt steps scans the reciprocal space more finely and thus captures more diffraction spots. In terms of tomography, the two-dimensional diffraction patterns are then combined to form a three-dimensional reciprocal space. Orientation of the crystal prior to recording the diffraction patterns is not necessary and should even be avoided in order to capture more symmetrically independent reflections. In addition, diffraction patterns of zone axes have a large amount of dynamical effects. Thus, non-oriented crystallites contain fewer dynamical effects and provide pseudo-kinematic data sets.

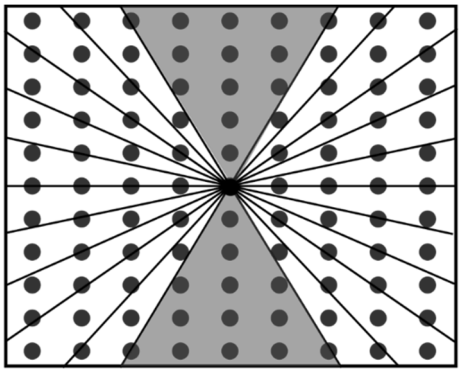

Figure 18: The reciprocal space is scanned within the largest possible tilt range. The volume, which is not reachable because of the microscope's geometry, is called missing cone and is marked in grey.

Since the use of NBD results in small diffraction disks, the diffraction pattern must be refocused via the intermediate lens because otherwise the disks could overlap for larger unit cells and weak intensities might be lost in the background noise of the camera. This changes the effective camera length, which must be calibrated. The intensity of the diffraction spots depends on the distance of their center to the intersection of the Ewald sphere. The smaller the tilt steps, the higher the probability to intersect the reflection in the center. Using PED during an ADT measurement captures more diffraction spots, also between the tilt steps and generates fewer dynamical effects, since intensities are integrated instead of just intersected. A precession angle of 0.5-1° is already sufficient.

ADT offers a distinct advantage over other 3D ED methods in that it can be fully automated in microprobe-STEM mode, for both diffraction and imaging. In terms of imaging, microprobe-STEM requires a lower electron beam dose to achieve high contrast and is less sensitive to the focus conditions [149]. Recently developed cameras that detect electrons directly are highly sensitive and enable very high frame rates, allowing for continuous tilting of crystals at a constant velocity while capturing electron diffraction images. This technique drastically reduces the illumination of the material with the electron beam, resulting in a faster acquisition of data and a much finer scanning of the reciprocal space due to the significant reduction in step size [43,44,53].

2.6.2. Data acquisition with Fast-ADT

In conventional ADT, after each tilt, the beam is placed back on the crystal in imaging mode with a diffraction pattern being recorded in diffraction mode afterwards [145]. The frequent switching between imaging and diffraction modes is very time consuming. In addition, the crystal must be beam stable in order to endure the long irradiation time. This is why the automated version, called Fast-ADT, is important for beam sensitive materials. By recording a tracking file prior to the measurement, the irradiation time is significantly reduced. Additionally, an extremely low electron intensity is used [57].

Fast-ADT can be run in TEM or STEM mode. For data acquisition, the beam settings are saved for both imaging and diffraction mode. For diffraction mode, the beam is set to a size of 50-200 nm and the beam shift is calibrated using the X and Y deflections. Because the crystal still moves slightly during the tilting process even if the eucentric height is set correctly, a tracking file must be recorded in imaging mode as a reference image, with the region of interest (ROI) marked to focus the beam on during the measurement. The beam is then set to the ROI. Finally, the initial parameters are loaded and the mode is changed to diffraction mode. After

the exposure time is adjusted as to not overexpose the camera and the diffraction pattern is centered, the acquisition of the tilt series can be started.

2.6.3. Data processing

After data acquisition, the data sets can be evaluated with programs like eADT [54] or PETS2 [55]. In the following, the data reconstruction process with eADT is explained (see Figure 19).

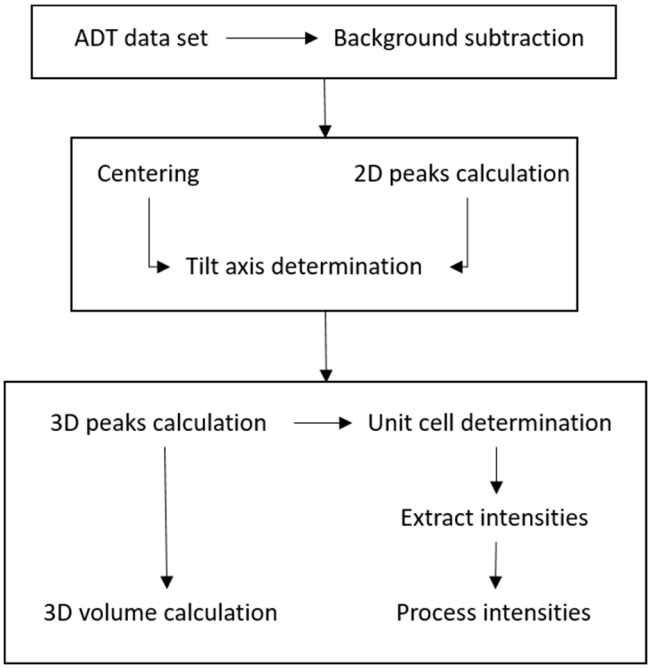

Figure 19: Typical procedure of a data extraction with eADT from an ADT data set.

First, the file type should be changed from .dm3 to mrc using the program Fast-ADT Data Processing created by Sergi Plana-Ruiz. After loading the mrc file into eADT, a background correction can be performed.

Next, the centering of individual images can be calculated and refined manually, if needed. There are two methods to locate the center of each diffraction pattern in a tilt series. Depending on the electron beam dose and camera being used, a primary beam stop may be necessary to prevent damage to the camera. In such cases, a set of Friedel pairs can be examined, with the intersection of the connecting lines of the respective pairs indicating the position 000. Without a primary beam stop, it can be assumed that the zero beam corresponds to the highest intensity with the greatest extent. In cases where diffracted intensities exceed that of the zero beam, the peak shape method can be used or deviations can be corrected manually. These centers can then be saved as a shift file.

Afterwards, 2D intensities are calculated by looking for high intensities of individual pixels above a certain threshold and grouping neighboring pixels into clusters. The minimum intensity threshold and the minimum number of points in a cluster can be defined automatically or by the user. The shape of the cluster is a circle, although slight variations are expected. The circle is formed around the center of each pixel cluster according to the threshold. The mean value of the intensities in the rim of the circle defines the background value. The pre selection of strong peaks by the min points in cluster limit is an effective indicator for true peaks. Any unwanted reflections can be excluded manually.

Using the centering and 2D intensities, the tilt axis is determined automatically. It is assumed that the position of the tilt axis remains approximately constant during the measurement. The reconstructed reciprocal space from the peak positions of the full tilt series should exhibit periodicities in multiple directions. To find the correct tilt axis, different positions of the tilt axis are probed. For this, the difference vectors of all reflections are calculated, resembling an autocorrelation of the three-dimensional reciprocal space. The center of the difference vector space is defined as the origin of a sphere and a stereographic projection is calculated from the sphere surface, which should display sharp and bright lines and points for the correct tilt axis position (see Figure 20) [165].

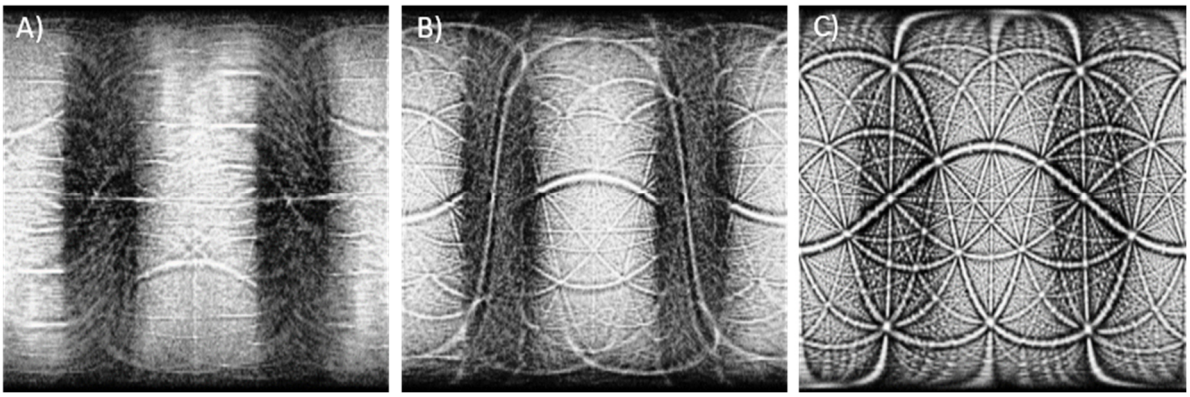

Figure 20: Stereographic projection of different tilt axes of an ADT data set of labradorite. A) depicts a tilt axis of -10°, B) of 30° and C) shows the correct tilt axis of 43.7° with sharp lines.

Then, a first 3D volume of the intensities is calculated using the module calculate 3D peaks. It generates a 3D data field by calculating the 3D coordinates of the identified 2D reflections. Trigonometric functions are used to determine these coordinates based on the tilt axis position, the shift file and the tilt step size. The intensities at the outer edge and the center, as well as artefacts, can be removed.

Afterwards, the cell search algorithm is then applied. The difference vectors of all reflection positions, calculated from the 3D peaks, contain many vectors pointing to spots with similar coordinates. They can be grouped based on three parameters, which can be set by the user: the minimum number of points within a cluster, the maximum distance between points in a cluster and the maximum distance of clusters from the origin. The difference vector space should closely approximate the translation grid from the measured reciprocal space. To describe the location of each cluster point, the basis vectors must be defined in such a way that they can be represented by an integer multiple of the basis vectors. eADT can automatically find these basis vectors by performing a cluster analysis to find the three shortest non-co-planar vectors [166] but the result can be corrected manually if needed. The basis vectors can be stored as a cell file, which includes an orientation matrix in pixels, as well as reciprocal and real space lattice parameters. The accuracy of this cell is not critical, as it only serves as a starting point and can be adjusted later.

The 3D volume is then calculated and parameters can be adjusted to minimize interfering reflections. The cell is adjusted in cell adjust so that all reflections are described by the grid. Here, all axis lengths as well as their angles can be changed. Furthermore, the 3D visualization of the diffraction spots can be used to analyze existing superstructures, detect areas of disorder or recognize and separate superimposed crystal lattices like twins. The cell parameter

determination has an accuracy of 1% [145]. The cell found must be multiplied by a factor to calibrate the effective camera length.

Then, the intensities can be extracted. To extract and index measured intensities, reciprocal grid points must be calculated from the previously determined orientation matrix and their coordinates transformed back to the diffraction patterns. Due to the few intersections of the reciprocal space by the 3D ED measurement and the measurement-related inaccuracies, it is unlikely that a theoretically calculated grid point will align exactly with the measured coordinates of the reciprocal space. Additionally, the excitation error of the diffracted reflections must be considered (see Figure 21).

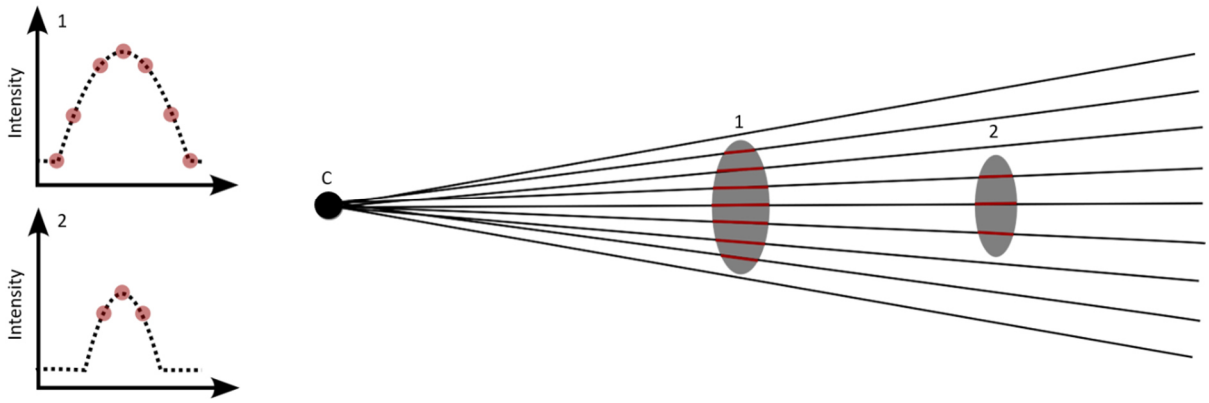

Figure 21: When extracting intensities, reflections can be visible on several diffraction patterns in the tilt series because of the excitation error, creating a rocking curve as an intensity profile.

To address these issues, defined intervals around a theoretical grid point are assumed and a set of possible coordinates for each grid point is established in order to define the coordinates to be integrated. The size of the box and the spatial extent perpendicular to the image (spike length) can be specified by the user. Each calculated position of a diffraction image is integrated in a square area where the background is determined and the adjusted intensity is stored. Depending on the tilt angle, there are several integrated values for each possible reflection, which can be plotted to create an intensity curve as a function of tilt angle resembling a symmetrical distribution function (rocking curve; see Figure 21). Reflections near the tilt axis are recorded throughout the tilt series. To assign a single intensity value to each hkl, either only the maximum value of each rocking curve or their integrals can be stored. Afterwards, all negative intensities are set to zero in the module process intensities. The resulting data is stored as hkl data set.

2.6.4. Structure determination

The aim of a structure solution is to identify the locations of individual atoms within the asymmetric unit. By disregarding dynamical scattering, the intensity of a reflection is proportional to the magnitude squared of the structure factor $I_{hkl} \sim |F_{hkl}|^2$. Unfortunately, from a diffraction intensity, only the magnitude of the vector F_{hkl} can be determined and not its phase. This is known as the phase problem. Therefore, the atomic positions cannot be determined directly from the diffraction intensities. Nonetheless, various methods exist to overcome this problem and determine the atom positions.

Direct Methods

In this approach, the strongest intensities and their indices are used to determine the phase angles of the reflections directly from the intensities. Harker and Kasper [167] were the first to establish phase relations through the Cauchy-Schwarz inequalities [168]. Unitary structure factors $U_{hkl} = F_{hkl}/Z$ are used, normalized to the number of electrons Z in the unit cell of the structure. $|U_{hkl}|^2 \leq 1$ and symmetry-related relations lead to the Harker-Kasper inequalities. For example, the inequality

$$U_{hkl}^2 \leq \frac{1}{2} + \frac{1}{2} U_{2h2k2l} \tag{45}$$

applies to centrosymmetric structures. For strong structure amplitudes with $U_{hkl}^2 > \frac{1}{2}$ the higher diffraction order U_{2h2k2l} must be positive. The sign of the structure factors can be determined from the inequalities and their combinations.

The Sayre equations [169] are based on the postulates that the electron density in a unit cell is always $\sigma_{xyz} \geq 0$ and that the electron density is not homogeneous but discretely distributed in space. Sayre observed that a structure factor is connected with the sum of products of other structure factors

$$F_{hkl} = s \sum_{h'k'l'} F_{h'k'l'} * F_{h-h',k-k',l-l'} \tag{46}$$

The intensity of the diffraction reflections decreases with higher diffraction angle 2θ and the structure factors are normalized by an expectation value $\sum_{j=1}^{N} f_j^2$ to allow for better comparability. The normalized structure factors are calculated by

$$E_{hkl} = \frac{F_{hkl}}{(\epsilon \sum f_j^2)^{\frac{1}{2}'}} \tag{47}$$

where ϵ is a weighting factor dependent on the point group. The statistical distribution of E values differ for non-centrosymmetric and centrosymmetric structures [105]. Using the Wilson plot

$$\langle |F_{hkl}|_{obs}^2 \rangle = \langle I \rangle = K \langle |F|^2 \rangle e^{-2B\langle s^2 \rangle} = K \sum_{j=1}^{N} f_j^2 e^{-2B\langle s^2 \rangle} \tag{48}$$

a preliminary isotropic deflection parameter B and scaling factor K can be determined from

$$\ln\left(\frac{\langle I \rangle}{\sum_{j=1}^{N} f_j^2}\right) = \ln(K) - 2B\langle s^2 \rangle \tag{49}$$

with $s = sin\theta/\lambda$ [170]. Hauptman and Karle [171] established the $\sum_2$ −relation for a triplet of strong reflections

$$S(E_h) \approx S(E_{h'}) S(E_{h-h'}) \tag{50}$$

where S is the sign, $h = [hkl]$ and $h' = [h'k'l']$. Accordingly, the $\sum_2 -$relation for strong reflections allows to calculate the sign S(E_h) of the other two reflections with a certain probability [105]. For non-centrosymmetric structures, instead of the sign, the total phase angle must be derived from the $\sum_2 -$relation via $\Phi_h \approx \Phi_{h'} + \Phi_{h-h'}$. It is attempted to determine the phase Φ_h from many $\sum_2 -$relations using the tangent formula

$$tan\Phi_h = \frac{\sum_{h'} \varkappa * \sin(\Phi_{h'} + \Phi_{h-h'})}{\sum_{h'} \varkappa * \cos(\Phi_{h'} + \Phi_{h-h'})} \quad (51)$$

where $\varkappa$ is a weighting factor by probabilities [105].

All in all, many estimation methods for the phase angles have been found [172]. For structure solution with direct methods, SIR2019 was used in this study [173]. The typical process of structure determination in SIR starts with the creation of a Wilson plot to determine K and B from the extracted intensities, followed by the calculation and sorting of E values by magnitude. A set of starting phase angles is assigned to the highest E values, new phase angles are calculated using the $\sum_2 -$relation and reflections are selected to define the zero point. The set of phase angles is extended by the tangent formula and different solutions are listed according to their probability. An electron density map is calculated from the magnitudes of the E values and phase angles and an attempt is made to localize the atoms. Finally, a set of E_c values is calculated and compared with the measured E_0 values from the diffraction experiment. The accuracy of the final atomic positions depends on the quality of the diffraction data, the completeness of the data set and the resolution. After the atom positions have been determined, the next step is to refine the model by minimizing the difference between the calculated and observed diffraction intensities. This is typically done by using a least-squares minimization algorithm that adjusts the atomic positions and other parameters such as atomic displacement factors and occupancy. The quality of the final model can be assessed using various validation tools such as the R-factor, which measures the agreement between calculated and observed intensities.

Charge flipping

The charge flipping algorithm developed by Oszlányi and Sütó [174] is a trial and error method for determining phase angles. In this method, random phases are assigned to the structure factors determined from experimental intensities. Using these structure factors, an electron density ρ is calculated through an inverse Fourier transform according to equation (16). Negative electron densities are corrected by setting them to positive (flipped) with the same magnitude. Next, a new set of structure factors G is calculated by performing Fourier transformation on the modified electron intensity g. These new structure factors are combined with the experimental structure factors to create a new set of structure factors F. They are used to calculate a new electron density ρ using the same procedure as before, creating a cycle, which is also known as Fourier recycling (see Figure 22). It produces an electron density map with a pixel size corresponding to the resolution d_{min}. The charge flipping algorithm relies only on the unit cell and the atoms it contains and does not require the specification of the space group. Once the structure is solved, the cell origin must be specified following crystallographic conventions.

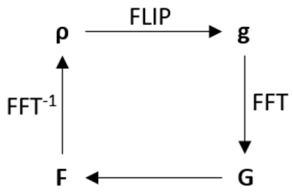

Figure 22: Schematic diagram of Fourier recycling in the charge flipping algorithm.

In Jana2020 [175], charge flipping via the program SUPERFLIP [176] can be selected as a method for structure solution. The structure can then be refined based on the kinematical or dynamical diffraction theory.

2.7. Energy dispersive X-ray spectroscopy

Energy dispersive X-ray spectroscopy (EDS) is a non-destructive technique that uses X-rays to probe the chemical composition of a material. It is often used in conjunction with SEM and TEM to provide a quantification of the chemical composition and an identification of materials.

X-ray emission

When the electron beam hits the sample, it causes the atoms to become excited and emit X-rays. The formula for X-ray generation is

$$E_x = hc/\lambda \tag{52}$$

where E_X is the energy of the X-ray radiation, h is Planck's constant, c is the speed of light and λ is the wavelength of the X-ray radiation. These X-rays are then detected and analyzed by the EDS detector which is either a silicon drift detector (SSD) or a lithium drifted silicon detector (LSD). SSDs have a higher count rate but LDS detectors have a higher energy resolution.

Characteristic X-ray emission and Bremsstrahlung

There are two types of X-rays detected by the energy dispersive X-ray spectrometer: Bremsstrahlung and characteristic X-ray radiation. Bremsstrahlung is produced when the primary electrons decelerate in the Coulomb field of the atomic nucleus. The energy lost by the electron is emitted in the form of Bremsstrahlung and can range from zero to the energy of the incident electron. This radiation is largest at lower energies (see Figure 23).

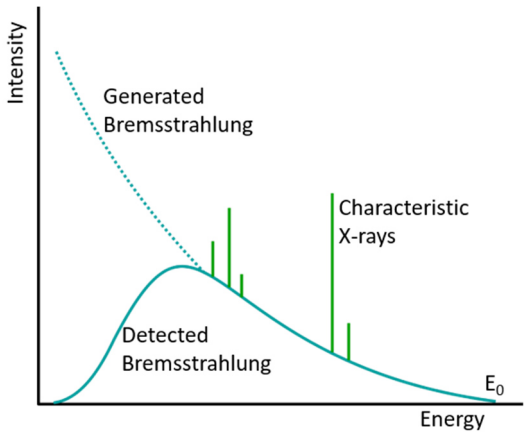

Figure 23: EDS spectrum of the intensity versus the energy of the X-rays. The generated Bremsstrahlung shown in turquoise is highest at lower energies. Characteristic X-rays displayed in green show distinct peaks for each element.

Characteristic X-rays are produced when the primary electron's energy is sufficient to ionize an inner shell of an atom (see Figure 24). The atom becomes excited and returns to a low-energy state when an electron from a shell further out fills the hole created by ionization. The energy difference can be released through different ways, such as the release of an X-ray quantum in a radiative transition or an Auger electron or valence band electron in a non-radiative transition. The probability of a non-radiative transition decreases as Z increases. Moseley's law states that energy is proportional to Z, meaning that the heavier the element, the higher the energy and the more lines are visible in the spectrum. The energy required for X-ray production increases with increasing Z since the primary energy should be about twice the energy required to force an electron out of that shell.

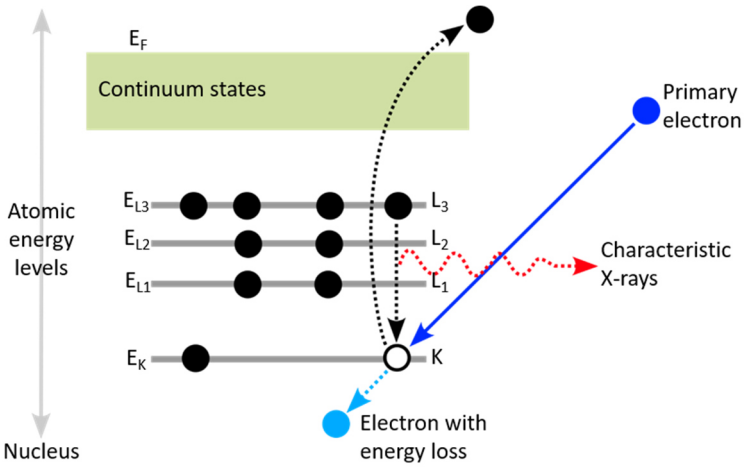

Figure 24: Formation of characteristic X-rays. When a primary electron knocks an electron from an inner shell of an atom, an electron from a shell further out fills the hole. The difference in energy can be released via characteristic X-rays.

Analysis

The energy of the X-ray is directly related to the atomic number of the element that emitted them. By measuring the energy of the X-rays, it is possible to determine the elemental composition of the material. The EDS spectrum is a plot of X-ray intensity versus energy (see Figure 23). The peaks in the spectrum correspond to the characteristic X-rays emitted by the different elements. Quantitative analysis is performed by comparing the intensity of the peaks in the spectrum to known standards. The detection limit is approximately 0.5 mol% so trace elements cannot be detected. Tilting the sample towards the detector can be useful when dealing with few counts [27].

2.8. X-ray powder diffraction

X-ray powder diffraction (XRPD) is a non-destructive analytical technique used to identify crystalline phases and obtain information about the crystal structure of a material. It is widely used as a standard technique in many fields. There are several different setups for XRPD measurements. The Debye-Scherrer and Bragg-Brentano geometries are the two common ones. Both setups involve exposing a powdered sample to a beam of X-rays and measuring the diffracted X-ray intensity as a function of the diffraction angle. The randomly distributed crystals always satisfy the Bragg condition (equation (3)). However, if there is a non-uniform distribution, a crystallographic preferred orientation can arise, also known as texture, resulting in a directionally dependent diffraction pattern.

Indexing

In the diffraction pattern, the diffraction peaks are labeled using their intensity versus the 2θ angle. The intensity and position of the diffraction peaks are dependent on the crystal structure, lattice parameters and orientation of the crystal lattice. The next step is to determine the indices of the crystal lattice planes responsible for each diffraction peak. After a rough estimate of the crystal structure has been determined, the structure can be refined via the Rietveld method. It involves optimizing the fit between the observed and calculated XRPD patterns by refining a set of parameters, including lattice parameters, atom positions, atomic displacement parameters and background intensity. The refinement is performed using a least-squares procedure [104].

Application and limits

XRPD has a wide range of applications in many fields of science. It is commonly used to identify and quantify materials and determine their crystal structure. Furthermore, XRPD is used in the quality control of various products, including pharmaceuticals and ceramics by checking their crystallinity and purity. It can also be used for stress analysis and to determine the orientation of crystallites in the sample. However, XRPD may produce inaccurate results if there is a preferred orientation of the crystals in the sample. Additionally, a small sample size might not produce sufficient diffraction peaks for analysis.

3. Materials

Silicates

Silicates, a diverse group of minerals composed primarily of silicon and oxygen, have long fascinated scientists due to their wide-ranging structures and properties. For example, quartz with its high hardness and resistance to weathering, is a key component of concrete and asphalt used for road construction. Feldspar, on the other hand, provides strength and durability to ceramics, glass and pottery. Silicate minerals dominate the Earth's crust, constituting approximately 95% of its volume. Through chemical reactions and physical breakdown, silicate minerals gradually release elements and compounds that interact with water, air and organic matter. The weathering process not only influences soil formation and fertility but also affects the overall composition of the oceans and the atmosphere.

In 1930, Bragg proposed a classification system for silicates based on the type and degree of linkage of tetrahedral units $(TO_4)^{4-}$ [177]. The major silicate groups identified by this classification are nesosilicates (ortho), sorosilicates, cyclosilicates (ring), inosilicates (chain), phyllosilicates (sheet) and tectosilicates (framework). Over the years, the understanding of silicates has expanded with the discovery of various substitutions and extensions to Bragg's classification. Berman [178] observed that Be^{2+} could replace Si^{4+} in silicate structures. Strunz [179] noted the substitution of P^{5+}, As^{5+}, Ge^{4+}, Ti^{4+} and Fe^{3+} for Si^{4+}, further enriching the diversity of silicate minerals. Zoltai [180] described silicates based on repeat units, refining the understanding of their arrangement and bonding patterns. Day and Hawthorne [62] categorized silicate structures into various dimensional groups based on the polymerization of tetrahedra (see Figure 25).

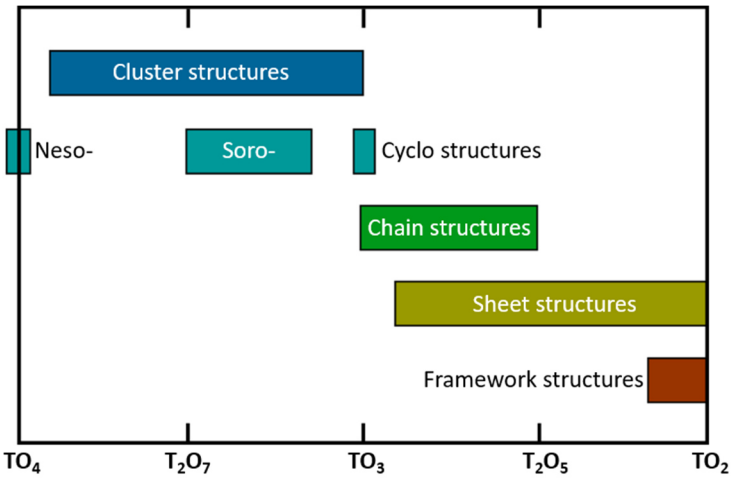

Figure 25: The classification of silicates after Day and Hawthorne [62]. The Si:O ratio decreases with increasing polymerization.

Hereby, the Si:O ratio decreases with increasing linkage. Cluster silicates lack infinite polymerization, meaning that the tetrahedral units remain isolated from each other. Chain, ribbon and tube silicates demonstrate infinite polymerization in one dimension. While chain silicates only comprise one continuous chain-like structure, ribbon silicates consist of several connected chains. In addition to the linear polymerization, the tetrahedral units in tube silicates also feature orthogonal linkages. The resulting structures resemble hollow cylinders, offering unique geometries and properties. Sheet silicates exhibit infinite polymerization in two dimensions. They often exhibit anisotropic properties due to the inherent directional nature of

their bonding. Framework silicates display three-dimensional infinite polymerization, resulting in a robust framework, providing exceptional structural stability. Framework silicates often possess high hardness and resistance to chemical weathering.

3.1. Illite

3.1.1. Clay minerals

Introduction to phyllosilicates

As the name suggests, clay minerals can be found in the clay fraction (<2 μm) of rocks [181]. Due to their layered structure, they are classified as phyllosilicates. They can be formed at temperatures between ~4°C (bottom of the ocean) and ~400°C (hydrothermal alteration) and in periods of several hours (laboratory conditions) to several hundred million years (burial diagenesis). They usually occur as platelets, but sometimes also form laths or needles, which have a large surface area. The surface is charged, making it possible for ions or charged molecules to be adsorbed. This process is called ion exchange and is measured with the so-called cation exchange capacity (CEC), which is the number of charged ions that can be fixed onto the surface. Generally, the more cations of a species occur in the solution, the more frequently they are adsorbed on the clay mineral surface. Some clay minerals can even absorb ions into their crystallographic structure. This attraction of ions is different for every species. It depends on the chemical composition of the clay mineral and the tendency of ions to stay in a hydrated state. Some clay minerals can also absorb water into their structure, which causes the layers to expand [182].

These physical and chemical activities enable clay minerals to play an important role in the interaction with the biosphere by ad- or absorbing organic molecules and rendering them inert or transporting them [182]. They can also be used to estimate geothermal gradients and paleo temperatures [183] and as raw material for various industrial purposes like paper coatings, lightweight aggregates, and ceramic products or cement [184].

For more information about the classification of clay minerals, as well as their transformation and the different facies in hydrothermal alterations, please refer to Appendix 1.

The structure of clay minerals

Clay minerals are composed of different layers. The sheets of which the layers are composed have stronger covalent bonds along their extension than the layers have to each other. This leads to a preferential growth in a two-dimensional array, resulting in a mostly platy morphology. The tetrahedral sheet consists of Si tetrahedra that are linked by sharing basal oxygen at three corners. All of the tetrahedra sites are filled [182]. The oxygen atoms form a hexagon with three equivalent a-axes (a_1, a_2, a_3) and b-axes (b_1, b_2, b_3) perpendicular to the respective a-axes. The length of the b-axis is related to the a-axis by $b_0 = a_0\sqrt{3}$ [181].

By joining the apical oxygen planes of two tetrahedral sheets in a close-packed junction, an octahedral sheet can be visualized in-between. This sheet is mainly occupied by Al^{3+}, Mg^{2+} or $Fe^{2+/3+}$. The number of cations can vary between 2 and 3 resulting in a charge of VI^{+}. Clay minerals with two tri-valent cation sites are called dioctahedral and those with three di-valent cation sites trioctahedral. On a single octahedral sheet, every oxygen is hydrated. The minerals that consist solely of this sheet are brucite ($Mg_3(OH)_6$, trioctahedral) and gibbsite ($Al_2(OH)_6$, dioctahedral). If one side of the octahedral sheet is linked to a tetrahedral sheet, the H content

decreases and a so-called 1:1 clay mineral is created. If both sides of the octahedral sheet are connected to a tetrahedral sheet, the H content decreases further and a 2:1 clay mineral is formed [182]. In dioctahedral 2:1 clay minerals, the octahedral sheet contains three symmetrically independent sites. Depending on the position of the remaining OH groups, this set of minerals is divided into two subgroups. If the OH groups occupy opposite apices of the vacant cation site they are called trans-vacant (tv) and if they are located on a shared edge, the minerals are called cis-vacant (cv) [59].

When isomorphous substitution takes place in the tetrahedral or octahedral sheet by replacing a cation with higher valency with a cation with lower valency (e.g., substitution of Si^{4+} by Al^{3+} in the tetrahedral sheet), a negative layer charge is created. It can either be satisfied by substitution in other layers (e.g. substitution of Mg^{2+} by Al^{3+} in the octahedral sheet) or by filling the interlayer with cations or hydroxide sheets [181]. Cations in the interlayer have a coordination number of 6-12 resulting in the preferential incorporation of larger ions like K^{+}, Na^{+} or Ca^{+}. Because of their weaker ionic bonds, the cations in this layer can be modified more easily than the ones in the tetrahedral or octahedral sheets. Clay minerals with a negative layer charge of 0.7-1 usually contain potassium as an interlayer cation while clay minerals with a negative charge of 0.25-0.6 can accept various combinations of ions and molecules, which makes it possible to incorporate water molecules and creates a swelling effect [185]. Clay minerals with a hydroxide sheet in their interlayer are called 2:1:1 clay minerals. Because of the weaker bonding, outside forces can modify the interlayer more easily than the other parts of the structure. Cations can be exchanged or adsorbed; in acid environments they can be leached out. Interlayer water or hydroxide sheets can be dehydroxylated [181]. Because of the high probability of isomorphous substitution in the tetrahedral and octahedral sheets, the composition of different clay mineral species is not fixed but can vary over a large range [182].

Distortions in the clay mineral structure

In 1984, Bailey published an informative paper about the basic crystal structure of micas [186]. The hexagonal geometry of the different layers is significantly distorted, especially in dioctahedral micas. In dioctahedral clay minerals, the adjacent octahedral Al^{3+} ions repel each other; however, because each Al^{3+} is repelled in three directions, they cannot move apart. This leads to the oxygen, which lie on a shared edge with the Al octahedra to move toward each other and results in O-O distances of 2.04-2.14 Å instead of 2.7-2.9 Å for the unshortened edges. This movement takes place diagonally and therefore causes the layer to be thinned in *c*-direction and expand in the *a*-*b* plane instead. The lateral dimensions of the tetrahedral sheet are usually larger than those of the octahedral sheet. This is counterbalanced by a rotation of adjacent tetrahedra in opposite directions in (001). Because of the attraction of the basal oxygen to the octahedral cations, every other basal oxygen moves toward the center of the 6-fold ring, making the symmetry of the sheet ditrigonal rather than hexagonal. This reduces the number of nearest neighbors from the interlayer cation from 12 to 6, with the other 6 being the second nearest neighbors. The smaller the rotation angle, the larger the ditrigonal ring of the tetrahedral sheet and the interlayer cavity [59] in which case the interlayer cation can sink in and shorten the *c*-axis [187]. In the tetrahedral sheets, the apical oxygen tilt slightly away from each other. The bridging basal oxygen will therefore be elevated by $\Delta z = 0.1\text{-}0.2$ Å out of their plane. Because the occupied octahedra in the octahedral sheet are smaller than the empty one, a stagger of the upper tetrahedral sheet to the lower one is created with values of 0.36-0.38a instead of the

ideal 0.33a. These distortions influence the fit of the sheets to one another and thus the stacking sequences of the layers and their stability.

3.1.2. Illite

The history of illite

Illite was first described by Grim et al. in 1937 as a "general term for the clay mineral constituent of argillaceous sediments belonging to the mica group" [188]. This broad description contained a considerable range in composition [189]. In 1953, Grim expanded the definition, adding that illite is smaller than 2 μm in size, shows no expanding lattice, is mostly dioctahedral and has interlayer cations, which are not interchangeable [190]. Additionally, it has a 10 Å spacing and can show disorder in the layer stacking. He suggested that illite and micas differ in the interlayer water content and that there is a solid solution between illite and muscovite. Yoder and Eugster [191] proposed that illite is disordered muscovite and that most illites are mixed layer structures. Reesman and Keller [189] tried to unite the broad definition of Grim [190] with the other viewpoint of illite as a pure and unique composition. Środoń and Eberl [192] defined illite as an Al-K dioctahedral mica like mineral, which is non-expanding and occurs in the clay fraction.

Illite formation can happen in various environments via different processes and chemical reactions and can also produce mixed layer minerals. Illite can be used to determine the degree of diagenesis in sedimentary basins via the Kübler Index (IC) [193]. Additionally, the age of a sediment can be determined by using K/Ar dating on illite [194]. For more information about the use of illite, its formation and illite-smectite mixed layer crystals, please refer to Appendix 2.

Mineralogical and crystallographic information

The cell parameters and space group of illite vary with the polytype and polymorph (see paragraph **Different polytypes of illite** below). $2M_1$, $2M_2$ and 3T are usually always cis-vacant, while 1M can be cis-, trans-vacant or mixed [59]. Illites have less potassium than micas in their interlayer, the amount varies between 0.55-0.7 [195] or 0.65-0.95 [184] depending on the source.

In illites, isomorphous substitution is more frequent than in muscovite [65]. This leads to a high variety in illite compositions, which is illustrated in Table 2. Tetrahedrally coordinated Si^{4+} is mainly substituted by Al^{3+}, while Fe^{3+} and Mg^{2+} substitute Al^{3+} in the octahedral sheet. With an increase in temperature the *a*- and *b*- axes change very little because the bonding within the layers is strong. In comparison, the length of the *c*-axis increases as the thickness of the weaker bonded interlayer increases with temperature, while the width of the tetrahedral and octahedral sheets does not change much [78].

While the cations in the tetrahedral sheet are statistically distributed, the degree of ordering of the octahedral cations is highly dependent on the composition [196]. Al^{3+} and Fe^{3+} tend to segregate from each other [197]. Although there is no long-range order in clay minerals with illitic composition, there is a short-range order of clustering of Fe^{3+} and dispersing of Mg^{2+} [198].

Table 2: Different compositions of illite found in literature.

Composition of illite	Citation	Remarks
$(K_{0.67}Na_{0.06})(Al_{1.09}Mg_{0.24}Fe_{0.66})(Si_{3.76}Al_{0.24})O_{10}(OH)_2$	[199]	1M
$(K_{0.6}Na_{0.06}Ca_{0.03})(Al_{1.64}Mg_{0.14}Fe_{0.18})(Si_{3.55}Al_{0.45})O_{10}(OH)_2$	[200]	1M
$(K_{x+y})(Al_{2-y}R^{2+}{}_y)(Si_{4-x}Al_x)O_{10}(OH)_2$ with $R^{2+}= Mg^{2+}$, Fe^{2+}	[186]	General formula
$(K_{0.83}Ca_{0.02})(Al_{1.79}Mg_{0.29}Fe_{0.03}Mn_{0.03})(Si_{3.22}Al_{0.78})O_{10}(OH)_2$	[76]	1M
$(K_{0.79}Na_{0.16}Ca_{0.02})(Al_{1.79}Mg_{0.12}Fe_{0.03}Mn_{0.01})(Si_{3.35}Al_{0.65})O_{10}(OH)_2$	[76]	$2M_1$
$(K_{0.78}Na_{0.001})(Al_{1.75}Mg_{0.1}Fe_{0.18})(Si_{3.32}Al_{0.78})O_{10}(OH)_2$	[201]	Fibrous
$(K_{0.81})(Al_{1.58}Mg_{0.22}Fe_{0.13})(Si_{3.61}Al_{0.39})O_{10}(OH)_2$	[66]	Fibrous
$(K_{0.75}Ca_{0.02})(Al_{1.62}Mg_{0.41}Fe_{0.04}Ti_{0.02})(Si_{3.31}Al_{0.69})O_{10}(OH)_2$	[202]	$2M_2$
$(K_{0.86}Na_{0.01}Ca_{0.01})(Al_{1.91}Mg_{0.03}Fe_{0.07}Mn_{0.01})(Si_{3.14}Al_{0.86})O_{10}(OH)_2$	[203]	$2M_1$
$(K_{0.86})(Al_{1.71}Mg_{0.31}Fe_{0.04})(Si_{3.27}Al_{0.73})O_{10}(OH)_2$	[204]	Fibrous $1M_{tv}$
$(K_{0.78}Na_{0.02}Ca_{0.02})(Al_{1.69}Mg_{0.34}Fe_{0.02})(Si_{3.35}Al_{0.65})O_{10}(OH)_2$ x nH_2O	[58]	1M

Different polytypes of illite

Polytypes are minerals with two or more phases (polymorphs) that differ in their crystal structures because of a different stacking of their layers. The nomenclature for clay minerals contains the number of the layers in the repeated unit (1, 2, 3) and a capital letter for the crystal system (M = monoclinic, O = octahedral, T = trigonal, H = hexagonal). In some cases, additional subscript numbers might be used to differentiate between polytypes with the same periodicity and symmetry. The stacking angle is defined by two successive stacking vectors, which are indicating the direction of the displacements or rotations. Illite and mica polytypes are described based on the $a_0/3$ stagger and the pseudohexagonal symmetry of the basal oxygen. If the stacking angle is 0°, the polytype has only one layer that is successively shifted along the *a*-axis and is called 1M. With a 180° stacking angle, the layers alternate between $+a_1$ and $-a_1$. This polytype is called 2O. When the layers are shifted along two axes, the polytypes are $2M_1$ or $2M_2$ for stacking angles of ±120° or ±60°, respectively. Similarly, a continuous shift in all three *a*- axes (a_1, a_2, a_3) leads to 3T for stacking angles of 120° and 240° and to 6H for stacking angles of 60° and 300° [181].

$1M_d$ illites are metastable and portray the original state of formation containing disordered layers of 1M illite [77]. They can be created by layer-by-layer illitization of smectite [205] or by dissolution and recrystallization obeying Ostwald ripening [77]. The Ostwald step rule dictates that a metastable system proceeds in steps towards a system with minimal free energy. Hereby, smaller crystals dissolve and reprecipitate onto larger ones [206]. They can crystallize directly by heterogeneous nucleation at low temperatures and pressure. The surfaces of two crystallites are not atomically flat which causes distortions and small misorientations at the interface leading to an imperfect oriented attachment. This can cause edge or screw dislocations. The disorder caused by the dislocations is visible in the diffraction pattern [200]. In this case the $a_0/3$ stagger occurs randomly which leads to a loss of periodicity of the basal oxygen atoms along c^* [207]. This disordered stacking causes streaking of non-00l reflections parallel to the c^*-axis with $k \neq 3n$, which is typical for the $1M_d$ structure [77]. Sometimes poorly defined reflections can be seen along the streaks, which arise from locally ordered domains of 1M or other polytypes. The periodicity of the octahedral atoms however, is not affected so that the

$k=3n$ reflections stay sharp [208]. $1M_d$ illite can be described as $1M_{r\text{-}n(120)}$ (n = 0, 1, 2) with random layer stacking sequences along the c^*-axis [209]. In turbostratical illites the layers are truly randomly stacked leading to diffuse streaks for $k \neq 3n$ and $k=3n$ based on the loss of periodicity of the basal oxygen atoms as well as the octahedral atoms [207].

With increasing temperature, $1M_d$ illite transitions to 1M illite [182]. In this polytype, the layers have the same orientation and the layer shift is $\frac{a}{3}$. The polymorphs differ by which two of the three octahedral cation sites (M1, M2, M2') are occupied. In trans-vacant 1M illite ($1M_{tv}$) the M2 and M2' octahedral sites are filled while M1 is empty, leading to the space group of $C2/m$. In cis-vacant 1M illite ($1M_{cv}$) M2 (or M2') is empty with M1 and M2' (or M2) being filled causing the space group to be $C2$. While the layer dimensions (a, b and γ) stay the same for $1M_{cv}$ and $1M_{tv}$, the layer displacement along a differs with $T_x = c * \cos(\beta)$ =-0.383a for $1M_{tv}$ and -0.308a for $1M_{cv}$, respectively [210].

At higher temperatures, 1M illite transforms to $2M_1$ illite [211]. If 1M illite occurs with $2M_1$ illite, it has high Mg [76] and sometimes high Fe contents [212]. 1M is therefore associated with large fluid/rock ratios and will be absent if the formation conditions do not favor high Mg contents [76]. Additionally, especially the $1M_{tv}$ polymorph may be preferred in environments with fluids that have a high K^+ supersaturation [213]. In contrast, $2M_1$ illite is usually detrital in sediments [214].

3.1.3. Fibrous illite

Fibrous or lath-shaped crystals are a special morphology of illite, which are generally formed under the influence of hydrothermal activity. Weaver described lath-shaped illite for the first time in 1953, having found it in greywacke [215]. He noted that the crystals contained less $Fe^{2+/3+}$ and Mg^{2+} than an average illite and suggested that larger laths consist out of smaller laths in the same orientation. Later research suggested that illite fibers actually contain more Mg^{2+} than the average platy illite. Blaise et al. [66] also suggested that the interlayer charge in the fibers is lower (0.7-0.9) compared to crystals with a platy morphology (0.8-1.0) because illite fibers have a higher Si content.

Formation requirements

Fibrous illite can be found in shales [216], veins [201], granite [201] but most often in sandstones that underwent hydrothermal episodes [66,68,69]. It crystallizes preferably in the pore space while platy illite forms epitactic overgrowths on K-feldspars [66].

In sandstones, the potassium for illite formation is derived from K-feldspar dissolution [217] or migrating fluids [218]. These can contain dissolved material from neighboring shales [219] or evaporite formations [194]. The formation of fibrous illite by the reaction of K^+ with kaolinite requires higher temperatures than illite formation from smectite illitization [220]; however, the reaction rate is rapid once it has started. The saturation state of illite is mainly dependent on SiO_2(aq), Al^{3+}, K^+ and H^+ activities [221]. For a system in equilibrium with quartz, a stability field for muscovite is created between K-feldspar and kaolinite, which leads to the formation of illite in their presence [222]. At lower temperatures, a supersaturation of the hydrothermal fluid concerning the K content is needed. At lower supersaturation, fibrous illite will crystallize [204]; at higher supersaturation, the crystals will be pseudohexagonal platelets [216]. For fibrous illite to form in the pore space, nucleation is the primary controlling factor [223], where

faster nucleation rates counterbalance slower crystal growth rates. The nucleation is heterogeneous and occurs on pore walls, particularly on energetically preferably substrates such as muscovite, detrital illite and kaolinite [68,224] with fibers growing into the available pore spaces [74]. This promotes the formation of fibrous illitic cement instead of the replacement of K-feldspar [225].

Different morphologies of illite point to several populations that formed under different conditions [66] or multiple phases of fluid migration. This can also have an effect on the polytype with illite fibers being $1M_{tv}$ and platy morphologies being $2M_1$, where platy crystals are formed at higher temperatures than fibrous ones. Thus, it is evident that the polytype, structure and chemical composition of illite are strongly dependent on variations in fluid composition, temperature and fluid/rock interactions [226].

Fibrous illites in reservoirs

In sandstones that are potentially used as oil or geothermal reservoirs, their quality is strongly dependent on the amount and type of cementation [70,71], which can be affected by extent, origin, type and timing of the cementation episode [227]. Illitic cement is the most restricting one [72]. Illite can occur as feldspar alterations, detrital grains, grain coatings, bridges between grains, pore linings or pore fillings [68,228]. The alteration of feldspar can cause a secondary porosity in the sandstone through dissolution but also liberates elements for clay mineral formation in the process [229].

The morphology of fibrous illite

Illites in sandstones were considered detrital before the first report of illite laths by Weaver [215]. In pores, illite occurs as very well-developed laths or fibers. Depending on the thickness, they can be rigid or flexible but are extremely fragile and break into very fine particles [74]. Güven [204] suggested a growth mechanism for these illites. In the illite layer, the chains of cations in the octahedral sheet sharing oxygen with the tetrahedral sheet have the same relationships as the silicon chains in the platy morphology. The growth chains are also called periodic bond chains [230]. Since there is no growth chain exposed in the [001] direction, the crystal can only extend along this axis after two-dimensional nucleation at a screw axis dislocation. The periodic bond chains in the layers are composed of Si-metal-copolymers. They are situated at an angle of 120° from each other and present equally favorable attachments for two-dimensional growth, resulting in the three main growth directions [100], $[\bar{1}10]$ and $[\bar{1}\bar{1}0]$ which are parallel to the growth fronts (010), (110) and $(1\bar{1}0)$ (see Figure 26A)). Thus, the habit of 1M illite crystals is controlled by the relative growth rates of these three directions. Depending on the growth rates, three different morphologies can develop (see Figure 26B)). If the growth rates are equal, a hexagonal habit is formed. For (pseudo-)rhombs to form, the (010) growth front has to be faster and for laths it has to be slower. In sandstones, laths have a $1M_{tv}$ polytype [68]. Some of these laths have a perfect morphology and {110} prism faces can be seen at the ends [74]. In $1M_{tv}$ illite the (110) and $(1\bar{1}0)$ growth fronts have many kinks and exposed octahedral cis-sites with broken bonds, which may cause them to grow faster. In addition, the (010) growth front exposes pairs of octahedral OH groups, which can form complexes with organic or inorganic functional groups. These can “poison” the growth face and inhibit the growth in this direction. For example, organic acids are very common in formation waters of clastic reservoirs [231]. During hydrothermal activities, oxalic acids can form complexes on the (010) face and stop the growth until the decay of the oxalate, leading to a

development of a fibrous habit with an elongation along the *a*-axis [232]. Güven [204] also noticed that illite fibers have a lower potassium content than cores they grow on and suggested that the difference arises because K^+ ions can be easily released along the long (010) faces. This shows that the morphology and composition of illite is at least to some extent dependent on the crystal structure [203,213].

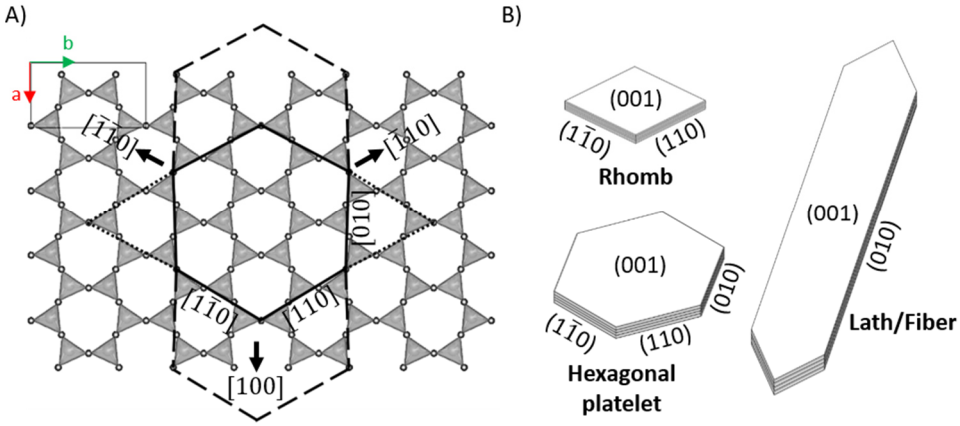

Figure 26: The morphology of Illite. A) The periodic bond chains run along the three growth directions [100], [$1\bar{1}0$] and [$\bar{1}10$]. The habit of the crystals is controlled by the relative growth rates. B) Three different habits can develop: rhombs, hexagonal platelets or laths/fibers.

Gümbelite is another type of fibrous illite, although it does not occur in pores of sandstones but more likely in hydrothermal veins e.g., in shales. It was first mentioned by Dana [233], but due to its structural and chemical similarities it was later found out that the mineral described is a Mg-rich illite [234]. In contrast to fibrous illite in sandstones, these vein fillings consist mainly of $2M_2$ illite with small amounts of $2M_1$ [202], with the elongated axis being parallel to <110> [235]. This could be caused by a high density of twinning and intergrowths. If the nucleation density on the vein walls is very high, a competition during crystals growth can occur [236]. Crystals that are oriented with their fast growing directions perpendicular to the vein wall will out-compete other crystals leading to fibers [202].

Kuwahara et al. [237,238] found another version of $2M_1$ lath shaped illite. Here, fibers were elongated along [100]; however, they only used Atomic Force Microscopy (AFM) to determine the lattice directions based on spiral centers on (001) caused by dislocations.

3.2. Labradorite

3.2.1. Feldspars

Feldspars are the most abundant minerals in the earth's crust. They are framework silicates, which incorporate aluminum into their tetrahedra. The fundamental structure, which was first presented by Taylor [239], consists of a three-dimensional network of tetrahedra. Tetrahedra pairs with opposite orientations form rings. Along the *a*-axis, the rings are connected by the apices of the tetrahedra, forming chains [88]. The T_1 and T_2 tetrahedra connect the double chains in the *c*- and *b*-direction, respectively [240]. The M position is located between the chains in the interstices of the framework [88]. The resulting sum formula is $MSi_{4-x}Al_xO_8$ with the M position mainly being occupied by K^+, Na^+ or Ca^{2+} and x = 1 for K^+, Na^+ and 2 for Ca^{2+}. Most natural feldspars are part of a ternary system with the end members being K-feldspar (Or,

KSi_3AlO_8), Albite (Ab, $NaSi_3AlO_8$) and Anorthite (An, $CaSi_2Al_2O_8$) [241] (see Figure 27). Albite and anorthite form a solid solution whose members are generally called plagioclase.

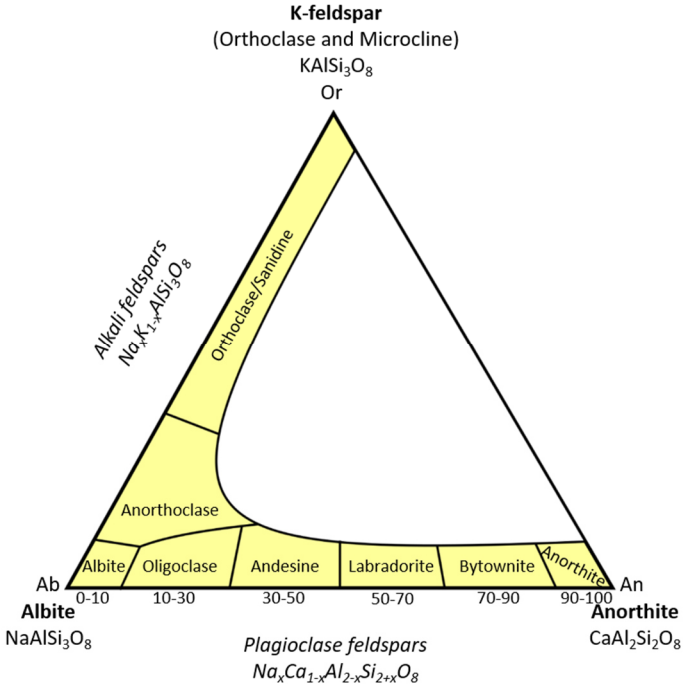

Figure 27: Ternary diagram of feldspar at ~800°C with end members Anorthite (An), Albite (Ab) and K-feldspar (Or). Compositions between albite and K-feldspar or anorthite are called alkali feldspar or plagioclase, respectively.

High temperature K-feldspars crystallize in the monoclinic space group $C2/m$. At lower temperatures, the crystal lattice begins to collapse. Smaller cations like Na^+ or Ca^{2+} cause the lattice to distort and the symmetry is reduced to $C\bar{1}$. This changes the length of the oxygen bonds as well as their angles [88]. At lower temperatures, Si-Al ordering takes place in the tetrahedra [241]. In order to enable a structural correlation between all feldspars, the crystallographic axes are not changed for triclinic feldspars, which leads to non-primitive unit cells for some plagioclase structures [242]. $C2/m$ has only two symmetrically independent tetrahedral positions T_1 and T_2. The elimination of the mirror plane due to Si-Al ordering creates four different tetrahedral positions in feldspars with triclinic symmetry: T_{1o}, T_{1m}, T_{2o} and T_{2m} [88]. Additionally, plagioclase has split M positions with a separation of ~0.8 Å [243]. This causes a distribution of Na^+ and Ca^{2+} on the two positions based on their environment of differing Al-Si distributions [244].

Plagioclase

In the plagioclase solid solution series there are various crystal structures present: the primitive anorthite structure, the body-centered anorthite structure, the intermediate structure and the albite structures [242]. The primitive anorthite structure $P\bar{1}$ shows so-called *a*-reflections with $h + k = 2n$, $l = 2n$ which are also called main reflections because they have the highest intensity. Additionally, there are reflections with $h + k = 2n$, $l = n$ (*c*-reflections), $h + k = n$, $l = n$ (*b*-reflections) and $h + k = n$, $l = 2n$ (*d*-reflections) present (see Figure 28A)). These reflections create a pseudo *C*-centering with a pseudo-repeat in the *c*-direction of half a unit cell, which is characteristic for anorthite under equilibrium conditions at room temperature [242]. Above 240°C anorthite has $I\bar{1}$ symmetry until its melting point at ~1557°C [245]. In the body-centered anorthite structure, *c*- and *d*-reflections are absent (see Figure 28B)). In-between

the anorthite and albite structures at An_{25-75}, the structure changes to the intermediate plagioclase structure in which there are only *a*-reflections present. In addition, a pair of extra satellite reflections (*e*-reflections) with a center of mass at a^*, b^*, $c^*/2$ can be observed indicating absent *b*-reflections (see Figure 28C)). *e*-reflections were first described by Chao and Taylor [89]. They become more diffuse with increasing Ab content [87]. All plagioclases with more than An_{55} show *f*-reflections around the *a*-reflections. These are second-order satellite reflections that are very faint but intensify with high anorthite content [246]. Xu et al. [91] discovered *f*-reflections in a Na-rich (An_{49}) e-plagioclase for the first time. At temperatures above ~950°C, the high albite structure is present. This structure only shows *a*-reflections, which causes a $C\bar{1}$ symmetry and a bisection of the *c*-axis to 7 Å (see Figure 28D)) [247]. The differences between the high and low albite form are mainly reflected by a change in the γ angle of 90.3° to 87.7°.

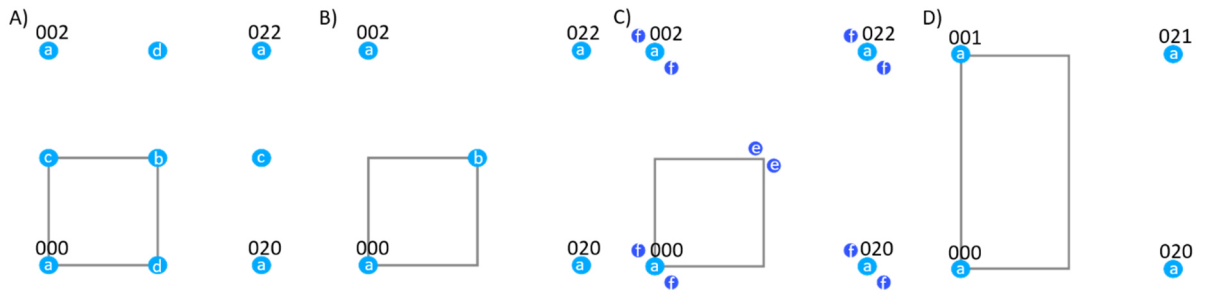

Figure 28: Schematic drawings of reflection arrangements along the [100] zone axis of various plagioclase phases. The unit cell is marked by a grey box. A) Primitive anorthite structure with the space group $P\bar{1}$. *a*-, *b*-, *c*- and *d*-reflections are visible. B) Body-centered anothite structure with the space group $I\bar{1}$. *c*- and *d*-reflections are absent. C) Intermediate plagioclase structure with the space group $X\bar{1}(\alpha\beta\gamma)0$. *a*-reflections are present and additionally, there are *e*-reflections around the absent *b*-reflections and *f*-reflections around the *a*-reflections. D) High albite structure with the space group $C\bar{1}$. Only *a*-reflections are present, leading to a doubling of the *c**-axis.

At each phase transformation, antiphase domains may be produced [248]. At low temperatures, there are three miscibility gaps in the plagioclase series, leading to lamellar intergrowths or domain textures [241]. They are associated with breaks in the Al-Si ordering schemes as a function of composition [249]. Pure albite is only stable up to An_5. At higher An contents the Peristerite miscibility gap causes the crystal to segregate into two phases with An_{1-5} and An_{20-25} [250]. The Huttenlocher miscibility gap is located at the anorthite end of the plagioclase series at An_{65-90} [241]. In-between, the Bøggild miscibility gap is present. The miscibility gabs will be explained in more detail in chapter 3.2.4.

Variability of the cell parameters

The unit cell parameters of feldspars are affected by composition, Al-Si ordering and strain. The γ angle is the most dependent on composition and Al-Si ordering [251] and decreases with increasing order [252]. In ordered structures, the mean Si-O and Al-O distances are different so that the tetrahedral occupancy can be calculated by using the average individual $\langle T_i - O \rangle$ and grand mean tetrahedral distances$\langle\langle T - O \rangle\rangle$ [253]:

$$Occ(Al) = 0.25(1 + n_{An}) + (\langle T_i - O \rangle - \langle\langle T - O \rangle\rangle / const. \quad (53)$$

with n_{An} being the An content, and the constant being ~0.13 Å for plagioclase.

Stress is mainly counterbalanced by a change of the so-called crankshaft chains. They connect the rings of four tetrahedra and can be shortened or extended easily [87] by changing the T-O-T angles [254]. Thereby, the dimensions of the tetrahedra change very little. Since the crankshaft chains extend along [100], the *a*-axis is the most compressible cell axis [254,255]. Thereby, the state of the Si-Al order has no major effect on the compressibility.

Twinning in feldspars

Feldspars are often severely twinned after one or various twin laws. The twin laws consist of a composition plane and a twin axis, which is a two-fold symmetry axis. Overall, there are around 20 twin laws defined [87] but some are indistinguishable from each other or not known in nature. The most common twins are albite, acline and pericline and albite-Carlsbad twins, the first three being lamellar twins [256]. Lamellar (polysynthetic) twinning is created by an interference of several growing crystals at the end stages of the crystallization period (growth twins) [257]. Another way of inducing twinning is stress (deformation twins). The width and nature of the twin lamellae are mainly dependent on the environment during the crystallization period and not on the composition or structure alone [257].

3.2.2. Labradorite

Labradorite was first found in 1770 on the Isle of Paul near Nain, Labrador, Canada, and described by Leske [258]. It occurs mainly in basalts, gabbros and mafic metamorphic rocks. It is part of the plagioclase series, with labradorite existing in the composition range between An_{50} and An_{70} [84]. The cell parameters in this compositional range vary between a = 8.1668–8.1809 Å, b = 12.8509–12.8723 Å, c = 14.2086–14.2148 Å, α = 93.5802–93.5325°, β = 116.23–116.1817° and γ = 89.8396–90.387°, with a cell volume of 1334.53–1339.8 $Å^3$ [60,259]. It is frequently twinned according to the albite or pericline laws and polysynthetic twins are often seen on (001) or (010) [84]. In addition to twinning, Labradorite contains a variety of different structural features, including a 3–6 nm modulated superstructure exhibiting *e*- and *f*-satellites, a 20–50 nm domain texture and a lamellar structure that is ~100 nm in size and causes the well-known schiller, also called labradorescence [85]. Labradorescence describes an interference with light on lamellae that are all oriented in the same direction, which causes a play of color that can range over the entire spectrum of the visible light [260]. Because of this, labradorite is mainly used as a gemstone. Labradorite may contain many inclusions, which are typically irregularly distributed within the crystal, with the most common ones being iron oxides such as hematite, magnetite, or ilmenite [261]. However, they do not affect the occurrence of labradorescence [262].

3.2.3. Labradorescence

Bøggild [260] first named the schiller of labradorite labradorescence and suggested that it is caused by an occurrence of lamellae with variable thickness in the crystal. Raman & Jayaraman [262] suggested that the lamellae were orthoclase inclusions and Chao and Taylor [89] thought that they were alternating in albite and anorthite structure. However, the lamellae actually consist of alternating Ca-rich and Na-rich labradorite. In bright-field TEM images, the lamellae of labradorite are alternating light and dark regions [263]. Depending on composition, their size can vary between 50–250 nm [264]. They are in principle periodic, but tend to branch out leading to a lack of long-range order. Miúra [264] observed that the thickness of the lamellae changes with the composition. Bown and Gay [242] discovered that there is no difference between the diffraction patterns of labradorites with and without labradorescence.

Labradorescence occurs because of optical interference of the lamellar structure [263]. The wavelength of the intensity maximum of the reflecting light, i.e., the color of the iridescence, can be explained by Bragg diffraction on a stack of varying thickness [263]. Lamellae were found to form along several orientations, but most often, labradorescence is seen in the direction of the *b*-axis [260]. That is, most lamellae are approximately parallel to the (010) plane [87,263,265]. Several sources claim the labradorizing plane deviates from the (010) plane by approximately 14°–15° [262,266]. The lamellae differ in Ca/Na content [86], with the broader lamellae being Ca-rich, while the narrower lamellae are enriched in Na^+ [265]. The composition of the Ca-poor and Ca-rich lamellae differs by up to 12%. All labradorites with schiller were thought to have orthoclase (Or) contents greater than 2 mol% [86] but Carpenter et al. [267] found lamellae in An_{49} with almost no Or content. With increasing An content, the size of Ca-rich lamellae increases rapidly while Ca-poor lamellae decrease in size and number [87]. The thicker the lamellae, the higher is the wavelength of the scattered rays ranging from dark blue to red. Based on the work of Bolton et al. [263], an equation was established by Miúra et al. [268] that displays the origin of the respective color of labradorite. The lamellae can be considered reflecting planes of light. The wavelength λ of the reflected light is dependent on the thickness of a pair of lamellae $d = (d_a + d_b)$, the refractive indice n and the glancing angle θ. The total reflection amplitude V can then be calculated by:

$$V = r + \sum_{n=1}^{N} [1 - e^{i\beta_a(1+\gamma_a)}] * e^{i(n-1)}[\beta_a(1+\gamma_a) + \beta_b(1+\gamma_b)] \quad (54)$$

with the overall thickness of the crystal being $N(d_a+d_b)$, the amplitude reflection coefficient r, and the Bragg equation for Ca- and Na- rich lamellae defining the term $\beta_m = 4\pi\lambda_m^{-1} n_m \sin\theta_m$, m = a, b and the distance $(1+\gamma_m)$ being a random variable of the symmetrical probability distribution of lamellae distances $f(\gamma)d\gamma$. If the lamellar thickness d is sufficiently small and N is sufficiently large, the observed average intensity $I = < |VV^*| > / r^2$ can be approximated by:

$$I \simeq \frac{e^{-2M}(1 + e^{-2\alpha_a}) - 2e^{-(2M+\alpha_a)}\cos\beta_a}{1 + e^{-2M} - 2e^{-M}\cos L} \quad (55)$$

where $M = \alpha_a + \alpha_b$, $L = \beta_a + \beta_b$ and $-\alpha_m(\beta_m)$ is the cumulant of the characteristic function $f(\gamma_m)$ and is described by $< e^{i(\beta_m \gamma_m)} > = e^{-\alpha_m(\beta_m)}$.

A detailed derivation of the equations can be found in Bolton et al. [263] and Miúra et al. [268]. Using equation (55), Miúra et al. [268] calculated the reflected intensity I as a function of λ_m, d_m, n_m, θ_m and σ_m (standard deviations of mean thicknesses of alternate lamellae). Based on these parameters, regression equations for the wavelength λ and thus the An content were derived.

$$\lambda = 3.105d - 21.178 \text{ [Å]} \quad (56)$$

$$An = 0.09d + 36.083 \text{ [mol\%]} \quad (57)$$

The results for various labradorescence colors are tabulated in Table 3.

Table 3: The labradorescence colors of labradorite with their respective required lamellar thickness d, wavelength λ and An content (after Miúra [268]).

Labradorescence color	Lamellar thickness d [nm]	Maximum wavelength λ_{max} [nm]	An content [mol%]
Near UV	80~125	270~380	44~47
Violet	~145	~445	~49
Blue	~160	~495	~50
Green	~180	~555	~52
Yellow	~190	~585	~53
Orange	~205	~630	~54
Red	~260	~800	~59
Near IR	~310	~960	~64

It is likely that the labradorite lamellae are formed by spinodal decomposition which is an important mechanism for the segregation of solid solutions between two end-members with the same structure. For more information on spinodal decomposition it is referred to Appendix 3. Labradorite shows typical indications of a spinodal decomposition process in TEM such as lamellae oriented approximately parallel to the (010) plane that show bifurcations, which occur during coarsening [269,270]. Additionally, labradorite shows diffraction contrast of the lamellae due to slight variations in lattice spacing and a periodic modulation with diffuse boundaries, where the diffraction pattern of a single phase shows satellite reflections [88]. The effect of potassium in this process remains undefinable. In alkali feldspars, small amounts of anorthite can cause a significant change in the solvus temperature, which is due to the extra charge [271]. However, since K^+ and Na^+ have the same charge, small amounts of orthoclase should not play such a distinct role in plagioclase [272].

3.2.4. e-plagioclase

At temperatures above 700°C, there is a solid solution between albite and anorthite since $Na^+ + Si^{4+}$ is equivalent to $Ca^{2+} + Al^{3+}$ and the stoichiometry is balanced by the change in the Al:Si ratio. At lower temperatures, in the compositional range in between albite and anorthite, neither of these ordering schemes are possible. The deviations from the 1:3 and 1:1 Al:Si ratios of the end members lead to an unfavorable energetic situation [88]. By reorganizing the structure and ordering the atomic positions, the energy of the solid solutions can be minimized. Since the Al/Si distribution is coupled to the Na/Ca distribution and the Al/Si ordering schemes are fundamentally different in albite and anorthite, this results in an incommensurate structure with satellite reflections of different periodicity imposed on the main reciprocal lattice [90]. Thus, the structures e1 and e2 are formed, which are Ca-rich and Na-rich respectively (see Figure 29) [88]. Therefore, three different miscibility gaps exist in the plagioclase series. The Peristerite intergrowth forms at $An_{2\text{-}20}$ and consists of albite and e2 plagioclase. In the Huttenlocher miscibility gap lamellar intergrowths of anorthite and e1 plagioclase occur at $An_{65\text{-}90}$ [88]. At ~An_{50}, a discontinuity occurs in the spacing and orientation of the satellites, as well as the cell parameters and solution enthalpy. This way e1 and e2 are easily distinguished from each other [88]. This marks the position of the Bøggild miscibility gap in which lamellar intergrowths of e1 and e2 are formed. Various endmember compositions of the Bøggild intergrowth are given in literature with An_{40}–An_{50} [88,265], $An_{35–40}$–$An_{50–55}$ [273], $An_{44–45}$ (lower limit) [251], An_{47}–An_{53} [87], An_{51}–An_{50} [260], An_{45}–An_{65} [84].

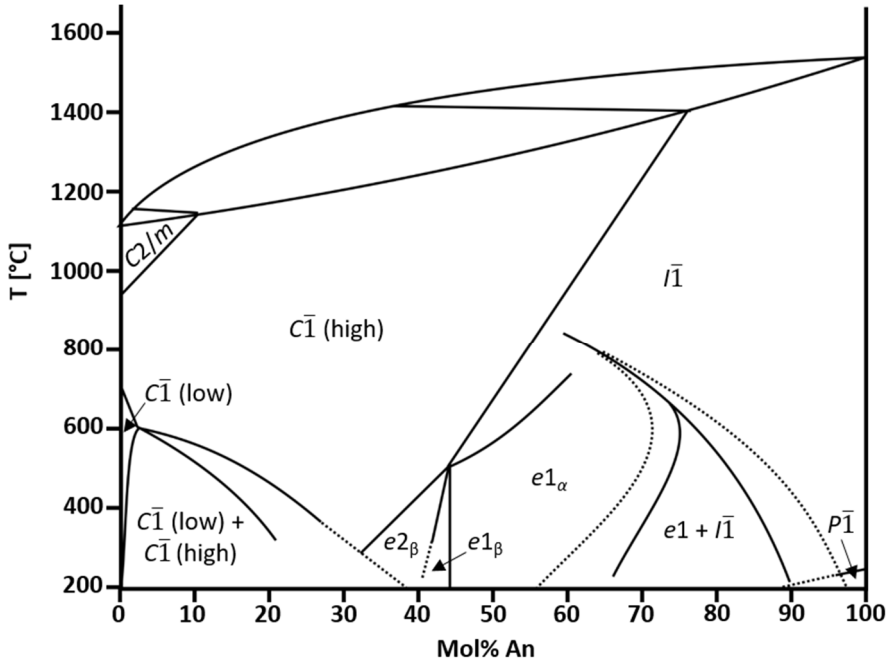

Figure 29: Phase diagram of the plagioclase series redrawn after Jin et al. [259]. Dashed lines indicate suspected phase boundaries. At higher temperatures, structures $C\bar{1}$ and $I\bar{1}$ are stable. At lower temperatures, the plagioclase series contains three miscibility gaps: Peristerite (~$An_{2\text{-}20}$), Bøggild (~$An_{40\text{-}50}$) and Huttenlocher (~$An_{65\text{-}90}$). In-between various solid solutions are stable, which have different structures at different compositions ($C\bar{1}$, e2, e1, $I\bar{1}$ and $P\bar{1}$). Close to the miscibility gaps lamellar intergrowths are formed.

s-reflections

The lamellae differ in An content by ~10%, which causes slightly different lattice constants [85]. However, the phase boundaries between them are coherent [87]. The lamellae merge without defects or stress because there is only a slight difference in cell parameters in the plagioclase series of 0.1% and the γ angle differs by only 0.4% [265]. This leads to slightly rotated lamellae around an axis perpendicular to the elongation so that their interfaces can accommodate for the different spacings [274]. This slight misorientation causes contrast in TEM bright-field mode [248] and a minor splitting of Kikuchi lines [86,265,273]. Additionally, so-called *s*-satellite reflections are formed close to the *a*-reflections, which correspond to the direction of the lamellae [86] and are nearly parallel to *b* [275]. With ~1500 Å, their period equals the size of the lamellae [274]. Since the structure factors for *e*-reflections are different for both lamellae, the modulation has a slightly different orientation, which can be seen by a broadening of the *e*-satellites [241,274]. However, *s*- as well as the different *e*-satellites cannot be resolved by experimental means [276].

e-reflections

The existence of satellite reflections results from a modulation of the ordering scheme. Their position is described by δh, δk, and δl ($\in \mathbb{R}$) with its origin being at the absent *b*-reflections [90]. Based on the satellite position, the modulation is described by the vector $q = \delta h\ a^* + \delta k\ b^* - \delta l\ c^*$ [242]. The direction of the modulation runs perpendicular to q, with a thickness of q. The satellites are weak when the scattering vector is almost parallel to the modulation vector [277]. The satellite reflections change continuously in orientation and spacing over the course of the lamellae [86,265]. Thus, the thickness and direction of q change

with increasing An content [91], although the direction remains close to the direction $(11\bar{4})$ [278]. For plagioclase, q has a magnitude of about 3–6 nm [274].

Domains in labradorite

The lamellae of labradorite can additionally contain domain textures with several 100 Å in size [279]. The domains are elongated with diffuse boundaries and smaller in the thinner lamellae with some domains lacking *e*-fringe contrast [279]. Morimoto [241] postulated that the domains are periodic antiphase bands separated by antiphase boundary bands. Jin & Xu [60] suggested that the domains are alternating $I1$-like related by inversion twins. The inversion boundary has a $I\bar{1}$ symmetry and is richer in calcium [91].

The modulated structure of labradorite

The modulated structure of labradorite has been widely discussed since Chao and Taylor [89] found satellite reflections in the diffraction patterns and many different theories on how the superstructure is created have been published. Megaw [280] provided the first attempt at an explanation for an ideal structure of An_{78} indicating four anorthite sub cells connected by two bridging sub cells, however, the cation distributions were not precisely given. In 1967, Korekawa and Jagodzinski mentioned for the first time that a density modulation wave of Na and Ca could be the reason for the *e*-satellites and that the Ca^{2+} and Na^{+} atoms are periodically separated in non-tetrahedral cation positions [275]. Nonetheless, the shifts of Ca, Na and the framework were not taken into account. Toman and Frueh [281] proposed a shift modulation of the framework and an ordering of Si/Al and Na/Ca based on the bond distances. They suggested that the main displacement direction is ~ parallel to the *b*-axis and only a small fraction of atoms in the structure need to possess displacements of magnitudes >0.25 Å. Kitamura and Morimoto [90] found that the modulation indicates a small-scale alternation of Na-rich and Ca-rich bands. Because sodium stays in the central part of the cation position while calcium can move further away, the shift is dependent on the M site occupancy. Hence, the more Ca-rich, the larger the shift. This in turn has a major influence on the Al-Si distribution, which results in a shift of the framework as well. They mentioned for the first time that the superstructure actually consists of two different modulation waves, a shift wave representing the shifts of all atoms and a density wave representing the change in occupancy. Korekawa et al. [278] found large anisotropic displacement factors, which they interpreted as positional disorder and suggested that the superstructure contains a weak density modulation of Ca/Na. Wenk et al. [244] interpreted their investigations on the superstructure as periodic stackings of basic units resembling a $I\bar{1}$ symmetry but with different stacking orders. Contradictory to Toman and Frueh [281], they suggested that the displacement of oxygen positions caused by Al-Si ordering contributes the most to the satellite reflections. After the introduction of space groups for the (3+1)D superspace by de Wolff et al. [282], Yamamoto et al. [283] chose to assign the triclinic space group $P\bar{1}\bar{1}$ to labradorite. They found that the displacive modulation contributes more to the satellite reflection intensity than the density modulation and that the substitution of Ca/Na is weak. Boysen and Kek [276] also mentioned that a density and shift modulation of Ca^{2+} and Na^{+} play a dominant role in the modulation.

The most complete and recent theory was developed by Xu [284], H. Xu et al. [91], Jin & Xu [60], Jin & Xu [251] and Jin et al. [259]. It states that the superstructure is composed of a modulation wave that describes the displacement and density change of all atoms in the average structure. In general, Na^{+} atoms remain in the central part of their position in the structure,

while Ca^{2+} atoms lie further away from their center. Thus, the larger the electron density offset, the more Ca-rich the composition. The modulation was assigned to arise from the Ca and Na positions, which also has a great influence on the distribution of Al^{3+} and Si^{4+} atoms in the tetrahedra where Al is preferably located around Ca. Thus, Al-Si and Ca-Na ordering are the major driving force for the formation of the modulation, which satisfies local charge balances. The modulation in the T-O distances arises from the Al-Si ordering.

Stability of e-plagioclase

The e-plagioclase structure has long been considered metastable [244] because Al/Si diffusion seemed too slow for equilibrium to be reached. However, some reasons support its actual stability. First, natural potassium feldspars can also reach a high Al/Si degree of order at temperatures of a few 100°C. Moreover, Al/Si diffusion distances of at least 100–200 nm are possible in the plagioclase structure, as shown by the occurrence of lamellae of this order in labradorite [249]. Additionally, the modulation period does not get longer as the cooling rate of e-plagioclase decreases, it gets longer with increasing An content [285].

With decreasing temperature, a typical sequence of stable structures is usually: disordered with high symmetry → incommensurately ordered → commensurately ordered [286], but in the case of plagioclase its: disordered → commensurately ordered → incommensurately ordered. Since a deviation from the commensurately ordered compositions (pure Ab and An) is energetically unfavorable, the possibility of an incommensurate structure increases [287].

3.3. Eveslogite

3.3.1. General information

The first information about eveslogite was published in 2003 by Menchikov et al. in Russian. It was first mentioned in an English paper as a new mineral by Jambor and Roberts in 2004 [288]. Eveslogite grows in fibers of up to 0.05 mm * 5 cm in size and forms plicated aggregates. With the sum formula $(Ca,K,Na,Sr,Ba)_{48}[(Ti,Nb,Fe,Mn)_{12}(OH)_{12}Si_{48}O_{144}](F,OH,Cl)_{14}$ it contains a large variety of elements and infrared spectra show the presence of OH/H_2O in the structure. It has a light brown to yellow-brown color and a vitreous to silky luster. The mineral is brittle with a splintery fracture and it has perfect cleavages along {001} and {010}. The Mohs hardness is 5 and based on the sum formula the calculated density is 2.93 g/cm³. Eveslogite is named after its type locality Mt. Eveslogchorr, Khibiny massif, Kola Peninsula, Russia, where it was found in a veinlet that cuts a nepheline syenite body. The Kola Peninsula is the north-eastern part of the Precambrian Baltic Shield. It contains complicated block structures, which have been reactivated several times by tectono-magmatic episodes. Various alkaline, ultramafic and carbonatic intrusions took place during the Devonian which formed the Kola Alkaline Province (KAP) [289]. It contains various nepheline syenites, foidalites and alkali syenites [290]. Through the subsidence of the Khibiny-Kontozero-Graben the Khibiny massif was created; the largest agpaitic nepheline syenite body in the KAP [291].

Men'shikov et al. [64] believed eveslogite to be monoclinic with the space group possibly being *P2/m*. They determined the unit cell parameters as: a = 14.069(3) Å, b = 24.937(5) Å, c = 44.31(2) Å, γ = 95.02(4)° and described the structure to be an astrophyllite-like heterophyllosilicate. In later publications, however, it was suggested that eveslogite rather is a chain- ribbon- and tube-silicate [61–63]. Both theories will be explained in the following.

3.3.2. Heterophyllosilicates

Heterophyllosilicates are phyllosilicates with a periodic substitution of silicon by titanium [292]. In the tetrahedral sheet of the TOT layer, rows of Si tetrahedra are replaced by rows of 5- or 6-coordinated Ti polyhedra [292]. Since the length of the O…O edges of the Ti polyhedra (2.7 Å) is very close to that of the Si tetrahedra, the substitution causes no strain [63]. These layers are called HOH layers (H = hetero substitution). They consist of a bafertisite-like module B = $I_2Y_4[X_2O_4Si_4O_{14}](O,OH)_2$ which can be intercalated with a mica-like module M = $IY_3[Si_4O_{10}](O,OH)_2$ with I,Y = interlayer and octahedral cations, X = Ti^{4+} or related cations. Bafertisite-like heterophyllosilicates (HOH) only contain bafertisite-like modules; astrophyllite-like heterophyllosilicates $(HOH)_A$ also have mica-like layers (see Figure 30A)).

Eveslogite was characterized by Men'shikov et al. [64], Ferraris and Gula [63] and Ferraris [292] as $(HOH)_A$-type heterophyllosilicate. Based on the cell parameters of Men'shikov et al. [64], it has an *a*-*b* base six times larger than astrophyllite and the length of the *c*-axis equals a thickness of four $(HOH)_A$ layers stacked along [001]. Additionally, the chemical data fits reasonably well to an astrophyllite-like chemical formula [63]. However, Ferraris and Gula [63] suggested that the infrared spectra of eveslogite show a structure that is more likely close to yuksporite, a microporous titanosilicate with channels along [100] (see Figure 30B)).

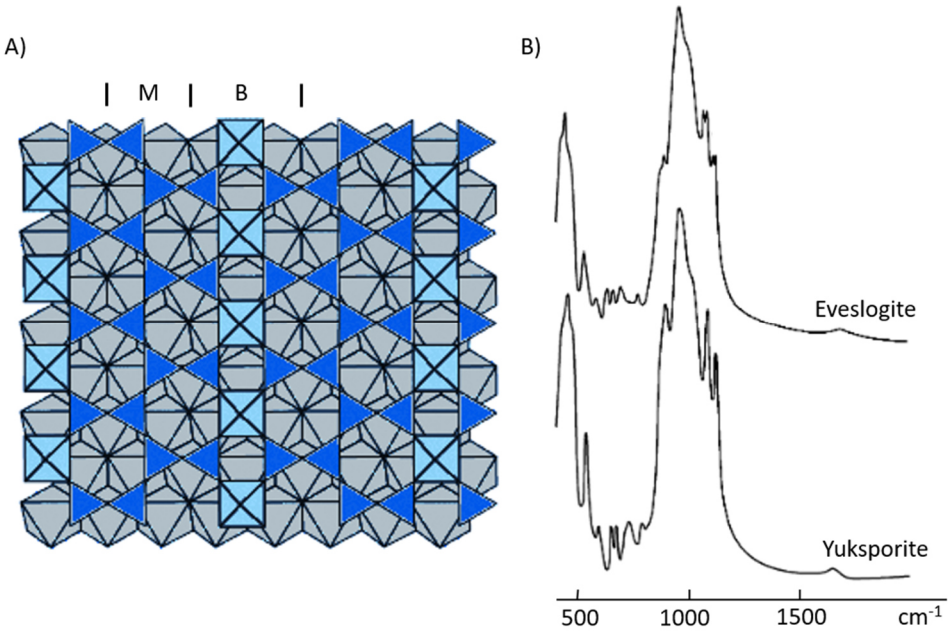

Figure 30: A) Astrophyllite-like heterophyllosilicate $(HOH)_A$ viewed parallel to the TOT layers. It consists of a bafertisite-like module (B) and a mica-like module (M). In the tetrahedral layer one row of Si tetrahedra (dark blue) is replaced by one row of Ti octahedra (light blue). The octahedral layer is shown in grey. (Redrawn after Ferraris and Gula [63]) B) Similar infrared spectra of eveslogite and yuksporite. (Redrawn after Chukanov et al. [61])

3.3.3. Chain-, ribbon- and tube-silicates

Chain-, ribbon- and tube-silicates were characterized by Day and Hawthorne [62] based on the connection of polymerizations of $(TO_4)^{4-}$ tetrahedra. In order to construct a hierarchy, they introduced a geometrical repeat unit ${}^{c}T_r$, with T = tetrahedron, c = connectivity (1-4) and r = number of T in a geometrical repeat unit; based on the minimum number of tetrahedra needed to generate a chain by translation (n_g). Additionally, the topological repeat unit ${}^{c}V_r$ (V = vertices) was introduced, where, in contrast to the geometrical repeat unit, only

topological properties are preserved, hence, the direction of branching of tetrahedra with only one connection is not taken into account. The excess charge of the silicate chains is balanced by cations in the interstitials. This leads to a structural unit, which is strongly bonded and a weakly bonded interstitial unit. The oxygen:tetrahedra (O:T) ratio decreases from 3.0 for chains to 2.5 for tubes as the structural connectivity increases. With increasing polymerization, the abundance of mineral species decreases.

Mineral examples for each geometrical repeat unit are listed in Table 4. Minerals containing more than one geometrical repeat unit are for example astrophyllite ($^{1}T_2$ $^{3}T_2$) or amphiboles ($^{2}T_2$ $^{3}T_2$). Additionally, there are structures with more than one type of structure unit. They are split into two sub-groups. The first group contains minerals with mixed one-dimensional polymerizations (chain, ribbon and tube structures), like charoite and denisovite. The second group consists of minerals with mixed-dimension polymerizations (clusters, chain-ribbon-tubes, sheets), like yuksporite. These structures can include structures like dreier triple chains (see Figure 31A) and D)), double dreier chains (see Figure 31B) and E)) and tubular hybrid dreier quadruple chains (see Figure 31C) and F)) (after Liebau [293]). Charoite contains all three of these polymerizations while denisovite contains only the first two. Yuksporite contains double dreier chains, which are connected to $[Si_2O_7]^{6-}$ dimers by heteroatoms forming nanorods.

Table 4: Examples of minerals ordered by their geometrical repeat unit.

$^{c}T_r$	Mineral	Ideal chemical formula	$^{c}V_r$	Space group	O:T	Citation
$^{2}T_2$	Pyroxenes	$XY[Si_2O_6]$*	$^{2}V_1$	*C2/c*, *Pbca*	3.0	[294]
$^{2}T_3$	Wollastonite	$Ca3[Si_3O_9]$	$^{2}V_1$	$P\bar{1}$	3.0	[295]
$^{2}T_4$	Batisite	$BaNa_2Ti_2[Si_4O_{12}]O_2$	$^{2}V_1$	*Imma*	3.0	[296]
$^{2}T_5$	Rhodonite	$CaMn_4[Si_5O_{15}]$	$^{2}V_1$	$P\bar{1}$	3.0	[297]
$^{2}T_6$	Stokesite	$Ca_2Sn_2[Si_6O_{18}](H_2O)_4$	$^{2}V_1$	*Pnna*	3.0	[298]
$^{2}T_{12}$	Alamosite	$Pb_{12}[Si_{12}O_{36}]$	$^{2}V_1$	*P2/n*	3.0	[299]
$^{1}T_2$ $^{3}T_2$	Astrophyllite	$K_2NaFe_7Ti_2[Si_4O_{12}]_2(OH)_4F$	$^{1}V_1$ $^{3}V_1$	$P\bar{1}$	3.0	[300]
$^{2}T_2$ $^{3}T_2$	Amphiboles	$A_{0\text{-}1}B_2C_5[T_8O_{22}]W_2$**	$^{2}V_2$ $^{3}V_2$	Mcl/orth	2.75	[301]
$^{3}T_{17}$ $^{3}T_{12}$ $^{2}T_4$ $^{3}T_2$	Charoite	$(K,Sr)_{15\text{-}16}(Ca,Na)_{32}$ $[Si_6O_{11}(O,OH)_6]_2[Si_{12}O_{18}$ $(O,OH)_{12}]_2[Si_{17}O_{25}(O,OH)_{18}]_2$ $(OH,F)_4(H_2O)_3$	$^{3}V_{17}$ $^{3}V_{12}$ $^{2}V_4$ $^{3}V_2$	$P2_1/m$	2.56	[99]
$^{3}T_{12}$ $^{2}T_4$ $^{3}T_2$	Denisovite	$K_{15}(Ca,Na)_48_8[Si_{60}O_{162}$ $(F_{16}O_2(OH)_2)](H_2O)_2$	$^{3}V_{12}$ $^{2}V_4$ $^{3}V_2$	*P2/a*	2.70	[101]
$^{2}T_4$ $^{3}T_2$ $^{1}T_2$	Yuksporite	$(Sr,Ba)_2K_4(Ca,Na)_{14}(Mn,Fe)$ $\{(Ti,Nb)_4(O,OH)_4[Si_6O_{17}]$ $[Si_2O_7]_3\}(H_2O,OH)_3$	$^{2}V_4$ $^{3}V_2$ $^{1}V_2$	$P2_1/m$	3.06	[97]

* X = mainly Mg^{2+}, Fe^{2+}, Mn^{2+}; Y = mainly Mg^{2+}, Fe^{2+}, Mn^{2+}, Ca^{2+}

** A = Na^{+}, K^{+}, Ca^{2+}; B = Na^{+}, Li^{+}, Ca^{2+}, Mn^{2+}, Fe^{2+}, Mg^{2+}; C = Fe^{2+}, Fe^{3+}, Mn^{2+}, Mn^{3+}, Al^{3+}, Mg^{2+}, Ti^{4+}, Li^{+}; T = Si^{4+}, Al^{3+}, Ti^{4+}; W = OH^{-}, F^{-}, Cl^{-}, O^{2-}

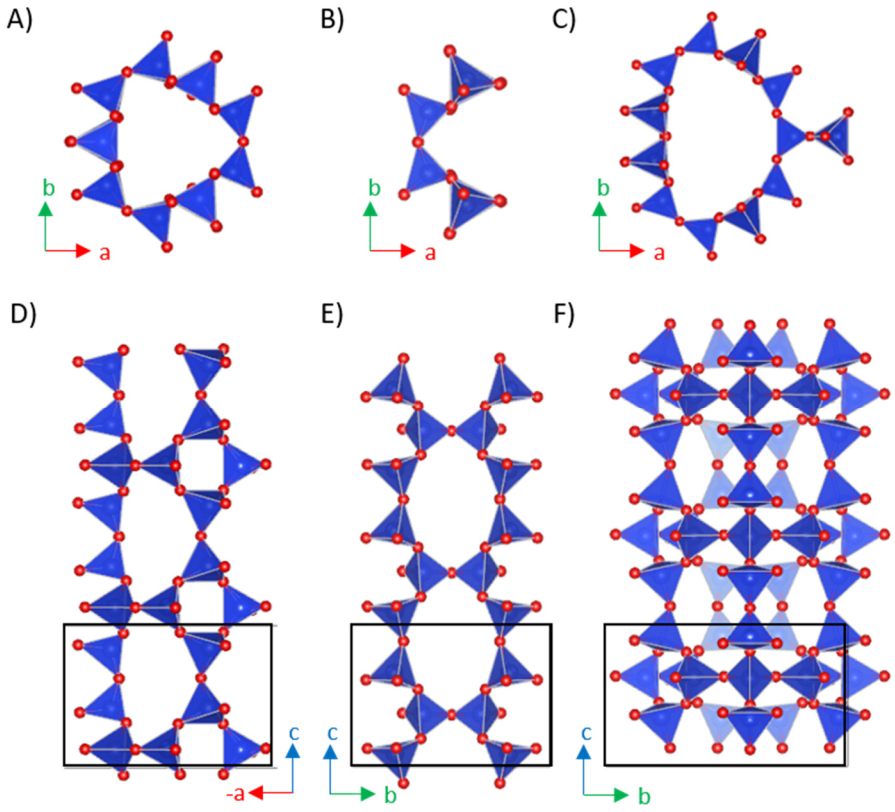

Figure 31: Different kinds of silicate complexes, which can occur in minerals with mixed polymerizations. A) and D) show a tubular loop-branched dreier triple chain $[Si_{12}O_{30}]^{12-}$. B) and E) represent a double dreier chain $[Si_6O_{17}]^{10-}$. C) and F) display a tubular hybrid dreier quadruple chain $[Si_{17}O_{43}]^{18-}$. The geometric repeat unit is marked by a black box.

3.3.4. A measure of complexity

With the increasing number of complex mineral structures being solved, problems of classifying the complexity have come up, since it lacked in exact and quantitative definition. Baur et al. [302] proposed two so-called parsimony indices for describing the topological and geometrical complexity in crystal structures. The topological parsimony index I_t is defined by

$$I_t = (t - e)/t \tag{58}$$

with t being the number of topologically distinct atom sites in the asymmetric unit and e the number of elements present. The crystallographic parsimony index I_C is defined by

$$I_C = (c - e)/c \tag{59}$$

with c being the number of crystallographically distinct atom sites. However, this index has little discriminative power, because neither index is sensitive to chemical complexity or symmetry and both only describe the relations between the number of chemical elements and atom sites. It may even happen that e>t and thus $I_t<0$.

As an alternative, Krivovichev introduced a new measure of complexity in 2013 [303] by calculating the topological information content I_G for each atom by

$$I_G = -\sum_{i=1}^{k} p_i \log_2 p_i \quad (60)$$

where k is the number of crystallographic orbits and p_i is the probability of the occurrence of an atom of the i^{th} crystal orbit and is defined by

$$p_i = m_i/v \quad (61)$$

with m_i being the multiplicity of the crystal orbit relative to the reduced unit cell and v being the number of atoms in the reduced unit cell. The topological information content per unit cell $I_{G,total}$ can then be calculated by

$$I_{G,total} = v * I_G \quad (62)$$

and the maximum topological information content $I_{G,max}$ by

$$I_{G,max} = \log_2 v \quad (63)$$

The topological information content can then be normalized by applying the following equation

$$I_{G.norm} = I_G/I_{G,max} \quad (64)$$

With this approach, both size- and symmetry-sensitive aspects of the structure are taken into account. Structures containing special features such as modularity, misfit relationships and nanoscale units like clusters or tubes (see chapter 3.3.3) tend to be more complex.

4. Experimental

4.1. Samples

Illite

The illite samples in this research were taken from the fibrous illitic cementation of the Remlingen sandstone (see Figure 32), which is a sandstone from the Upper Buntsandstein (Triassic) [304]. The Remlingen site was chosen as a representative example within the Upper Rhine Graben. There, the reservoir fluids typically consist of brines with total dissolved solids (TDS) ranging from 25 to 130 g/L [305]. There are only a few investigations using Remlingen sandstone [306–308], all of which are related to the project ReSalt – Reactive Reservoir Systems, for which the experiments were also conducted in this case. The Remlingen sandstone has a porosity of 12.90% and a permeability of $5.5*10^{-17}$ m^2 [309]. A sandstone with comparable permeability but lower porosity is the Flechtingen sandstone from the Upper Rotliegend (Permian).

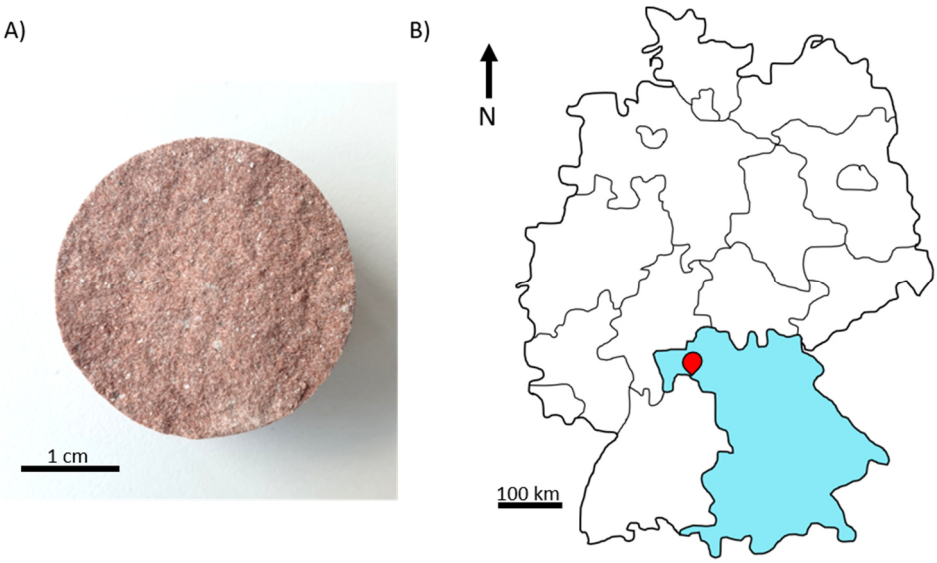

Figure 32: A) Remlingen sandstone plug. Illite is part of the cementation. B) The sample from A) was found in Remlingen, Bayern, Germany, marked in red.

In order to determine the changes in the sandstone depending on different brines, autoclave experiments were performed by Dustin Hering within the scope of a master thesis [310]. Illite fibers occur in both unaltered and altered sandstones. In order to investigate the changes, the unaltered sandstone samples were first analyzed with polarizing microscopy. For this, thin sections were created by the working group crystallography of the Ruhr-University-Bochum. In a next step, the sandstone samples were characterized via ESEM. Here, a fracture surface was created which was then carbon coated. The samples were examined in the center of the plug as well as in the peripheral area (up to ~200 μm inside) to identify any differences. For closer examinations, powdered samples were prepared for TEM studies. The material used was scraped from the unaltered sandstone. For the altered sandstone, fluid filtrates were used accordingly.

Autoclave experiments with brines

For autoclave experiments, the Remlingen sandstone was drilled to plugs of 3 cm in diameter and 2 cm in height. Since the drilling inevitably involves the addition of tap water for cooling

and lubrication, the specimens were then cleaned in an ultrasonic bath for 45 s with deionized water. Subsequently, all samples were dried at 60°C for three days.

The mineral composition of the unaltered sandstone was determined by ESEM with EDS, point counting in a polarizing microscope and XRPD. Table 5 shows the initial qualitative composition of Remlingen sandstone.

Table 5: Qualitative composition of Remlingen sandstone.

Mineral	Content [%v/v]	Method
Apatite	<<1	ESEM with EDS
Barite	<1	ESEM with EDS
Biotite*	1.5	Point counting
Calcite	<1	XRPD
Chlorite	4	XRPD, ESEM with EDS
Hematite	1	XRPD, ESEM with EDS
Illite/mica	13	XRPD, ESEM with EDS
Muscovite*	1.5	Point counting
K-feldspar	18	XRPD, ESEM with EDS
Quartz	62	XRPD, ESEM with EDS
Rutile	<<1	ESEM with EDS
Smectite	<1	XRPD
Zircon	<<1	ESEM with EDS
*part of illite/mica		

For the alteration of the sandstone in the autoclaves, three different fluids were used:

- Synthetically produced fluid
- Hydrothermal brine from Bad Nauheim
- 0.5% Hydrochloric acid

The synthetic brine was produced based on the commercially available mineral water “Gerolsteiner Medium”. In addition to 1 L of “Gerolsteiner Medium”, the synthetic brine, which will be referred to as synthetic Gerolstein brine in the following, also contains 4.9 g of calcium chloride. For the hydrothermal brine from Bad Nauheim no substances were modified or added. The main components of the fluids as well as their TDS values are shown in Table 6.

Table 6: Composition of the fluids used for sandstone alteration.

Fluid	TDS [mg/L]	Na^+ [mg/L]	K^+ [mg/L]	Mg^{2+} [mg/L]	Ca^{2+} [mg/L]	Cl^- [mg/L]	SO_4^{2-} [mg/L]	HCO_3^- [mg/L]
Synthetic Gerolstein brine	5891.2	62.9	14.3	77.8	1561.1	2381.6	65.7	1732.4
Bad Nauheim brine	27944.4	8526.8	313.9	119.6	1321.7	15216.4	155.4	2086.2
0.5% HCl	6733.6	48.0	58.6	88.6	139.2	5450.1	839.6	0

The experiments took place for up to 14 days at 30°C, 90°C and 150°C. The samples, which were chosen for this research stayed in the autoclaves for 3 days at 90°C. After the experiments, the fluids were filtered in order to preserve the washed-out material.

Additionally, barite precipitation experiments were performed by Philipp Zuber, since barite is also known to cause scaling in geothermal reservoirs due to its low solubility. In order to investigate the relation between changes in crystal size or morphology and additives like salts or inhibitors in the fluid, three different crystallization series were analyzed: variation of NaCl content at room temperature, at 90°C and with the addition of an inhibitor along with NaCl. For TEM analysis, powdered samples were produced. The morphology of barite crystals in the crystallization experiments underwent significant changes upon the addition of NaCl and/or DTPMP. These added substances affected the surface energies on specific facets of the crystals or attached to them, thereby inhibiting growth in that direction and altering the crystal morphology. A detailed description of the results of the barite investigations and their interpretation can be found in Appendix 4.

Labradorite

The labradorite used for the electron microscopic examinations displays labradorescence, transitioning from deep blue to yellow and exhibits strong twinning (see Figure 33A)). The crystal originates from Ampanihy, Atsimo-Andrefana, Toliara Province, Madagascar (see Figure 33B)). To ensure uniformity, all samples were obtained from a region displaying yellow labradorescence. In addition to powdered samples, ion-milled samples were also prepared. To achieve a comprehensive characterization and explore all major axes, three sections were created at 90° angles to each other. One section was cut parallel to the labradorescence, while two sections were cut perpendicular to it. Among these perpendicular sections, one encompassed the macroscopic twins, while the other two ran parallel to the observed twins.

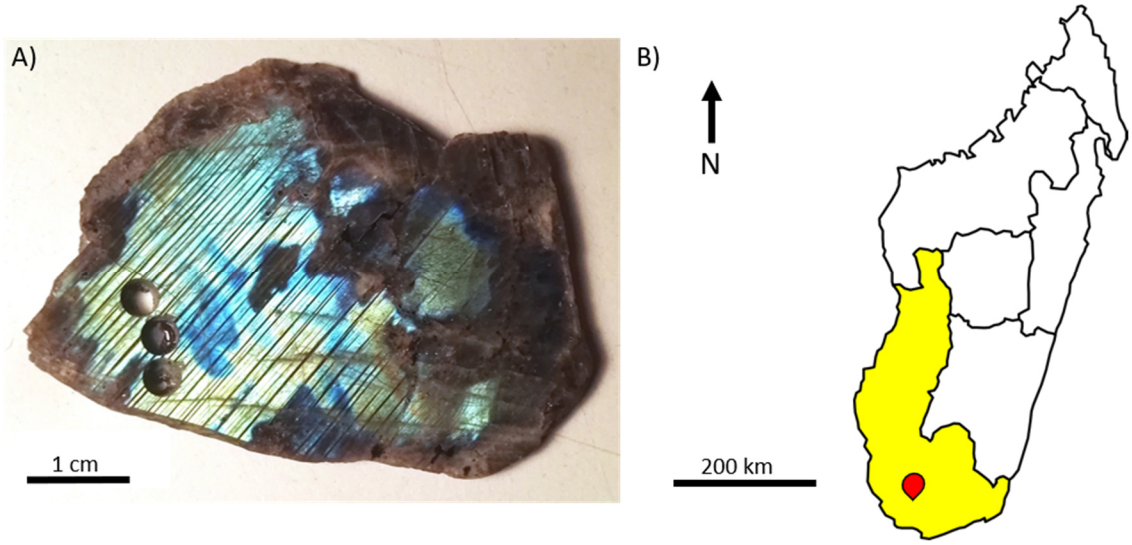

Figure 33: A) Labradorite displaying labradorescence ranging from dark blue to yellow. The samples were taken in a yellow area (lower left corner). Additionally, polysynthetic twinning can be seen. B) Map of Madagascar with the Toliara Province, the place of discovery of the labradorite, marked in yellow [311]. The sample shown in A) is from the southern area Ampanihy, Atsimo-Andrefana.

Eveslogite

The eveslogite sample originates from its type locality Mt. Eveslogchorr, Khibiny massif, Kola Peninsula, Russia. The crystals have a light brown color and a fibrous morphology (see Figure 34). Eveslogite was prepared as powdered samples. Additionally, three thinfoil samples were prepared via focused ion beam microscopy (FIB) by the working group electron microscopy at the Institute for Solid State Physics, University of Bremen, Germany.

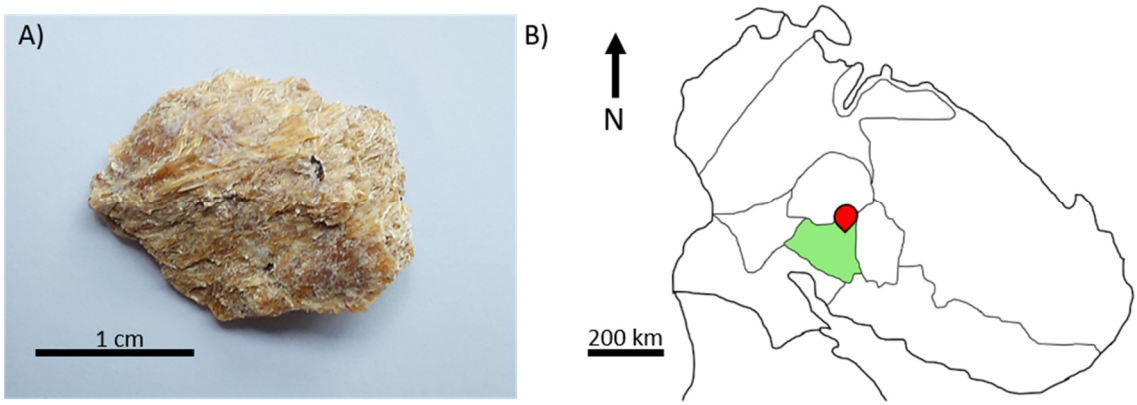

Figure 34: A) Eveslogite specimen. The sample is from Mt. Eveslogchorr, Kola Peninsula, Russia, which is marked in B).

4.2. Sample preparation

In this study, two types of sample preparation were prepared for the TEM investigations: powdered and ion-milled samples. Powdered samples provided an overview of the material due to the availability of numerous particles with varying orientations for analysis. Moreover, the preparation process was gentle on the sample and required minimal effort and time. Nevertheless, a drawback of powdered samples was the unknown original orientation. For research questions where the exact orientation of the material was important, ion-milled samples were prepared. They allowed for the definition of the orientation in advance, enabling the examination of a specific area of the material. However, this preparation method was more time-consuming and put more strain on the specimen.

4.2.1. Powdered sample

For powder sample preparation, a small piece of material was mortared with a few drops of a dispersing agent, such as ethanol. With a pipette the suspension was dropped onto a carbon coated copper grid. Alternatively, the suspension was sprayed onto the grid via an ultrasonic dispenser. For TEM imaging, holey carbon films were chosen (see Figure 35A)). However, if the sample was used for 3D ED measurements, continuous carbon films were preferred because they held onto more crystals. Particularly insulating samples were coated with carbon to increase conductivity.

4.2.2. Ion-milled sample

In cases where the material to be analyzed was excessively large or irregularly shaped, it was advantageous to use a saw to extract a specific region of interest from the sample. In this study, an IsoMet™ low-speed saw from Buehler, Lake Bluff, IL, USA, was used. For this purpose, the specimen was affixed to a glass carrier using Crystalbond and then clamped into the water-

cooled saw. Crystalbond becomes liquid at 170°C but solidifies at room temperature. It can be dissolved in acetone.

In the next step, the sample size was decreased further to fit the grid. This was done by using an ultrasonic disc cutter (Model 601) from Gatan, Pleasanton, CA, USA. This particular drill had a hole diameter equivalent to that of the grid. To begin the drilling process, the sample was once again fixed onto a glass support using Crystalbond and affixed onto the drill pad. A suspension containing SiC and water was applied onto the sample, which acted as an abrasive agent. It was imperative to ensure that the specimen was always sufficiently moistened during drilling to guarantee adequate cooling. Pressure was applied onto the sample with the drill until it was cut entirely.

To polish the specimen, a Tripod Multiprep from Allied High Tech Products, Inc., Rancho Dominguez, CA, USA, was employed. Prior to commencing, the specimen holder had to be polished utilizing a 6 μm abrasive sheet to achieve a flat and smooth surface. Next, the sample was adhered onto the holder with Crystalbond. Furthermore, a section of the specimen holder remained devoid of Crystalbond to enable calibration for measuring the specimen thickness.

To affix the abrasive sheets to the tripod plate, water was used. The adhesive forces caused them to adhere flat. The initial stage commenced with a 15 μm abrasive sheet, followed by 6 μm, 3 μm, 1 μm and 0.5 μm. During each pass, a minimum of three times the grit size of the prior abrasive sheet was removed. Furthermore, as the fineness of the sheet increased, the polishing speed was reduced. Throughout the polishing process, the abrasive sheet remained moistened with water to facilitate cooling and reduce friction, thus refining the polishing result. At 1 μm and 0.5 μm hexylene glycol, a lubricant, was used in lieu of water to further reduce friction. Both sides of the specimen underwent this procedure and, if necessary, the specimen holder was re-polished in-between. Following the last polishing process, the specimen should not surpass a thickness of 30 μm (see Figure 35B)).

In order to glue the grid onto the sample, the specimen support should still be attached to the specimen. An Uhu brand epoxy resin was used as an adhesive, which was a two-component adhesive with a 1:1 ratio that remained malleable for 45 minutes. A thin layer of adhesive was applied to the entire grid, which was placed onto the cleaned surface of the specimen afterwards, lightly pressed down and left to cure overnight. Afterwards, the specimen attached to the grid was separated from the specimen holder using acetone. For this purpose, molybdenum grids were used (100mesh or 75mesh). Some grids were cut in half for use with special TEM holders, such as the tomography holder.

As a last step, the sample was ion-milled. For this, a DuoMill 600 from Gatan was used, which shoots Ar ions at a 15° angle onto the rotating specimen. The sample was placed in a special sample holder with protection. Ion-milling began at a voltage of 4 kV, which was gradually reduced to 3.5 kV as the process continued. The ion beam was maintained between 0.75-1 mA per gun throughout the process. After every 30 min to 1 h, the sample was removed and observed through a polarizing microscope in order to monitor the progress (see Figure 35C)). For this purpose, a Zeiss Axio Lab.A1, Carl Zeiss AG, Oberkochen, Germany, was used. The sample was considered sufficiently thin when small holes appeared in the center of some grids (see Figure 35D)). Finally, the sample was gently ion-milled again at 1 kV for 15-20 min to remove amorphous parts.

To enhance the conductivity of the sample, carbon vapor deposition was carried out. The process involved enclosing the sample in a cylinder and creating a vacuum on the inside. A carbon filament was fixed in the cylinder and a protective flap was placed in front of it to shield the sample. Once the vacuum was created, the carbon filament was pre-annealed at lower temperatures for a short time period to remove any impurities. Then the protective flap was removed and carbon was vaporized onto the sample through two to three shock anneals.

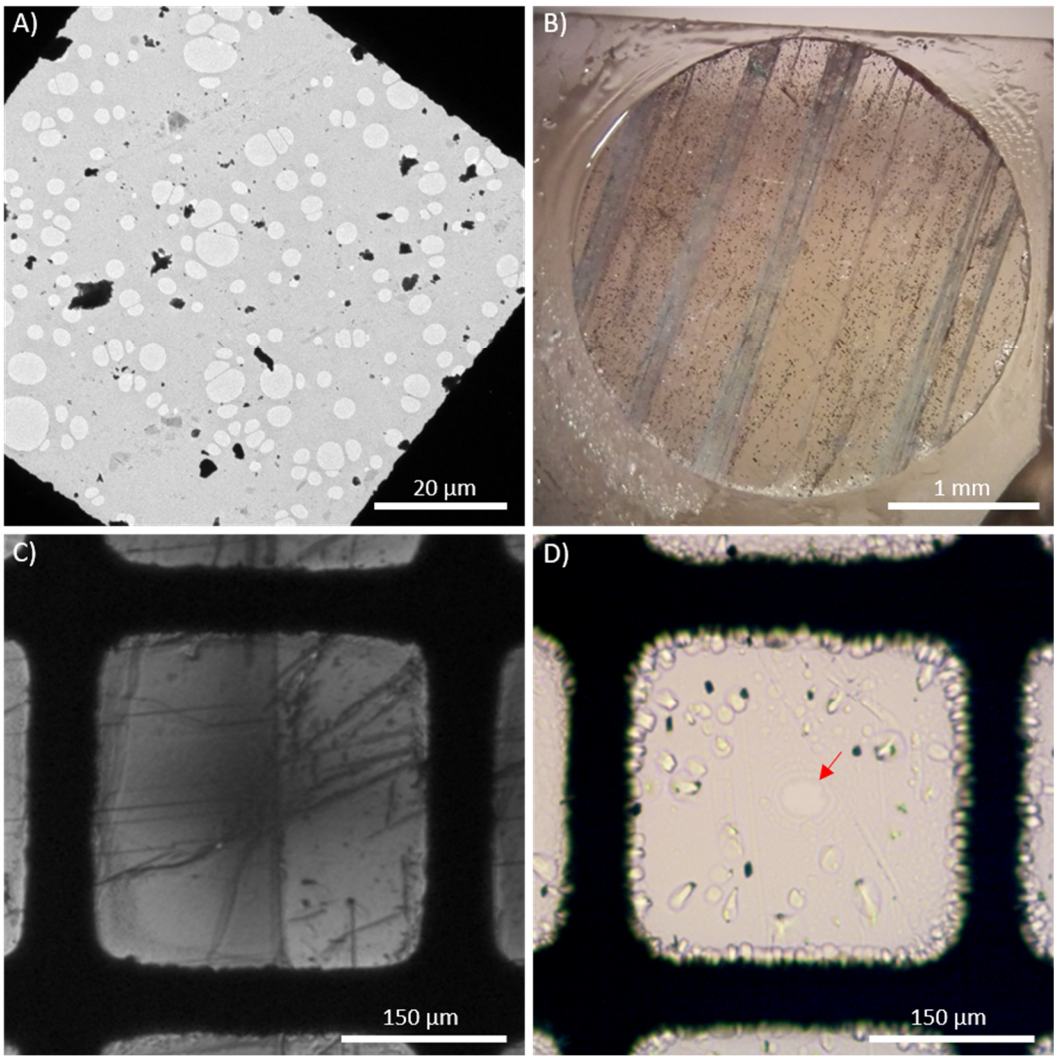

Figure 35: Different sample preparation techniques for TEM investigations. A) A powdered sample of calcium carbonate. The TEM bright-field image shows a single mesh of a Cu grid coated with a holey carbon film and calcium carbonate particles. B)-D) show the process of achieving an ion-milled labradorite sample. B) A selected area was drilled to fit the grid and polished. C) After ion-milling a dark shadow is visible with crossed polarizers in the polarizing light microscope in the area of the mesh where the Ar ions thinned the sample. D) Bright-field light microscope image of a finished sample. A small hole can be seen in the center of the mesh (marked by a red arrow).

4.3. Scanning electron microscopy

For SEM investigations an ESEM Quanta 200 FEG by FEI, Eindhoven, the Netherlands, was used. EDS was measured with an EDAX Genesis System. The ESEM measurements were carried out at 12.5 kV and spot size 4 under high vacuum conditions ($<1.3^{-4}$ mbar).

4.4. Transmission electron microscopy

All TEM investigations were performed with a JEOL 2100F, Tokyo, Japan, (200 kV) or a FEI Tecnai F30 (300 kV). A 2k x 2k CCD camera (Ultrascan100 from Gatan) was used at the JEOL. A tomography attachment for the JEOL single tilt holder was used as a sample holder. When tilting in two directions was required, a JEOL dual tilt beryllium holder was used. EDS was performed using an X-Max80 detector from Oxford Instruments, High Wycombe, UK. For STEM, an ADF detector was used. A 4k x 4k CCD camera (Ultrascan400 from Gatan) and a tomography sample holder from E. A. Fischione Instruments Inc., Export, PA, USA, were used at the FEI instrument. EDS was performed with an EDAX detector (Mahwah, NJ, USA). For STEM, a HAADF detector was used.

The largest aperture and spot size 1 were used for imaging in bright-field mode at the JEOL 2100F. If the sample was electron beam sensitive, the TEM examinations were performed with a medium spot size and the second largest condenser aperture. If radiation damage could still be detected, an even smaller spot size or condenser aperture was selected.

4.5. Automated diffraction tomography

Automated Diffraction Tomography (ADT) was used to record three-dimensional diffraction data of a crystal. For ADT measurements, a Fast-ADT measurement routine was utilized as a plug-in for Digital Micrograph 3, for TEM mode (JEOL) and STEM mode (FEI), which was performed in NBD mode [57].

For data acquisition in TEM mode with the JEOL 2100F microscope, the smallest spot size of 0.5 nm and the smallest condenser aperture of 10 μm was used. The selection of α depended on the desired beam size (see Table 7). For the FEI Tecnai F30 microscope, the procedure was similar except for the imaging being performed in STEM. Here, spot size 6, gun lens 8 and a condenser aperture of 10 μm was used. First, the beam conditions for imaging and diffraction were recorded and the beam shift was calibrated using the X and Y deflections of the beam. To ensure that the crystal does not move off axis during tilting, the eucentric height was mechanically adjusted. Next, a tracking file was recorded in 5° steps, which served as a reference image. In TEM mode, the exposure time of the tracking images usually had to be increased to 1-5 s due to the low diffraction contrast of small crystals. In STEM mode, an exposure time of $<$1 s was sufficient. On the images of the tracking file the ROI was marked. The correct beam size for the measurement was loaded, which ranged from 70 nm to 200 nm. The beam was set to the ROI and changed to diffraction mode. The diffraction image was centered with the deflection coils and the exposure time was adjusted so that the camera was not overexposed. The exposure times mainly ranged from 0.5-1 s, with the exposure times at the JEOL microscope generally being slightly longer than the ones at the FEI microscope. Additionally, the camera length was adjusted to ensure that the diffraction spots were dispersed over the whole area. Finally, the initial parameters were loaded and the Fast-ADT routine was started. If possible, data sets were taken from -60° to +60° in 1° steps. If the ROI overlapped with other crystals, lower angles were chosen to ensure a data set of high quality. In some cases, the step size was decreased to 0.2° or 0.1° to guarantee a higher resolution of the 3D reciprocal space.

Table 7: Preferred α setting for the respective beam sizes of ADT measurements.

α	α1	α2	α3	α4	α5
Beam size	$<$50 nm	~50 nm	60-100 nm	100-200 nm	$>$200 nm

In most cases, a precession angle of 1° was applied via DigiSTAR from NanoMEGAS, Brussels, Belgium. During the alignment, the beam pivot points were first adjusted in imaging mode, followed by the descan in diffraction mode and the image pivot points imaging mode. Iteration was performed until the beam remained unchanged in all modes with precession switched on and off. Finally, fine adjustments were made on the diffraction pattern just before the measurement to prevent splitting of the reflections with slight variations in the height of the sample.

For illite, 31 data sets were recorded, seven of the unaltered sample, five of the sample altered with brine from Bad Nauheim and 19 of illite altered with synthetic Gerolstein brine. The two best data sets of the unaltered sandstone (crystal3 and crystal4) were measured at the JEOL microscope in TEM mode. Each data set contained 116 diffraction images, acquired in a tilt range from -55° to +60° in 1° steps with a precession angle of 1°. The beam had a diameter of 100 nm, the exposure time was 1 s and the camera length 30 cm. For analysis of the disordered data sets of the illite altered with synthetic Gerolstein brine, the tilt steps and exposure time were reduced to 0.2° or 0.1° and 0.2 s or 0.1 s, respectively, and no PED was used.

For labradorite a total of 40 data sets were taken, 29 from all three ion-milled samples and 11 from powdered samples. The best data sets were recorded in STEM mode with a tilt range of -60° to +60° and a beam size of 150 nm, a camera length of 1 m, an exposure time of 1 s and a precession angle of 1°. The satellite reflections were clearly visible.

For eveslogite, 14 data sets were recorded. Additional data sets were recorded by Mariana Klementova in Prague, Czech Republic. At the FEI microscope, the data was recorded in STEM mode on powdered samples and thinfoils. The tilt range was -60° to +60°, the beam size 120 nm, the camera length 1 m and the exposure time 1 s.

The obtained three-dimensional reciprocal space was then analyzed with the programs eADT [145] and PETS2 [55]. The cell had to be multiplied by a factor to calibrate the effective camera length, allowing for the extraction of the intensities from the raw data. The data sets were then used for structure analysis in SIR2019 [173] and Jana2006/Jana2020 [175]. The crystal structures were visualized with VESTA 3 [312]. The recorded data sets including their tilt range, step size, beam size, exposure time, precession angle, tilt axis, cell parameters and included axes can be found in Appendix 5. Structure comparisons were performed with the program COMPSTRU of the Bilbao Crystallographic Server [313]. Complexity measurements for eveslogite were done with the module “information measures” implemented in the software ToposPro [314].

5. Results

5.1. Research questions

For illite, the primary objectives of this research are to investigate the structure using 3D ED, explore the changes in the structure and stacking when exposed to different brines and assess the consequences of illite structure changes on the longevity of geothermal plants. The following questions will be addressed:

- What are the optimal experimental conditions and parameters to obtain accurate and reliable structural information?
- What insights can be gained from the 3D ED analysis of illite regarding its polymorphism, lattice parameters and crystallographic orientation?
- How does the interaction with different brines affect the structure and stacking of illite?
- Are there any identifiable trends in the changes observed in the illite structure?
- What new models can be developed to describe the disorder in illite more effectively in order to complement and enhance XRPD data analysis?

Since labradorite contains complex structures at different scales, part of this thesis is dedicated to analyzing all of these structures on a single labradorite sample. The internal structures of labradorite include twinning, lamellae, domains and the average as well as incommensurately modulated atomic structure. Thus, different to the illite investigation, the aim is to unravel the hierarchical structure of labradorite. This includes:

- What sample preparation techniques have to be applied in order to see all of the internal structures in the TEM?
- How can the different internal structures be described and what is their relation?
- What are the optimal experimental conditions and parameters to obtain accurate and reliable structural information?
- What are the crystallographic orientation and lattice parameters of labradorite for a specific composition?
- What is the incommensurate structure of a single labradorite lamella and how does it compare to the average one?
- Are the results comparable to the structure solved by X-ray diffraction techniques, making 3D ED an adequate tool for solving incommensurate crystal structures?

The last part of this dissertation aims to investigate various aspects of eveslogite, including the determination of its complex structure, comparison with similar minerals and classification of its complexity. The following questions will be addressed:

- What are the challenges in solving the structure of eveslogite using traditional crystallographic methods?
- Can alternative techniques, such as 3D ED and advanced electron microscopy, be employed to overcome the difficulties in structure determination?
- Are the previous assumptions about eveslogite correct?
- What is the crystal structure of eveslogite?
- How can the complexity of eveslogite be characterized and classified based on its structural features and other relevant parameters?
- How does the crystal structure of eveslogite compare with ones found in the same area?

5.2. Illite

Large parts of this chapter are published in Schäffer et al. [308] and Götz et al. [315].

5.2.1. Autoclave experiments with brine

The unaltered Remlingen sandstone showed slightly rounded grains primarily composed of quartz and K-feldspar. The cementation components were identified as quartz, feldspar and fibrous illite, with hematite platelets clustering between some illite fibers. Moreover, the illite fibers extended into the pores of the sandstone, creating a mesh-like structure (see Figure 36A)). Similar findings have been documented in the case of Flechtingen sandstone by Fischer et al. [228] and Jacob et al. [67].

For the altered sandstones, hydrochemical data from the autoclave experiments involving hydrochloric acid, Bad Nauheim and synthetic Gerolstein brine revealed a combination of dissolution and precipitation processes. Among all the samples, feldspar exhibited the most common dissolution occurrences, primarily along the two cleavage planes {001} and {010}. This finding aligns with previous studies conducted by Morrow et al. [316] and Tenthorey et al. [317]. On the other hand, the impact of dissolution on other minerals was comparatively small. Interestingly, this type of dissolution was also present in the unaltered sandstones (see Figure 36B)). Consequently, it was inferred that the fluids only affected the cementation rather than the grains themselves.

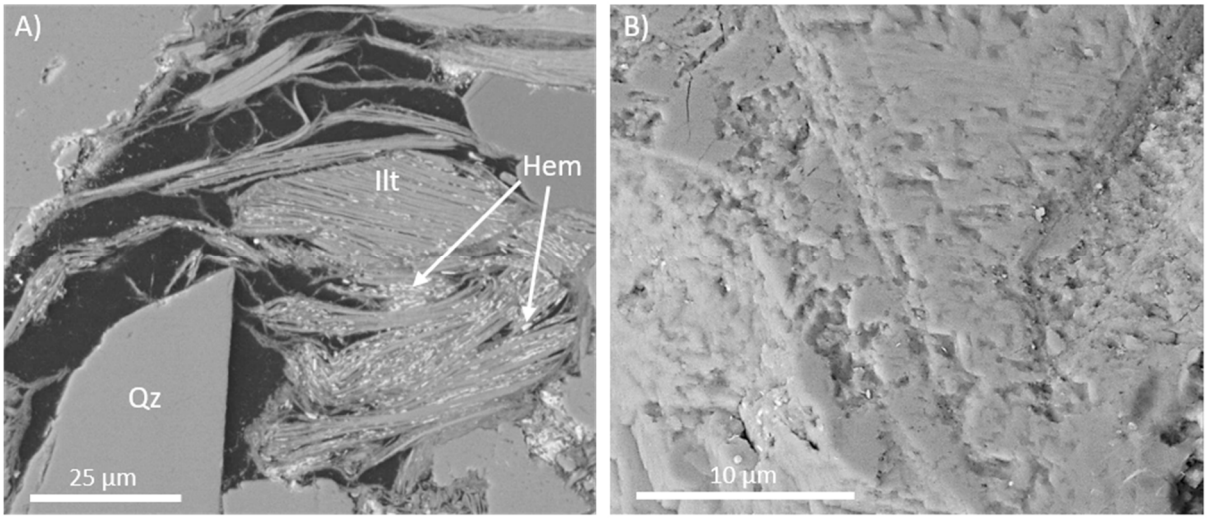

Figure 36: Unaltered Remlingen sandstone. A) SEM-BSE image of a thin section depicting the illitic cementation. It extends into the pores, creating a fibrous meshwork. Hematite platelets are agglomerated between the fibers. B) SEM-BSE image displaying a partially dissolved K-feldspar. The dissolution process primarily occurred along the two cleavage planes {001} and {010}.

During the autoclave experiments using Bad Nauheim and synthetic Gerolstein brine, the formation of various phases was observed, primarily near the edge of the plug, extending approximately 600-700 μm towards the center. Figure 37 illustrates an example of these precipitates in the Remlingen sandstone after alteration at 90°C with Bad Nauheim brine. Among the precipitates, the largest ones were calcium carbonate crystals with acicular and rhombohedral habits, as depicted in Figure 37A) and B). The acicular crystals consisted exclusively of calcium carbonate, while the rhombohedral crystals contained trace amounts of magnesium, up to ~1 at%. The size of the calcium carbonate crystals varied depending on the duration of the experiment, with needle-shaped crystals reaching a maximum size of around

60 μm and rhombohedral crystals reaching a maximum size of approximately 25 μm. Furthermore, deposits of NaCl were observed, forming layers surrounding grains or accumulating within grooves and fractures, as shown in Figure 37C). Additionally, a phase containing iron was detected (see Figure 37D)), appearing as aggregates measuring a few μm, with individual crystals rarely exceeding a size of 200 nm.

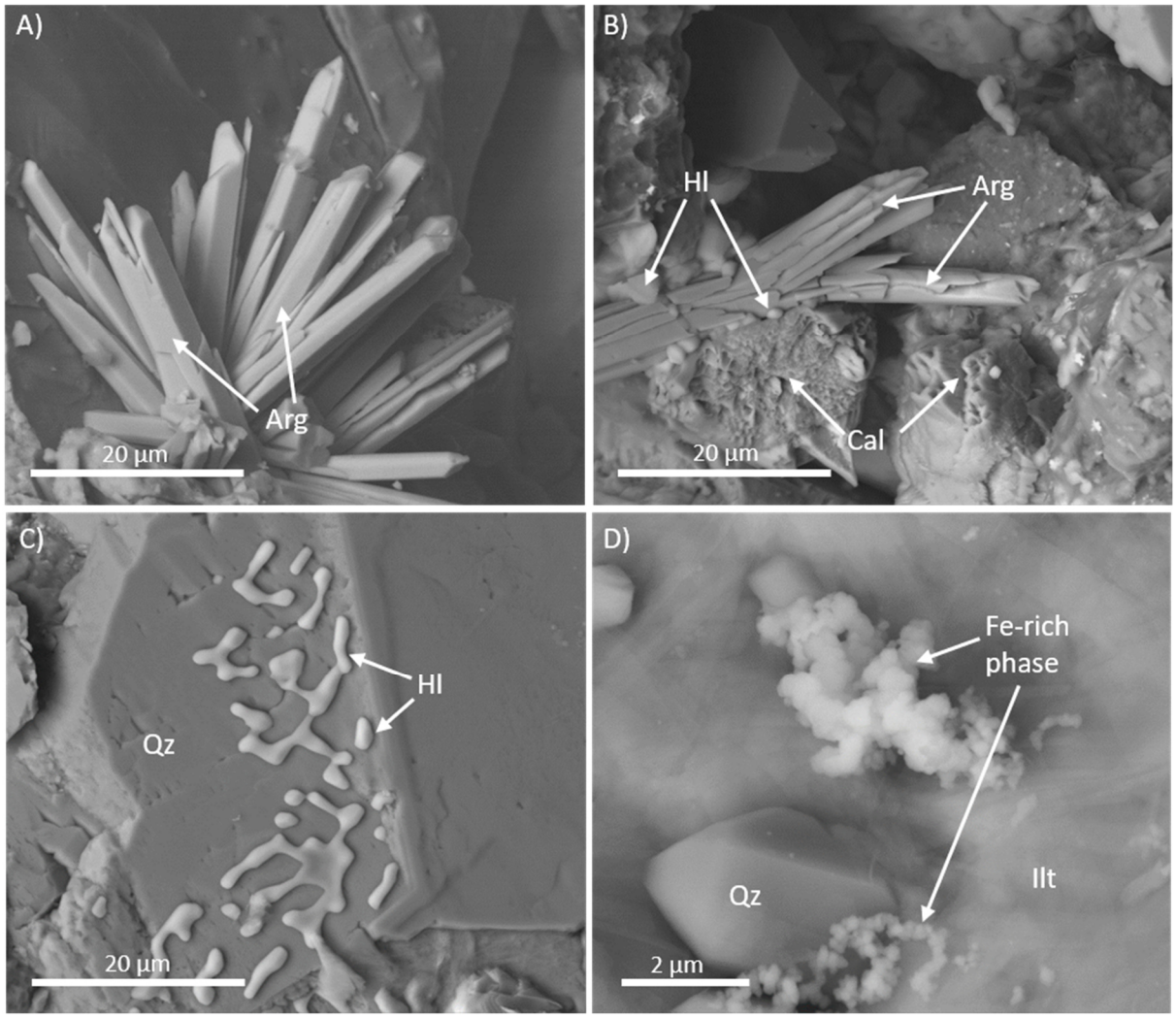

Figure 37: The SEM-BSE images exhibit the precipitates discovered in altered Remlingen sandstone at 90°C. These include acicular calcium carbonate (aragonite; Arg) as shown in A), rhombohedral calcium carbonate (calcite; Cal) as depicted in B), halite (Hl) illustrated in C) and a Fe-rich phase displayed in D). The mineral abbreviations follow the conventions established by Whitney and Evans [318].

TEM measurements were employed to differentiate between calcium carbonate phases with and without Mg. Initially, EDS analysis was utilized to identify the distinct calcium carbonates based on their Mg content. Subsequently, Fast-ADT measurements were conducted. The obtained cell parameters revealed that the pure calcium carbonate phase was aragonite (experimental cell parameters: a = 5.057 Å, b = 8.012 Å, c = 5.540 Å, α = 89.2°, β = 90.4°, γ = 89.4°) and the Mg-containing phase was identified as calcite (experimental cell parameters: a = 5.036 Å, b = 4.953 Å, c = 17.064 Å, α = 90.2°, β = 89.8°, γ = 119.4°). To validate these findings, a structure solution was performed with the hkl data using SIR2019 and the determined structures were consistent with those documented in literature for aragonite [319] and calcite [320]. Regarding the Fe-rich phase, its diffraction patterns appeared amorphous in the TEM studies, making further characterization unfeasible. Grundl and Delwiche [321]

proposed precipitation mechanisms for such poorly crystalline Fe-rich phases: First, small precursor molecules are formed, followed by the growth to colloidal particles and the condensation to a precipitate. The presence of calcite, aragonite and halite was confirmed through XRPD measurements conducted directly on the washed-out and filtered material. The resulting powder diffractogram is depicted in Figure 38A), while Figure 38B) provides an image of the filtered material.

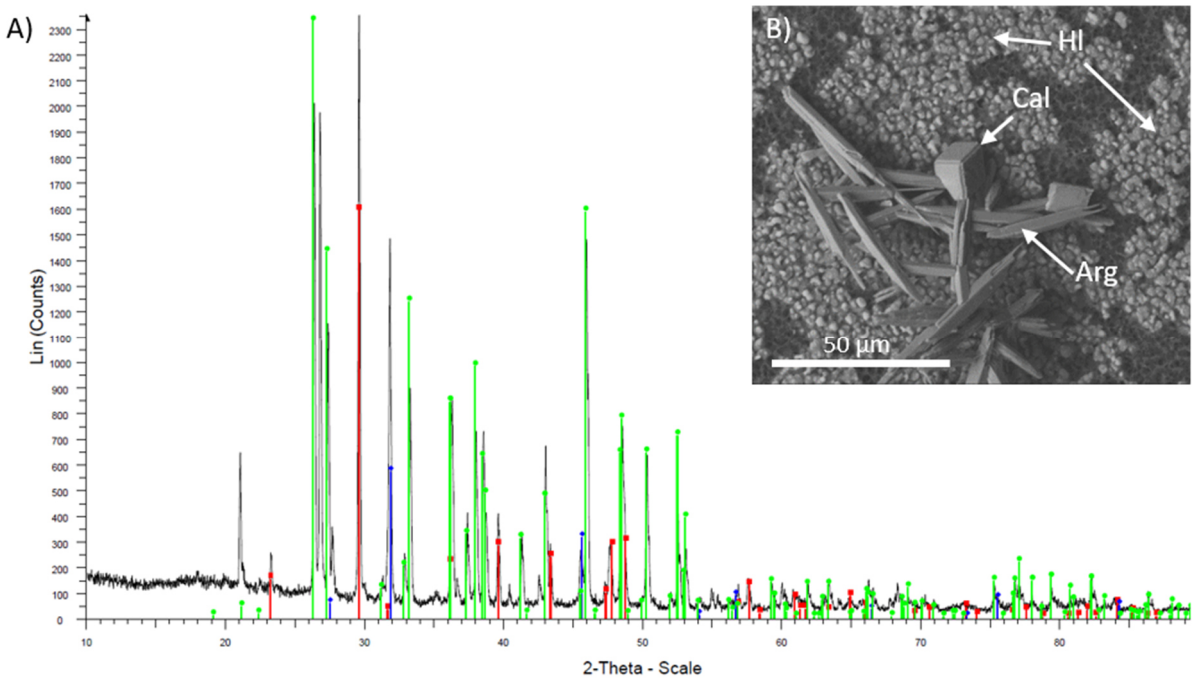

Figure 38: The precipitates collected after subjecting Remlingen sandstone to Bad Nauheim brine at 90°C were analyzed using XRPD. The resulting powder diffractogram in A) displays the distinctive peaks corresponding to calcite (in red), aragonite (in green) and halite (in blue). The peak at around 21 2θ arises from the compound used to secure the filter paper on the sample holder. The filter paper (B) used for the XRPD analysis shows aragonite, calcite and halite as deposited crystals.

Iron oxides were present in both the unaltered and brine-altered sandstones. Among them, hematite was the most prevalent iron oxide, typically forming hexagonal platelets measuring around 1 μm in size. These platelets primarily accumulated within illitic pore fillings (see Figure 39A)). Occasionally, larger hematite crystals were also present, as shown in Figure 39B). However, in autoclave experiments using hydrochloric acid, the hematite platelets were absent in the reaction fringe (see Figure 39C)). This resulted in the bleaching of the reaction fringe, as hematite was responsible for the sandstone's characteristic red color (see Figure 39D)). These observations indicate that during the autoclave experiments, the fluids only penetrated approximately 700 μm into the plug, leaving the rest of the sandstone unaffected.

The fibrous illite present in the cementation was subjected to closer examination via TEM. EDS measurements provided an average composition of the fibrous illite in the unaltered sandstone of $K_{0.72}(Al_{1.54}Fe_{0.09}Mg_{0.41})(Si_{3.57}Al_{0.43})O_{10}(OH)_2$. It should be noted that due to the high beam dose applied during EDS measurements, a certain percentage of potassium was expected to volatilize since the ions are not firmly fixed in the interlayer. Therefore, the potassium content could not be considered definitive. However, as the measurements were conducted using identical settings, they remained comparable to each other. Compositions of different fibers showed significant variations, but in general, the unaltered illite contained slightly more potassium on average compared to the one altered with Gerolstein brine (see Table 8).

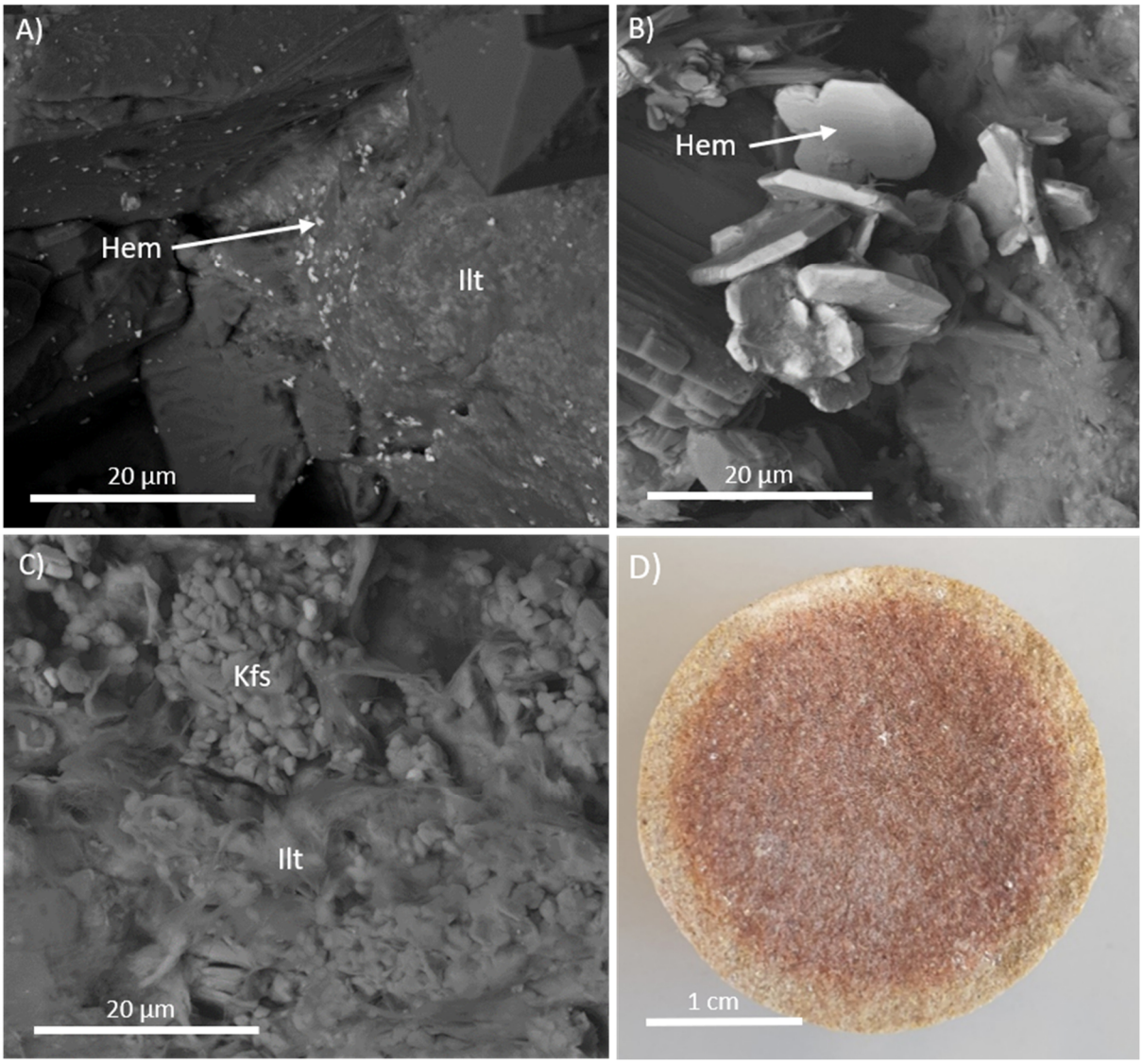

Figure 39: A) In the unaltered Remlingen sandstone, hematite (Hem) was primarily present in the form of small hexagonal platelets embedded within an illite matrix. However, larger hexagonal platelets were occasionally observed, as shown in B). C) After the autoclave experiments with hydrochloric acid, the reaction fringe of the sandstone plug no longer contained hematite within the illitic pore filling. D) Consequently, the absence of hematite crystals resulted in noticeable bleaching. These observations indicate that the fluid used in the experiments was only able to penetrate approximately 700 µm into the surface of the sandstone plug. The mineral abbreviations follow the conventions established by Whitney and Evans [318].

Approximately 10-15 fibers were measured for each sample. In case of the illite altered with brine from Bad Nauheim, precise measurements could not be obtained due to particle agglomeration on its facets. Consequently, the beam either contained the particles or only a very small area of the illite, rendering these results incomparable to the others.

Considering that the structure, including the polytype and chemical composition of illite, is strongly influenced by variations in fluid composition, temperature and fluid-rock interactions [226], further investigations were carried out to determine the structure of illite on individual fibers. Additionally, the impact of brines on the illite structure and its subsequent effects on the sandstone were explored.

Table 8: Average EDS measurements and the resulting illite compositions for the unaltered sandstone and the sandstones altered with Gerolstein brine and Bad Nauheim brine. Illites altered with Gerolstein brine exhibited a slightly lower potassium content compared to the unaltered illites. However, EDS measurements from illite fibers altered with Bad Nauheim brine were not comparable due to the presence of agglomerated particles on the facets of the fibers.

Sandstone	Average EDS measurement [at%]						
	K	Al	Mg	Fe	Si	O	Sum
Unaltered	3.58(33)	9.91(39)	2.05(30)	0.47(9)	17.80(44)	66.18(41)	99.99
Gerolstein	3.30(13)	9.53(21)	1.94(12)	0.36(9)	17.18(27)	67.68(36)	99.99
Bad Nauheim	1.83	5.58	1.53	8.47	12.52	70.07	100.0

Sandstone	Average illite composition								
	Interlayer	Octahedra			Tetrahedra		Anions		Charge
	K	Al	Mg	Fe	Si	Al	O	OH	
Unaltered	0.72(4)	1.54(6)	0.41(4)	0.09(4)	3.57(7)	0.43(6)	10	2	-0.01
Gerolstein	0.69(2)	1.54(5)	0.40(3)	0.07(2)	3.56(6)	0.44(5)	10	2	-0.12

5.2.2. Structure determination with 3D ED

The illite fibers contained in the cementation and the pore networks of the sandstone (see Figure 40A)) were easily distinguishable in the TEM due to their distinctive morphology. Individual illite fibers measuring approximately 50 nm in size were selected for data acquisition using Fast-ADT (see Figure 40B)). Among the collected data sets, crystal3 and crystal4 were deemed the most suitable for further analysis and structure determination.

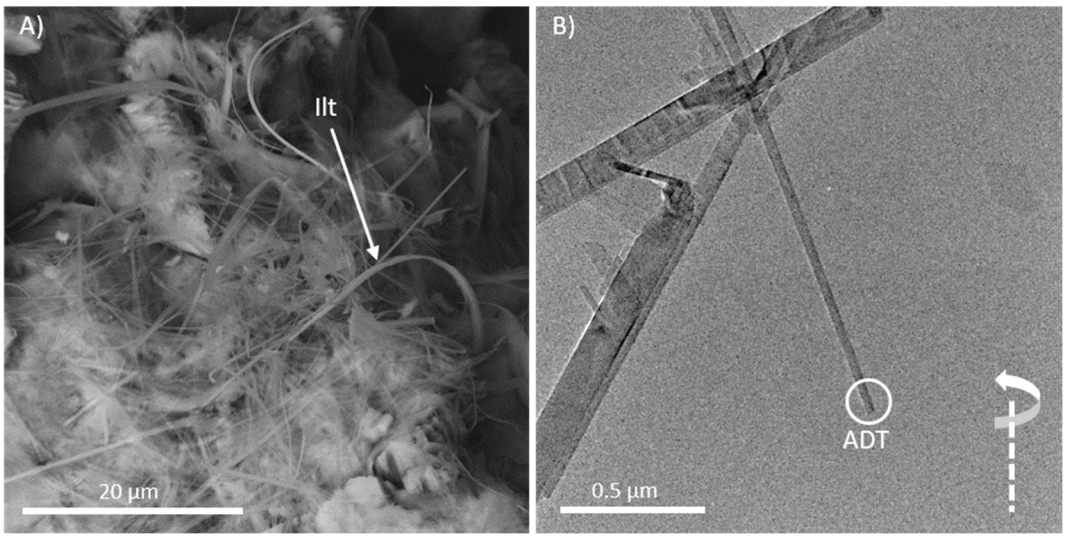

Figure 40: Illite fibers within the Remlingen sandstone. A) SEM-BSE image of illite fibers (Ilt) in a pore of Remlingen sandstone. B) The TEM bright-field image provides a closer view of the illite fibers. One fiber, approximately 50 nm in size, was selected for an ADT data set, indicated by the white circle (crystal3). The tilt axis is displayed in the lower right corner of the figure. Mineral abbreviations follow the conventions established by Whitney and Evans [318].

The analysis of the reconstructed three-dimensional reciprocal space yielded the experimental cell parameters of the illite structure: a = 5.077(3) Å, b = 8.793(5) Å, c = 9.910(5) Å with $\alpha = \gamma = 90°$ and $\beta = 101.5°$. The calculated cell volume was 433.52 $Å^3$. To account for the influence of the effective camera length, a scaling factor of 1.025 was applied. This adjustment

rendered the cell parameters comparable to those reported by Drits et al. [59] for the Silver Hill sample, which were: a = 5.208 Å, b = 9.020 Å, c = 10.166 Å with α = γ = 90° and β = 101.5°.

Figure 41 illustrates the main zones [100], [010] and [001], with the corresponding unit cells marked by black lines. In the [001] zone, only reflections with $h + k = 2n$ were observed, indicating a *C*-centering with the associated general extinctions. Similarly, the main zones [010] (*h0l: h = 2n*) and [100] (*0kl: k = 2n*) displayed these reflection conditions. No additional extinction conditions were identified beyond these observations. Consequently, the possible space groups considered for the illite structure were limited to the monoclinic space groups *C*2, *C*2/*m*, or *C*2/*c*.

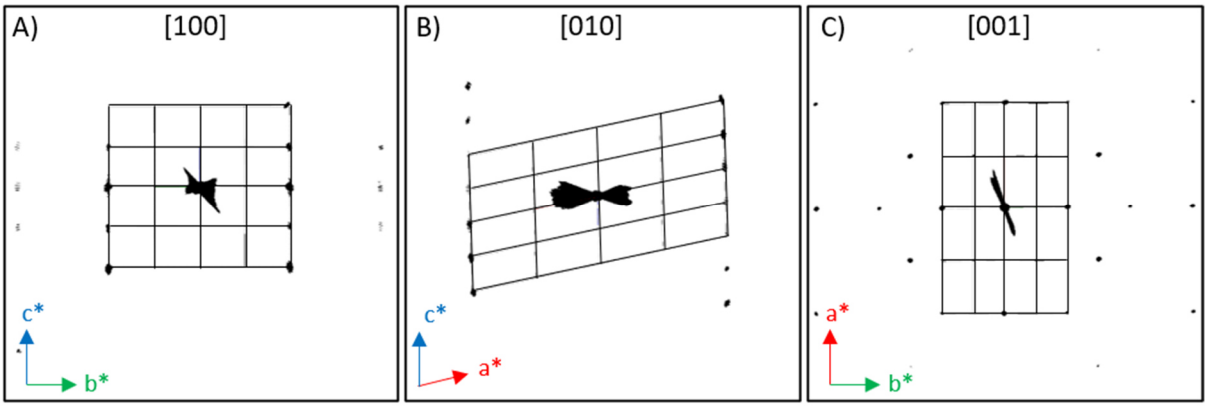

Figure 41: The three main zones of illite A) [100], B) [010] and C) [001]. The unit cell is indicated by black lines, while the red arrows represent the *a**-axis, the green arrows represent the *b**-axis and the blue arrows represent the *c**-axis. The *C*-centering is evident in all three zones, as indicated by the presence of extinct reflections.

Electron diffraction data were extracted from two different fibers (crystal3 and crystal4) of the same sample using the program PETS2 [55]. The obtained data were used for structure solution in the *C*2/*m* space group using in Jana2006 [175]. In the beginning, the chemical composition of the sample was set to $KAl_2Si_4O_{10}(OH)_2$ with a formula unit of Z = 2, resulting in a calculated density of 2.78 g/cm^3. Crystal3 achieved a completeness of 77.27% in reciprocal space, while crystal4 achieved a completeness of 78.31%, which was sufficient for structure determination using a charge-flipping algorithm [322] from Superflip [176]. The structure consists of tetrahedral (T) and octahedral (O) sheets formed by silicate tetrahedra and aluminum octahedra aligned along the *c*-axis. The tetrahedral sites can be partially occupied by Al^{3+} and the octahedral sites by Fe^{3+} or Mg^{2+}. K^+ ions occupy an intermediate layer (I) between the TOT layers. The highest potentials were assigned to K, Al and Si, the lowest potentials to the oxygen atoms. Refinement of the structure, based on kinematical diffraction theory, converged at a weighted R value (wR(all)) of 21.77% and 24.08% for crystal4, respectively. All relevant crystallographic and refinement data are presented in Table 9. The resulting structure was found to be reasonable, with acceptable positive isotropic displacement factors (U(iso)). The hydrogen atoms were not included in the kinematical refinement process. Structure solutions were also attempted with the space groups *C*2 and *C*2/*c*, which were allowed based on the observed extinction conditions. However, when compared with known illite structures of these space groups solved by X-ray diffraction, it was found that the octahedral and tetrahedral layers in the proposed solutions were displaced with respect to each other. In contrast, in the structure solutions performed here, the Si^{4+} and Al^{3+} atoms were aligned in the *c*-direction, which only is the case for *C*2/*m* illites. Therefore, the structures corresponding to the *C*2 and *C*2/*c* space groups were excluded from further consideration.

Table 9: Crystallographic information of illite and refinement information, including the final dynamical refinements of each crystal.

Composition	$K_{0.85}(Al_{1.51}Mg_{0.4}Fe_{0.09})\ (Si_{3.55}Al_{0.45})O_{10}(OH)_2$		
a [Å]	5.208	α = γ	90°
b [Å]	9.020	β	101.5°
c [Å]	10.166	Cell volume [Å³]	477.56
Space group	*C*2/*m*	Z	2
Structure solution	Charge flipping	Max. diffraction vector g(max)	1.6
Superflip repeats	10	Max. excitation error (matrix)	0.01
Max. cycles	2000	Max. excitation error (refinement)	0.1
Delta value	0.9	RSg(max)	0.4
Starting model	Random phases	DSg(min)	0
Peak search	Peaks from Jana	Number of integration steps	128
Crystal	Crystal3	Crystal4	Crystal3-4
Refinement	Dynamical	Dynamical	Dynamical
Completeness [%]	77.27	78.31	78.44
Reflections	1125 = 751 + 374 / 158	1081 = 653 + 423 / 151	2208 = 1404 + 804 / 261
Reflections/parameter ratio	7.12	7.16	8.46
GOF(obs) [%]	5.17	6.18	6.65
GOF(all) [%]	4.26	4.83	5.18
R(obs) [%]	8.10	10.09	9.66
R(all) [%]	13.40	17.99	15.99
wR(obs) [%]	9.38	11.27	11.29
wR(all) [%]	9.57	11.50	11.49

Applying dynamical refinement based on the kinematical structure model, the sample thickness was determined to be 47 nm for crystal3 and 65 nm for crystal4, with corresponding wR(all) values of 9.48% and 11.50%, respectively. Refinement of the K site occupancy led to a potassium content of 0.85 for crystal3 and 0.88 for crystal4. Considering the geometry of the octahedral and tetrahedral layers with respect to each other, the H atom must bond to O4, indicating that the structure of the illite fibers corresponds to a $1M_{tv}$ polymorph [210]. The displacement factors were refined anisotropically and generally exhibited acceptable positive values. However, negative values were observed for K1 and the oxygen atoms. Additionally, a smearing effect along the *c*-axis was present for all atoms due to the limited data available in this direction, as the crystals had a preferred direction and could not be measured in a full 180° range due to microscope constraints.

By merging the data sets of crystal3 and crystal 4 (designated as crystal3-4), only a slight improvement in completeness of the reciprocal space was achieved, reaching 78.44%. Dynamical refinement was performed on both data sets, resulting in a converged wR(all) value

of 11.49%. The occupancy of the K site was refined to 0.86. The anisotropic temperature factors mostly fell within a realistic positive range. However, the smearing effect along the *c*-axis that was observed initially persisted.

The structure solutions obtained for crystal3, crystal4 and crystal3-4 yielded highly comparable structures with only minor differences. The smallest deviation was observed for Si1, with a variation of 0.0014 Å between crystal3 and crystal4. Furthermore, the K site remained identical in all structures as it occupies a special position. The largest deviation was found for O4, with a difference of 0.1276 Å between crystal3 and crystal4. The average deviations were 0.0447 Å between crystal3 and crystal4, 0.015 Å between crystal3 and crystal3-4 and 0.0299 Å between crystal4 and crsytal3-4, respectively. Moreover, the occupancy of the K position exhibited a maximum variation of only 3% across the different structure solutions and the atomic distances displayed a very small range of variability (see Table 10). These small differences validate the accuracy of the obtained results. Since merging the data sets did not lead to any improvement, further structure analysis was continued solely using data from crystal3.

Table 10: Atom distances of the illite structures of crystal3, crystal4 and crystal3-4.

Atom 1	Atom 2	Crystal3 [Å]	Crystal4 [Å]	Crystal3-4 [Å]
K1	O2#t-1,0,0	3,030(7)	2,978(11)	3,020(7)
	O2#s2t2,0,1	3,030(7)	2,978(11)	3,020(7)
	O3	2,970(6)	2,992(8)	2,975(5)
	O3#s2t1,0,1	2,970(6)	2,992(8)	2,975(5)
	O3#s3t1,0,1	2,970(6)	2,992(8)	2,975(5)
	O3#s4	2,970(6)	2,992(8)	2,975(5)
Si1	O1	1,627(10)	1,615(14)	1,622(9)
	O2	1,593(4)	1,604(6)	1,591(3)
	O3	1,620(7)	1,613(9)	1,622(6)
	O3#s4c2	1,623(5)	1,617(6)	1,622(4)
Al1	O1	1,968(5)	1,999(8)	1,980(5)
	O1#s2t1,0,0	1,968(5)	1,999(8)	1,980(5)
	O1#s3c2t1,0,0	1,953(7)	1,981(11)	1,966(7)
	O1#s4c2t-1,0,0	1,953(7)	1,981(11)	1,966(7)
	O4	1,917(11)	1,901(16)	1,905(10)
	O4#s2t1,0,0	1,917(11)	1,901(16)	1,905(10)

Since the EDS measurements showed small amounts of Fe and Mg in addition to K, Al, Si and O, these were included in the structure solution in the next step by partial occupation based on the average EDS measurements. According to Geatches and Wilcox [323], illites that have Fe^{3+} and Mg^{2+} on the octahedral position always crystallize as a $1M_{tv}$. Dynamical refinement with a fixed occupation of 0.3775 Al, 0.0225 Fe, and 0.1 Mg on the octahedral position resulted in a wR(all) value of 9.57%. The atom positions are summarized in Table 11 and the resulting illite structure is depicted in Figure 42. It was observed that the occupancy of the K1 position was 14% higher compared to the average EDS measurements for the unaltered illite. Consequently, the composition of illite in the unaltered sandstone was determined to be $K_{0.85}(Al_{1.51}Mg_{0.4}Fe_{0.09})(Si_{3.55}Al_{0.45})O_{10}(OH)_2$.

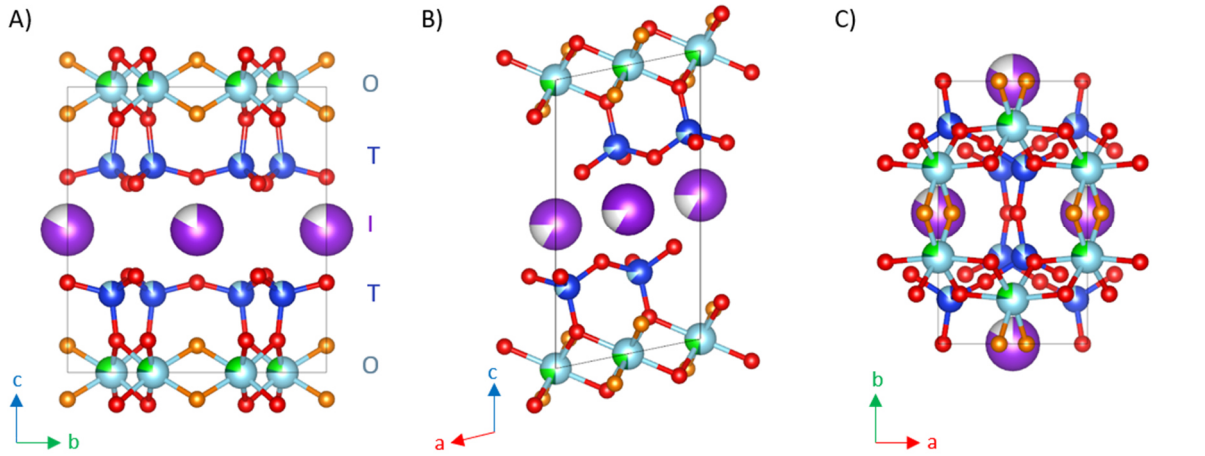

Figure 42: The illite structure as a $1M_{tv}$ polytype is depicted along the main directions A) [100], B) [010] and C) [001]. The structure comprises of sheets of Si tetrahedra (T) and Al octahedra (O) oriented along the *c*-axis, with an intermediate layer (I) containing K^+ ions. Within the octahedral sheet, an OH group is present (depicted in orange). Light blue represents Al, dark blue represents Si, dark green represents Fe, light green represents Mg, purple represents K and red represents O.

Table 11: Atom positions (x, y, z), occupancy (occ) and anisotropic displacement factors (U(aniso)) of the $1M_{tv}$ illite structure of crystal3.

Atom	x	y	z	Occ	U(aniso)
K1	0.5	0	0.5	0.85	0.28(3) 0.036(3) -0.005(8) 0 -0.013(4) 0
Si1	0.9206(5)	0.1700(3)	0.2741(5)	0.89	0.0050(16) 0.0121(16) 0.008(4) 0.0012(11) -0.001(2) 0.0041(17)
Al1’				0.11	
Al1	0.5	0.1701(4)	0	0.76	0.009(2) 0.026(2) 0.028(7) 0 0.005(3) 0
Fe1’				0.05	
Mg1’				0.2	
O1	0.8537(9)	0.1894(4)	0.1119(9)	1	0.009(2) 0.020(3) 0.081(9) -0.0055(17) 0.010(4) 0.005(3)
O2	0.9673(12)	0	0.3142(11)	1	0.038(4) 0.008(3) 0.049(11) 0 -0.002(5) 0
O3	0.6822(8)	0.2363(5)	0.3369(8)	1	0.014(2) 0.034(3) 0.019(7) 0.0085(18) -0.006(3) -0.002(3)
O4	0.4087(17)	0	0.0937(19)	1	0.081(6) 0.030(4) 0.113(18) 0 -0.013(8) 0

In a next step, the obtained illite structure was compared to a similar $1M_{tv}$ illite structure reported by Drits et al. [59] (Sample Silver Hill). However, in their study, they did not refine the partial occupancies of the interlayer, tetrahedral and octahedral cation positions. The octahedral cation position showed the smallest deviation, with a difference of 0.0307 Å. Furthermore, the K site was identical in both structures because it is located on a special position. The largest deviation was observed for O2, with a difference of 0.1079 Å. On average, the deviation between the two structures was 0.055 Å, indicating good agreement between the atom positions in this study and the literature structure.

5.2.3. Morphology

Typically, the morphology of illite crystals is primarily influenced by the [100], [1$\bar{1}$0] and [$\bar{1}\bar{1}$0] growth directions, resulting in the formation of pseudo-hexagonal platelets. However, in the $1M_{tv}$ structure, the (110) and (1$\bar{1}$0) facets exhibit kinks and exposed octahedral cis-sites with broken bonds, which can promote faster growth. This leads to a fibrous or lath-like habit, where the (010) plane assumes significantly larger dimensions compared to the platelet morphology, as discussed in chapter 3.1.3 (compare with Figure 26) [204]. Additionally, the (010) plane of the $1M_{tv}$ structure contains reactive OH groups (see also Figure 42A)), which have the capability to adsorb inorganic or organic complexes, thereby inhibiting growth in this direction. Such complexes have formed, for example, in the presence of Bad Nauheim brine. In the experiments, it was observed that the OH groups of the illite facilitated the attachment of FeO_xH_x aggregates on the (010) facet, with iron originating from the brine, as shown in Figure 43. This subsequently led to a secondary broadening of the fibers.

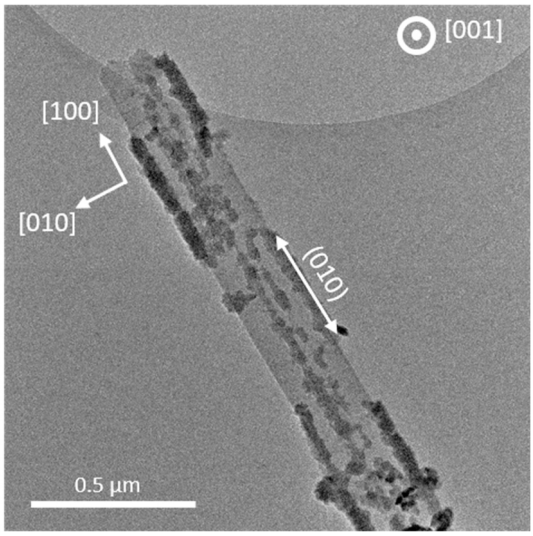

Figure 43: In the TEM bright-field image, secondary agglomerations of FeO_xH_x can be observed on the (010) planes of the illite fiber, which has undergone alteration with Bad Nauheim bine.

5.2.4. Influence of different brines

To investigate the influence of the fluids on illite, TEM and ADT analysis were conducted on illite fibers from the unaltered sandstone and sandstones subjected to autoclave experiments using brine from Bad Nauheim and synthetic Gerolstein brine (altered for 3 days at 90°C). A comparison was made among these samples (see Figure 44A)-C)).

In the diffraction patterns, the unaltered sandstone exhibited well-defined diffraction spots, even for large and thick illite fibers, indicating an intact crystal structure (see Figure 44D)). In the samples altered with brine from Bad Nauheim, the diffraction spots appeared slightly elongated along the c^*-axis, which corresponds to the stacking direction of the TOT layers (see Figure 44E)). Conversely, the samples altered with synthetic Gerolstein brine displayed a distinct smearing of the diffraction spots in the c^*-direction. In the projection along the a^*-axis, there was a high regularity along the b^*-axis, where the reflections of every third row were discrete while the rows in between exhibited varying degrees of diffusion (see Figure 44F)).

To further investigate the interaction of the illite fibers during alteration, XRPD measurements were conducted on the sandstone altered with Gerolstein brine. Two measurements were taken:

one from the altered rim and another from the unaltered middle of the plug. The middle section showed a higher illite content of 20%, whereas the rim had a slightly lower illite content of 15%. However, due to the presence of numerous other minerals with partially overlapping peaks and the relatively low illite content, it was not possible to determine any potential structural changes with this method.

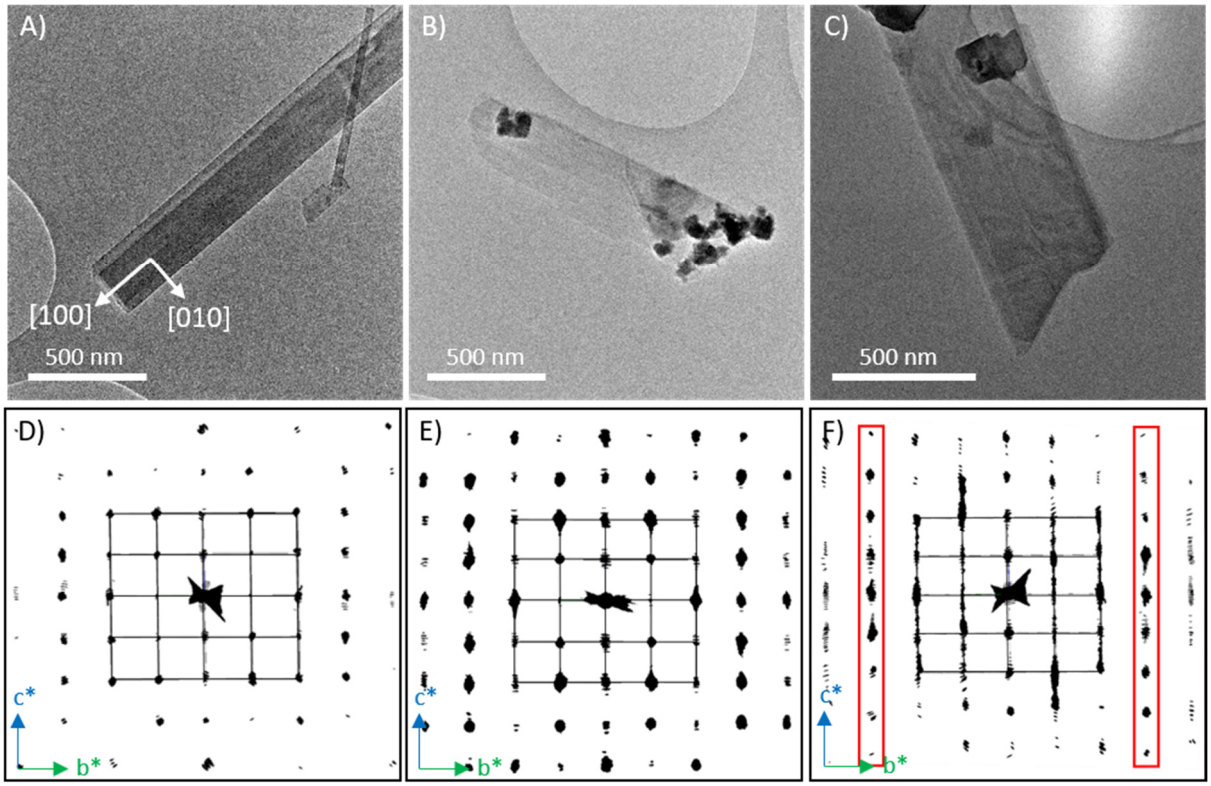

Figure 44: A)-C) The illite fibers are shown in TEM bright-field images representing A) the unaltered sandstone, B) the autoclave experiments with brine from Bad Nauheim and C) the autoclave experiments with synthetic Gerolstein brine. The orientation of the fibers is exemplified in A). D)-F) Projections of the three-dimensional reciprocal space along the *a**-direction. In D), the unaltered illite exhibits clearly defined diffraction spots. The smearing of reflections in the *c**-direction becomes more pronounced in E) for the experiments with Bad Nauheim brine and further increases in F) for the experiments with synthetic Gerolstein brine. In F), it can be observed that every third row along *b** shows reduced smearing, indicated by the red markings.

5.2.5. Disorder

In order to explore the streaking phenomenon in more detail, the entire 3D reciprocal space was divided into three categories based on the degree of disorder along the *c**-axis: discrete, semi-diffuse and diffuse reflections. Using this categorization, the conditions required for discrete reflections were calculated. For a structure containing stacking faults of *a*-*b* planes, the structure factor along a rod can be expressed as:

$$F(hkl) = \sum_{j=1}^{N} f_j \exp\left(2\pi i\big(h(x+\Delta x) + k(y+\Delta y) + l(z)\big)\right) \tag{65}$$

By separating the terms in the exponent, the following equation is obtained:

$$F(hkl) = \sum_{j=1}^{N} f_j \exp\big(2\pi i(hx+ky+lz)\big) \exp\left(2\pi i\big(h(\Delta x) + k(\Delta y)\big)\right) \tag{66}$$

Diffuse scattering occurs if the second exponent deviates from the complex number (1.0, 0.0). Therefore, if no diffuse scattering is observed, the condition

$$\big(h(\Delta x) + k(\Delta y)\big) = integer = 0 mod(1) \tag{67}$$

must be satisfied. As the extinction rules in the diffraction pattern follow a (pseudo-)hexagonal symmetry, the pattern was re-indexed to a hexagonal unit cell. As an example, this transformation converted the slightly diffuse reflection 130_{mcl} into 110_{hex} and the discrete reflection 330_{mcl} into 300_{hex}. Within the hexagonal setting, this resulted in simplified extinction rules for no diffuse scattering:

$$\big(1(\Delta x) + 1(\Delta y)\big)_{hex} = integer \tag{68}$$

$$(3(\Delta x) + 0(\Delta y))_{hex} = integer \tag{69}$$

which can be interpreted as the classical rule $\Delta x_{hex} = \frac{1}{3}$ and $\Delta x_{hex} = -\Delta y_{hex}$. Transforming the vector $[\frac{1}{3},-\frac{1}{3},0]_{hex}$ back into monoclinic space using the equations:

$$a_{hex} = a_{mcl} + 0 + 0 \tag{70}$$

$$b_{hex} = -\frac{1}{2}a_{mcl} + \frac{1}{2}b_{mcl} + 0 \tag{71}$$

leads to a monoclinic vector of $[\frac{1}{2},-\frac{1}{6},0]_{mcl}$. A schematic drawing of the *C*-centered monoclinic cell and the primitive hexagonal cell including the shift vector is displayed in Figure 45.

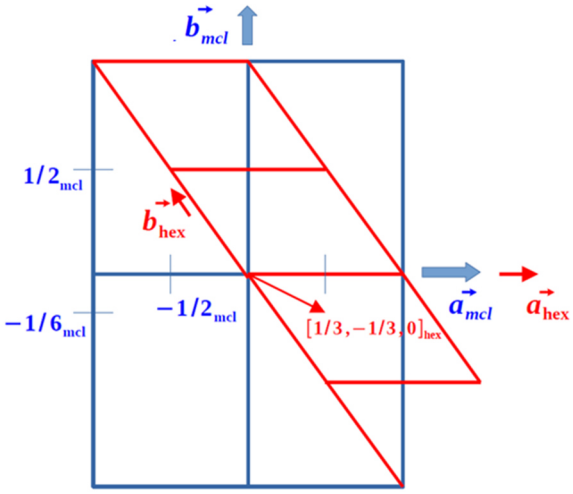

Figure 45: Schematic drawing of the unit cell of illite along the *c*-axis. The *C*-centered monoclinic cell is shown in blue and the primitive (pseudo-)hexagonal cell in red. The shift vector of $[\frac{1}{3},-\frac{1}{3},0]$ in the hexagonal system can be expressed as $[\frac{1}{2},-\frac{1}{6},0]$ in the monoclinic system.

The same procedure can be applied in monoclinic space, but three reflections are required:

$$(2(\Delta x) + 0(\Delta y))_{mcl} = integer \tag{72}$$

$$(1(\Delta x) + 3(\Delta y))_{mcl} = integer \tag{73}$$

$$(0(\Delta x) + 6(\Delta y))_{mcl} = integer \tag{74}$$

This also yielded $\Delta x_{mcl} = \frac{1}{2}$ and $\Delta y_{hex} = \frac{1}{6}$ and in combination, $\Delta x_{mcl} = -3y_{hex}$, resulting in the same translation vector. This rule describes the shift of a TOT layer required to generate the pattern of diffuse reflections observed in Figure 46A). Based on the determined illite structure, a new model for the disordered illite with varying amounts of stacking faults was simulated using DISCUS. In this model, each TOT layer and the intermediate layer were assumed to consist of one layer and the possible shifts were applied to the subsequent TOT layer. The simulation results for a probability of 0.7, where 1.0 represents a perfect crystal, are shown as black dashed lines in the graphs of Figure 46B)-D).

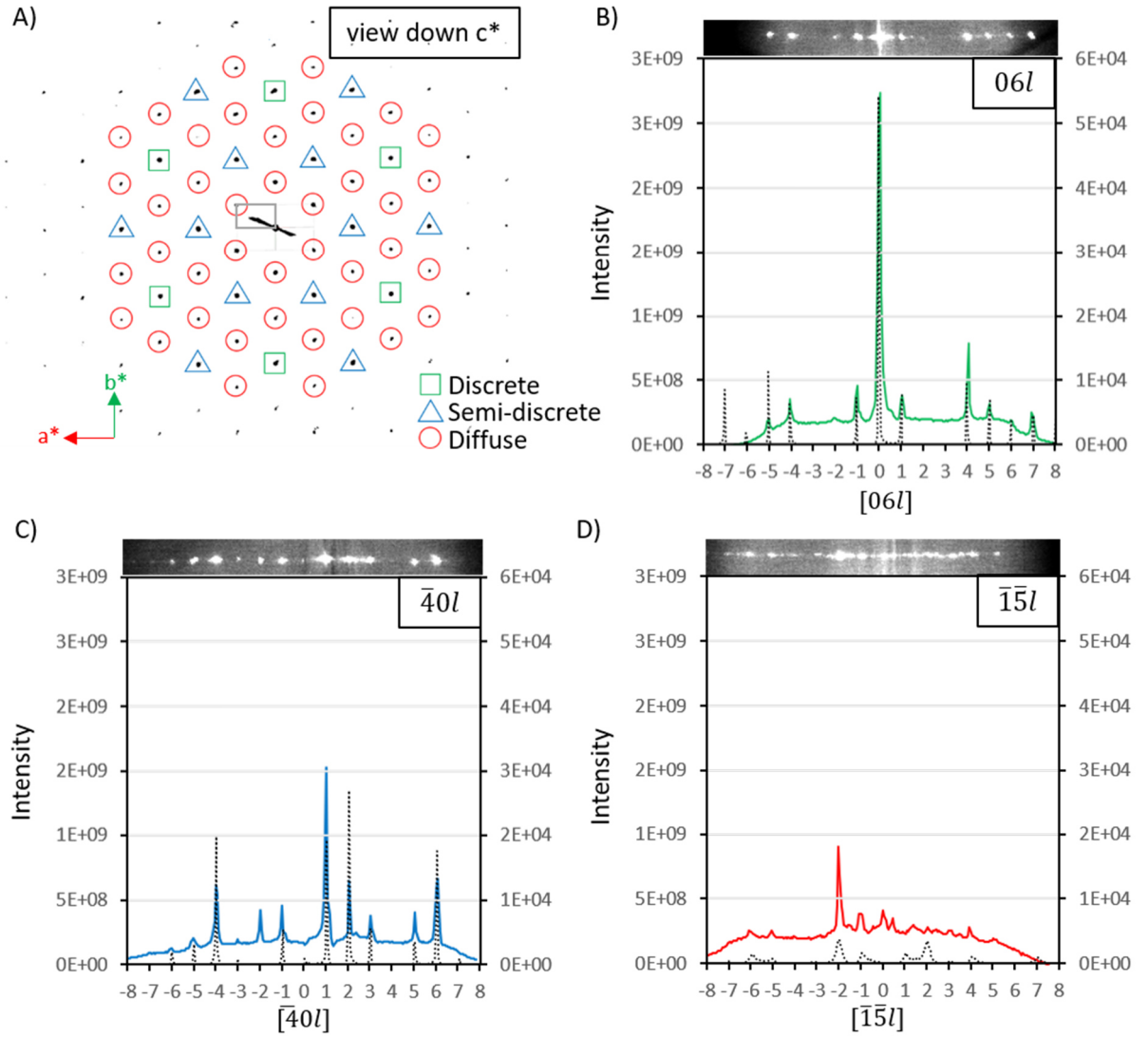

Figure 46: Analysis of the 3D reciprocal space of an illite fiber altered with synthetic Gerolstein brine exhibiting diffuse scattering. A) Projection of the 3D reciprocal space along the (001) direction, with the grey marking indicating the unit cell. Red circles represent hkl indices exhibiting diffuse scattering, blue triangles represent semi-discrete reflections and green squares represent discrete reflections. B)-D) show selected rods for each category. The simulated diffraction pattern, with a stacking fault probability of 30%, is depicted as a black dashed line (intensity displayed on the right y-axis), while the experimental data is shown in color (intensity displayed on the left y-axis). In B), the discrete reflections of 06l are illustrated. Their intensity is split into thin, non-broadened peaks. C) presents the semi-discrete reflections of $\bar{4}$0l, displaying peak broadening in the intensity distribution. An additional reflection at $\bar{4}\bar{2}$l can be observed in the experimental data, which is absent in the simulated data. D) exhibits the diffuse streaks of $\bar{1}\bar{5}$l, where peak intensities are reduced and widely dispersed along the (001) direction.

Next, the experimental data was extracted from the eADT cut volume module and compared with the simulations. For the discrete reflections, the intensity relations of the Bragg reflections matched well (see Figure 46B)). However, for some rods, the semi-discrete reflections exhibited additional reflections in the experimental data that should have been extinct (see Figure 46C)). The diffuse rods showed similarities to the simulation but had some outliers in intensity (see Figure 46D)).

5.3. Labradorite

Some structures of labradorite can be visible to the naked eye or under an optical microscope with low magnification. Nonetheless, the primary method employed in this study was electron microscopy, which enabled the examination of the arrangement of the hierarchical internal structure of labradorite.

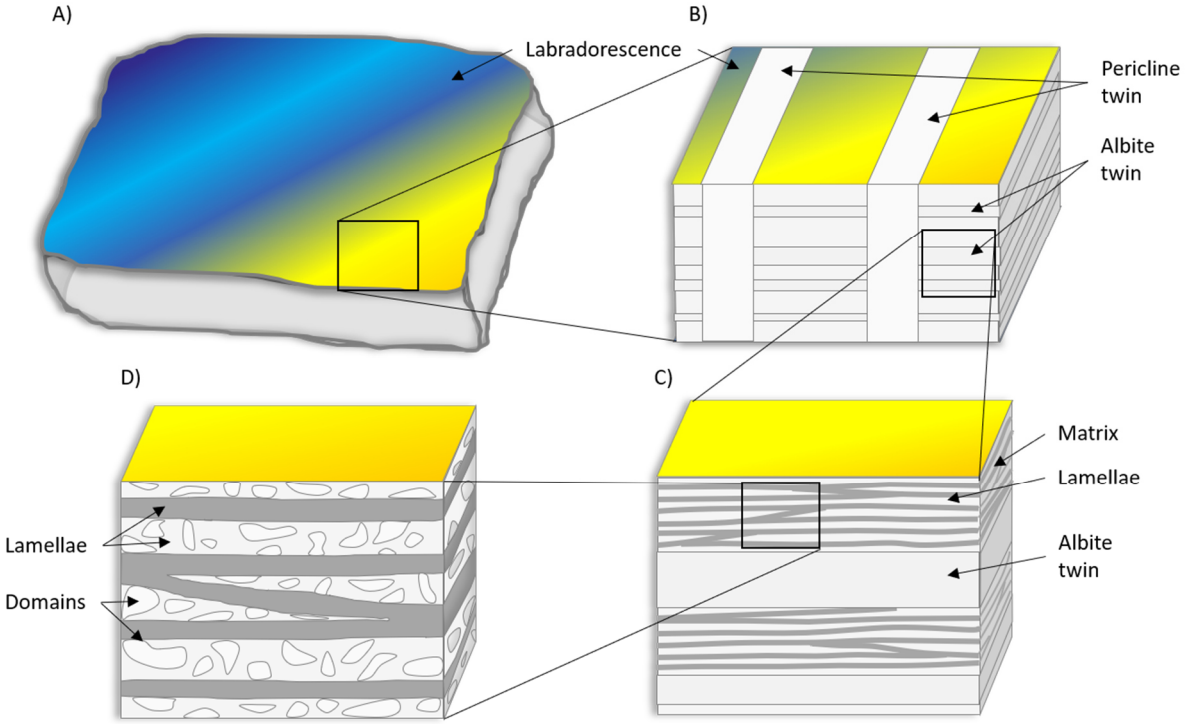

Figure 47: This schematic illustration depicts the different structures observed in labradorite, while not being drawn to scale. A) The labradorescence, visible in dark blue to yellow, can be seen macroscopically. B) provides a magnified depiction of A) displaying albite (0.2–1 µm) and pericline twins (~ 200 µm). C) An even more magnified view of the albite twins, indicating the presence of alternating thicker and thinner lamellae (~ 100 nm) that lie approximately parallel to each other and within the plane of labradorescence. D) At an even higher magnification of the larger lamellae, small domains (20–50 nm) can be observed, which are exclusively contained within them.

Subsequently, various structural features illustrated in Figure 47, beginning with albite and pericline twins, will be presented and analyzed individually. Large parts of this chapter are published in Götz et al. [324].

5.3.1. Twins

Within this particular labradorite specimen, two distinct types of polysynthetic twins were observed and identified: albite and pericline twins (see Figure 48A)). While pericline twinning can already be seen with the naked eye (see Figure 33A) in chapter 4.1), albite twinning becomes visible only under crossed nicols when viewed through a polarizing microscope (see Figure 48B)). Both types of twins can be observed within a single cut when viewed

approximately along the *a*-axis. Albite twins typically have a width ranging from 0.2 to 1 μm and intersect with significantly larger pericline twins, approximately 200 μm in size, at an angle of around 90°. It is important to note that albite twins are absent in the pericline twins.

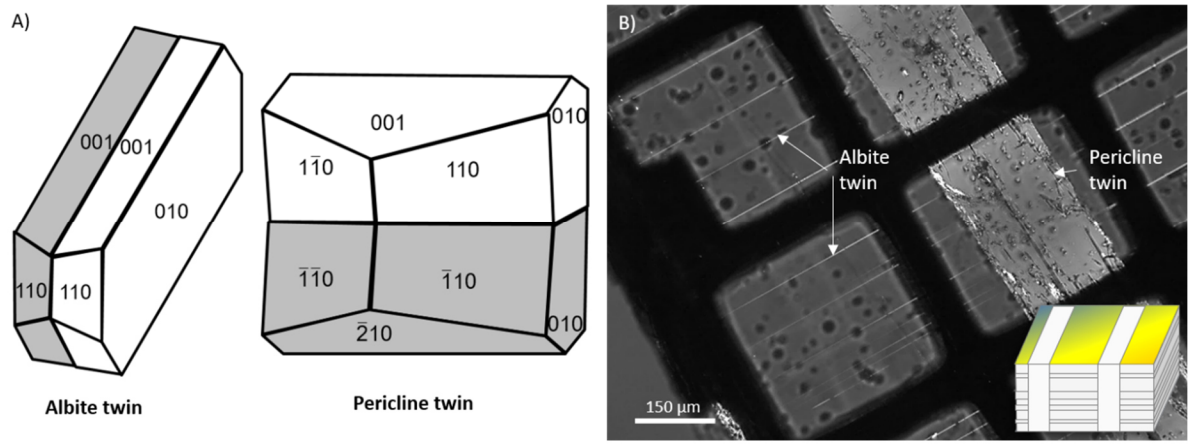

Figure 48: A) A schematic drawing depicting an albite and a pericline twin. B) Labradorite that was cut perpendicular to the twinning plane and the labradorescence under crossed nicols in a polarizing microscope. The image reveals the presence of polysynthetic albite twins, intersected by pericline twins at approximately 90°. No albite twins were observed within the pericline twin. The insert in the bottom right corner of B) was extracted from Figure 47.

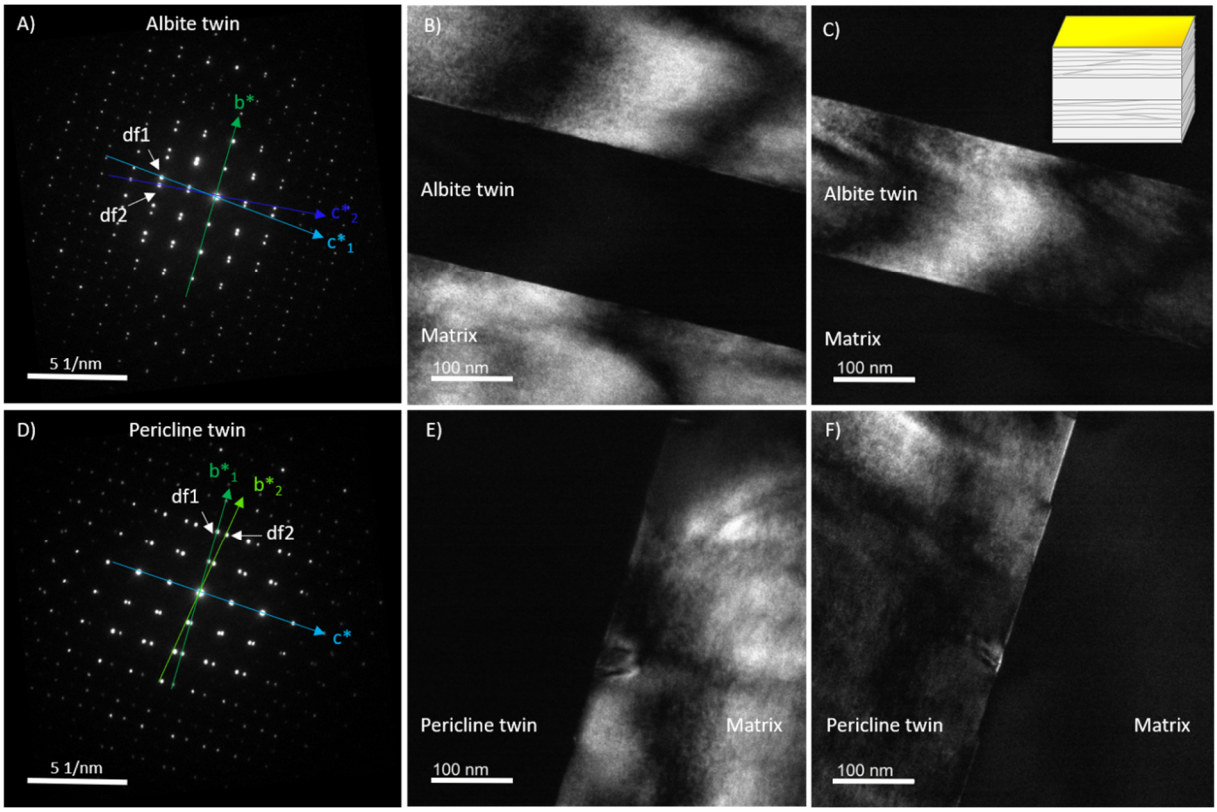

Figure 49: TEM images showcasing twinning in labradorite. Images A)–C) exhibit the twin boundary of an albite twin, while images D)–F) present the twin boundary of a pericline twin. A) displays a diffraction pattern along the zone axis [100], revealing the splitting of diffraction spots along c^*, resulting in c^*_1 and c^*_2. B) represents a dark-field image of df1, which corresponds to the c^*_1-axis and only illuminates the matrix. In contrast, C) shows the dark-field image of df2 (part of the c^*_2-axis), where only the albite twin is illuminated. D) shows a diffraction pattern along the zone axis [100] exhibiting split diffraction spots along the b^*-axis, generating b^*_1 and b^*_2. E) represents a dark-field image of df1, which lies on the b^*_1–axis and exclusively displays diffraction information from the matrix. F) is the dark-field image of df2, aligned with b^*_2, solely revealing diffraction information from the pericline twin. The insert in the top right corner of C) was extracted from Figure 47.

In the TEM, diffraction patterns of the [100] zone obtained at the twin boundary of an albite twin reveal split diffraction spots along the c^*-axis, resulting in c^*_1 and c^*_2 (see Figure 49A)). When a dark-field image is produced from a diffraction spot along the c^*_1- or c^*_2-axis, the diffraction contrast originates solely from either the matrix or the twin, respectively (see Figure 49B) and C)). Similarly, the diffraction pattern of a pericline twin boundary exhibits a split b^*-axis, resulting in b^*_1 and b^*_2 (see Figure 49D)). As with albite twinning, the dark-field images of diffraction spots along the b^*_1- or b^*_2-axis only show the matrix or the twin illuminated (see Figure 49E) and F)). Thus, the diffraction pattern containing the b^*_1- or c^*_1-axis is generated by the matrix, while the pattern containing b^*_2- or c^*_2-axis is created by the respective twins.

5.3.2. Lamellae and local domains

When the samples were cut perpendicular to the labradorescence plane, bright-field imaging revealed the presence of alternating thick and thin lamellae. These lamellae generally run parallel to each other, with only a few instances of intersection. However, in the case of pericline twins, the lamellae exhibit a different orientation and intersect the matrix lamellae at an acute angle.

To obtain a better visualization of the lamellae, dark-field imaging was employed in the TEM. Depending on the choice of diffraction spots used for dark-field imaging (see Figure 50A)), different features of the labradorite became visible. By selecting the 020 reflection for dark-field imaging, a distinct contrast between the Ca-rich (dark) and Ca-poor (bright) lamellae was observed, indicating a significant difference in diffraction contrast (see Figure 50B)). The boundaries between the lamellae appeared diffuse due to a gradual change in composition from one lamella to the next, rather than an abrupt transition.

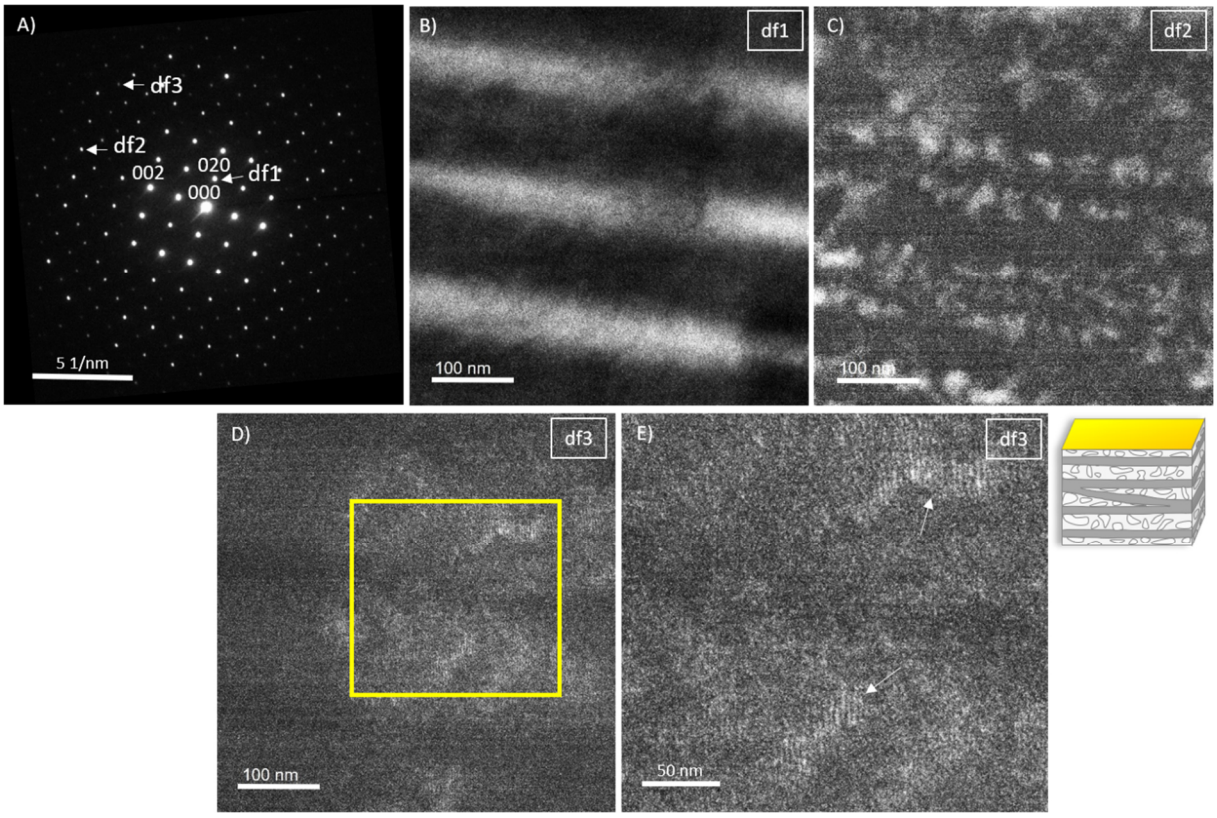

Figure 50: A) The TEM diffraction pattern along the [100] zone axis displays the labradorite matrix, with specific diffraction spots df1-df3 marked by arrows. These selected diffraction spots were used to create dark-field images

presented in B)-E). B) Dark-field image of 020, where the Ca-rich (dark) and Ca-poor (light) lamellae are clearly visible. C) Dark-field image of a pair of *e*-satellites located between 014 and 015, revealing domains within the lamellae. D) Dark-field image of 064 with the yellow-framed area magnified in E). The *e*-fringes can be observed in certain regions, with an approximate spacing of 3 nm. The insert on the right of E) was extracted from Figure 47.

The TEM dark-field image presented in Figure 50C) reveals additional domains, approximately 50 nm in size, with diffuse boundaries. These domains are exclusively observed within the Ca-rich lamellae when employing a pair of *e*-satellites for dark-field imaging. Conversely, no such domains were observed in the Ca-poor lamellae. It is believed that these domains formed during the phase transition from the high temperature $C\bar{1}$ phase to the low temperature e-plagioclase phase, which is consistent with previous experimental findings by Benna et al. [325] and Nemeth et al. [326] involving Sr-feldspar and Ca-rich plagioclase, respectively. Within the domains, *e*-fringes measuring approximately 3 nm in width, perpendicular to the vector *q*, indicate a modulation (see Figure 50D) and E)).

The lamellae are not completely perpendicular to the *b*-axis; rather, they are tilted by approximately 11°. To determine their thickness, the width of 232 thick lamellae and 232 thin lamellae, all parallel to each other, was measured. The thicker lamellae exhibited an average thickness of 129 nm, while the thinner lamellae were about 64 nm thick.

To determine the composition variations between the lamellae, an EDS linescan was conducted on seven lamellae, as depicted in Figure 51. The number of counts for the elements were initially normalized to the total counts at each distance to account for thickness variations. Then, the counts were multiplied by the respective k factor and converted from wt% to mol%. The average composition of the yellow regions was found to be $Ca_{0.53}Na_{0.42}K_{0.05}Si_{2.43}Al_{1.53}Fe_{0.04}O_8$. The EDS linescan revealed that the thicker, brighter lamellae were enriched in Ca and depleted in Na, while the opposite was observed in the thinner, darker lamellae. The content of Al, Si, K and Fe is illustrated in Figure 52. The Ca-rich lamellae exhibited an increase in Al content and a decrease in Si content, aligning with expectations (see Figure 52A)). Considering the general formula for plagioclase $Ca_{1-x}Na_xAl_{2-x}Si_{2+x}O_8$, with x ranging from 0 to 1, the determined variation in the Si/Al content can be explained. Although the Fe content displayed some variability due to the high noise level in the EDS spectra caused by the low count rate for Fe, there was a general trend that followed the Al content across the lamellae (see Figure 52B)). This suggests the potential incorporations of $Fe^{2+/3+}$ in the tetrahedral position replacing Al^{3+} [327,328]. The Na and K content increased in the Ca-poor lamellae (see Figure 52C)). The K content exhibited high noise levels due to its low concentration but followed the Na curve, which was expected since K^+ occupies the same position as Na^+ in the crystal structure. To obtain the average composition of labradorite, all spectra of the linescan were averaged. Assuming only Ca^{2+}, Na^+ or K^+ occupying each cation position, the An content was calculated to be 53.4 mol%.

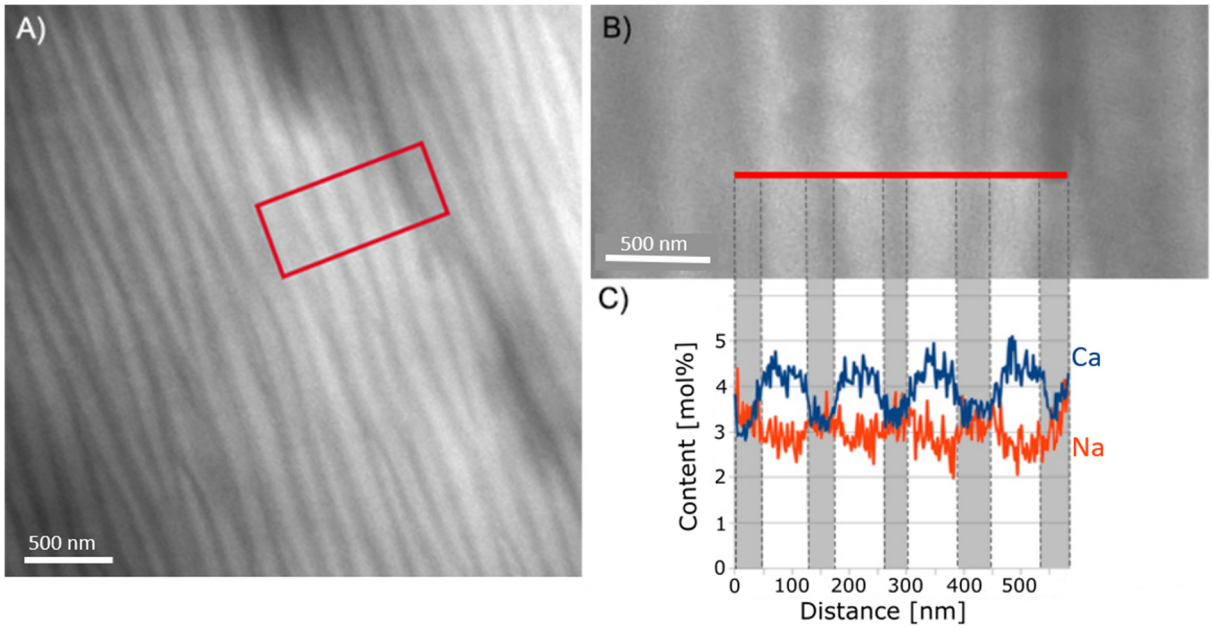

Figure 51: A) The STEM-ADF image displays the lamellae of labradorite in the [001] zone within a specific region of the matrix. An enlargement of the red-framed area is presented in B), with a red line indicating the position of the linescan. C) The Na and Ca content, measured in mol%, are plotted against the distance in nm.

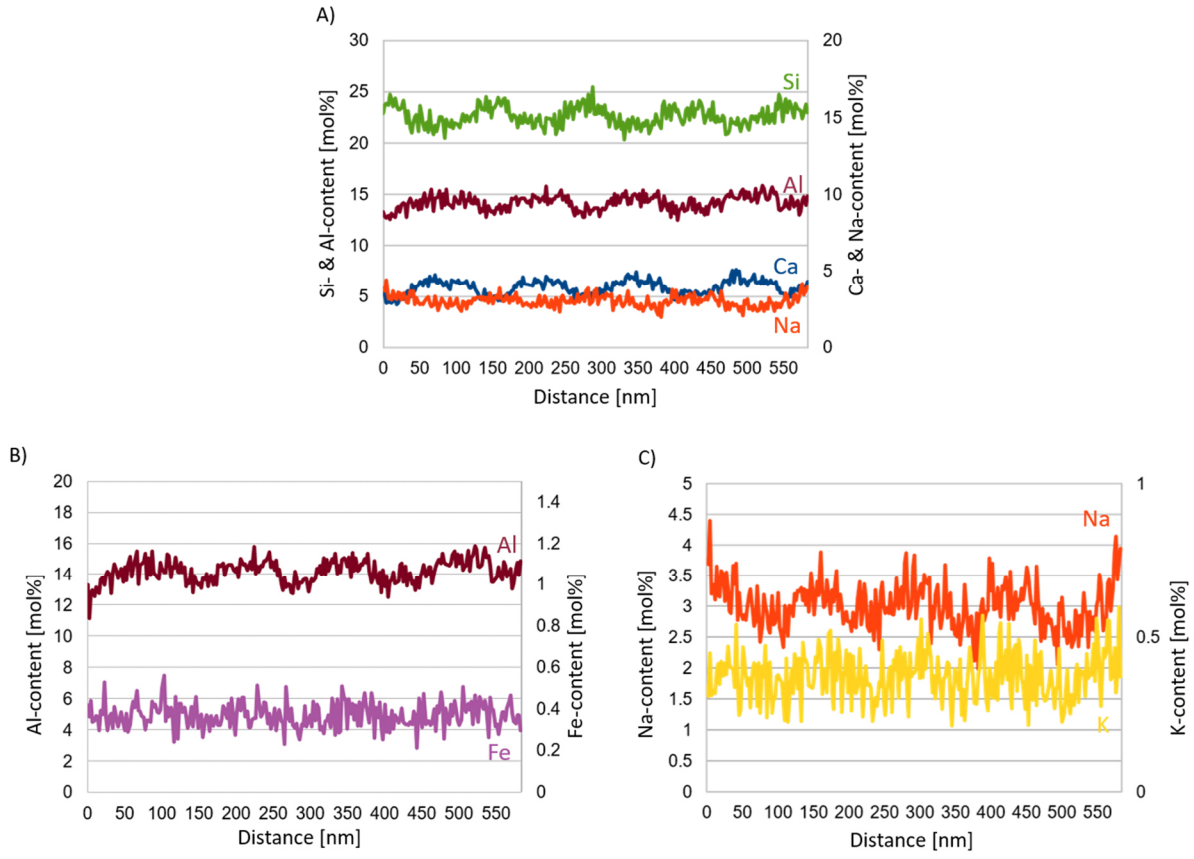

Figure 52: The EDS linescans are plotted to showcase the element content in mol% against the distance in nm. A) Si, Al, Ca and Na; B) Al and Fe; C) Na and K. To effectively represent the trend of each element, two y-axes are provided in each diagram.

5.3.3. Atomic scale investigations – HRTEM imaging

Figure 53A) presents a high-resolution image captured in the [010] direction. The FFT plot in Figure 53B) displays the a^*- (a = 8.2 Å) and c^*-axes (c = 7.1 Å). The angle between a^* and c^* measures approximately 64°, which corresponds to the ~116° angle of β in real space. The HRTEM image was filtered using the diffraction spots of the labradorite cell with a doubled *c*-axis, encompassing the satellite reflections that indicate the modulation vector. A mask using the 002 and the 200 reflections was applied and another mask was created that incorporated the satellite reflections. The filtered FFT in Figure 53B) includes the satellites but no significant changes were observed when comparing the unmodulated and modulated FFTs, as the modulation vector is inclined to the [010] direction. In Figure 53C), the labradorite structure is oriented along [010] and superimposed on a magnified region of Figure 53A), demonstrating good agreement with the high-resolution structure. Si and Al are represented in blue, positioned at the bright spots, while Ca and Na are shown in yellow, situated at the borders of the dark regions. The FFT of the HRTEM image reveals additional maxima, attributed to a modulation. The distance between these satellites indicates a periodicity of 4.3 nm. To accurately calculate the actual modulation of labradorite, it was necessary to measure and reconstruct the labradorite diffraction space in three dimensions.

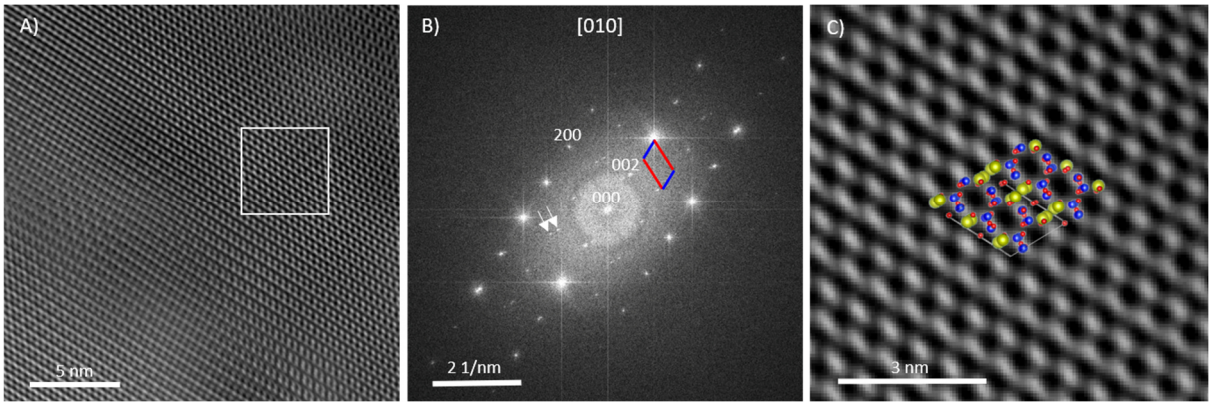

Figure 53: A) High-resolution TEM image of labradorite captured in the [010] direction displaying intensity modulation due to variations in sample thickness across the image. The image is filtered using the cell that has a doubled *c*-axis, as depicted in its FFT shown in B). The FFT displays the *a**-axis in red and the *c**-axis in blue, with white arrows indicating the presence of satellite reflections. In C), the top right region (enclosed in a white box) of the filtered HRTEM image from A) is magnified, demonstrating a close match with the high-resolution structure of labradorite. Si and Al are represented in blue, Na and Ca in yellow and O in red.

5.3.4. Average crystal structure solution

In order to acquire 3D ED data using ADT, a lamella was chosen that extended into the thinned hole (see Figure 54). These lamellae, rich in calcium, exhibit greater stability at higher temperatures compared to the Na-rich plagioclase. Consequently, the Ca-rich lamellae are more resilient to ion thinning. By focusing solely on the Ca-rich lamellae in the EDS linescan (see Figure 51 in chapter 5.3.2), it was determined that the An content in the extending lamellae is approximately 60%, surpassing the average concentration observed across multiple lamellae.

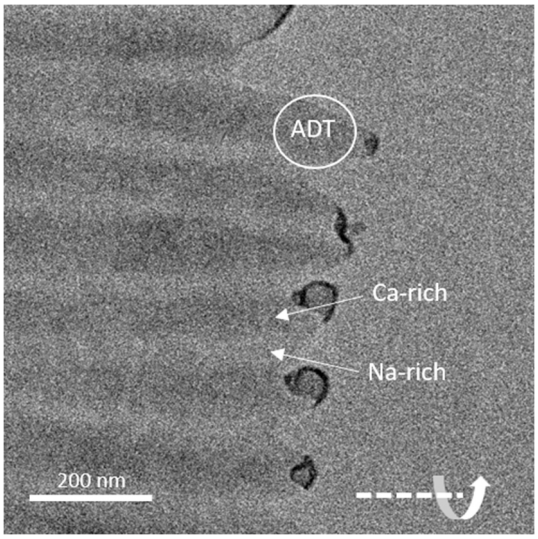

Figure 54: TEM bright-field image displaying the lamellae, with the Ca-rich lamellae appearing thicker and extending deeper into the thinned hole due to their enhanced resistance to ion milling. The white circle indicates the location from which the ADT data sets were collected, while the bottom right corner shows the horizontal tilt axis.

Out of 40 recorded ADT data sets, two sets (orientation 1 and 2 from the same lamella) were selected for further evaluation, structure analysis and refinement due to their superior visibility of satellite reflections. The analysis of the reconstructed three-dimensional reciprocal space yielded the following cell parameters: a = 8.164(2) Å, b = 12.898(3) Å, c = 7.163(2) Å, α = 94.28(3)°, β = 116.52(2)°, γ = 89.47(2)°. This cell closely matched the unit cell reported by Jin et al. [259] for a similar composition of An_{52} (Sample 7147A): a = 8.1640(3) Å, b = 12.8534(2) Å, c= 14.2098(4) Å, with a single-cell value of 7.1049 Å, and α = 93.6187(11)°, β = 116.2531(15)°, γ = 89.781(3)°. The maximum deviation in cell axes and angles was less than 1%.

Figure 55 illustrates the three main orientations along with the main zones [100], [010] and [001] and the complete reciprocal space viewed down *c**. In Figure 55D), the view down *c** only displays reflections with *hkl: h + k = 2n,* indicating a *C*-centered cell. Apart from these reflection conditions, as well observable in the main zones [010] (*h0l: h = 2n*) and [100] (*0kl: k = 2n*), no additional absences were detected. These observations align with the space group $C\bar{1}$ [244], which encompassed all basic reflections.

Furthermore, the 3D-reconstructed space reveals satellite reflections (see orange arrows in Figure 55A) and B)) that are not part of the basic structure. Nevertheless, these reflections exhibit a regular pattern. As illustrated in Figure 28C) in chapter 3.2.1, *f*-satellite reflections are situated around *a*-reflections, while *e*-satellite reflections surround the locations *b*-reflections are absent. Since the basic cell derived from the ADT diffraction volume is unable to account for the *b*-reflections in the structure, it is necessary to double the *c*-axis, as depicted by the blue lines in Figure 55A) and B).

Using the program PETS2 [55], electron diffraction data were extracted for both the single cell without satellite reflections and the doubled cell including satellite reflections. The structure was initially solved without satellite reflections in space group $C\bar{1}$ using Jana2006 [175] with a composition of $Na_{0.36}Ca_{0.60}K_{0.04}Si_{2.4}Al_{1.6}O_8$, as determined from EDS measurements. The structure had Z = 4, resulting in a density of 2.72 g/cm³. The data sets achieved a maximum completeness of 84.29%, which was a sufficient coverage of the reciprocal space to solve the

average structure of labradorite using the charge-flipping algorithm [322] implemented in Superflip [176]. An origin shift of ¼, -¼, 0 was required for direct comparison with the crystal structure determined using X-ray radiation [60]. The crystallographic details are presented in Table 12.

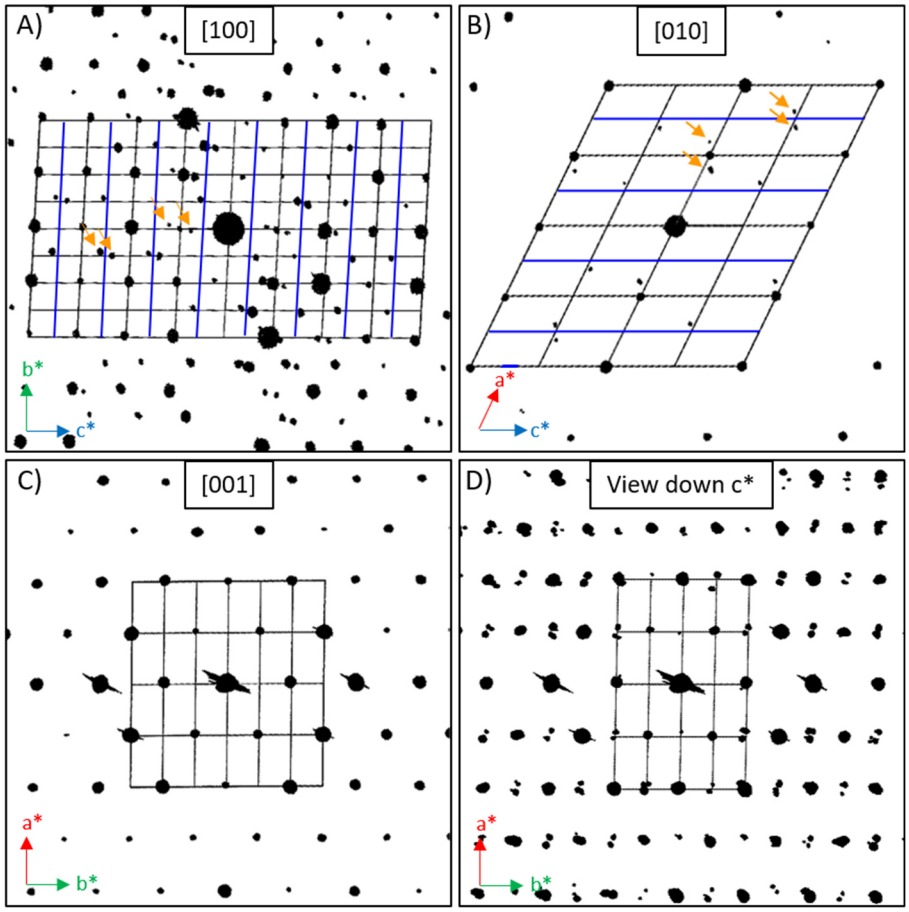

Figure 55: The reconstructed three-dimensional reciprocal space is projected and cut into three main zones, with the unit cell of labradorite depicted by black lines. Blue lines represent the doubled *c*-axis. A) illustrates the [100] direction, B) represents the [010] direction and C) displays the [001] direction. In D) the projection of the reciprocal space along *c** is shown, revealing *C*-centering and the presence of satellite reflections. The orange arrows in A) and B) highlight the position of the satellite reflections.

The labradorite structure is composed of four interconnected Al/Si tetrahedra forming a framework, along with two cation positions (M) that exhibit slightly irregular coordination polyhedra. A detailed visualization of the structure with the respective names of all the atoms can be seen in Figure 56. Among the cations, Ca^{2+}, Na^{+} and K^{+} (M1) were assigned the highest potential with octahedral coordination. After refinement, an additional potential adjacent to M1 was identified and attributed to Ca (M2; occupancy of M1 + M2 = 1). The occupancies of the four tetrahedral positions containing Si^{4+} and Al^{3+} were determined by calculating the average T-O distances using equation (53). For the average and individual distances of the tetrahedra please refer to the table in Appendix 6. Applying equation (53) yielded Al occupancies of 0.36, 0.54, 0.31 and 0.38 for T_{2o}, T_{1o}, T_{1m} and T_{2m}, respectively, which correspond well with the Ca/Na content. These occupancies were kept fixed during the refinement process.

Table 12: Crystallographic details concerning the labradorite structure and its refinement.

Composition	$Na_{0.36}Ca_{0.60}K_{0.04}Si_{2.4}Al_{1.6}O_8$			
Z	8 (4)*	Charge flipping		
a [Å]	8.164	Repeat superflip	10 runs	
b [Å]	12.8534	Max cycles	2000	
c [Å]	14.2098 (7.1049)*	Delta value	0.9	
α [°]	93.6187	Starting model	Random phases	
β [°]	116.253	Peak search	Peaks from Jana	
γ [°]	89.781	Dynamical refinement		
Cell volume [Å³]	1334.15	Max diffraction vector g(max)	1.6	
Space group	$X\bar{1}(\alpha\beta\gamma)0$ $(C\bar{1})$*	Max excitation error (matrix)	0.01	
δh	0.0580(15)	Max excitation error (refine)	0.1	
δk	0.0453(33)	RSg(max)	0.4	
δl	-0.1888(28)	DSg(min)	0	
Modulation period [nm]	3.23	No. of integration steps	128	
Completeness [%]	84.29	Resolution [Å]	0.6	

Refinement	Single cell		Double cell	
	Kinematical	Dynamical	Kinematical	Dynamical
Reflections	865 = 837 + 28 / 127	2926 = 2601 + 325 / 358	4312 = 3629 + 683 / 233	7734 = 4105 + 3629 / 222
Reflection/ parameter ratio	6.8	8.2	18.5	34.84
No. of satellite reflections (first; second order)	-	-	1727 = 1359 + 368; 1722 = 1432 + 290	
GOF(obs) [%]	25.21	5.34	30.70	16.56
GOF(all) [%]	24.85	5.02	28.19	12.36
R(obs) [%]	23.95	8.31	45.06 (33.68, 50.20, 52.50)‘	29.87 (18.67, 38.59, 56.60)‘
R(all) [%]	25.23	9.22	50.01 (34.86, 59.42, 58.60)‘	51.73 (20.56, 83.28, 112.1)‘
wR(obs) [%]	30.89	10.42	50.79 (43.81, 51.11, 55.48)‘	36.66 (21.87, 42.74, 59.11)‘
wR(all) [%]	31.04	10.49	51.10 (43.92, 51.81, 55.81)‘	38.02 (22.09, 48.27, 61.49)’

*values in brackets are describing the single cell;

‘values in brackets are describing the values for main reflections, first-order satellite reflections and second-order satellite reflections

Refinement

The kinematical least squares refinement converged at a wR(all) value of 31.04%. Although the resulting structure was reasonable, certain atomic displacement factors showed negative values. To address this issue, a dynamical refinement was performed using the kinematical structure model as a basis. The data obtained from orientations 1 and 2 yielded a sample thickness of 528 and 870 Å, respectively, and an overall wR(all) of 10.49%. All atom positions and occupancies for the kinematical and dynamical refinement are tabulated in Appendix 7 and Appendix 8.

The refined occupancy of Ca in both M positions led to an overall Ca content of approximately 0.64, which is consistent with the findings from EDS measurements. At 4σ, no residual electron potential remained, indicating satisfactory occupation of all atomic positions. However, some anisotropic displacement factors continued to exhibit negative values throughout the dynamical refinement. The atomic displacement factors of nearly all atoms, except O2, displayed elongation along the *b*-axis due to the absence of diffraction information in the data sets. Notably, the M2 position exhibited a very high ADP directed towards the M1 position, indicating the presence of a modulation that was not considered in the average structure solution based on the main reflections.

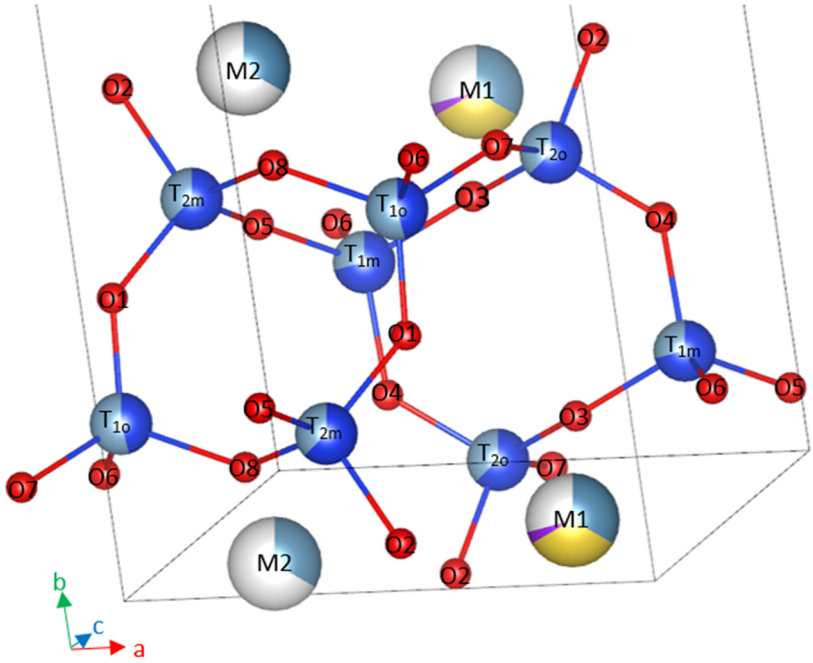

Figure 56: Part of the labradorite structure displaying the respective names of each atom. Unit cell indicated by black lines.

The dynamical structure solution reveals slight variations in atom positions compared to the kinematical solution. The T_{2o} position exhibits the smallest displacement, with a difference of 0.0061 Å, while the M1 position shows the largest displacement, with a difference of 0.1017 Å. The average difference between the two structures is 0.0335 Å. When compared to the average labradorite structure reported by Jin and Xu [60], the smallest and largest displacement also occur in the T_{2o} position, with a discrepancy of 0.006 Å, and the M1 position, with a difference of 0.1796 Å, respectively. The average displacement for this comparison is 0.032 Å. The bond lengths for T-O (expected to be 1.618 for Al and 1.596 for Si) and M-O (expected to be

2.336 for Na and 2.33 for Ca) fall within a reasonable range. The maximum T-O distance is 1.697 Å for T_{1o}-O8. The distance between M1 and M2 is 0.78 Å.

5.3.5. Modulated crystal structure solution

To provide a comprehensive description of the labradorite structure, it was essential to consider its incommensurate nature. The modulation vector q $(0.0580(15)a^* + 0.0453(33)b^* - 0.1888(28)c^*)$ corresponds to half the distance between the *e*-reflections, resulting in a length of 6.46 nm. The distance between the second-order *f*-reflections and the *a*-reflections is $q/2$ (3.23 nm). The modulation vectors of the *e*- and *f*-reflections are parallel and form a straight line connecting the *a*-reflections with both *e*- and *f*-reflections. The q vector is at an angle of 34° to the c^*-axis and lies approximately along the $(11\bar{4})$ direction. It is 9.25 times longer than the cell vector in this direction (3.49 Å), confirming the incommensurate characteristics of labradorite as it is not an integer multiple of the cell vector.

To incorporate *e*-reflections into the data set for structure solution, a double *c*-axis of 14.2098 Å was employed (refer to Figure 55). Moreover, to index the first- and second-order satellite reflections present in the data set, the modulation vector q was applied. This necessitated a specific centering condition of (½ ½ ½ 0), (0 0 ½ ½), (½ ½ 0 ½) and the expansion of the 3D space to a (3+1)D superspace. The space group $X\bar{1}(\alpha\beta\gamma)0$ was used in this context, classified as 2.1.1.1 in Stokes et al. [329] and described in chapter 2.3.

Kinematical refinement

Using the initial average crystal structure refined solely based on main reflections (see chapter 5.3.4), a kinematical refinement was carried out, resulting in a wR(all) of 51.10%. This value can be further divided into 43.92% for main reflections, 51.81% for first-order satellites and 55.81% for second-order satellites (for details see Table 12). During the structure refinement, isotropic atomic displacement factors were maintained and each atom was subjected to harmonic position modulations up to the second order. In addition, second-order occupancy modulations were employed for the M and T sites. Figure 57 depicts the resulting average structure of modulated labradorite and the average atomic positions are presented in Table 13. For a comprehensive listing of all modulation waves, refer to Appendix 9 for position modulation waves and to Appendix 10 for occupancy modulation waves.

This structure is in good agreement with the structure solution obtained from the single cell with a doubled *c*-axis. The T_{2o} site exhibits the smallest displacement of 0.0239 Å, whereas M2 displays the most significant position difference, with a value of 0.1338 Å. The average displacement was determined to be 0.0532 Å. When compared to the modulated labradorite structure proposed by Jin and Xu [60], the minimum difference in atom positions is observed for T_{1m}, with a value of 0.016 Å, while the maximum differences are 0.0762 Å for O4 and 0.0747 Å for M2, respectively. The average displacement was calculated to be 0.0455 Å. The average T-O bond distances are consistent with anticipated values. However, due to the modulation, the range of individual bond lengths is rather broad. The maximum ranges for each tetrahedron are as follows: T_{1o}-O1 (1.27–1.99 Å), T_{2o}-O3 (1.35–1.83 Å), T_{1m}-O4 (1.43–2.05 Å), T_{2m}-O5 (1.32–1.96 Å). For a comprehensive list of all bond lengths, refer to

Table 14.

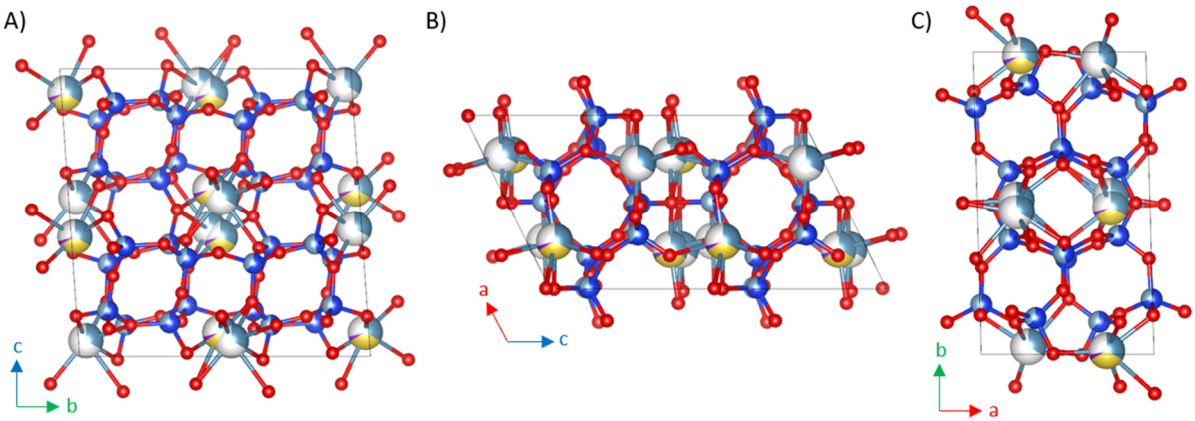

Figure 57: Average structure of labradorite viewed along A) the [100] direction, B) the [010] direction and C) the [001] direction. Ca is displayed in light blue, Na in yellow, K in purple, Si in dark blue, Al in grey and O in red.

Table 13: Average positions of the atoms in the modulated labradorite structure (x, y, z) with occupancy (occ) and isotropic atomic displacement factors (U(iso)).

	x	y	z	occ	U(iso) [Å]
M1Ca	-0.2268(15)	0.4879(12)	0.0836(10)	0.32	-0.0101(16)
M1Na				0.33	
M1K				0.03	
M2Ca	-0.226(3)	0.526(3)	0.0548(18)	0.32	-0.022(3)
T_{1o}Si	0.0077(9)	0.1649(8)	0.1091(6)	0.46	-0.0077(19)
T_{1o}Al				0.54	
T_{1m}Si	0.0048(10)	0.8176(8)	0.1168(6)	0.69	-0.0012(19)
T_{1m}Al				0.31	
T_{2o}Si	0.1877(9)	0.6079(8)	0.1589(6)	0.64	-0.007(2)
T_{2o}Al				0.36	
T_{2m}Si	0.1801(10)	0.3799(8)	0.1769(6)	0.62	-0.001(2)
T_{2m}Al				0.38	
O1	0.0163(12)	0.2885(10)	0.1390(8)	1	-0.014(2)
O2	0.0830(15)	0.4976(12)	0.1402(10)	1	0.004(3)
O3	0.3067(14)	0.6338(11)	0.2797(9)	1	-0.005(3)
O4	0.0148(12)	0.6834(10)	0.1093(8)	1	-0.015(3)
O5	0.3156(16)	0.3584(13)	0.1222(11)	1	0.009(3)
O6	-0.0018(15)	0.8702(12)	0.0113(10)	1	0.004(3)
O7	0.3080(15)	0.6065(12)	0.0958(9)	1	0.001(3)
O8	0.2983(15)	0.3938(12)	0.3096(10)	1	0.001(3)

Table 14: Average and individual bond lengths of the kinematically refined modulated structure of labradorite.

T	O	Average distance [Å]	Min. distance [Å]	Max. distance [Å]	T	O	Average distance [Å]	Min. distance [Å]	Max. distance [Å]
T_{2o}	O2	1.61(6)	1.49(6)	1.70(6)	T_{2o}	O4	1.64(4)	1.49(5)	1.79(5)
	O3	1.59(4)	1.35(5)	1.83(5)		O7	1.60(6)	1.36(6)	1.82(6)
T_{1o}	O1	1.62(5)	1.27(5)	1.99(5)	M1	O4	3.17(6)	2.73(6)	3.73(6)
	O6	1.72(6)	1.62(6)	1.92(6)		O5	3.57(7)	2.83(7)	4.34(7)
	O7	1.73(5)	1.41(5)	2.03(5)		O6	2.42(6)	2.17(6)	2.99(6)
	O8	1.71(4)	1.66(5)	1.78(5)		O7	2.61(6)	2.31(6)	2.81(6)
T_{1m}	O3	1.69(4)	1.49(4)	1.90(4)		O8	2.37(7)	1.99(7)	2.63(7)
	O4	1.73(5)	1.43(5)	2.05(5)		M2	1.02(9)	0.37(11)	1.58(11)
	O5	1.68(6)	1.56(6)	1.78(6)	M2	O1	3.62(9)	2.71(10)	4.39(10)
	O6	1.68(6)	1.59(6)	1.77(6)		O2	2.35(7)	2.07(8)	2.67(8)
T_{2m}	O1	1.67(5)	1.32(5)	1.96(5)		O3	3.52(10)	2.94(10)	3.95(10)
	O2	1.71(6)	1.59(6)	1.83(6)		O4	2.69(8)	2.19(10)	3.42(10)
	O5	1.63(6)	1.45(6)	1.73(6)		O5	2.83(9)	2.20(10)	3.54(10)
	O8	1.70(5)	1.54(5)	1.90(5)		O6	2.43(3)	1.96(9)	2.91(9)
M1	O1	3.16(6)	2.63(6)	3.55(6)		O7	2.52(8)	2.28(9)	2.71(9)
	O2	2.37(5)	1.99(6)	2.67(6)		O8	2.48(9)	2.40(10)	2.67(10)
	O3	2.78(7)	2.16(7)	3.48(7)					

To visualize the modulation in the (3+1)D space, the labradorite structure was approximated across multiple cells (4x*a*, 4x*b*, 4x*c*). Figure 58A) displays the structure along the $[1\bar{1}0]$ direction, which is approximately perpendicular to the modulation vector. To demonstrate the variation in atom positions and the M and T site occupancy, a single layer of M positions was extracted parallel to $[1\bar{1}0]$. The M positions exhibit modulation between Na-rich/Ca-poor and Na-poor/Ca-rich compositions. This modulation is further depicted by plotting the occupancy of the M position against the modulation in Figure 58B). The Na occupancy of the M1 position was fixed to modulate in the same manner as the K occupancy and complementary to the Ca occupancy of M2. While the additional coupling of the Si/Al ratio on each position based on the Ca occupancy has been considered, it is not shown in Figure 58B). Within a single modulation period, the M1 site alternates between preferred Ca and Na occupancies. The Ca occupancy of the M2 position reaches its maximum at approximately the same *q* as that of the M1 position.

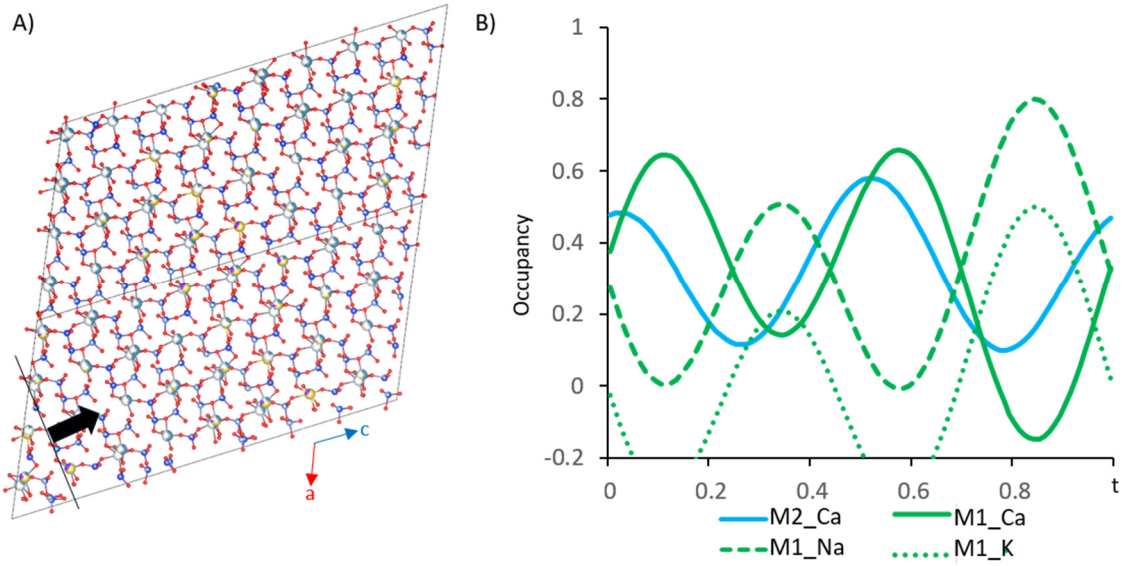

Figure 58: A) The modulated structure of labradorite is illustrated across four cells along the *a*-, *b*- and *c*-axis, respectively. The viewing direction is $[1\bar{1}0]$, offering a perpendicular view to the modulation vector $[11\bar{4}]$ (indicated by the black line) and the modulation direction (shown as a black arrow). Only a single layer of M positions is displayed. B) The modulation of M site occupancy is plotted against *q*. M1 is represented in green and M2 is depicted in cyan.

Figure 59 showcases de Wolff's sections, which exemplarily highlight the position modulation of the two M positions and the T_{2o} tetrahedron, including its adjacent oxygen (O2, O3, O4, O7). These sections are presented in (3+1)D superspace, where the four axes correspond to the three main axes of the cell (x1–3) and the modulation vector (x4). The de Wolff's sections illustrate the observed electron potential for a specific atom in black, while the position modulation of that atom along the modulation vector is depicted in color. For this analysis, the sections were chosen with a variable x4 and x3, while x1 and x2 remained fixed. The harmonic modulations up to the second order significantly improve the position of each atom, enabling them to closely match their observed electron potential. The position modulation of the M sites also influences the tetrahedra and the adjacent oxygen, leading to similar modulations patterns in those atoms.

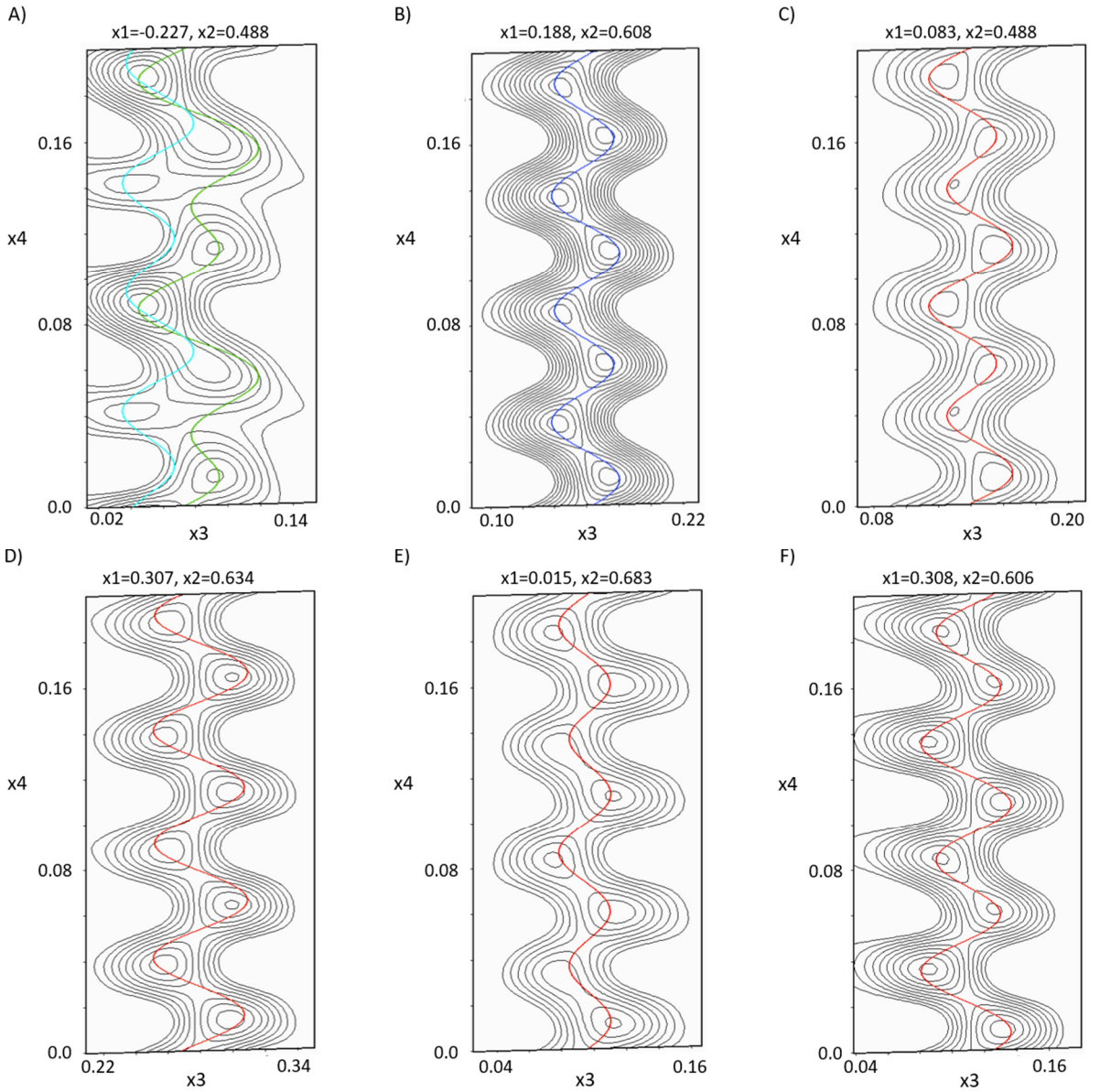

Figure 59: The position modulation of each atom is represented in de Wolff's sections, where their observed electron potential is plotted in the x4 (modulation direction) versus the x3 (*c*-axis) plane, while keeping the x1 (*a*-axis) and x2 (*b*-axis) value constant. A) displays the section for both M positions. B) The section for T_{2o} and its adjacent oxygen C) O2, D) O3, E) O4 and F) O7. The M2 position is represented in cyan, M1 in green, T_{2o} in blue and O in red.

Dynamical refinement

In a next step, the dynamical refinement of the modulated structure model, based on the kinematical refinement, was performed. Because of limitations of the software Jana2020, dynamical refinement was only possible on the satellite reflections of one data set, while for the other data set only main reflections were refined. This reduced the completeness of the data needed for the modulation refinement The refinement with a dampening factor of 0.1 converged at a wR(all) value of 38.02% with 22.09%, 48.27% and 61.49% for the main reflections, first-order satellite reflections and second-order satellite reflections, respectively. Compared to the kinematical refinement, the wR(all) value of the dynamical refinement was 13.08% lower, although this improvement was mainly due to the significantly lower wR(all) value of the main reflections (over 20%). The R values of the satellite reflections did not improve significantly, those of the second-order satellite reflections were even higher than in

the kinematic refinement. The average structure remained similar. Throughout the dynamical refinement, most of the isotropic displacement factors stayed negative. Compared to the kinematical model, the average deviation was 0.0833 Å and the minimum deviation was 0.0162 Å for O7. The M1 position had the highest value with 0.5086 Å. Comparing the dynamically refined structure to the one solved by X-ray diffraction led to similar results. Here, the maximum deviation was 0.454 Å for the M1 position and 0.109 Å for M2. However, the fit of the rest of the atom positions was generally better, with the minimum deviation being 0.0072 Å for T_{1o}, leading to a slightly lower average deviation of 0.07214 Å. The atom positions of the average structure can be found in Appendix 11. The bond lengths of the structure have reasonable average values, however, the variation is high due to the modulation. The largest differences in bond lengths for each tetrahedron are: T_{1o}–O7 1.35–2.15 Å, T_{2o}–O7 1.32–1.88 Å, T_{1m}–O3 1.49–1.98 Å and T_{2m}–O8 1.32–1.94 Å. The average, minimum and maximum bond lengths for the dynamically refined labradorite structure are tabulated in Appendix 12.

Compared to the kinematical model, the position and occupation modulations changed significantly. The harmonic position modulations as well as the occupation modulations up to the second order are tabulated in Appendix 13 and Appendix 14, respectively. The occupancies of the M positions alternate between Ca-rich and Na/K-rich states. However, the range of the values is very high, modulating strongly between positive and negative for each atom species of the M positions (see Figure 60).

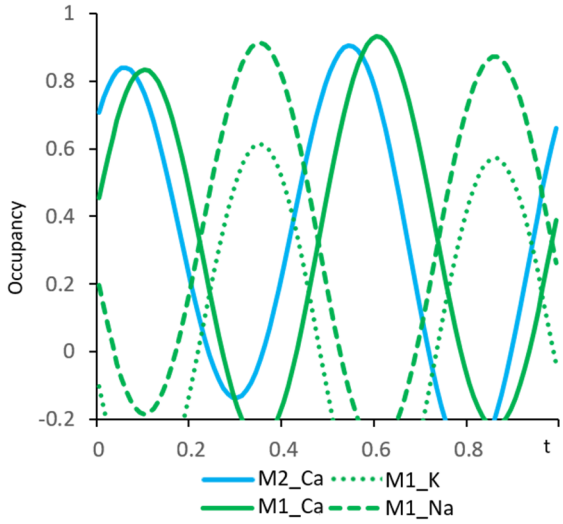

Figure 60: Occupation modulation of both M positions after the dynamical refinement where the occupancy is plotted against *q*. M1 is shown in green and M2 in blue. The occupancies modulate strongly between positive and negative values.

The harmonic position modulations show a general agreement with the electron potential for most of the atom positions. In Figure 61, de Wolff's sections (x3 vs. x4) for both M positions, T_{2o} and its adjacent oxygen O2, O3, O4 and O7 are shown. While the modulation of the atom positions generally follows the distribution of the observed electron potential, there is a slight mismatch along the direction of the modulation, especially for the oxygen atoms. The M positions show the least agreement, modulating too strong for the observed electron potential.

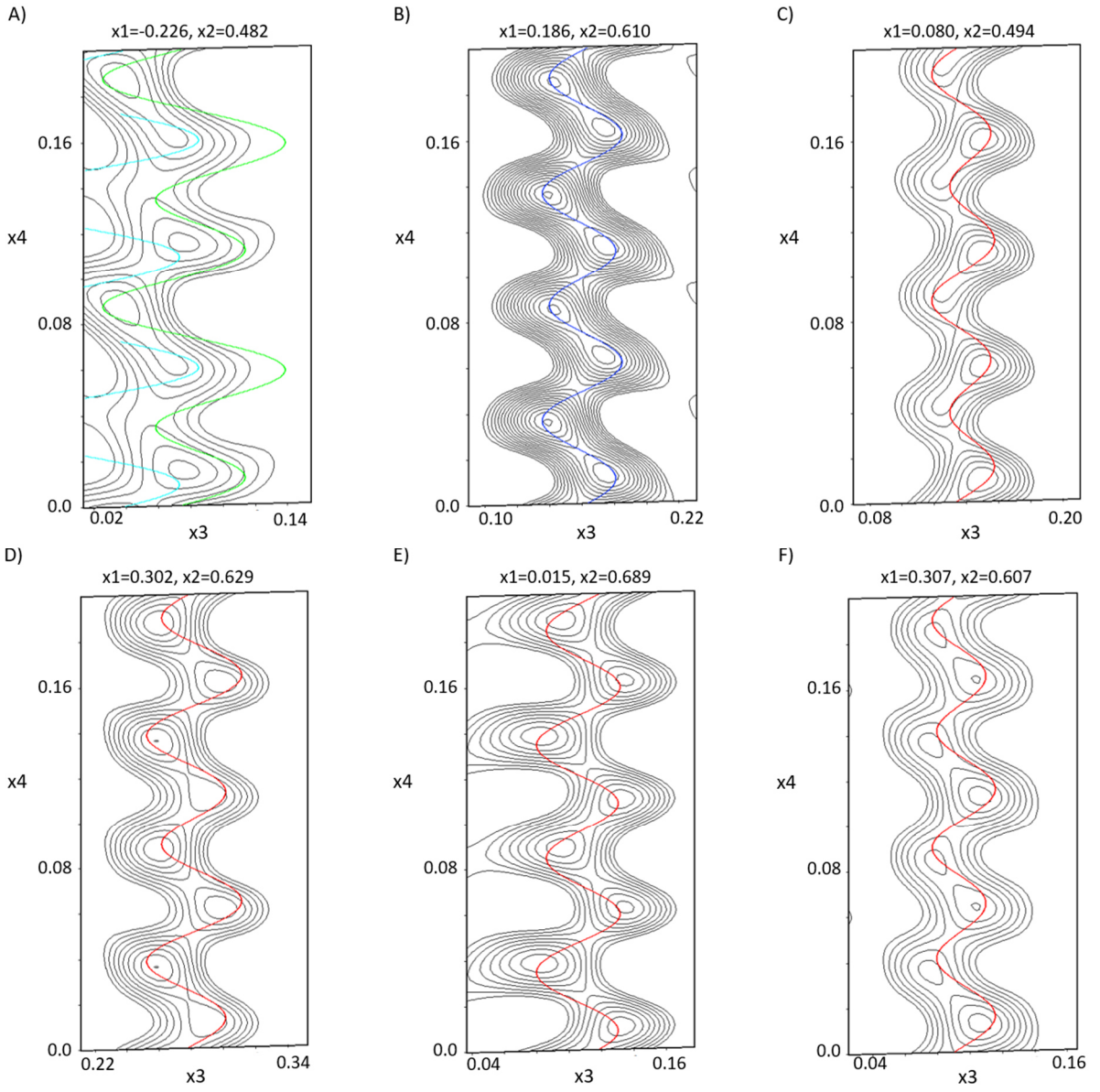

Figure 61: De Wolff's sections of the position modulation of A) both M positions, B) T_{2o} and its adjacent oxygen C) O2, D) O3, E) O4 and F) O7. The observed electron potential is plotted in the x4 (modulation direction) versus x3 (*c*-axis) plane, while keeping the x1 (*a*-axis) and x2 (*b*-axis) value constant. The atom positions are shown in color: M2 in cyan, M1 in green, T_{2o} in blue and O in red. The position modulations show a slight mismatch compared to the observed electron potential.

5.4. Eveslogite

5.4.1. Cell parameter determination

For eveslogite, 14 data sets were acquired with Fast-ADT and STEM-ADT, the best data sets being cry8 (see Figure 62A)), cry17_1 and cry18_1.

During data evaluation with eADT, it was observed that the cell parameters proposed by Men'shikov et al. [64] (a = 14.069 Å, b = 24.937 Å, c = 44.31 Å, α = γ = 90°, β = 95.2°) did not successfully assign indices to all of the diffraction spots (see Figure 62B)). The diffraction spots that were not indexed exhibited a consistent pattern and were present in every data set, suggesting the possibility of twinning at a nanoscale level.

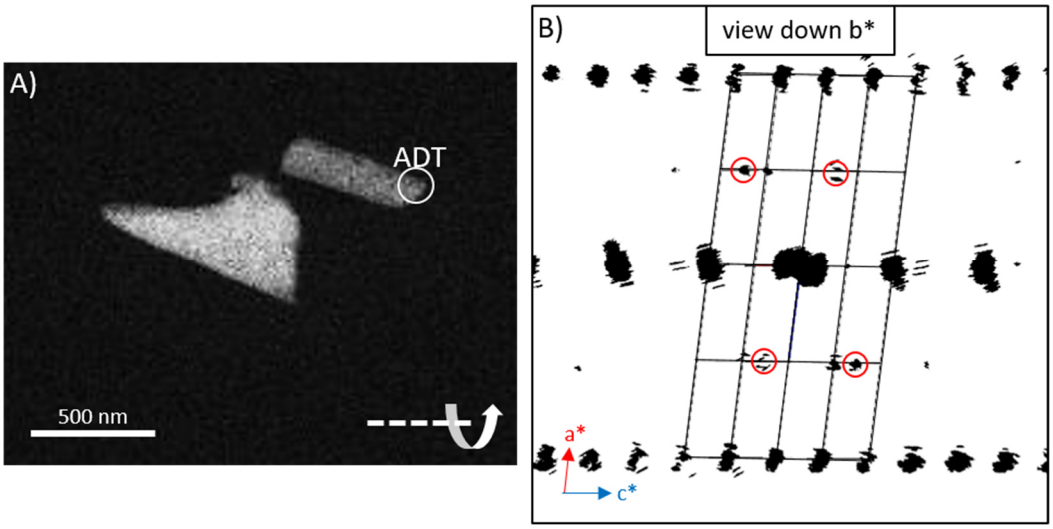

Figure 62: A) STEM HAADF image of two eveslogite crystals. An ADT data set was taken at the tip of the right crystal (cry8; white circle). The tilt axis is displayed in the lower right corner of the figure. B) Projection of the reciprocal space of eveslogite along the *b**-axis of the cell proposed by Men'shikov et al. [64]. The reflections marked with red circles are not intersected by the unit cell.

Consequently, the proposed unit cell was disregarded. Instead, new experimental cell parameters were determined using eADT: a = 14.95 Å, b = 46.54 Å, c = 16.62 Å, α = 90.07°, β = 109.77°, γ = 90.48°. By employing this revised cell, all diffraction spots within the [100] and [001] zones could be accurately indexed (see Figure 63 A) and C)). In the [010] zone and the projection along *b**, an apparent splitting of the *a**-axis confirmed the presence of a twinned structure (see Figure 63B) and D)). Based on the reflection conditions in the three-dimensional reciprocal space, specifically *0k0: k = 2n*, the space group $P2_1$ was assigned. For further analysis, two data sets (crystal3 and crystal8), which were recorded by M. Klementova in Prague and contained no twinning, were utilized. A refinement of the unit cell with PETS2 resulted in the following cell parameters: a = 14.23587 Å, b = 44.82416 Å, c = 15.90576 Å, α = γ = 90°, β = 109.6582°, with a cell volume of 9558.08 $Å^3$.

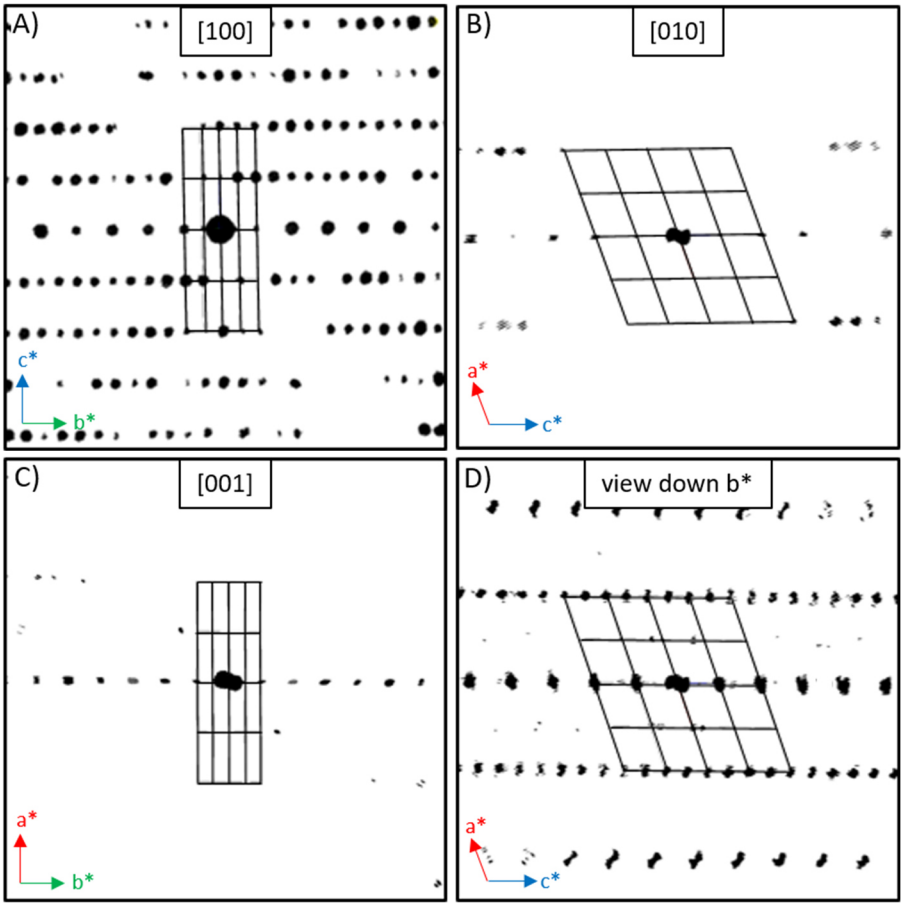

Figure 63: The main zones of the eveslogite cell A) [100], B) [010] and C) [001] and the view of the three-dimensional reciprocal space along *b** (D) with the unit cell depicted by black lines. The split *a**-axis caused by the twinning is only visible in [010] and the view down *b**.

5.4.2. Structure determination

The structure determination of eveslogite was carried out using JANA2020 with data sets analyzed by PETS2. For a comprehensive understanding of the structure determination and refinement process, please refer to Table 15. The structure was analyzed using SUPERFLIP, employing charge flipping of random phases and utilizing peaks from Jana. Subsequently, a kinematical refinement was performed, employing a dampening factor of 1. This refinement process involved 54790 reflections and 1065 parameters, resulting in a reflection/parameter ratio of 51.45. The refinement successfully converged, yielding a residual wR(all) value of 28.54%.

Figure 64A) illustrates the resulting structure of eveslogite along the main direction [100]. Within the unit cell, there are 345 symmetrically independent atom positions. All atom positions, including their respective occupancies and temperature factors, are listed in Appendix 15. The temperature factors were refined isotropically and consistent for each atom species. They converged to reasonable values, with the highest U(iso) value of 0.0223 Å^2 attributed to the K positions.

Table 15: Crystallographic information as well as information about the kinematical refinement of eveslogite.

Sum formula	$K_{17.5}(Ba,Sr)_4(Na,Ca)_{40}[(Ti,Nb,Fe,Mn)_{11}Si_{62}O_{179}(OH,F)_{12}(O,OH)_{13}](H_2O)$		
Composition	$K_{17.5}Ba_{1.848}Sr_{2.152}Na_{11.909}Ca_{28.091}Ti_{6.7}Nb_{1.6}Fe_{1.7}Mn_{1.0}Si_{62}O_{200}F_5H_n$		
a [Å]	14.23587	Kinematical refinement	
b [Å]	44.82416	Reflections	54790 = 30466 + 24324 / 1065
c [Å]	15.90576	Reflection/parameter	51.45
α [°]	90	GOF(obs) [%]	3.23
β [°]	109.6582	GOF(all) [%]	2.58
γ [°]	90	R(obs) [%]	19.91
Z	2	R(all) [%]	24.99
Cell volume [Å³]	9558.08	wR(obs) [%]	27.33
Space group	$P2_1$	wR(all) [%]	28.54
Density [g/cm³]	2.8435		

Notably, the structure's framework comprises 62 SiO_4 tetrahedra, which assemble into chains and two distinct types of tubes, which run along the [100] direction (see Figure 64B)). The Si-O bond lengths were constrained to values of 1.61 Å with a standard deviation of 0.01. All bond distances are tabulated in Appendix 16. Within the periphery of the tubular structures, there are 13 polyhedra that were categorized based on the height of their potential. As a result, the four strongest positions are occupied by (Ba,Sr), while the nine weaker potentials are occupied by K. The occupancies of the (Ba,Sr) positions refined to reasonable values. Additionally, seven K^+ atoms, each with an occupancy of 0.5, are situated within the channels of the tubes. In one of the tubular structures, two octahedra are occupied by (Ti,Nb), with a slight preference observed for Nb on both sites during the occupancy refinement. The other so called double-tube comprises eight $(Ti,Nb,Fe,Mn)O_6$ octahedra, referred to as MO_6. The occupancies of the M positions within the MO_6 were not refined but rather assigned based on average EDS measurements. Consequently, the occupancies for Ti, Nb, Fe and Mn in each M position were determined as 0.740, 0.048, 0.134 and 0.079, respectively. A similar procedure was followed for the $(Fe,Mn)O_5$ square pyramid, with occupancies set at 0.63 and 0.37 for Fe and Mn, respectively. The tubular structures are separated by 40 $(Ca,Na)O_X$ polyhedra that form ribbons extending along the [100] direction. The occupancies of these polyhedra were refined; however, 14 positions did not yield reasonable values. In such cases, sites where the Ca occupancy refined to >1 were set to contain 0.99 Ca and 0.01 Na. High Na occupancies were handled accordingly. Overall, among the 40 $(Ca,Na)O_X$ polyhedra, a higher abundance of calcium was observed in 30 of them, while ten displayed a higher abundance of sodium.

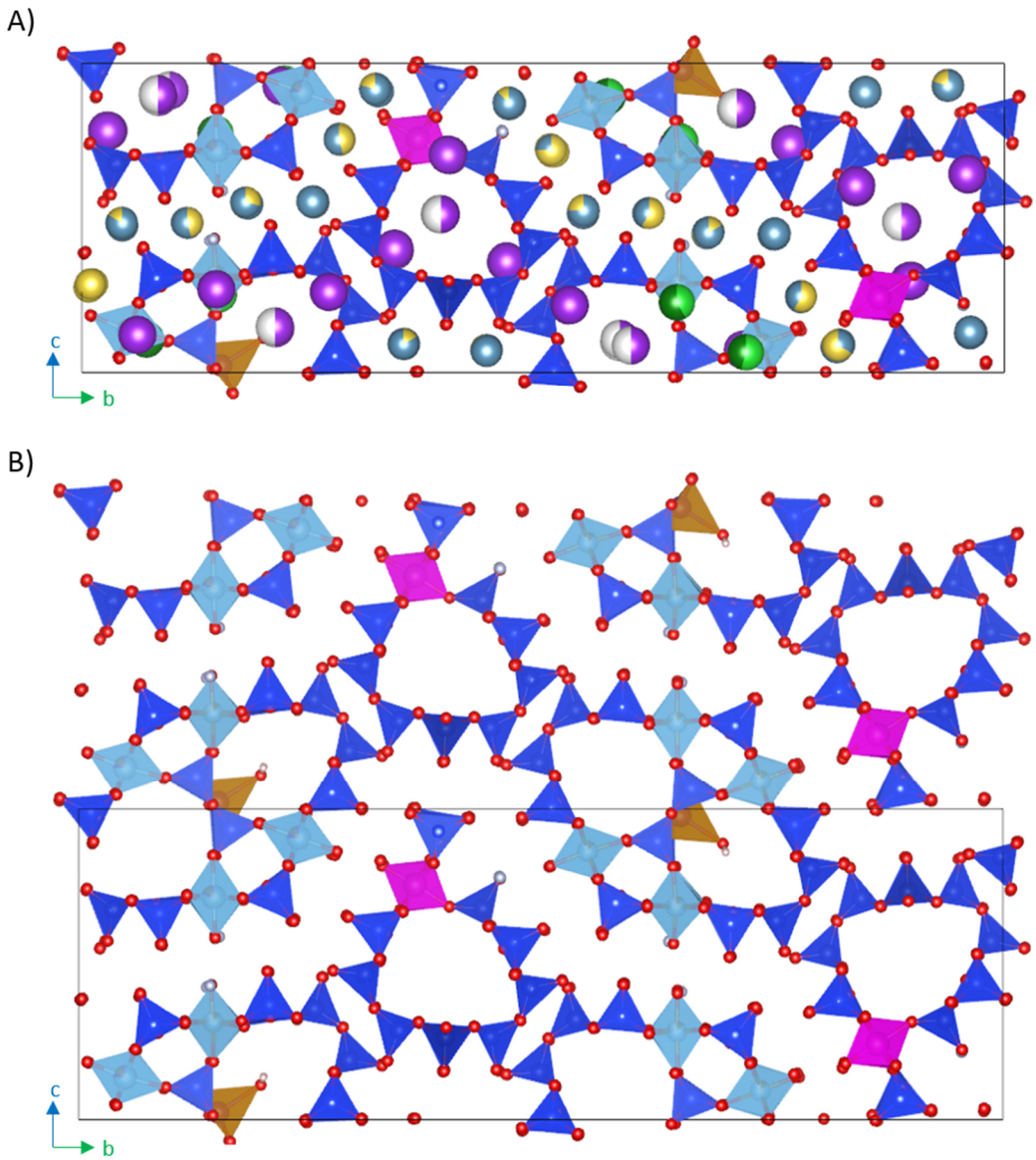

Figure 64: Structure of eveslogite viewed along the *a*-axis. A) The structure of eveslogite containing all atom positions and B) containing only the structural network. The unit cell is marked by a black box. Si is represented in dark blue, M in light blue, (Ti,Nb) in pink, (Fe,Mn) in orange, Ba in light green, Sr in dark green, K in purple, Ca in blue-grey, Na in yellow, O in red, F in grey and H in white.

Major structural details of the eveslogite structure

The eveslogite structure is composed of heterosilicate tubular chains and double-tubes as essential building blocks, extending infinitely along the *a*-axis in a 1:1 ratio. These building blocks consist of silicate-only partial structures known as dreier periodic chains. These chains are formed by corner-sharing SiO_4 tetrahedra and can be either unbranched or loop-branched, creating single, xonotlite-like double, or triple chains [293]. Additionally, the tubular chains and double-tubes contain finite $[Si_2O_7]^{6-}$ diortho-silicate groups. These groups are always connected to (Ti,Nb,Fe,Mn)-heterocations (M), which form $M(O,H_2O,F,Cl)_6$ octahedra or a $M(O,H_2O,F,Cl)O_5$ square pyramid at a specific position within the double-tubes.

Figure 65A) illustrates the tubular loop-branched dreier triple chain of the heterosilicate tubular chains in eveslogite. Similar structural building units are found in related minerals such as charoite-90 [100], charoite-96 [99] and denisovite [101], which is why the tubular chains are

called charoite-like tubes from here on. However, these minerals lack transition metals as defining elements. In their tubes, an idealized composition of $[Si_{12}O_{30}]^{12-}$ is observed, with each Si^{4+} having one available O^{2-} atom for bonding with cations like Ca^{2+}, Na^{+}, K^{+} or Ba^{2+}. If the structural building units containing the M-cations in the charoite-like tubes are disregarded, the appropriate designation for the outermost single chain would be unbranched dreier single chain, while the entire dreier triple chain would be termed a hybrid dreier triple chain since branched and unbranched chains are combined. However, if the M position is indeed considered as a substituting species for Si^{4+}, then the entire dreier triple chain would be classified as loop-branched. Each MO_6 octahedron in the chain has six available O bonds and three of these bonds connect to the opposite borders of the loop-branched dreier triple chains, forming a tube. Two of the remaining bonds connect with the $[Si_2O_7]^{6-}$ groups outside the tube, linking consecutive MO_6 octahedra along the *a*-direction. The remaining O atom is available for bonding with alkaline or alkaline-earth cations.

To gain insight into the underlying topology of the tubular loop-branched dreier triple chain, it can be dissected along the tube axis and unfolded onto a plane, forming a periodic band with finite width across the band. Within the repeat unit (4^68^6), there are six 4-rings and six 8-rings. Additionally, there are infinite chains of 6-rings (6^2), comprising two opposing MO_6 octahedra, two $[Si_2O_7]^{6-}$ groups and two SiO_4 tetrahedra from the adjacent dreier triple chain of the (4^68^6) unit (see Figure 65B)). The (4^68^6) and (6^2) sub-graphs possess distinct topologies but are not disjoint; they cannot be separated and unfolded into a shared net while preserving their individual topologies. A plausible graph symbol representing the combined charoite-like tube of eveslogite would be (4^68^6);(6^2). The (6^2) component functions as an exoskeleton of sorts, preventing the unfolding of the (4^68^6) portion.

The second prominent feature within the eveslogite structure is the double-tube, which exhibits an endoskeleton. Figure 65C) displays the projection of the double-tube along its tube axis (*a*-axis). Remarkably, it bears strong resemblance to the corresponding heterosilicate nanorods found in yuksporite, as described by Krivovichev et al. [97], thus being called yuksporite-like tube from here on. An essential module separates unbranched dreier double silicate chains situated at the opposite ends of the long diameter of the ellipsis. This module is rich in hetero-cations in the form of MO_6 octahedra. These octahedra occupy the corners of a cube-like orthorhombic prism known as the "M-cube" (see Figure 65D)) and are interconnected by two distinct, symmetrically independent $[Si_2O_7]^{6-}$ diortho-silicate groups. The first group runs parallel to the tube axis and is positioned at the opposing ends of the short diameter of the ellipsis, connecting solely with MO_6 octahedra. The second group is wrapped within the interior of the nanorod and crosses the axis, earning the designation of "horizontal" $[Si_2O_7]^{6-}$ groups.

Along the tube axis, two consecutive horizontal $[Si_2O_7]^{6-}$ groups display alternating orientations, with their tetrahedra facing upward and downward. The apical oxygens of these tetrahedra face each other, resulting in the formation of a quadratic planar coordination around a (Fe,Mn) cation at the center of the cross-section. An additional H_2O molecule, roughly perpendicular to the quadratic plane, completes the square-pyramidal coordination around the (Fe,Mn) cation. The polarity in the polar space group $P2_1$ of eveslogite is determined by the (Fe,Mn)-O_{apical} vector. The inward orientations of the tetrahedra, alternating between upward and downward, within a given M-cube impose a reversed order of orientations in the neighboring M-cubes. Consequently, the adjacent M-cubes do not contain $(Fe,Mn)O_5$ groups but remain vacant. This explains the formation of the superstructure in eveslogite, where the

lattice parameter a is doubled (14.1898 Å) compared to that of yuksporite (7.1260 Å), where all horizontal $[Si_2O_7]^{6-}$ groups possess the same arrangement of orientations within their respective M-cubes. In eveslogite, the (Fe,Mn) positions within the filled M-cubes are fully occupied, while the unfilled M-cubes remain empty. Conversely, all M-cubes in yuksporite are uniformly filled, albeit with reduced occupancy.

Similar to the charoite-like tubes, the circumference of the yuksporite-like tube can be described using 4-, 6- and 8-rings, denoted by the symbol ($4^{12}6^88^4$). However, in contrast to the charoite-like tube, the yuksporite-like tube lacks outward building units but instead possesses intricate inward ones. These units are confined within two consecutive M-cubes, with one M-cube containing a $(Fe,Mn)O_5$ square pyramid, while the adjacent M-cubes remain empty. Each M-cube accommodates two horizontal $[Si_2O_7]^{6-}$ groups that traverse the axis of the double-tube. Through visual inspection and searching for rings in the nodal representation, approximately 37 distinct rings with orders of 1 (for (Fe,Mn)-O_{apical}), 3, 4, 7, 8, 10 or 12 were identified. Consequently, an easily comprehensible and intelligible graph representation for this partial structural unit, as well as for the double-tube as a whole, proves to be elusive.

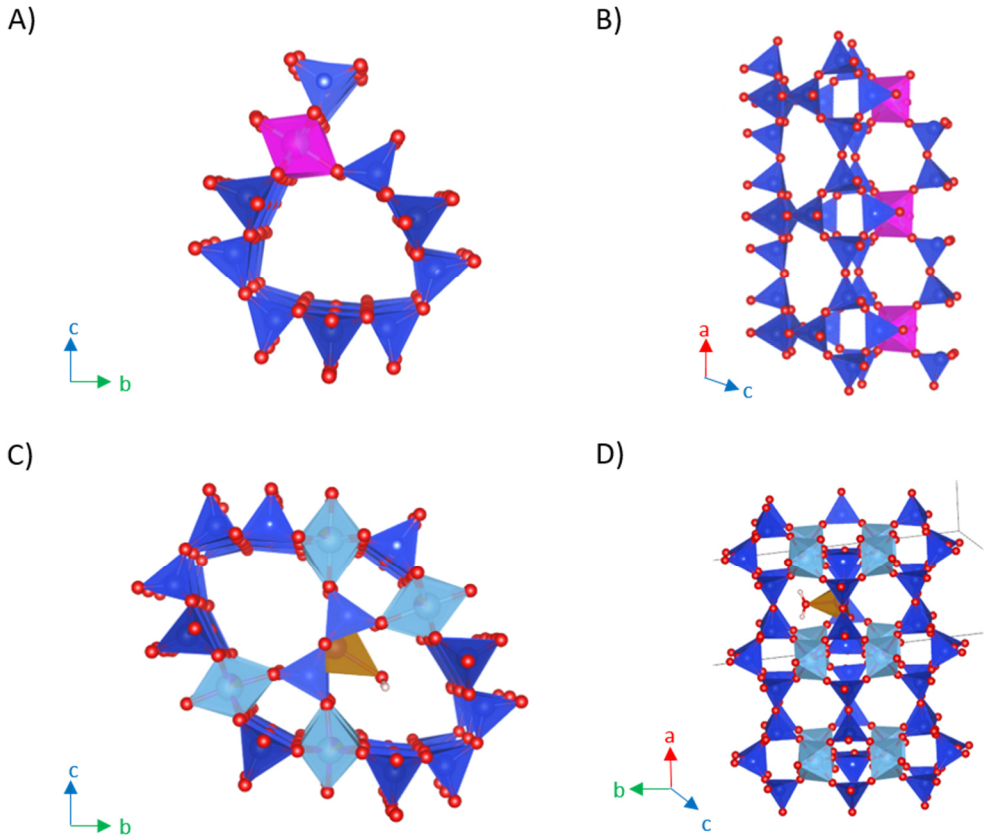

Figure 65: Structural elements of the eveslogite structure. A) View along the *a*-axis of the charoite-like tube containing two dreier triple chains consisting purely of SiO_4 tetrahedra (dark blue) and one unbranched dreier single chain, where $(Ti,Nb)O_6$ octahedra (pink) substitute for one row of SiO_4 tetrahedra. Attached to the tube is a $[Si_2O_7]^{6-}$ group. B) The charoite-like tube viewed along the *b*-axis. The six-membered rings of the $(Ti,Nb)O_6$ octahedra and adjacent SiO_4 tetrahedra can be seen. C) The yuksporite-like tube viewed along the *a*-axis. It consists of two unbranched dreier double chains on each end of the ellipsis, which are connected to $[Si_2O_7]^{6-}$ groups via MO_6 octahedra (light blue). The inner $[Si_2O_7]^{6-}$ groups are linked by $(Fe,Mn)O_5$ square pyramids (orange). D) View of the yuksporite-like tube along [329]. The MO_6 octahedra form a prism-like structure, called "M-cube". Only every second M-cube is occupied by a $(Fe,Mn)O_5$ square pyramid along the *a*-axis.

Comparison with EDS measurements

EDS measurements were conducted on eveslogite crystals using TEM. The results can be seen in Appendix 17. They revealed a wide array of elements, primarily including Si^{4+}, Ca^{2+}, Na^{+}, K^{+} and Ti^{4+}, with minor amounts of Sr^{2+}, Ba^{2+}, Fe^{3+}, Nb^{5+} and Mn^{2+}. Some crystals exhibited the presence of F^{-} and Cl^{-}. The average of the EDS measurements is shown in Table 16. To facilitate a better comparison with the structure, the EDS measurements were extrapolated to align with a sum formula featuring 62 Si^{4+} atoms, assuming that all Si positions had been accounted for in the structure solution. The composition range among the different crystals was notably broad. For instance, the number of Ca^{2+} atoms per sum formula varied from 24.1 to 37.4, Na^{+} ranged from 10.0 to 22.1, K^{+} spanned from 12.3 to 21.1 and F^{-} varied from 0.0 to 11.3 atoms per sum formula (see Table 16). On the other hand, elements, such as Sr^{2+} or Fe^{3+}, exhibited minimal variation across various EDS measurements. During the structure analysis, the composition was based on the average of the EDS measurements, if the positions did not refine to a reasonable value, yielding a sum formula of:

$K_{17.5}(Ba,Sr)_4(Na,Ca)_{40}[(Ti,Nb,Fe,Mn)_{11}Si_{62}O_{179}(OH,F)_{12}(O,OH)_{13}](H_2O)$

and a composition of:

$K_{17.5}Ba_{1.848}Sr_{2.152}Na_{11.909}Ca_{28.091}Ti_{6.7}Nb_{1.6}Fe_{1.7}Mn_{1.0}Si_{62}O_{200}F_5H_n.$

This composition corresponded to a density of 2.84 g/cm^3.

Table 16: EDS measurements of eveslogite. The measurements are normalized for 62 Si^{4+} in the sum formula.

EDS	Ca	Na	K	Ba	Sr	Ti	Fe	Nb	Mn	Si	F	Cl
Range	24.1-37.4	10.0-22.1	12.3-21.1	0.9-3.3	2.0-3.4	5.0-8.5	1.3-2.5	0.7-3.3	0.8-1.5	62	0.0-11.3	0.0-2.4
Average	28.5	9.9	15.6	2.0	2.6	6.7	1.7	1.6	1.1	62	3	1

Comparison of the structure with a STEM HAADF image

A comparison between the determined structure of eveslogite and a filtered STEM HAADF image was conducted. The HAADF image, oriented along [100], clearly displays distinct tubes present in the structure (see Figure 66A)). Superimposing the solved structure onto the STEM HAADF image reveals a close agreement in atom positions (see Figure 66B) and C)). It is worth noting that minor discrepancies in atom positions could be attributed to a slight sample mistilt relative to the electron beam during the acquisition of the image. To further examine the structure, HAADF simulations were performed using the determined structure (see Figure 66D)). The simulations exhibit a strong correspondence with the intensity distribution observed in the STEM HAADF image (compare Figure 66C) and D)). The bright cross-like structure observed in the HAADF image can be attributed to the presence of the M-cube in the yuksporite-like tubes, while another prominent bright spot belonging to the charoite-like tubes corresponds to the (Ti,Nb) position.

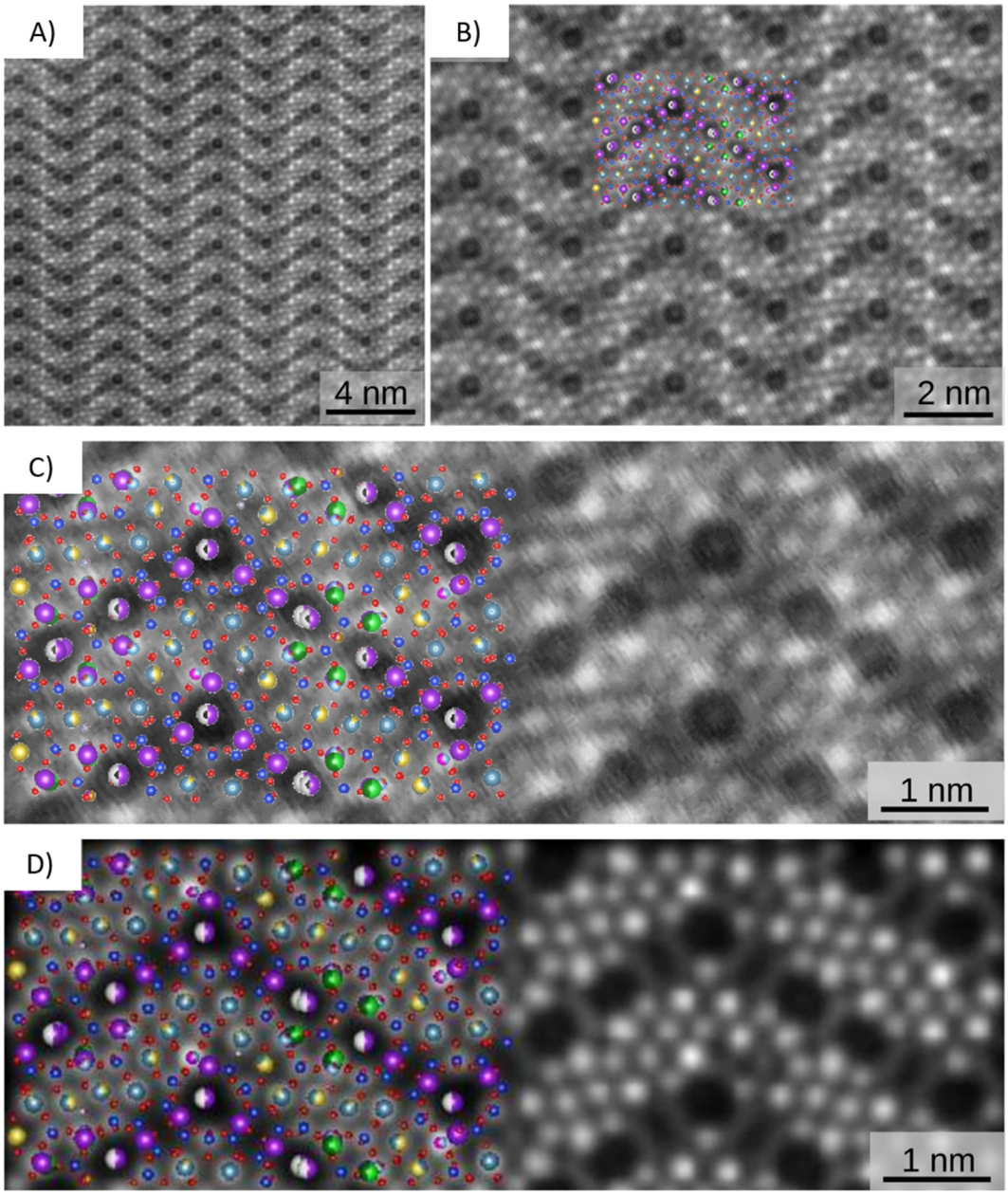

Figure 66: HAADF image analysis of the eveslogite structure. A) Filtered STEM HAADF image of eveslogite along the *a*-axis. B) and C) Zoomed in view overlayed with the structure of eveslogite. The atom positions match nicely. D) Simulated HAADF image based on the determined eveslogite structure. Si is displayed in dark blue, K in purple, Ba in light green, Sr in dark green, Ca in blue-grey, Na in yellow, Ti in light blue, Nb in pink, Fe in orange, Mn in magenta, O in red, F in grey and H in white. (HAADF image and simulations obtained by Marco Schowalter)

Placing of the hydrogen atoms

Due to the close proximity of heavy scattering atoms, the data set quality was insufficient to determine the positions of hydrogen atoms accurately. However, based on their connections within the structure, certain oxygen atoms are unable to be protonated due to their involvement in bridging Si-Si or Si-M bonds. Terminal oxygen atoms of SiO_4 tetrahedra that bond to three $(Ca,Na)O_X$ polyhedra and terminal oxygen atoms of MO_6 octahedra also cannot bond with hydrogen. Nevertheless, there are still oxygen atoms that retain the potential for protonation. All oxygen atoms are categorized based on their bonding partners in Table 17.

Table 17: Every oxygen position in the structure of eveslogite sorted in various topological categories that determine whether or not the oxygen atom can be protonated.

Topological type	Oxygen atoms in the eveslogite structure	Assignment
Bridging Si-Si	3, 6, 7, 8, 9, 12, 15, 16, 17, 21, 22, 25, 27, 28, 30, 31, 33, 34, 36, 38, 39, 40, 44, 49, 54, 61, 62, 63, 65, 66, 69, 70, 72, 75, 78, 80, 86, 87, 92, 95, 97, 100, 103, 107, 110, 112, 113, 115, 116, 121, 122, 125, 129, 130, 132, 136, 150, 151, 160, 161, 162, 170, 196, 198, 200, 204	Cannot be protonated O
Bridging M-Si	1, 2, 18, 24, 26, 29, 32, 37, 47, 48, 50, 57, 59, 60, 68, 79, 81, 90, 104, 105, 114, 119, 123, 124, 126, 131, 133, 139, 140, 141, 142, 143, 145, 148, 153, 154, 155, 156, 157, 158, 164, 167, 171, 173, 174, 176, 177, 183, 186, 189, 190, 195, 203	Cannot be protonated O
Terminal O of MO_6 octahedra not bonded to Si	4, 5, 46, 52, 55, 108, 120, 144, 152, 168	Cannot be protonated O
Terminal O of SiO_4 tetrahedra bonded to 3 Ca/Na	10, 14, 19, 20, 23, 35, 41, 42, 45, 53, 56, 64, 73, 76, 77, 82, 84, 91, 98, 99, 111, 118, 127, 134, 135, 138, 146, 149, 165 169, 172, 179, 181, 182, 184, 185, 191, 197, 199, 201, 202, 205	Cannot be protonated O
Terminal O of SiO_4 tetrahedra bonded to 2 Ca/Na	11, 13, 43, 51, 58, 67, 71, 74, 85, 88, 94, 101, 117	Can be protonated O, OH
Not bonded to Si and/or M, bonded to 3 Ca/Na	83, 93, 96, 102, 106, 109, 147, 159, 187, 188, 192, 194	Should be protonated OH, F
Bonded to inter-stitial Fe^{3+} ion inside rods	193	Should be water molecule H_2O

The apical oxygen of the $(Fe,Mn)O_5$ square pyramid can form bonds with two hydrogen atoms, thus forming H_2O. Additionally, there are 12 oxygen atoms that only bond with three $(Ca,Na)O_X$ polyhedra, which should be protonated. Furthermore, the 13 apical oxygen atoms of SiO_4 tetrahedra, which connect to two $(Ca,Na)O_X$ polyhedra, can also undergo protonation. Based on the refined occupancies and assuming the bond valences of the cations as shown in

Table 18, the eveslogite structure exhibits a charge deficit of -26.5 without the addition of hydrogen. However, the mentioned oxygen positions allow for the potential protonation of 26 sites. Among these positions, five are unsuitable for hydrogen bonding as the surrounding cations would come too close to the hydrogen. Therefore, these oxygen positions were replaced with fluorine. As for the remaining oxygen positions, the attachment of hydrogen atoms can achieve net neutrality depending on the occupancy of the cation positions. In the composition described here, 19.5 oxygen atoms, in addition to the water molecule and five F positions, should be protonated to maintain charge balance.

Table 18: Cations in the eveslogite structure with their (assumed) valence and preferred coordination polyhedra.

Cation species	Valence	Polyhedra
K	I	Flexible, 6-8
Na	I	Octahedra
Ca	II	Flexible, 6-8
Sr	II	Flexible
Ba	II	Flexible
Ti	IV	Octahedra
Nb	V	Octahedra
Fe	III	Octahedra
Mn	II	Tetrahedra
Si	IV	Tetrahedra

5.4.3. Twinning

During the evaluation of the data using eADT, it was observed that a considerable number of data sets exhibited diffraction spots that could not be indexed based on the determined cell parameters. These spots displayed a regular pattern, suggesting the presence of nanoscale twinning. To visualize this twinning phenomenon, two identical cells with different orientation matrices were superimposed onto the three-dimensional reciprocal space, resulting in the indexing of all diffraction spots (see Figure 67A)). The twinning was primarily visible in the a^*-c^* plane along the main directions. Specifically, the a^*-axis is split, while the b^*- and c^*-direction remain unchanged. At every $4a^*$ interval, the cells intersect at a common diffraction spot (see Figure 67A)). The orientation relationship between the two individuals of the twinned crystal corresponds to the twin matrix given by:

$$\begin{matrix} 1 & 0 & 0 \\ 0 & -1 & 0 \\ -0.75 & 0 & -1 \end{matrix}$$

In the monoclinic crystal system, one of the most common twin laws involves a twofold rotation about the a-axis, with a twin matrix given by:

$$\begin{matrix} 1 & 0 & 0 \\ 0 & -1 & 0 \\ (2c\cos\beta)/a & 0 & -1 \end{matrix}$$

For the determined unit cell parameters, the term $(2c\cos\beta)/a$ evaluates to -0.75, which perfectly aligns with the extracted matrix for the twinning in eveslogite. The twinning is most clearly observed along the b-axis, where a splitting of the c-axis can be seen (see Figure 67B)).

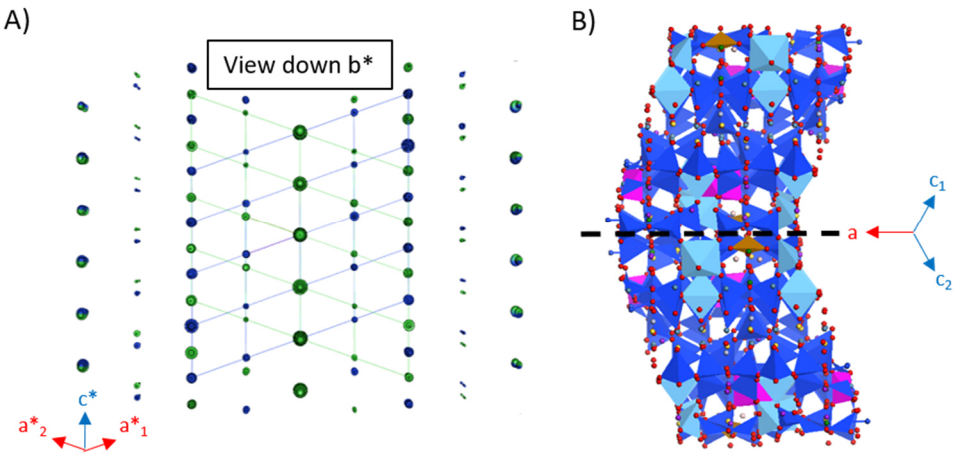

Figure 67: Twinning in eveslogite. A) Projection along the *b**-axis of the reciprocal space of a twinned individual. The two unit cells (green and blue) can be distinguished by the split *a**-axis. B) The twins are defined by a two-fold rotation about *a*. They are connected via the [001] plane, which can be seen when viewed along the *b*-axis. Si is displayed in dark blue, M in light blue, (Ti, Nb) in pink, (Fe, Mn) in orange, Ba in light green, Sr in dark green, K in purple, Ca in blue-grey, Na in yellow, O in red, F in grey and H in white.

The structural nature of the twinning can be understood by taking the polarity of the two different tubes into account (see Figure 68A)). In the charoite-like tube, the (Ti,Nb)O_6 octahedron has five of its oxygen shared with SiO_4 tetrahedra while the sixth one is pending. The respective bond is oriented outwards with respect to the tube. As mentioned in chapter 5.4.2, the polarity of the yuksporite-like tube is determined by the presence of the (Fe,Mn)-H_2O bond in the tube interior. Since the twinning operator is a twofold rotation around the *a*-axis, the twinning operation changes the orientations of the vectors into opposite directions (see Figure 68B)). Thus, the twinning involves the rotation of the tubes around their axes and formation of domains with different polarity directions.

When observing the position of the twofold rotation (see Figure 68B)) in the eveslogite structure, the possibility of twinning becomes apparent. It is located at the MO_6 octahedra of opposing yuksporite-tubes with the (Ca,Na)O_X polyhedra between them (see black box in Figure 69A)). In the absence of twinning, the MO_6 octahedra within an individual exhibit a distinct arrangement with one octahedron positioned slightly higher along the *a*-axis compared to the other (see white arrows in Figure 69B)). However, if the MO_6 octahedra of one of the yuksporite-like tubes select an alternative available gap within the (Ca,Na)O_X ribbon, their coordinates along the *a*-axis become slightly lower than the octahedra in the other yuksporite-like tube. This results in a splitting of the *c*-axis (see Figure 69C)). The ease with which this transition can occur accounts for the abundance of twinning in eveslogite.

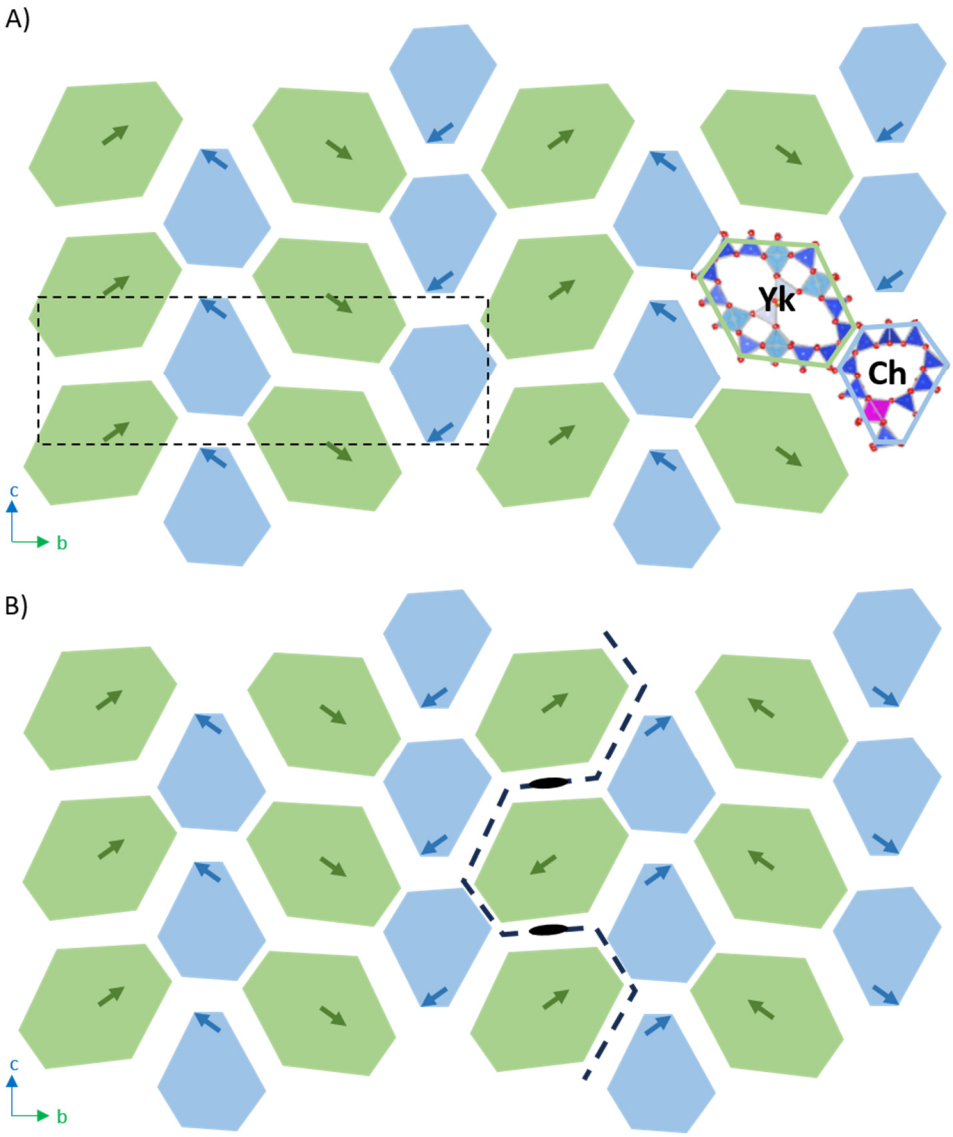

Figure 68: Schematic projection of the structure of eveslogite displayed as yuksporite-like (Yk, green) and charoite-like (Ch, blue) tubes. A) Untwinned eveslogite crystal structure. The unit cell is shown as black dashed box. B) Twinned eveslogite crystal with two twin components related by twofold rotation around the *a*-axis. The green and blue arrows show the orientation of the Fe-H_2O and Nb-O bonds, respectively. The black dashed line indicates the twin boundary and the black ellipses indicate a twofold axis acting as twin operator.

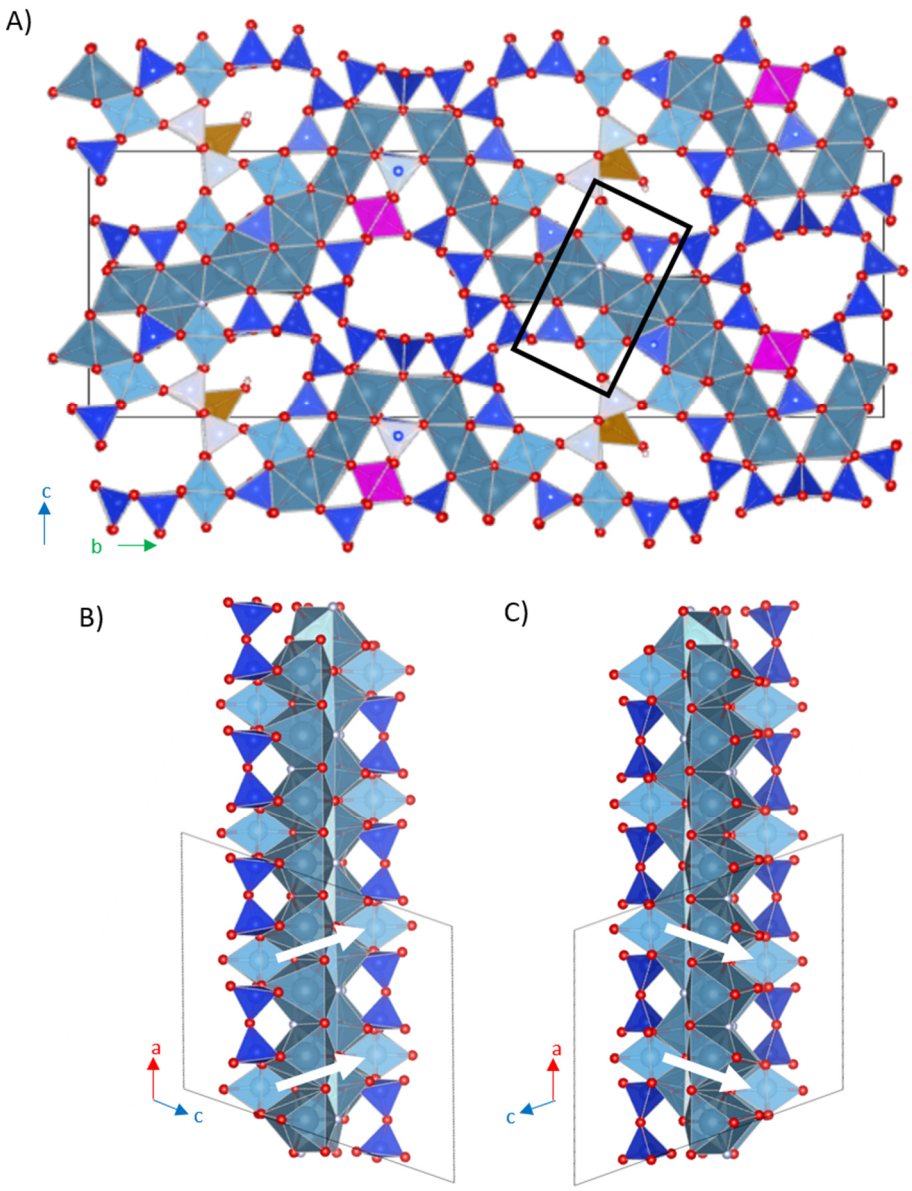

Figure 69: A) Eveslogite structure of an untwinned crystal. The position of the twofold rotation is marked by a black box and shown in B) and C) along the *b*-axis. The MO_6 octahedra of the opposing yuksporite-like tubes have two options, B) and C), to arrange along the $(Ca,Na)O_X$ ribbon. The position of the octahedra relative to each other changes (indicated by white arrows), causing a splitting of the *c*-axis and thus the twinning.

6. Discussion

6.1. Illite

The analysis of the autoclave experiments involving Bad Nauheim brine and synthetic Gerolstein brine revealed that the precipitates were only present at the periphery of the plug, indicating limited fluid penetration during the autoclave tests, approximately limited to 600-700 μm. This finding aligns with the observation of the outer 700 μm of the plug being bleached after reacting with hydrochloric acid. The formation of halite crystals was only observed in experiments where brines containing the required Na^+ and Cl^- ions were present. It is likely that halite precipitation occurred during the drying process rather than the experiment itself, as indicated by the massive nature of the precipitation (see chapter 5.2.1, Figure 37C)) and crystallization within the filter pores (see chapter 5.2.1, Figure 38B)). On the other hand, calcite and aragonite crystals only precipitated in association with the brines, where Ca^{2+} ions were available, providing evidence of a strong interaction. Under normal pressure conditions, calcite is the stable phase of $CaCO_3$ [330]. However, under high calcium supersaturation, aragonite also forms regardless of the low pressure. Unlike aragonite, calcite can incorporate Mg^{2+} ions, which are present in both brines, into its structure. This finding supports the observations by Sun et al. [331], who described that the growth of calcite is hindered by the inclusion of Mg^{2+}, whereas the growth of aragonite remains unaffected. This may explain why a greater quantity of aragonite was observed in the precipitates than calcite.

Illite EDS measurements revealed that the potassium content of 0.69(2) of the illite altered with Gerolstein brine had a low variance since all examined fibers had come into contact with the fluid. Nevertheless, the actual average potassium content might have been even lower because fibers with less potassium in the interlayer are increasingly unstable and thus separate more easily. However, these thinner fibers do not provide enough signal for a quantifiable EDS measurement due to their low cross-section so they likely were not measured. In contrast, the potassium concentrations of the illite in the unaltered sandstone varied significantly. This variability could be attributed to the material being scraped off the sandstone plug during sample preparation. As a result, various types of fibers were contained, including completely unaltered ones, but also fibers that might have been in contact with fluids previous to the batch experiments.

Fast-ADT measurements of the fibrous illite in the cementation of the sandstone yielded cell parameters of: a = 5.204(4) Å, b = 9.013(5) Å, c = 10.158(5) Å with $\alpha = \gamma = 90°$ and $\beta = 101.5°$. Using these data sets, the structure of illite was successfully solved in the space group *C*2/*m* as $1M_{tv}$. By conducting measurements specifically on the tip of a single crystal fiber, contamination from other minerals and polycrystalline regions were avoided. Attempts to merge two data sets with the aim of enhancing the quality of the atomic displacement factors by increasing the completeness of the recorded reciprocal space did not yield improved results. This was due to the preferred orientation of the illite crystals, resulting in a comparatively consistent missing cone in the data sets. The dynamical refinement of the structure ultimately converged at a final wR(all) value of 9.57%, which is considered reasonable for 3D ED. During the dynamical refinement process, it was observed that the occupancy of K refined to 0.86, exhibiting a 14% difference from the K content of 0.72(4) measured using EDS. This confirmed that some K^+ atoms had migrated due to beam-induced effects during the EDS measurements, primarily attributed to the high electron dose. In contrast, during the ADT measurements, where a significantly lower beam dose was applied, the K^+ atoms remained in the interlayer and the

occupancy accurately reflected the actual K content. It can be assumed that contrary to HRTEM analysis, the atomic structure was not altered by the electron beam. Kogure and Drits [332] discovered that HRTEM observations of $1M_{cv}$ illite introduce changes in the structure. The illite was dehydroxylated, which caused the octahedral cations to migrate and form a tv-like arrangement so that in HRTEM images it looked identical to dehydroxylated $1M_{tv}$ illite. This effect was caused by heating via electron radiation, which was kept at a minimum during ADT measurements.

The small grain size of illite and the fact that it often occurs either as a phase mixture or as an interstratified mineral, makes its identification very difficult [185,333]. Additionally, many illites lack 3-dimensional order, which further complicates the study of their crystal structures [334]. In the past, there has been one attempt of an illite structure refinement on XRPD data conducted by Gualtieri et al. [58]. The illite they used for their structure refinement was nearly pure 1M with 30% cis vacant layers, an expandability of 10%. With the starting model of muscovite they reached the conclusion that Si^{4+} is partly replaced by Al^{3+} in the tetrahedral position (T), the octathedral position (O) is mainly occupied by Al^{3+} and partly by Mg^{2+} and the main interlayer cation is K^{+} [323]. This was supported by X-ray fluorescence (XRF) measurements performed on the <1.5 μm fraction of the bulk material. Gualtieri et al. determined the basic structure unit and calculated the possible position of the interlayer water molecule. Nonetheless, the final fit of the refinement was still imperfect and a consistent overall pattern could not be created. The biggest issue in their calculations was the observation/refinement parameter ratio of only 2.4, which led to ADP's having to be refined together. Additionally, the interlayer occupancy had to be fixed to 0.8 because it was constantly underestimated to be ~0.63. The low number of independent observations arose from the small number of peaks due to the low symmetry of illite. Additionally, these few peaks were anisotropically broadened because of planar disorder in the structure.

The reflection/parameter ratio of 7-8 in the refinement of the fibrous illite in this thesis allowed for more free parameters, leading to more detailed results. By measuring EDS on single fibers a much more detailed chemical composition of the diffraction volume could be obtained compared to the XRF measurements on bulk material. Occupancies of Al on the tetrahedral position and Fe and Mg on the octahedral position could be added and the anisotropic displacement factors were refined independently. Furthermore, the occupancy of the K position could be refined. Compared to the structure of Gualtieri et al. [58], the bond lengths varied within a smaller range with Si-O = 1.593-1.627 Å (1.53-1.7 Å), Al-O = 1.917-1.968 Å (1.6-2.4 Å) and K-O = 2.970 Å (2.88 Å) (Gualtieri et al. [58] values in brackets). While the basic crystal structure was similar, the atom positions showed some significant differences. The maximum deviation was 0.3871 Å for O2 with an average deviation of 0.1756 Å. Since the composition of the fibrous illite solved by Fast-ADT was more comparable to an illite structure reported by Drits et al. [59], this structure was also used for comparison. Here, the largest deviation was only 0.1079 Å for O2. The average deviation of 0.055 Å shows that the illite structure solution from this study agrees more with the structure postulated by Drits et al. However, Drits' structure was not refined but modeled based on the chemical composition derived by XRF and the unit cell obtained from XRPD. Though, no partial occupancies were used for the tetrahedral and octahedral position, they were kept strictly Si and Al. Based on these facts, it is evident that the limitations of XRPD were reached in solving the illite structure, which could not be adequately described by the refinement. Using 3D ED for structure solution led to results close to the modeled structure for illite with no issue during refinement.

The altered illite fibers exhibited diffuse scattering attributed to stacking faults along the *c*-axis, following the shift $[\frac{1}{2},-\frac{1}{6},0]_{mcl}$. However, this shift differed from the previously documented $1M_d$ structure in literature, where a single tetrahedral sheet is shifted by $\frac{a}{3}$ [77]. Consequently, the presented data unveils a novel form of disorder in illite. The newly proposed model of illite disorder, generated using DISCUS, offers a qualitative explanation for the disorder observed in this illite crystal. However, for a more quantitative description, additional adjustments, particularly related to K^+ exchange in the interlayer, should be considered.

Peltz et al. [68] conducted similar studies on illite found in Flechtingen sandstone (Rotliegend) using XRPD and SEM analysis. Although Flechtingen sandstone shares similarities with Remlingen sandstone, it is much more heterogeneous. Unlike the present research, the chemical composition of the illites in Peltz et al.'s study could not be determined due to the limited resolution of the SEM-EDS system. Their XRPD measurements revealed that 77 wt% of the illite consisted of the $1M_d$ structure, while 16 wt% consisted of the $1M_{tv}$ structure. Based on their findings, Peltz et al. proposed that illite formed through the alteration of feldspar grains predominantly exhibited the $1M_d$ structure, whereas the pore-filling fibers demonstrated growth in the $1M_{tv}$ structure. However, the current study could show by employing 3D ED that disordered illite structures can arise not only from the alteration of other minerals but also from the alteration of the illite fibers themselves.

The varying degrees of disorder observed in the illite samples can be attributed to the interaction between the illite structure and the fluid used. The process is presumably similar to the experiments of Hu et al. [335] where the effects of brine cation compositions were studied on biotite dissolution and changes in surface morphology at 55-95°C and 102 atm CO_2 with 1 M NaCl, 0.4 M $MgCl_2$ and 0.4 M $CaCl_2$. In salt solutions, faster ion exchange reactions with the K^+ ion of the interlayer occurred than in water. Ion exchange with larger hydrated cations led to a slight expansion of the interlayer, which caused bumps and cracks on the surface of the biotite. Additionally, some illite grew epitaxially on biotite. They suggested that this illite could detach easily because of stress build up in the connecting bonds caused by the changed surface morphology of the biotite. Schlabach [336] also postulated a preferential release of K^+ from the interlayer position. They observed this for biotite, phlogopite and muscovite for the entire pH range, with the dissolution rates decreasing significantly with increasing pH. In addition, they detected a dissolution of Mg and Fe from the octahedral sheet, since the Mg-O and Fe-O bonds, in contrast to Al-O bonds, require less energy to be broken. Dong et al. [199] found out that illite dissolution rates vary widely from $\sim 4*10^{-12}$ mol/m^{2}s [337] to $6*10^{-15}$ mol/m^{2}s [338]. With a dissolution rate of $2.4*10^{-10}$ mol/m^{2}s, a pH of 6 and 25°C it would take ~171 days to dissolve an illite needle, while it would only take 1.7 days to dissolve a needle at a pH of 2.9. Since the dissolution rates are different depending on the crystallographic orientation in illites, it would have mainly taken part along the layers. Even elements that have previously been protected within the illite interlayers could be leached later due to the size reduction of the crystallites [66].

Based on these findings, it is probable that the TOT layer of the fibrous illite, which is tightly connected through Si tetrahedra and Al octahedra, remained unaffected by the fluid. However, the K^+ ions in the intermediate layer were exposed along the [010] direction, making them susceptible to dissolution (compare Figure 42 in chapter 5.2.2) [199]. It is important to note that the (001) plane represents the cleavage plane of mica (perfect cleavage perpendicular to the *c*-axis), exposing the K^+ ions in the *a*-*b* plane. Due to the fibrous morphology, the (010)

facet offers a large surface area for ion exchange [204]. In the case of brine from Bad Nauheim, characterized by a relatively high potassium content of 314 mg/L and a high TDS content of 27944 mg/L, the ion exchange occurred only to a lesser extent and the K^+ ions remained predominantly in the interlayer. As a result, no significant differences in the diffraction patterns were detected, indicating that the illite structure remained comparable to that of the unaltered sandstone. However, in synthetic Gerolstein brine with a significantly lower potassium content of 14 mg/L and a TDS content of 5891 mg/L, more K^+ ions were able to dissolve via the (010) facet. This finding was supported by EDS measurements, which revealed that the illite altered with synthetic Gerolstein brine contained less potassium than the unaltered illite. The absence of positive charge from the dissolved K^+ ions reduced the stability between the TOT layers. As a result, the layers were more prone to displacement and disorder in their stacking, leading to a smearing of the diffraction reflections. Furthermore, the lack of charge of the K^+ ions facilitated the separation of the TOT layers from each other, causing the illite fiber bundles to fan out. As a result, portions of the layer packets can be detached by the fluid and transported elsewhere. These mobile fibers can interact and intertwine with other illite fibers, creating structures observed in SEM studies, as shown in Figure 70.

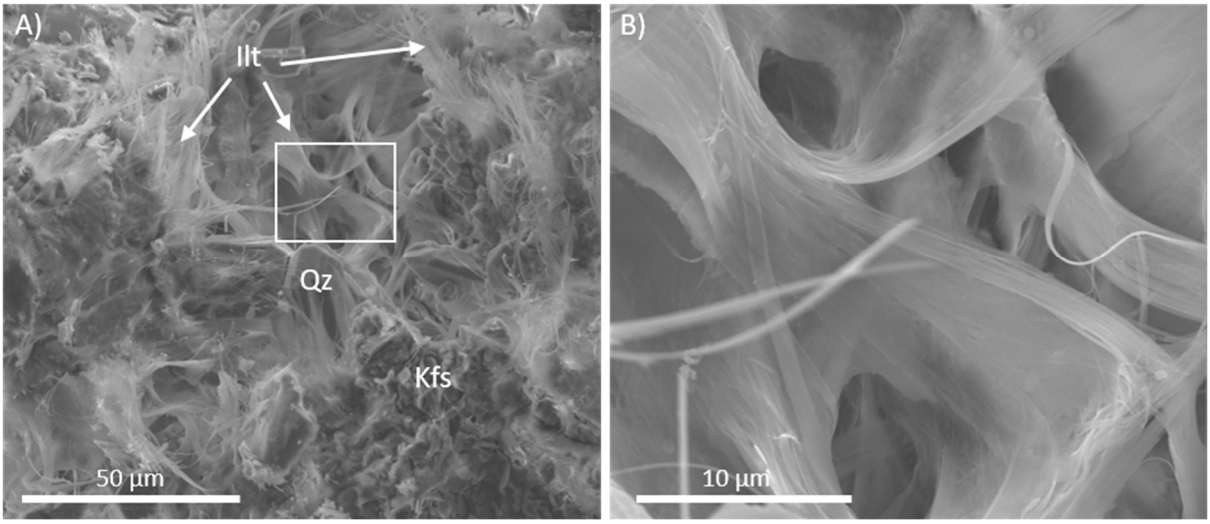

Figure 70: A) SEM-SE image of a cluster of illite fibers observed within the pore space of the sandstone that underwent alteration with synthetic Gerolstein brine. B) A closer view of the white square in A) reveals the illite fibers in more detail. These illite fibers can easily be fanned out and readily transported by the fluid.

In the unaltered sandstone sample, agglomerates of illite predominantly consisted of parallel fibers with well-defined facets. However, in the samples that were altered with synthetic Gerolstein brine, the illite agglomerates exhibited less distinct fibers that were considerably more interwoven. XRPD studies conducted on the plugs obtained from the autoclave experiment using synthetic Gerolstein brine align with the findings from TEM studies, confirming the mobility of the illite fibers. In contrast to the unaltered sandstone, the altered edge of the Gerolstein plug exhibited a decrease in the illite content from 20% to 15%. The mobile illite fibers were primarily found in the filtered fluid instead. Conversely, the fluid filtrates obtained from the experiments conducted with brine from Bad Nauheim contained only a minimal number of illite fibers, indicating a very limited discharge of illite fibers and suggesting a low level of alteration.

Many researchers have concluded that fibrous authigenic illite significantly decreases permeability [67,184,201,224,225,227,229,339]. Authigenic illite fibers are usually found in

the pores and pore throats [67], where, with their high surface area, they have a higher microporosity than other clay minerals, meaning that a comparable solid volume will invade more of the pore volume [225]. Illite fibers tend to extend far into the pore space thus significantly increasing flow path tortuosity [73] and reducing the amount of flow paths in the initial pore system [68]. Their fragility makes them prone to tangling or breaking leading to a migration of illite fibers by fluid movement through the pores, which can cause a blockage of pore throats [72,74,75]. This has a negative effect on the productivity of oil field sandstone reservoirs [223,340,341] as well as geothermal plants [67,201]. Small amounts of only 2-3 wt% of illite can be sufficient to cause a decline in productivity [71]. The decrease in permeability can be up to 200-fold [224]. Illite migration can be especially troubling during stimulation, production or enhanced recovery in hydrocarbon reservoirs [74]. Thus, the growth of fibrous illite in the pore space may destroy an otherwise promising sandstone reservoir [229].

6.2. Labradorite

The structure solution of Labradorite with its incommensurate crystal structure is a challenging task for both X-ray and electron diffraction but allows for a direct comparison of the two approaches. To compare the properties of labradorite with the findings of Miúra et al. [268], it was necessary to take into account the thickness of a lamellae pair. By using equation (56), a total thickness of 193(2) nm yields a wavelength of 3.105 * 193(2) nm - 2.1178 nm = 597(6) nm. This wavelength indicates a yellow labradorescence color, which is consistent with the observed color. Equation (57) suggests that this corresponds to an An content of 0.09 * 193(2) + 36.083 mol% = 53.45(18) mol%, which aligns well with the measured An content of approximately 53.4%. Furthermore, the measured Or content of 5.1 mol% is in agreement with the statement made by Nissen et al. [86] that all labradorites exhibiting schiller typically have an Or content of at least 2 mol%.

The labradorite lamellae exhibit a tilt of around 11° with respect to the *b*-axis. While most of the lamellae studied in literature thus far have been found to be tilted at approximately 14° to the *b*-axis [262,266], other angles ranging from 9 to 21° have also been observed [260]. Therefore, the orientation of these lamellae appears to be consistent with the typical positions.

In order to analyze the satellite reflections in the labradorite structure, it was necessary to double the *c*-axis. The modulation vector q was compared with the findings of Jin et al. [259] and the corresponding graphs can be seen in Figure 71. Since the graphs are based on the bulk anorthite content, 53% An was used for this labradorite sample, even though the modulation was refined on a single lamella with an anorthite content of 64%. The modulation was assumed to not change in each lamella but on a larger scale. All values of q were found to be within the expected range for a labradorite with approximately 53% An content and the length of the satellite vector was consistent at 3.23 nm. According to the nomenclature proposed by Jin et al. [259], this labradorite can be classified as an e_α-labradorite due to the modulation period of q, where e_α has a shorter period compared to e_β. Although the δl value falls more within the e_β range, slight inaccuracies in the measurement of the modulation vector can account for this discrepancy. In e_α all traces of the $C\bar{1}$ structure were removed by going through an intermediate stage. This could happen by forming lamellae in the Bøggild miscibility gap, which happens in extremely slow cooled plutonic rocks. Another way of losing the $C\bar{1}$ structure is by forming the $I\bar{1}$ anorthite structure before forming e-plagioclase. However, between An_{45} and An_{55} $I\bar{1}$ is not stable at any temperature, leaving lamellae formation as the only possibility to reach an e_α structure. A special form of e-plagioclase is the e_γ structure, which shows weak and diffuse

e-reflections leading to poorly defined modulation vectors. This is only preserved in quenched volcanic plagioclase [259].

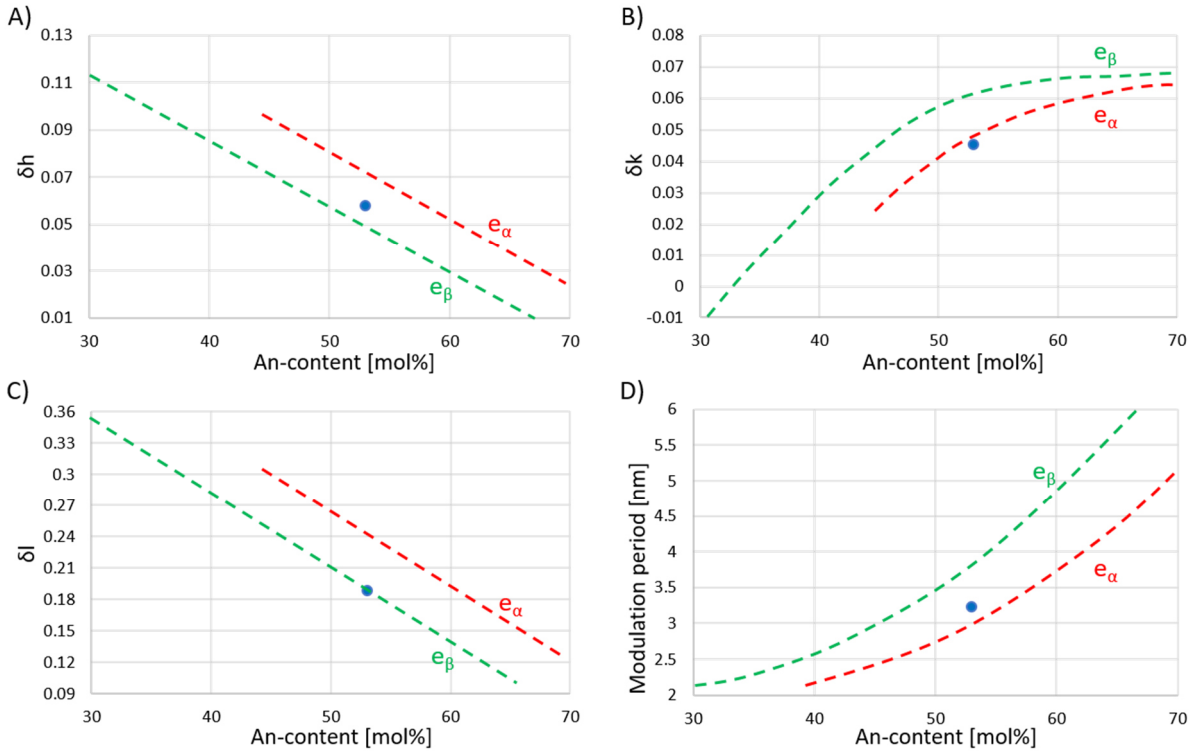

Figure 71: Coordinates a) δh, B) δk, C) δl and D) period of the modulation vector *q* plotted against the An content. The values of the labradorite studied here are displayed as a blue dot and agree with the ranges given for an An content of 53 mol%. The values predominantly follow the e_{α}-line (shown in red) instead of the e_{β}-line (shown in green). E_{α}- and e_{β}-line redrawn after Jin et al. [259].

A single Ca-rich lamella was utilized for the structure solution. The average An content of the Ca-rich lamellae was determined to be 60% with EDS, which is reasonably consistent with the refined An content of the structure solution of 64%. The occupancy of the tetrahedral positions was not solely based on the EDS results, as labradorite does not exhibit an equal Si/Al ratio in all tetrahedral positions. Instead, the tetrahedral occupancies were calculated considering the T-O bond lengths of individual tetrahedra. Although this method provided a guiding principle, the accuracy of the occupancy calculations was not as precise as in X-ray diffraction due to the approximate 0.5% error in bond lengths in the case of electron diffraction. Nonetheless, the occupancies calculated by using this method ($Al(T_{1o})$ = 54% (57%), $Al(T_{2o})$ = 36% (29%), $Al(T_{1m})$ = 31% (31%), $Al(T_{2m})$ = 38% (34%)) closely align with those defined in the X-ray structure of Jin and Xu [60] (results in brackets) used for crystal structure solution. Although there are some discrepancies in atomic positions and distances between the 3D ED data and X-ray diffraction data, these variations remain within reasonable limits with larger errors calculated for electron diffraction data.

The dynamical refinement of the incommensurately modulated labradorite structure yielded a less satisfactory fit compared to the kinematically refined model. This is primarily due to the fact that in the dynamical refinement, only satellite reflections from one data set could be considered, which reduced the completeness of the data. As a consequence, the modulation pattern was affected. The range of distances did not decrease compared to the kinematical refinement. Despite the overall poorer fit after the dynamical refinement, the wR(all) value was

13% better than in the kinematical refinement. However, this improvement is mainly attributed to the much better wR(all) value of the main reflections ($22.09\%_{dyn}$ vs. $43.92\%_{kin}$), whereas the wR(all) values of the satellite reflections were similar or worse compared to the kinematical refinement ($48.27\%_{dyn}$ and $61.49\%_{dyn}$ vs. $51.81\%_{kin}$ and $55.81\%_{kin}$, for first- and second-order satellites, respectively). The discrepancy in the dynamical refinement is manifested by unreasonable occupancies of the M position, fluctuating greatly between positive and negative values. As far as the positional modulation is concerned, it does not change significantly for the tetrahedra and oxygen atoms. The observed electron potential is still described reasonably well, but it is shifted slightly along the modulation direction. However, considerable differences are observed in the positional modulation of the M position (see Figure 72A)-C)). When compared to the kinematic refinement, which shows a good fit (see Figure 72D)-F)), the dynamical refinement exhibits extreme deviations from the electron potential, which is no longer fully described by the modulation. Compared to the structure solved using X-ray diffraction, the dynamically refined labradorite structure only shows minimal deviations in the T and O positions but significant deviations in the M position as well. While the deviations in the T and O positions are smaller than in the kinematical refinement (e.g. only 0.0072 Å for T_{1o}), the deviations in the M position are substantially higher due to its extensive modulation and the lack of data for refinement. As labradorite is a framework silicate, the values for the tetrahedral positions cannot vary as much. The M position has the most degrees of freedom and hence, the absence of data has the most significant impact on it.

Based on the characteristic internal structures, the following steps during the formation of the studied labradorite are proposed. The ordering schemes of Na-rich and Ca-rich plagioclase were incompatible, leading to spinodal decomposition, where the material separates into distinct Ca-rich and Na-rich lamellae. As the transformation progressed, coarsening took place, resulting in bifurcations within the lamellae, which further enhance the complexity of the labradorite's internal arrangement [269,270,342]. Despite these developments, the overall order within the crystal was not yet optimal. However, due to the relatively low temperature during this stage, the atoms were constrained in their movement and hence underwent only small, subtle fluctuations. These minute movements, however, gave rise to a periodic modulation, which manifested as satellite reflections.

In the case of the labradorite studies by Jin & Xu [60] a different formation pathway was observed. Although this mineral lacks lamellae, it still exhibits modulation within its structure. They proposed that in the beginning, the crystal experienced a rapid reduction in temperature, preventing spinodal composition and the subsequent formation of lamellae. Nevertheless, the temperature then remained at a level that was sufficiently high to induce slight atomic fluctuation, leading to the formation of a distinctive modulation pattern.

As the adjustment of cell parameters for each lamella is limited, introducing a modulation into the structure becomes essential to accommodate the different compositions. The modulation primarily arises from the displacement of M positions, where Ca undergoes more significant movement from its original position compared to Na [91]. However, the displacement of M positions also impacts other atoms in the unit cell, particularly leading to a pronounced modulation of oxygen atoms located near the M positions. The modulation in M position occupancy further influences the modulation of the tetrahedral occupancies [90]. The substitution of Na^+ by Ca^{2+} in the M1 site induces internal pressure due to the larger size of Ca^{2+} compared to Na^+. Within the labradorite framework, this pressure is counterbalanced by alterations in the T-O-T angles, causing a contraction of the so-called crankshaft chains [254].

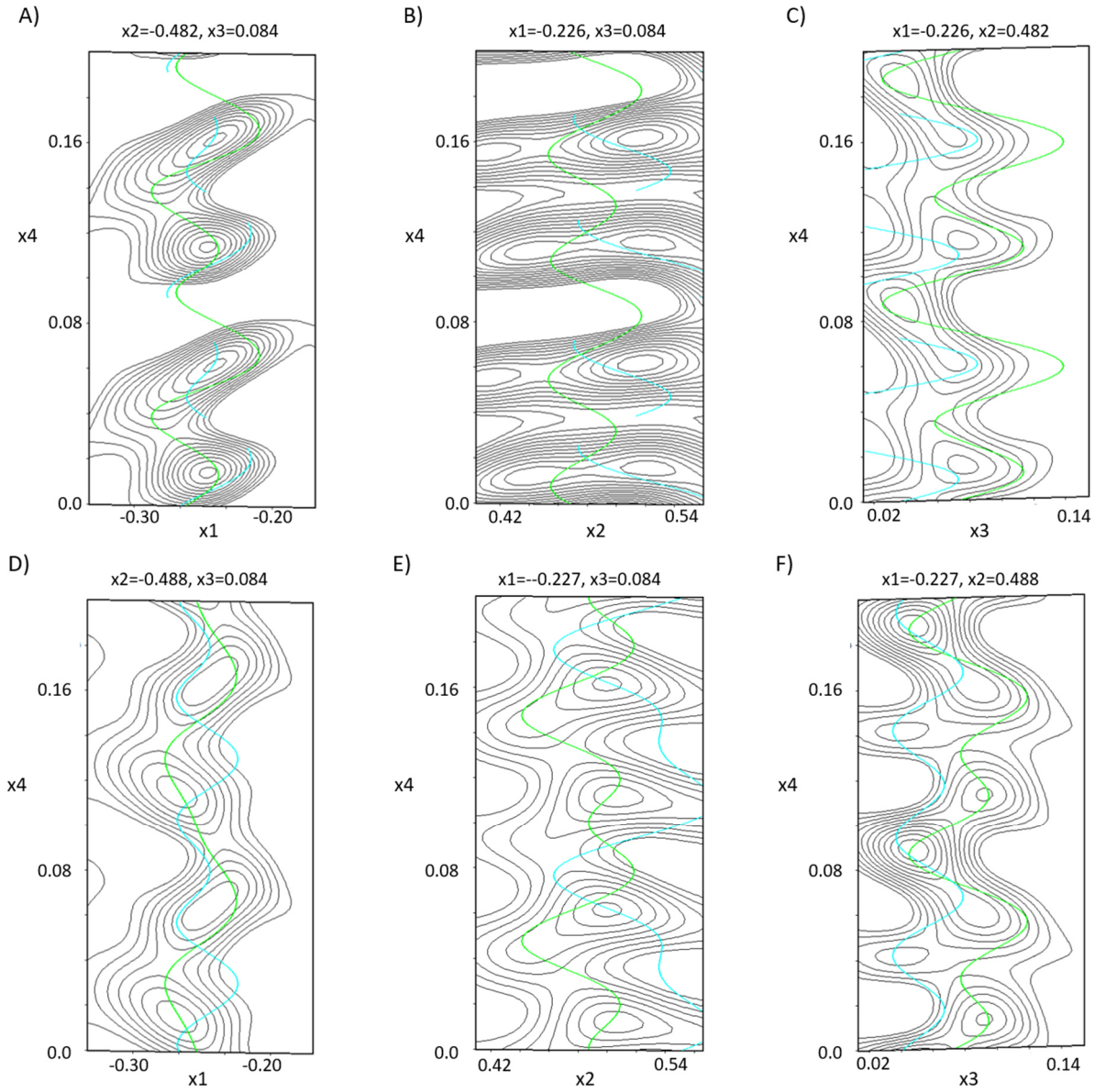

Figure 72: De Wolff's sections of the M positions of the incommensurately modulated structure of labradorite. A)-C) show the sections x1 vs. x4, s2 vs. x4 and x3 vs. x4 after the dynamical refinement, D)-F) show the respective sections after the kinematical refinement. M1 is displayed in green, M2 in cyan. The positional modulation after the kinematical refinement shows a better fit on the observed electron potential than after the dynamical refinement.

6.3. Eveslogite

The determination of the cell parameters was performed using two different programs, namely eADT and PETS2. Upon applying a correction factor of 0.952, in order to account for the effective camera length, the cell parameters derived by eADT and PETS2 closely resembled each other. The largest discrepancy was observed for the *b*-axis with a difference of around 1%.

Measuring a single crystalline area was only possible using 3D ED. The crystals displayed strong twinning on a nanoscale, making it challenging to obtain untwinned data sets. The twinned data sets could be used to resolve the twinning in eveslogite with eADT, which is represented by a two-fold rotation about the *a*-axis. The characterization and understanding of the twinning aided in correctly interpreting the crystal structure. The structure solution, however, was only successful on untwinned data sets. The wR(all) value of the refinement converged at a value of

28.54%, which is considered reasonable for a kinematical refinement of a structure of such considerable size. Interestingly, the determined structure of eveslogite revealed that it belongs to chain-, ribbon- and tube-silicates, sharing similarities with minerals such as yuksporite, charoite and denisovite. This finding contrasts the previous suggestion made by Men'shikov et al. [64], which proposed that eveslogite was a heterophyllosilicate of the astrophyllite-type. Instead, it confirms the theory of Chukanov et al. [61], stating that eveslogite is structurally similar to yuksporite.

Due to the limitations in the quality of the data set, the precise positions of the hydrogen atoms in the structure could not be determined directly. However, an indirect approach was employed by deriving their positions based on the characteristics of the oxygen bonds. This method aimed to achieve net neutrality within the structure. However, the final positioning proved to be challenging. This was primarily due to the fact that the EDS measurements showing the composition of the eveslogite crystals, and with that also the occupancies and hence the charge of various positions, varied significantly with each particle. This way, only a selection of possible oxygen atoms that may be protonated could be given, in order to achieve charge balance for a range of compositions. During the refinement process, the occupancies of the positions were refined freely, if they resulted in reasonable values. If certain occupancies did not yield reasonable values, the average values from the EDS measurements were applied. This approach ensured that the contents of every atom species fell within the range of the EDS measurements.

The significant variation in composition observed within the different eveslogite crystals could be one of the reasons why the simulation of the STEM HAADF image does not align perfectly with the experimental image. While the positions of the atoms agree well between the simulation and the STEM HAADF image, there are slight differences in contrast. For instance, the bright cross originating from the M-cube is clearly visible in the filtered STEM HAADF image but not in the simulation. This discrepancy may be attributed to the fact that the specific area where the HAADF image was captured contained a higher concentration of heavier elements (such as Nb^{5+}) occupying the respective M positions. The higher concentration would result in a brighter appearance compared to the simulations, which assume the average composition of the EDS measurements on the M positions.

In order to classify the complexity of the eveslogite structure, the topological information content was calculated with ToposPro, based on equation (60) in chapter 3.3.4. With the extremely complex topological information content per unit cell, eveslogite is situated in the top three of the most complex minerals up to date (see Table 19). Only the zeolite mineral paulingite [343] and fantappieite [344], a mineral with a 33-layer stacking sequence, both containing disorder, place higher.

Table 19: The most complex minerals measured by their topological information content. Calculations of paulingite and fantappieite by [303]. The topographic information content per atom I_G, topological information content per unit cell $I_{G,total}$, the normalized topological information content $I_{G,norm}$, as well as the number of atoms in the reduced unit cell v, are compared.

Mineral	Sum formula	v	I_G [bits/atom]	$I_{G,total}$ [bits/UC]	$I_{G,norm}$
Paulingite	$K_6Ca_{16}(Al_{38}Si_{130}O_{336})(H_2O)_{113}$	1278	5.295	6766.998	0.531
Fantappieite	$(Na_{82.5}Ca_{33}K_{16.5})(Al_{99}Si_{99}O_{396})(SO_4)_{33}(H_2O)_6$	821	7.245	5948.330	0.748
Eveslogite	$K_{17.5}(Ba,Sr)_8(Na,Ca)_{40}[(Ti,Nb,Fe,Mn)_{11}Si_{62}O_{179}(OH,F)_{12}(O,OH)_{13}](H_2O)$	690	8.430	5817.012	0.894

There are several minerals that are found in the same region as eveslogite and have comparable structures: charoite, denisovite and yuksporite. Charoite (see Table 4 in chapter 3.3.3) is a violet semi-precious stone that can only be found in the Murun massif, Yakutia, Russia [345]. There are four different polytypes of charoite, two of which have been extensively studied: charoite-90 and charoite-96. They crystallize in the space group $P2_1/m$ and their unit cell parameters are a = 31.96(6) Å, b = 19.64(4) Å, c = 7.09(1) Å, β = 90.0(1)° [100] and a = 32.11(6) Å, b = 19.77(4) Å, c = 7.23(1) Å, β = 95.85(9)° [99], respectively. The different polytypes are intergrown in nanocrystalline fibers. The structure consists of a double dreier chain $[Si_6O_{17}]^{10-}$ (see Figure 31B) and E) in chapter 3.3.3), a tubular loop-branched dreier triple chain $[Si_{12}O_{30}]^{12-}$ (see Figure 31A) and D) in chapter 3.3.3) and a tubular hybrid dreier quadruple chain $[Si_{17}O_{43}]^{18-}$ (see Figure 31C) and F) in chapter 3.3.3) [100]. They occur between ribbons of edge-sharing $(Ca,Na)O_6$ octahedra and extend parallel to [001]. The tubes are filled with K^+, Ba^{2+}, Sr^{2+}, Mn^{2+} and H_2O (see Figure 73A)). Because apical oxygen can bond the chains to the (Ca,Na) ribbons in two distinct ways, order-disorder layers with *P(2)mm* symmetry are formed which succeed each other along the *a*-axis. They are related by the operations $2_{½}$ or $2_{-½}$ parallel to *c*. By applying these translations two maximum degrees of order (MDO) are formed. Charoite-90 (MDO1) is created by an alternation of $2_{½}$ and $2_{-½}$; charoite-96 (MDO2) by an application of only $2_{-½}$. Additionally, the sequence $2_{½}$, $2_{½}$, $2_{-½}$, $2_{-½}$ leads to a doubling of the *a*-axis, which creates the polytype charoite-2a. If the sequence is disordered, charoite-d is formed which can be recognized by diffuse streaks along *h0l* for $l = 2n + 1$ [99]. The order-disorder effects can be seen as micro lamellae caused by stacking faults with a vector of ½ along [100] [100].

Denisovite (see Table 4 in chapter 3.3.3) is a needle-shaped mineral that, like eveslogite, can be found at Mt. Eveslogchorr, Khibiny massif, Kola Peninsula, Russia [346], and additionally at the Murun massif, Yakutia, Russia [347]. It crystallizes in the space group $P2/a$ and has the following unit cell parameters: a = 31.0964(8) Å, b = 19.5701(5) Å, c = 7.21526(12) Å, β = 96.6669(6)°. The fibers are 200-500 nm in size and show diffuse streaks along *a** for *hkl* with $l = 2n + 1$ [98]. Similar to charoite, the structure contains a dreier double chain $[Si_6O_{17}]^{10-}$ (see Figure 31B) in chapter 3.3.3) and a tubular loop-branched dreier triple chain $[Si_{12}O_{30}]^{12-}$ (see Figure 31A) in chapter 3.3.3), which expand along [001] [62], but no tubular hybrid dreier quadruple chain (see Figure 31C) in chapter 3.3.3). The tubes are occupied by K^+ and H_2O (see Figure 73B)). Like in charoite, the chains are connected by ribbons of edge sharing $(Ca,Na)O_6$ octahedra and the disorder along [100] is caused by the rigid dreier chains connecting to the different sides of the octahedral ribbons. The neighboring chains can be shifted by 1/4 [001]

or -1/4 [001] [101]. Unlike charoite, no ordered polytype has been observed because multiple stacking faults are already present in the range of a few unit cell repetitions. The disorder can be described by [100] nano-lamellar twinning or changing the space group to *P*2/*n* [98].

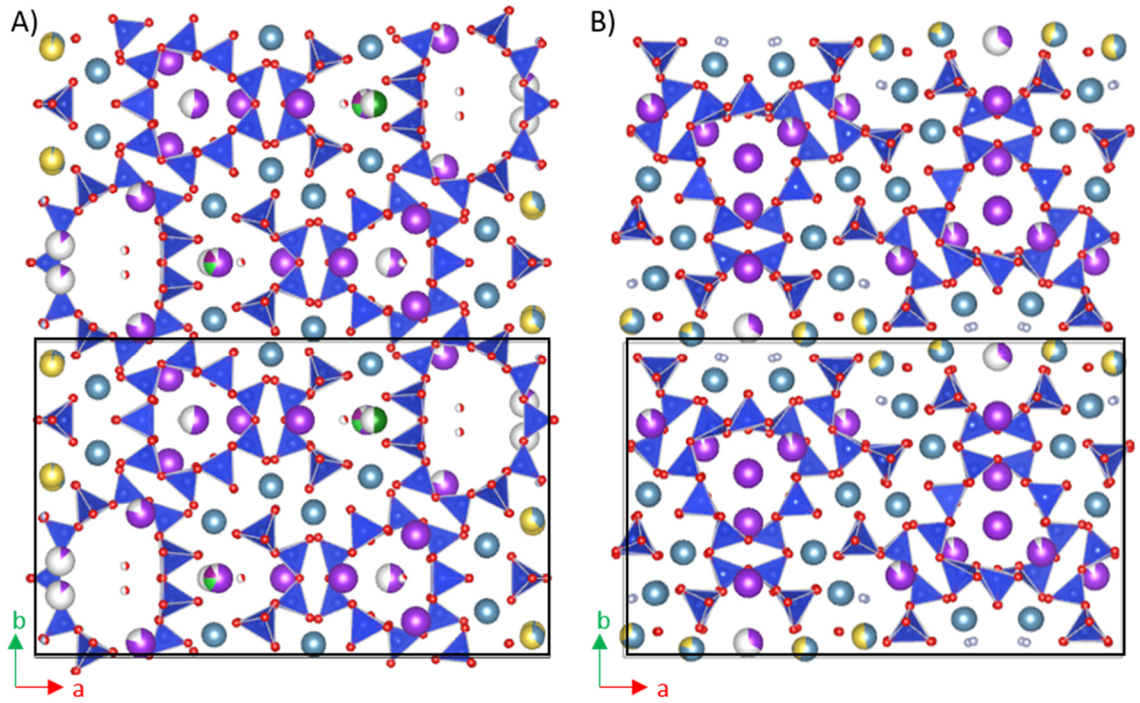

Figure 73: Crystal structures of A) charoite and B) denisovite. Si is displayed in dark blue, Ca in grey-blue, Na in yellow, K in purple, Sr in dark green Ba in light green, O in red, F in light grey.

Yuksporite is a rare monoclinic titanosilicate mineral that can be found near Mt. Yukspor, Khibiny massif, Kola Peninsula, Russia [348] and in the Murun massif, Yakutia, Russia [349]. It crystallizes in the space group $P2_1/m$ (see Table 4 in chapter 3.3.3) and grows as needle like crystals with the unit cell parameters being: a = 7.126(3) Å, b = 24.913(6) Å, c = 17.075(7) Å, β = 101.89°, V = 2966.4(17) Å^3. The structure was solved by Krivovichev et al. [97] with X-ray diffraction on a single 6*6*50 μm crystal. It has two distinct $[Si_2O_7]^{6-}$ dimers and two symmetrically distinct $[Si_6O_{17}]^{10-}$ ribbons (double dreier chain) [62]. The ribbons link to sheets of CaO_6 octahedra and $(CaO_6OH)^{11-}$, $(CaO_5(OH)_2)^{10-}$, $(NaO_5(OH)_2)^{11-}$ polyhedra, which run parallel to the *a*-*c* plane (see Figure 74A)). The ribbons are connected to the dimers through $(Ti,Nb)O_6$ octahedra creating porous $(Ti,Nb)_4(O,OH)_4[Si_6O_{17}]_2[Si_2O_7]_3$ rods, which extend along [100] and have an elliptical cross section of 16*19 Å (see Figure 74B) and C)) [97]. The rods contain channels, which are occupied by K^+ along [100] and Na^+, Sr^{2+}, Ba^{2+} or H_2O along [010] [62]. Eight membered rings with open diameters of 3.2 Å create internal pores [97]. Day and Hawthorne [62] suspected eveslogite to contain topologically identical $[Si_6O_{17}]^{10-}$ ribbons.

Out of these three minerals, eveslogite bears the most resemblance to yuksporite. One component of the eveslogite structure is the double-tube, which is similar to the nanorods found in yuksporite [97]. However, a notable difference was observed in eveslogite, where only half of the M-cubes are occupied by alternating square pyramidal $(Fe,Mn)O_4H_2O$ units or vacancies, which causes a doubling of periodicity along the tube axis (see Figure 75A)). In yuksporite, each M-cube is occupied by $(Fe,Mn)O_2(H_2O)_3$ with a reduced occupancy of 0.25 (see Figure 75B)). Consequently, the mean occupancy of M-cubes by pyramids is 0.25 for yuksporite and 0.5 for eveslogite. In eveslogite, each Fe^{3+} atom is coordinated by four oxygen atoms derived from two

oppositely oriented $[Si_2O_7]^{6-}$ groups and one apical H_2O molecule. Conversely, in yuksporite, Fe^{3+} is coordinated by two oxygen atoms from $[Si_2O_7]^{6-}$ groups and three H_2O molecules, two at the base and one apical. Assuming ideal symmetry for the double-tubes (no distinction between Fe^{3+} and Mn^{2+}, fully relaxed), they possess a local symmetry of *pmmm*. However, considering the Fe-O_{apical} vector, the symmetry is reduced to *p2mm* in eveslogite and *pm11* in yuksporite. The Fe-O_{apical} vector in eveslogite imparts its polarity on the structure, resulting in the polar space group $P2_1$ instead of $P2_1/m$ as observed in yuksporite.

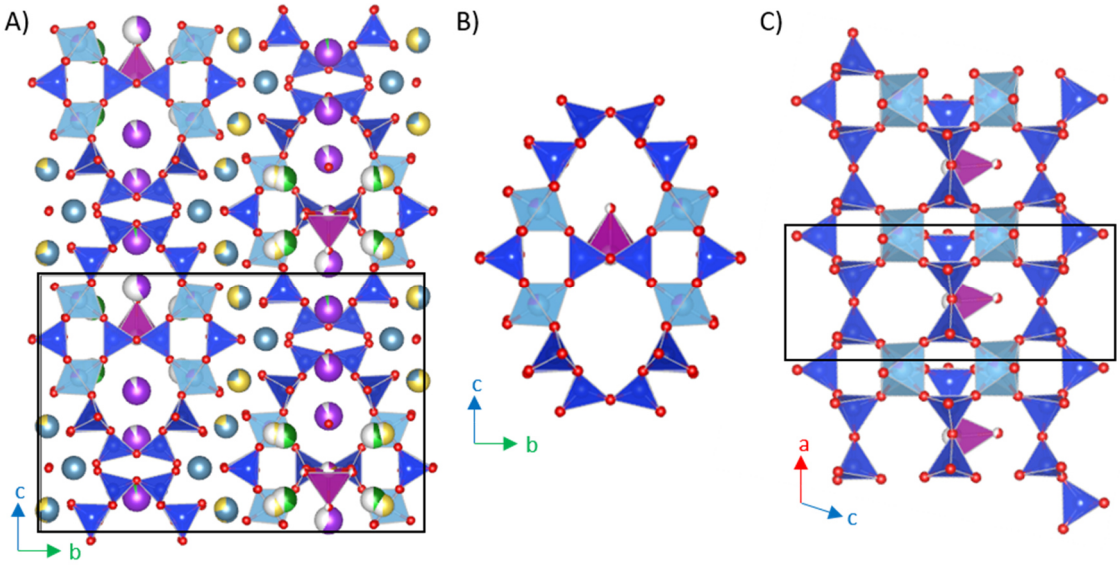

Figure 74: A) Atomic structure of yuksporite along [100]. The black box marks the unit cell. B) and C) show the silicate structure, which is made up of nanorods containing (Ti,Nb) as hetero-atoms and including a $(Fe,Mn)O_5$ square pyramid shown in magenta. The black box marks the geometric repeat unit. Si is shown in dark blue, Ca in blue-grey, Na in yellow, K in purple, Sr in dark green, Ba in light green, Ti in light blue, Nb in pink, Fe in brown, Mn in violet, O in red.

Some structurally related minerals such as charoite-96 [99] or denisovite [101] exhibit order-disorder characteristics, which are caused by shifts of the $[Si_2O_7]^{6-}$ groups along the $(Ca,Na)O_X$ ribbon. In the case of eveslogite, the $[Si_2O_7]^{6-}$ modules bridge the gap between two adjacent $(Ca,Na)O_X$ polyhedra on both sides of the ribbon. Additionally, the MO_6 octahedra are firmly fixed within the available space on both sides (see Figure 75C)). Consequently, a shift of a/4 (with a ~7 Å repeat unit) is unlikely. This stands in contrast with charoite and denisovite, where the absence of MO_6 octahedra in the tubes allows for easier displacement (see Figure 75D)).

With its tubular structure, eveslogite has the potential to be used as a template for new synthetic materials. The atoms in the tubes might be exchangeable without destroying the rest of the structure network. Additionally, compared to charoite or denisovite, the eveslogite structure cannot obtain disorder and the nanotwinning leaves the tubes intact. The combination of two kinds of tubular structures, which could increase the field of application is especially interesting. Applications similar to the zeolite ETS [15,350,351] are imaginable, which is the synthetic counterpart to the titanosilicate mineral zorite, found also at the Kola Peninsula in Russia [14]. ETS is produced on a multi-ton scale and is used for size-selective adsorption of molecules in their tubes [15,352]. Their pore size is tunable, allowing for the separation of gases with similar sizes, such as N_2/O_2 (3.6/3.5 Å) and CH_4/N_2 (3.8/3.6 Å) [13]. Eveslogite itself, however, is not suitable for direct application, as its strongly varying composition fails to provide a constant product quality. Additionally, with a sole source discovered, there are only limited resources

available and due to the largely unknown formation conditions, synthesis is currently not feasible.

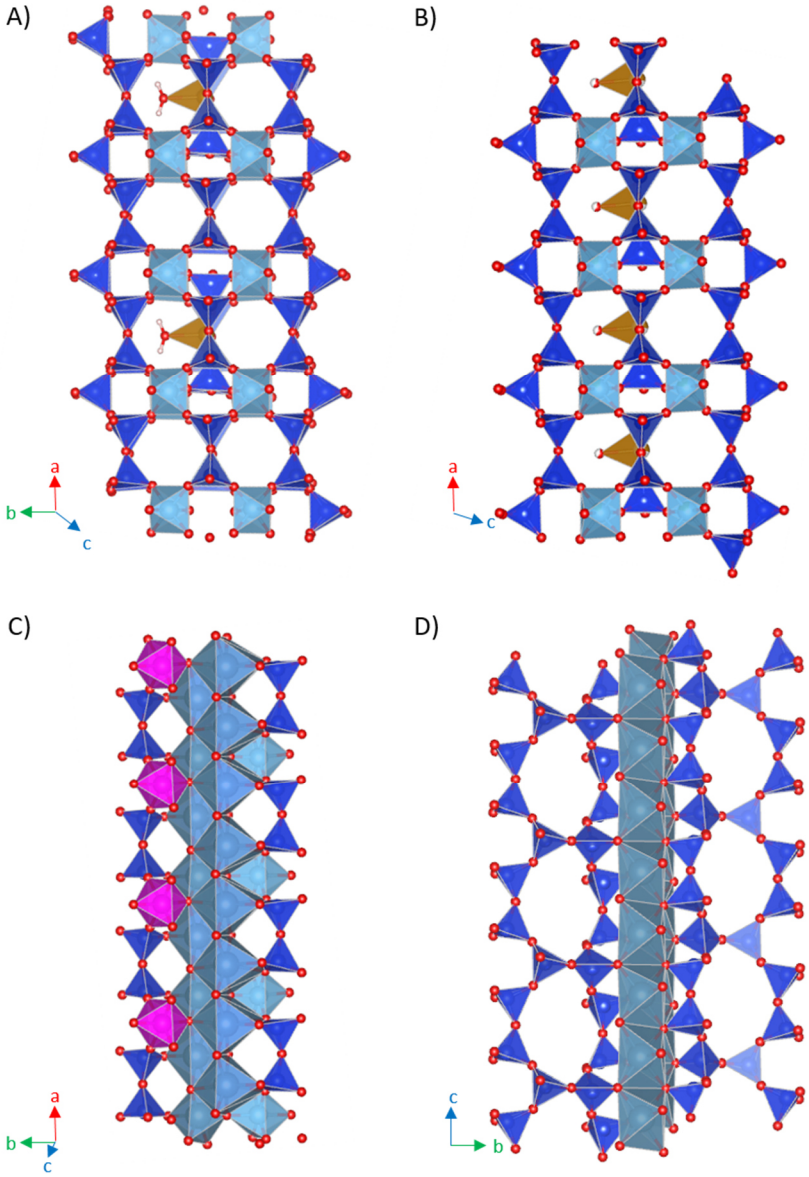

Figure 75: Eveslogite compared to similar structures. A) and B) comparison with yuksporite, C) and D) comparison with denisovite. A) The yuksporite-like tube of eveslogite is illustrated along [329]. The $(Fe,Mn)O_4H_2O$ square pyramids can be observed in every other M-cube. B) The nanorod of yuksporite is presented along the *b*-axis. The square pyramid is visible in each M-cube along the *a*-axis. C) A part of the eveslogite structure depicting the $(Ca,Na)O_X$ ribbon in-between the $[Si_2O_7]^{6-}$ groups, the $(Ti,Nb)O_6$ octahedra and the MO_6 octahedra of the charoite-like tube and the yuksporite-like tube, respectively. The heterocations cause the $(Ca,Na)O_X$ ribbon to be fixed in place. D) A section of the denisovite structure comparable to the one of eveslogite in C). In this case, the absence of heterocations results in a ¼ shift of $[Si_2O_7]^{6-}$ groups along the *c*-axis, leading to disorder in the structure.

6.4. Methodology

Sample pereparation

During the preparation of the materials in this study, several issues arose. In the case of illite, only a small amount (<20%) was present in the sandstone. The fluid filtrates contained even less illite, as aragonite and calcite constituted the majority of the flushed-out particles in this

case. Fortunately, the fibrous morphology of illite made it easy to identify in the TEM. The only mineral with a similar morphology was aragonite, but it formed fibers on a much larger scale, allowing it to be clearly distinguished from illite. This saved a considerable amount of time, EDS measurements and hence, beam exposure.

With labradorite and eveslogite powder samples, the main issue was twinning, which was not readily apparent in the crystals. To address this, ion-milled samples were prepared for labradorite. The preparation process was complex, requiring the identification of the correct orientations and precise further processing. The thinnest areas on the ion-milled samples were often rolled up at the hem, which made measuring on these sections impossible. Moreover, the samples were frequently uneven due to the presence of numerous natural inclusions and twins, which acted as preferred thinning sites. Consequently, only a few suitable positions were available for accurate measurements. Since the composition and width of the lamellae varied across the sample, all measurements had to be conducted within a small and consistent region. Thus, selecting areas that were thin enough to yield good diffraction data with minimal dynamic effects but also contained regions suitable for EDS measurements was crucial. Moreover, the chosen area had to be single-crystalline and free from twinning boundaries or impurities. To maximize the availability of such regions, the samples were carefully thinned to minimize the rolling effect of the thin areas. Additionally, an orientation was chosen where both twinning direction and lamellae were perpendicular to the electron beam, allowing for measurements to be performed on a single lamella while avoiding twins.

Data acquisition

To examine the illite fibers, Fast-ADT data sets were recorded using different tilt step sizes, specifically 1°, 0.2° and 0.1°. The 1° tilt steps, combined with a precession angle of 1°, proved sufficient for solving the structure of unaltered illite by providing a satisfactory resolution of the three-dimensional reciprocal space. However, when characterizing the diffuse streaks, the 1° tilt steps did not provide enough information, particularly in areas further away from the zero beam where gaps were more prevalent. In these cases, data sets with 0.2° or 0.1° tilt steps were utilized. Precession was not applied in order to avoid integrating the diffuse scattering. This method enabled a higher resolution and facilitated a comparison with simulated diffraction patterns. While decreasing the tilt step size enhanced the resolution of the three-dimensional reciprocal space and potentially lead to higher-quality data sets, a standard method of using 1° tilt steps with additionally applied electron beam precession was maintained for general structure determination. This decision was made because the increased time required for smaller tilt steps did not significantly outweigh the improvement in data quality. To achieve time-saving benefits and improve the signal to noise ratio, the use of a direct detection camera is recommended.

The Fast-ADT data sets of labradorite were recorded in TEM (JEOL) and STEM (FEI) mode. General analysis of the three-dimensional reciprocal space could be performed with both kinds of data sets but successful structure solution of labradorite was achieved only with Fast-ADT data sets acquired using STEM mode. The primary reason for this is that STEM HAADF imaging allows for clear element contrast. Consequently, even very small crystals can be observed, appearing bright in comparison to the carbon film in the background. On the other hand, TEM bright-field imaging, which relies on diffraction contrast, only reveals minimal contrast for small particles. This can make particles nearly invisible, especially considering the already low contrast caused by the low intensity of the beam due to the use of NBD. This can lead to the

loss of the crystal during the acquisition and overall increased measurement times. In the case of labradorite, the lamellae could also be observed in TEM bright-field imaging because they show diffraction contrast. However, the contrast changed while tilting the specimen, making it challenging to ensure that the beam remains on a specific lamella throughout the measurement. In contrast, STEM mode imaging allowed for consistent observation of a single lamellae during the entire measurement due to the constant element contrast, even during specimen tilting. Additionally, the JEOL microscope that was used had a less exact goniometer. This led to larger errors in the lattice parameters and variation in the tilt steps. Thus, data analysis with PETS2 was not as successful as with the data from the FEI microscope. Issues arose especially during the optimization of the frame geometry where in case of the JEOL data, tilt steps were often severely over- or underestimated. This made it necessary to manually check the fit of each frame after the optimization. For less complex structures, the effect of these issues was not as significant, so that the structure could still be analyzed (e.g. illite). For complicated structures, like labradorite and eveslogite, however, data sets from FEI TEM were preferable since the data extraction with PETS2 ran much smoother with less errors.

Even the smallest particles in the eveslogite powder sample were twinned, making acquiring untwinned data extremely challenging. In the FIB sections, twinning was easier to identify, but there were very limited measurement positions available because of the small size of the sample. When tilting the crystal, it was extremely difficult to maintain the same position, as the twinning did not produce any element contrast for the HAADF STEM mode. The diffraction contrast, which was partially present, changed or disappeared upon tilting. As a result, single-crystal data sets could not be obtained in this case either. As a potential solution, strongly scattering particles (e.g. gold particles, as used for tomography of biological samples) could be added to the sample for orientation during the tilting process. These particles have to be small enough not to obstruct important areas and need to be present in sufficient quantity so that a corresponding gold particle could be used for orientation of every region of interest. While this method is a promising approach, it still shows room for improvement.

Software for data comparison

During the comparison of the labradorite structure, it was noticed that the COMPSTRU program could not handle modulated structures or their average positions because it was not familiar with superspace groups. As a result, the modulations could only be compared qualitatively through image comparison. The average positions of the modulated structure had to be recalculated for the cell with half the *c*-axis and the space group $C\bar{1}$. Subsequently, they could be compared using the COMPSTRU program.

Modulated structures also posed a challenge when comparing cif files. Incommensurate structures could not be processed with various compare cif programs, which were required to be used before the publication of cif files. Moreover, these programs were not designed for structures from electron diffraction experiments, leading to many apparent errors that are however normal for 3D ED (e.g. a higher R value). This can cast doubt on the credibility of structure analysis by 3D ED, even though the structures proved to be valuable for the scientific community in many cases.

Data quality

As evident from the dynamic refinement of the labradorite structure, in most cases, having a good data set as a basis for refinements is more crucial than performing a dynamical refinement.

With a good data set, even a purely kinematical refinement can be highly informative, making a dynamical refinement less important. A good data set should possess as many of the following characteristics as possible: well-defined reflections, high completeness, small tilt steps, no preferred orientation and thin crystals. These factors help minimize dynamic effects. In a well-established kinematical model, the atomic positions and occupancies change only minimally during dynamical refinement, primarily resulting in an improved R value. However, as observed in the example of labradorite, a lower R value does not necessarily indicate an improved structure. Kinematical refinements with higher R values, as seen in eveslogite, can still represent crystallographically meaningful structures.

Due to its fibrous or lath-like morphology, illite crystals always exhibited a preferred orientation with the c-axis aligned along the electron beam direction. As a result, all crystals on the sample holder were in a similar orientation. Since a complete 180° tilt cannot be achieved during ADT data acquisition, a part of the reciprocal space always remained in the missing cone due to this preferred orientation. This can be a significant issue, especially for structures with low symmetry because attaining close to 100% completeness of the reciprocal space is practically impossible. The highest completeness achieved of the illite measurements after merging was 78%. Given that the basic structure of illite was relatively straightforward, it could still be solved with a lower completeness, even though the c-axis was not fully resolved in the data set. However, for more complex structures, attention should be paid to obtaining a higher completeness. To create the possibility of investigating flat crystals in different orientations, the particles can be embedded in epoxy resin and ultrathin sections can be cut using an ultramicrotome. Alternatively, the embedded powder can be polished and subsequently ion-milled similar to an ion-milled sample. However, this method requires additional effort and may subject the crystals to more stress.

7. Conclusion

The knowledge of both the average crystal structure as well as special crystallographic features resulting from defects like twinning, superstructure, modulation or disorder is mandatory for the comprehensive description and thus improved understanding of the physical properties of materials. Silicates as such already provide a vast amount of crystal structures, enlarged by a variety of defects, leading to highly complex structures. For this study, three complex silicates were selected for structural investigation. Eveslogite, a strongly twinned mineral, with a fully unknown crystal structure. Illite with different degrees of disorder, for which only a muscovite derived structure existed and labradorite exhibiting an incommensurate modulation combined with hierarchical twinning. The difficulties in crystal structure determination by conventional X-ray methods was in all three cases caused by a small crystal or domain size. To address this, 3D ED in the form of Fast-ADT [57] in combination with other electron microscopic methods was applied. The application of 3D ED has provided valuable insights into the structural details and characteristics of these minerals, leading to a deeper understanding of their behavior.

One of the notable contributions of this research is the direct determination of the crystal structure of illite fibers using 3D ED on single nano crystals. By accurately solving the $1M_{tv}$ polytype and identifying disorder within the illite fibers, this study has surpassed the limitations of conventional XRPD techniques [58]. The ability of 3D ED to avoid contamination from other clay minerals and illite polytypes has improved the accuracy and reliability of the results. The use of smaller tilt steps provided an improved resolution of the diffuse streaks, offering valuable insights into the disorder observed in illite fibers. A novel form of illite disorder was unveiled, differing from the previously documented $1M_d$ structure reported in literature. Previously, $1M_d$ illites were attributed to alteration products of feldspars in hydrothermal sandstones. However, this study revealed that a disordered structure can also arise from the alteration of illite fibers. The newly established model of the disordered illite structure can complement the existing model and enhance the accuracy of refinements based on XRPD data, providing a more comprehensive understanding of the illite structure.

The recent findings also provided insights into the arrangement and local aggregation of the illite fibers within the pores of the sandstone, highlighting their dependence on the potassium content of the fluid involved. It has been observed that a lower potassium content in the brine leads to increased migration and interweaving of illite fibers. This phenomenon can potentially cause pore clogging, leading to a reduction in rock permeability [184,224,225,227,229,339]. Considering the implications, it is evident that altered sandstones with illitic pore filling may not be ideal for long-term geothermal applications. However, if their use is necessary, it is recommended to employ brines with a high potassium content. Alternatively, appropriate measures should be taken to prevent the escape of K^+ ions from the illite interlayers, thereby averting destabilization of the illite structure. Furthermore, it is crucial to ensure that the fluid used has minimal to no content of substances that can react with the free OH groups of illite. This precaution is essential to prevent the accumulation of secondary phases leading to a broadening of the fibers and a subsequent increased clogging of the pores.

The structural features of labradorite including the complex hierarchical structure across multiple scales, ranging from the macroscopic level down to the atomic scale, were unraveled by a combination of several imaging and diffraction methods. In particular, 3D ED was applied to solve the average crystal structure as well as to describe the incommensurate modulation. By employing polarizing microscopy, labradorite samples were carefully selected and prepared as

ion-milled samples in three different orientations. These samples were then investigated using TEM and STEM imaging techniques, allowing for a direct correlation between the observed features in the polarization microscope and the imaging results. The analysis revealed the presence of various structural elements in labradorite, including twins, lamellae and additional domains with *e*-fringes. Albite and pericline twins were found to penetrate the labradorite crystal. Pericline twins, in particular, exhibited a slightly different orientation of the lamellae due to the difference in the direction of b^* compared to the matrix. This difference in orientation resulted in labradorescence at different glancing angles. The lamellae, responsible for the labradorescence, were identified as alternating Ca-rich and Na-rich based on STEM EDS linescans. The overall thickness of a lamellae pair, influenced by the Na/Ca ratio, matched well with the yellow color of labradorescence and the calculated An content aligned precisely with the measured An content. 3D ED allowed for the analysis of a single Ca-rich lamella, providing data sets suitable for ab initio crystal structure analysis of both the average crystal structure and its complex incommensurate modulation. The modulation arises from the system's inability to attain a Ca/Na-ordered state, resulting in alternating Ca-rich and Na-rich lamellae with slight chemical and structural differences. While the modulation occurs due to the incommensurate structure of labradorite, it does not have an impact on the labradorescence. The proposed formation pathway sheds light on the complex internal arrangement of labradorite. In the structure solution, 3D ED provided sharper and more precisely defined density maps than the results from X-ray diffraction due to the interaction of the electron beam with the atomic core. Additionally, the distribution along the modulation vector exhibited differences and was more clearly defined for 3D ED data compared to X-ray data. This discrepancy may be attributed to the restriction of the data to a single Ca-rich lamella. Despite these differences, the average structures derived from single crystal X-ray diffraction and 3D ED exhibited minimal deviations. These findings highlight the potential of 3D ED in solving and accurately refining complex crystal structures with low symmetry and a modulation vector with components along each main direction.

In a next step, the hitherto unknown crystal structure of eveslogite was envisaged. The application of 3D ED and STEM HAADF enabled the investigation of the structure of eveslogite at the nanoscale, overcoming limitations posed by its small crystal size and complex twinning. Traditional XRPD techniques were insufficient in this regard. Contrary to previous findings, new cell parameters were proposed with a revised cell volume and space group. The building blocks of the eveslogite structure consist of charoite-like tubes and yuksporite-like tubes extending along the *a*-axis. They are interconnected by ribbons of $(Ca,Na)O_X$ polyhedra. Contrary to yuksporite, only half of the M-cubes were occupied by alternating $(Fe,Mn)O_4H_2O$ square pyramids or vacancies, resulting in a doubling of the periodicity along the tube axis. Compared to charoite and denisovite, eveslogite did not display disorder because the presence of MO_6 octahedra in the yuksporite-like tubes hinders the displacement along the $(Ca,Na)O_X$ ribbon. The mineral eveslogite, which exhibits the largest crystal structure ever solved by 3D ED, could be classified as a chain-, ribbon- and tube-silicate instead of a heterophyllosilicate as proposed by Men'shikov et al. [64]. The twinned data sets helped resolve the twinning in eveslogite, which involves a two-fold rotation about *a*. The findings of this research shed light on the complex structure of eveslogite, emphasizing the importance of avoiding twinning and acquiring data from single nanometer-sized crystals using 3D ED. Polar crystals, such as eveslogite, have gained significant interest due to their potential for various practical applications. Their unique electrical properties make them valuable for various uses across multiple industries. The synthesis of materials similar to eveslogite, like zorite [14] and its

synthetic counterpart ETS-4 [352], has opened up new possibilities for harnessing their advantageous characteristics and incorporating them into technological advancements.

Overall, this thesis not only enhances the understanding of the characterized minerals but also showcases the power of advanced electron microscopy techniques in unraveling the intricate structures of minerals. It has successfully demonstrated the significance of 3D ED in the analysis of complex silicate structures. By using a rapid data acquisition with Fast-ADT combined with a low radiation dose and a high contrast in STEM imaging mode, nanometer-sized particles can be measured and structure alterations during the data set acquisition can be avoided. The exceptional resolution and capability to investigate nanoscale features make 3D ED a powerful tool in understanding the intricate details of crystal structures and their modifications. The findings presented in this research contribute to advancing the field of silicate mineralogy and provide a foundation for further studies on complex silicates. The utilization of 3D ED in this research area opens up new possibilities for exploring and characterizing a wide range of materials with complex structures.

In order to improve 3D ED data sets, direct detection cameras should be used. These detectors are already available and significantly reduce the acquisition time while improving the data set resolution [353–355]. Faster cameras are also required for the analysis of disorder phenomena. Through finer slicing of the reciprocal space, diffuse scattering can be displayed without gaps, leading to a better fit of the simulation to the experimental data. Additionally, cif file services like check cif have to be adapted to manage electron diffraction data and its quality similar to single crystal X-ray diffraction data. Furthermore, atomic structure factors and adjusted weighting schemes for reflections are needed and tracking routines can be improved. As a result, the quality of 3D ED structure solution will approach that of X-ray diffraction, even though the crystals are in the nanometer range.

In recent years, 3D ED has been increasingly applied by multiple research groups in scientific institutions around the world. However, the greatest endorsement for 3D ED is the emergence of the first dedicated electron diffractometers in the past few years, developed by Eldico and Rigaku [163,356]. This development allows for a much broader access to this initially highly specialized method, enabling its application to a wide range of materials in the near future.

Literature

[1] Kulasekara H and Seynulabdeen V 2019 A Review of Geothermal Energy for Future Power Generation *2019 5th International Conference on Advances in Electrical Engineering (ICAEE)* 2019 5th International Conference on Advances in Electrical Engineering (ICAEE) pp 223–8

[2] Stober I 2014 Hydrochemical properties of deep carbonate aquifers in the SW German Molasse basin *Geotherm. Energy* **2** 13

[3] Lüders V, Plessen B, Romer R L, Weise S M, Banks D A, Hoth P, Dulski P and Schettler G 2010 Chemistry and isotopic composition of Rotliegend and Upper Carboniferous formation waters from the North German Basin *Chem. Geol.* **276** 198–208

[4] Stober I and Bucher K 2015 Hydraulic and hydrochemical properties of deep sedimentary reservoirs of the Upper Rhine Graben, Europe *Geofluids* **15** 464–82

[5] Agemar T, Weber J and Schulz R 2014 Deep Geothermal Energy Production in Germany *Energies* **7** 4397–416

[6] Boch R, Leis A, Haslinger E, Goldbrunner J E, Mittermayr F, Fröschl H, Hippler D and Dietzel M 2017 Scale-fragment formation impairing geothermal energy production: interacting H2S corrosion and CaCO3 crystal growth *Geotherm. Energy* **5** 4

[7] Wanner C, Eichinger F, Jahrfeld T and Diamond L W 2017 Causes of abundant calcite scaling in geothermal wells in the Bavarian Molasse Basin, Southern Germany *Geothermics* **70** 324–38

[8] Griffiths L, Heap M J, Wang F, Daval D, Gilg H A, Baud P, Schmittbuhl J and Genter A 2016 Geothermal implications for fracture-filling hydrothermal precipitation *Geothermics* **64** 235–45

[9] Orywall P, Drüppel K, Kuhn D, Kohl T, Zimmermann M and Eiche E 2017 Flow-through experiments on the interaction of sandstone with Ba-rich fluids at geothermal conditions *Geotherm. Energy* **5** 20

[10] Regenspurg S, Feldbusch E, Byrne J, Deon F, Driba D L, Henninges J, Kappler A, Naumann R, Reinsch T and Schubert C 2015 Mineral precipitation during production of geothermal fluid from a Permian Rotliegend reservoir *Geothermics* **54** 122–35

[11] Schmidt R B, Bucher K, Drüppel K and Stober I 2017 Experimental interaction of hydrothermal Na-Cl solution with fracture surfaces of geothermal reservoir sandstone of the Upper Rhine Graben *Appl. Geochem.* **81** 36–52

[12] Tranter M, Wetzel M, De Lucia M and Kühn M 2021 Reactive transport model of kinetically controlled celestite to barite replacement *Advances in Geosciences* European Geosciences Union General Assembly 2021, EGU Division Energy, Resources & Environment (ERE) - EGU General Assembly 2021, Online, 19–30 April 2021 vol 56 pp 57–65

[13] Depmeier W 2009 Minerals as advanced materials *Cryst. Res. Technol.* **44** 1122–30

[14] Mer'kov A N, Bussen I V, Goiko E A, Kul'chitskaya E A, Men'shikov Y P and Nedorezova A P 1973 Raite and zorite - new minerals fromthe Lovozero Tundra *Zap. VMO* 54–62

[15] Kuznicki S M, Bell V A, Nair S, Hillhouse H W, Jacubinas R M, Braunbarth C M, Toby B H and Tsapatsis M 2001 A titanosilicate molecular sieve with adjustable pores for size-selective adsorption of molecules *Nature* **412** 720–4

[16] Behrens E A, Poojary D M and Clearfield A 1998 Syntheses, X-ray Powder Structures, and Preliminary Ion-Exchange Properties of Germanium-Substituted Titanosilicate Pharmacosiderites: HM3(AO)4(BO4)3·4H2O (M = K, Rb, Cs; A = Ti, Ge; B = Si, Ge) *Chem. Mater.* **10** 959–67

[17] Lamberti C 1999 Electron–hole reduced effective mass in monoatomic …–O–Ti–O–Ti–O–… quantum wires embedded in the siliceous crystalline matrix of ETS-10 *Microporous Mesoporous Mater.* **30** 155–63

[18] Rocha J and Anderson M W 2000 Microporous Titanosilicates and other Novel Mixed Octahedral-Tetrahedral Framework Oxides *Eur. J. Inorg. Chem.* **2000** 801–18

[19] Zecchina A, Xamena F X L i, Pazè C, Palomino G T, Bordiga S and Areán C O 2001 Alkyne polymerization on the titanosilicate molecular sieve ETS-10 *Phys. Chem. Chem. Phys.* **3** 1228–31

[20] Mittemeijer E J 2011 *Fundamentals of Materials Science: The Microstructure–Property Relationship Using Metals as Model Systems* (Berlin, Heidelberg: Springer)

[21] Smart L and Moore E 2004 *Solid State Chemistry* (London: CRC)

[22] Chao K-J, Lin J-C, Wang Y and Lee G H 1986 Single crystal structure refinement of TPA ZSM-5 zeolite *Zeolites* **6** 35–8

[23] Dinnebier R E and Billinge S J L 2008 *Powder Diffraction: Theory and Practice* (Royal Society of Chemistry)

[24] Corma A, Diaz-Cabanas M J, Jorda J L, Rey F, Sastre G and Strohmaier K G 2008 A Zeolitic Structure (ITQ-34) with Connected 9- and 10-Ring Channels Obtained with Phosphonium Cations as Structure Directing Agents *J. Am. Chem. Soc.* **130** 16482–3

[25] Schmidt M U, Hofmann D W M, Buchsbaum C and Metz H J 2006 Kristallstrukturen von Pigment Red 170 und Derivaten, bestimmt aus Röntgenpulverdiagrammen *Angew. Chem.* **118** 1335–40

[26] Goldstein J I, Newbury D E, Michael J R, Ritchie N W M, Scott J H J and Joy D C 2017 *Scanning Electron Microscopy and X-Ray Microanalysis* (Springer)

[27] Williams D B and Carter C B 2008 *Transmission electron microscopy: a textbook for materials science* (New York: Springer)

[28] Faruqi A R, Cattermole D M, Henderson R, Mikulec B and Raeburn C 2003 Evaluation of a hybrid pixel detector for electron microscopy *Ultramicroscopy* **94** 263–76

[29] Rose H 1990 Outline of a spherically corrected semiaplanatic medium-voltage transmission electron microscope *Optik* **85** 19–24

[30] Kisielowski C, Freitag B, Bischoff M, van Lin H, Lazar S, Knippels G, Tiemeijer P, van der Stam M, von Harrach S, Stekelenburg M, Haider M, Uhlemann S, Müller H, Hartel P, Kabius B, Miller D, Petrov I, Olson E, Donchev T, Kenik E, Lupini A, Bentley J, Pennycook S, Anderson I, Minor A, Schmid A, Duden T, Radmilovic V, Ramasse Q, Watanabe M, Erni R, Stach E, Denes P and Dahmen U 2008 Detection of Single Atoms and Buried Defects in Three Dimensions by Aberration-Corrected Electron Microscope with 0.5-Å Information Limit *Microsc. Microanal.* **14** 469–77

[31] Van Aert S, Verbeeck J, Erni R, Bals S, Luysberg M, Dyck D V and Tendeloo G V 2009 Quantitative atomic resolution mapping using high-angle annular dark field scanning transmission electron microscopy *Ultramicroscopy* **109** 1236–44

[32] Jinschek J R, Batenburg K J, Calderon H A, Kilaas R, Radmilovic V and Kisielowski C 2008 3-D reconstruction of the atomic positions in a simulated gold nanocrystal based on discrete tomography: Prospects of atomic resolution electron tomography *Ultramicroscopy* **108** 589–604

[33] Dorset D L, Roth W J and Gilmore C J 2005 Electron Crystallography of Zeolites-the MMW family as a test of direct 3D structure determination *Acta Crystallogr. Sect. A* **61** 516–27

[34] Kolb U, Mugnaioli E and Gorelik T 2011 Automated Electron Diffraction Tomography - a new tool for nano crystal structure analysis *Cryst. Res. Technol.* **46** 542–54

[35] Kolb U, Gorelik T and Otten M T 2008 Towards automated diffraction tomography. Part II—Cell parameter determination *Ultramicroscopy* **108** 763–72

[36] Kolb U, Gorelik T, Kübel C, Otten M T and Hubert D 2007 Towards Automated Diffraction Tomography: Part I - Data Acquisition *Ultramicroscopy* **107** 507–13

[37] Feyand M, Mugnaioli E, Vermoortele F, Bueken B, Dieterich J M, Reimer T, Kolb U, de Vos D and Stock N 2012 Automated Diffraction Tomography for the Structure Elucidation of Twinned, Sub-micrometer Crystals of a Highly Porous, Catalytically Active Bismuth Metal–Organic Framework *Angew. Chem. Int. Ed.* **51** 10373–6

[38] Jiang J, Jorda J L, Yu J, Baumes L A, Mugnaioli E, Diaz-Cabanas M J, Kolb U and Corma A 2011 Synthesis and Structure Determination of the Hierarchical Meso-Microporous Zeolite ITQ-43 *Science* **333** 1131–4

[39] Krysiak Y, Barton B, Marler B, Neder R B and Kolb U 2018 Ab initio structure determination and quantitative disorder analysis on nanoparticles by electron diffraction tomography *Acta Crystallogr. Sect. Found. Adv.* **74** 93–101

[40] Mugnaioli E, Andrusenko I, Schüler T, Loges N, Dinnebier R E, Panthöfer M, Tremel W and Kolb U 2012 Ab Initio Structure Determination of Vaterite by Automated Electron Diffraction *Angew. Chem. Int. Ed.* **51** 7041–5

[41] Mugnaioli E and Kolb U 2013 Applications of automated diffraction tomography (ADT) on nanocrystalline porous materials *Microporous Mesoporous Mater.* **166** 93–101

[42] Zhang D, Oleynikov P, Hovmoller S and Zou X 2010 Collecting 3D electron diffraction data by the rotation method *Z. Für Krist.* **225**

[43] Gemmi M, La Placa M G I, Galanis A S, Rauch E F and Nicolopoulos S 2015 Fast electron diffraction tomography *J. Appl. Crystallogr.* **48** 718–27

[44] Simancas J, Simancas R, Bereciartua P J, Jorda J L, Rey F, Corma A, Nicolopoulos S, Pratim Das P, Gemmi M and Mugnaioli E 2016 Ultrafast Electron Diffraction Tomography for Structure Determination of the New Zeolite ITQ-58 *J. Am. Chem. Soc.* **138** 10116–9

[45] Wang Y, Takki S, Cheung O, Xu H, Wan W, Öhrström L and Ken Inge A 2017 Elucidation of the elusive structure and formula of the active pharmaceutical ingredient bismuth subgallate by continuous rotation electron diffraction *Chem. Commun.* **53** 7018–21

[46] Gemmi M, Mugnaioli E, Gorelik T E, Kolb U, Palatinus L, Boullay P, Hovmöller S and Abrahams J P 2019 3D Electron Diffraction: The Nanocrystallography Revolution *ACS Cent. Sci.* **5** 1315–29

[47] Bowden D, Krysiak Y, Palatinus L, Tsivoulas D, Plana-Ruiz S, Sarakinou E, Kolb U, Stewart D and Preuss M 2018 A high-strength silicide phase in a stainless steel alloy designed for wear-resistant applications *Nat. Commun.* **9** 1374

[48] Hua W, Chen H, Yu Z-B, Zou X, Lin J and Sun J 2014 A Germanosilicate Structure with 11×11×12-Ring Channels Solved by Electron Crystallography *Angew. Chem. Int. Ed.* **53** 5868–71

[49] Mugnaioli E, Gorelik T and Kolb U 2009 “Ab initio” structure solution from electron diffraction data obtained by a combination of automated diffraction tomography and precession technique *Ultramicroscopy* **109** 758–65

[50] Palatinus L, Corrêa C A, Steciuk G, Jacob D, Roussel P, Boullay P, Klementová M, Gemmi M, Kopeček J, Domeneghetti M C, Cámara F and Petříček V 2015 Structure refinement using precession electron diffraction tomography and dynamical diffraction: tests on experimental data *Acta Crystallogr. Sect. B Struct. Sci. Cryst. Eng. Mater.* **71** 740–51

[51] Kolb U, Gorelik T E, Mugnaioli E and Stewart A 2010 Structural Characterization of Organics Using Manual and Automated Electron Diffraction *Polym. Rev.* **50** 385–409

[52] Cichocka M O, Ångström J, Wang B, Zou X and Smeets S 2018 High-throughput continuous rotation electron diffraction data acquisition via software automation *J. Appl. Crystallogr.* **51** 1652–61

[53] Nannenga B L, Shi D, Leslie G W and Gonen T 2014 High-resolution structure determination by continuous rotation data collection in MicroED *Nat. Methods* **11** 927–30

[54] Kolb U, Krysiak Y and Plana-Ruiz S 2019 Automated electron diffraction tomography - development and applications *Acta Crystallogr. Sect. B* **75** 463–74

[55] Palatinus L, Brázda P, Jelínek M, Hrdá J, Steciuk G and Klementová M 2019 Specifics of the data processing of precession electron diffraction tomography data and their implementation in the program *PETS2.0 Acta Crystallogr. Sect. B Struct. Sci. Cryst. Eng. Mater.* **75** 512–22

[56] Wan W, Sun J, Su J, Hovmöller S and Zou X 2013 Three-dimensional rotation electron diffraction: software RED for automated data collection and data processing *J. Appl. Crystallogr.* **46** 1863–73

[57] Plana-Ruiz S, Krysiak Y, Portillo J, Alig E, Estradé S, Peiró F and Kolb U 2020 Fast-ADT: A fast and automated electron diffraction tomography setup for structure determination and refinement *Ultramicroscopy* **211** 112951

[58] Gualtieri A F, Ferrari S, Leoni M, Grathoff G, Hugo R, Shatnawi M, Paglia G and Billinge S 2008 Structural characterization of the clay mineral illite-1M *J. Appl. Crystallogr.* **41** 402–15

[59] Drits V A, Zviagina B B, McCarty D K and Salyn A L 2010 Factors responsible for crystal-chemical variations in the solid solutions from illite to aluminoceladonite and from glauconite to celadonite *Am. Mineral.* **95** 348–61

[60] Jin S and Xu H 2017 Solved: The enigma of labradorite feldspar with incommensurately modulated structure *Am. Mineral.* **102** 21–32

[61] Chukanov N V, Dubovitsky V A, Vozchikova S A and Orlova S M 2008 Discrete and functional-geometric methods of infrared spectroscopy of minerals using reference samples *Geol. Ore Depos.* **50** 815–26

[62] Day M C and Hawthorne F C 2020 A structure hierarchy for silicate minerals: chain, ribbon, and tube silicates *Mineral. Mag.* **84** 165–244

[63] Ferraris G and Gula A 2005 Polysomatic Aspects of Microporous Minerals - Heterophyllosilicates, Palysepioles and Rhodesite-Related Structures *Rev. Mineral. Geochem.* **57** 69–104

[64] Men'shikov Y, Khomyakov A, Ferraris G, Belluso E, Gula A and Kulchitskaya E 2003 Eveslogite, (Ca,K,Na,Sr,Ba)24[(Ti,Nb,Fe,Mn)6(OH)6Si24O72](F,OH,Cl)7, a new mineral from the Khibina alkaline massif, Kola Peninsula, Russia *Zap Vseross Miner. Obshch* **132** 59–67

[65] Drits V A, McCarty D K and Zviagina B B 2006 Crystal-Chemical Factors Responsible for the Distribution of Octahedral Cations Over trans- and cis-Sites in Dioctahedral 2:1 Layer Silicates *Clays Clay Miner.* **54** 131–52

[66] Blaise T, Clauer N, Cathelineau M, Boiron M-C, Techer I and Boulvais P 2016 Reconstructing fluid-flow events in Lower-Triassic sandstones of the eastern Paris Basin by elemental tracing and isotopic dating of nanometric illite crystals *Geochim. Cosmochim. Acta* **176** 157–84

[67] Jacob A, Peltz M, Hale S, Enzmann F, Moravcova O, Warr L N, Grathoff G, Blum P and Kersten M 2021 Simulating permeability reduction by clay mineral nanopores in a tight sandstone by combining computer X-ray microtomography and focussed ion beam scanning electron microscopy imaging *Solid Earth* **12** 1–14

[68] Peltz M, Jacob A, Grathoff G H, Enzmann F, Kersten M and Warr L N 2022 A FIB-SEM Study of Illite Morphology in Aeolian Rotliegend Sandstones: Implications for Understanding the Petrophysical Properties of Reservoir Rocks *Clays Clay Miner.* **70** 84–105

[69] Wilson M D and Pittman E D 1977 Authigenic Clays in Sandstones: Recognition and Influence on Reservoir Properties and Paleoenvironmental Analysis *SEPM J. Sediment. Res.* **47** 3–31

[70] Heidsiek M, Butscher C, Blum P and Fischer C 2020 Small-scale diagenetic facies heterogeneity controls porosity and permeability pattern in reservoir sandstones *Environ. Earth Sci.* **79** 425

[71] Zaidi S R, Shen S, Al-Shehry A A and Mehta S 2010 Origin and Occurrence of Illite Clay Mineral in Unayzah Sandstone Reservoirs in Central Saudi Arabia *GEO 2010* GEO 2010 (Manama, Bahrain,: European Association of Geoscientists & Engineers)

[72] Darling T 2005 Production geology issues *Well Logging and Formation Evaluation* (Gulf Professional Publishing) pp 137–54

[73] Stalder P J 1973 Influence of Crystallographic Habit and Aggregate Structure of Authigenic Clay Minerals on Sandstone Permeability *Geol. En Mijnb.* **52** 217–20

[74] Güven N, Hower W F and Davies D K 1980 Nature of Authigenic Illites in Sandstone Reservoirs *J. Sediment. Petrol.* 761–6

[75] Wilson M J, Wilson L and Patey I 2014 The influence of individual clay minerals on formation damage of reservoir sandstones: a critical review with some new insights *Clay Miner.* **49** 147–64

[76] Peacor D R, Bauluz B, Dong H, Tillick D and Yan Y 2002 Transmission and Analytical Electron Microscopy Evidence for High Mg Contents of 1M Illite: Absence of 1M Polytypism in Normal Prograde Diagenetic Sequences of Pelitic Rocks *Clays Clay Miner.* **50** 757–65

[77] Grubb S M B, Peacor D R and Jiang W-T 1991 Transmission Electron Microscope Observations of Illite Polytypism *Clays Clay Miner.* **39** 540–50

[78] Collins D R and Catlow C R A 1992 Computer simulation of structures and cohesive properties of micas *Am. Mineral.* **77** 1172–81

[79] Smyth J R, Dyar M D, May H M, Bricker O P and Acker J G 1997 Crystal Structure Refinement and Mössbauer Spectroscopy of an Ordered, Triclinic Clinochlore *Clays Clay Miner.* **45** 544–50

[80] Neder R B, Burghammer M, Grasl TH, Schulz H, Bram A and Fiedler S 1999 Refinement of the Kaolinite Structure From Single-Crystal Synchrotron Data *Clays Clay Miner.* **47** 487–94

[81] Adams J M 1983 Hydrogen Atom Positions in Kaolinite by Neutron Profile Refinement *Clays Clay Miner.* **31** 352–6

[82] Bish D L 1993 Studies of clays and clay minerals using x-ray powder diffraction and the Rietveld method Clay Minerals Society meeting on computer applications in clay mineralogy (San Diego: Los Alamos National Lab., NM (United States))

[83] Bish D L and Von Dreele R B 1989 Rietveld Refinement of Non-Hydrogen Atomic Positions in Kaolinite *Clays Clay Miner.* **37** 289–96

[84] Okrusch M and Matthes S 2013 *Mineralogie: Eine Einführung in die spezielle Mineralogie, Petrologie und Lagerstättenkunde* (Berlin, Heidelberg: Springer)

[85] Olsen A 1977 Lattice parameter determination of exsolution structures in labradorite feldspars *Acta Crystallogr. Sect. A* **33** 706–12

[86] Nissen H U, Champness P E, Cliff G and Lorimer G W 1973 Chemical evidence for exsolution in a labradorite *Nat. Phys. Sci.* **245** 135–7

[87] Smith J V and Brown W L 1988 *Feldspar Minerals: 1 Crystal Structure. Physical, Chemical, and Microtextural Properties* (Berlin, Heidelberg: Springer)

[88] Putnis A 2001 *An Introduction to Mineral Sciences* (Cambridge: Cambridge University Press)

[89] Chao S H and Taylor W H 1940 Isomorphous replacement and superlattice structures in the plagioclase felspars *Proc. R. Soc. Lond. Ser. Math. Phys. Sci.* **176** 76–87

[90] Kitamura M and Morimoto N 1977 The superstructure of plagioclase feldspars. A modulated coherent structure of the e-plagioclase 14

[91] Xu H, Jin S and Noll B C 2016 Incommensurate density modulation in a Na-rich plagioclase feldspar: *Z* -contrast imaging and single-crystal X-ray diffraction study *Acta Crystallogr. Sect. B Struct. Sci. Cryst. Eng. Mater.* **72** 904–15

[92] Palatinus L, Klementová M, Dřínek V, Jarošová M and Petříček V 2011 An Incommensurately Modulated Structure of η'-Phase of $Cu_{3+x}Si$ Determined by Quantitative Electron Diffraction Tomography *Inorg. Chem.* **50** 3743–51

[93] Boullay P, Palatinus L and Barrier N 2013 Precession Electron Diffraction Tomography for Solving Complex Modulated Structures: the Case of $Bi_5Nb_3O_{15}$ *Inorg. Chem.* **52** 6127–35

[94] Lanza A E, Gemmi M, Bindi L, Mugnaioli E and Paar W H 2019 Daliranite, $PbHgAs_2S_5$: determination of the incommensurately modulated structure and revision of the chemical formula *Acta Crystallogr. Sect. B Struct. Sci. Cryst. Eng. Mater.* **75** 711–6

[95] Plana-Ruiz S 2020 *Development & Implementation of an Electron Diffraction Approach for Crystal Structure Analysis*

[96] Steciuk G, Boullay P, Pautrat A, Barrier N, Caignaert V and Palatinus L 2016 Unusual Relaxor Ferroelectric Behavior in Stairlike Aurivillius Phases *Inorg. Chem.* **55** 8881–91

[97] Krivovichev S V, Yakovenchuk V N, Armbruster T, Döbelin N, Pattison P, Weber H-P and Depmeier W 2004 Porous titanosilicate nanorods in the structure of yuksporite, $(Sr,Ba)_2K_4(Ca,Na)_{14}(□,Mn,Fe)\{(Ti,Nb)_4(O,OH)_4[Si_6O_{17}]_2[Si_2O_7]_3\}(H_2O,OH)_n$, resolved using synchrotron radiation *Am. Mineral.* **89** 1561–5

[98] Mugnaioli E, Rozhdestvenskaya I, Czank M, Depmeier W, Schowalter M, Rosenauer A and Schmidt M U 2016 Structure, polytypism and disorder of denisovite, K14Ca42Na6Si60O162F16(OH)4*2H2O, obtained by a combination of (S)TEM imaging, electron diffraction tomography and X-ray powder diffraction EMC (Rimini)

[99] Rozhdestvenskaya I, Mugnaioli E, Czank M, Depmeier W, Kolb U and Merlino S 2011 Essential features of the polytypic charoite-96 structure compared to charoite-90 *Mineral. Mag.* **75** 2833–46

[100] Rozhdestvenskaya I, Mugnaioli E, Czank M, Depmeier W, Kolb U, Reinholdt A and Weirich T 2010 The structure of charoite, $(K,Sr,Ba,Mn)_{15-16}(Ca,Na)_{32}[(Si_{70}(O,OH)_{180})](OH,F)_{4.0}.n\ H_2O$, solved by conventional and automated electron diffraction *Mineral. Mag.* **74** 159–77

[101] Rozhdestvenskaya I V, Mugnaioli E, Schowalter M, Schmidt M U, Czank M, Depmeier W and Rosenauer A 2017 The structure of denisovite, a fibrous nanocrystalline polytypic disordered `very complex' silicate, studied by a synergistic multi-disciplinary approach employing methods of electron crystallography and X-ray powder diffraction *IUCrJ* **4** 223–42

[102] Sheldrick G M 2015 A short history of SHELX *Acta Crystallogr. Sect. A* 3–8

[103] Müller U 2011 *Symmetriebeziehungen zwischen verwandten Kristallstrukturen: Anwendungen der kristallographischen Gruppentheorie in der Kristallchemie* (Wiesbaden: Vieweg+Teubner)

[104] Kleber W, Bautsch H-J, Bohm J and Klimm D 2010 *Einführung in die Kristallographie* (Oldenbourg)

[105] Massa W 2007 *Kristallstrukturbestimmung* (Wiesbaden: Teubner)

[106] Halliday D, Resnick R and Walker J 2013 *Fundamentals of Physics* (John Wiley & Sons)

[107] Dutta A K 1953 Electrical Conductivity of Single Crystals of Graphite *Phys. Rev.* **90** 187–92

[108] Aronson J R and Emslie A G 1980 Effective optical constants of anisotropic materials *Appl. Opt.* **19** 4128–9

[109] Grimaldi F M 1665 *Physico-Mathesis de lumine, coloribus, et iride, aliisque adnexis libri duo* (Bologna)

[110] von Laue M 1913 Die Interferenzerscheinungen an Röntgenstrahlen, hervorgerufen durch das Raumgitter der Kristalle *Hayez Impr. Académie R. Belg.*

[111] Bragg W H and Bragg W L 1913 The reflection of X-rays by crystals *Proc. R. Soc. Lond. Ser. Contain. Pap. Math. Phys. Character* **88** 428–38

[112] Hunklinger S 2014 *Festkörperphysik* (Boston: De Gruyter Oldenbourg, Berlin)

[113] Ewald P P 1913 Zur Begründung der Kristalloptik *Ann. Phys.* **345** 817–43

[114] Spieß L, Teichert G, Schwarzer R, Behnken H and Genzel C 2018 *Moderne Röntgenbeugung: Röntgendiffraktometrie für Materialwissenschaftler, Physiker und Chemiker* (Wiesbaden: Springer Spektrum)

[115] Zou X, Hovmoller S and Oleynikov P 2011 *Electron Crystallography: Electron Microscopy and Electron Diffraction* (Oxford, New York: Oxford University Press)

[116] Prince E 2004 *International Tables for Crystallography, Volume C: Mathematical, Physical and Chemical Tables* (Springer: Dodrecht)

[117] Broglie L de 1924 XXXV. A tentative theory of light quanta *Lond. Edinb. Dublin Philos. Mag. J. Sci.* **47** 446–58

[118] Neder R B and Proffen T 2008 *Diffuse Scattering and Defect Structure Simulations: A Cook Book Using the Program DISCUS* (Oxford, New York: Oxford University Press)

[119] Krysiak Y 2018 *Unordnung im Nanobereich: Schichtstrukturen unter dem Elektronenmikroskop* (Mainz: Johanes Gutenberg-Universität Mainz)

[120] Larson L A, Williams J M and Current M I 2011 Ion Implantation for Semiconductor Doping and Materials Modification *Rev. Accel. Sci. Technol.* **04** 11–40

[121] Jagozinski H 1987 Diffuse X-rays scattering from crystals *Prog. Cryst. Growth Charact.* **14** 47–102

[122] Welberry T R 1985 Diffuse X-ray scattering and models of disorder *Rep. Prog. Phys.* **48** 1543

[123] Gehlen P C and Cohen J B 1965 Computer simulation of the structure associated with locas order on alloys *Phys. Rev. A* **139** 844–55

[124] Proffen T and Neder R B 1997 DISCUS: a program for diffuse scattering and defect-structure simulation *J. Appl. Crystallogr.* **30** 171–5

[125] Brindley G W 1980 Order–Disorder in Clay Mineral Structures *Crystal Structures of Clay Minerals and their X-Ray Identification* vol 5, ed G W Brindley and G Brown (Mineralogical Society of Great Britain and Ireland) p 0

[126] Wones D R and Eugster H P 1965 Stability of biotite: experiment, theory, and application1 *Am. Mineral.* **50** 1228–72

[127] Spinnler G E, Self P G, Iijima S and Buseck P R 1984 Stacking disorder in clinochlore chlorite *Am. Mineral.* **69** 252–63

[128] Viani A, Gualtieri A F and Artioli G 2002 The nature of disorder in montmorillonite by simulation of X-ray powder patterns *Am. Mineral.* **87** 966–75

[129] van Smaalen S 2007 *Incommensurate Crystallography* (Oxford, New York: Oxford University Press)

[130] Shechtman D, Blech I, Gratias D and Cahn J W 1984 Metallic phase with long-range orientational order and no translaional symmetry *Phys. Rev. Lett.* **53** 1951–3

[131] Preston G D 1938 The diffraction of X-rays by an age-hardening alloy of aluminium and copper. The structure of an intermediate phase *Lond. Edinb. Dublin Philos. Mag. J. Sci.* **26** 855–71

[132] de Wolff P M 1974 The pseudo-symmetry of modulated crystal systems *Acta Crystallogr. Sect. A* **30** 777–85

[133] van Smaalen S 2009 An elementary introduction to superspace crystallography *Z. Für Krist. - Cryst. Mater.* **219** 681–91

[134] Marmeggi J C, Lander G H, van Smaalen S, Brückel T and Zeyen C M E 1990 Neutron-diffraction study of the charge-density wave in alpha-uranium *Phys. Rev. B* **42** 9365–76

[135] Janner A and Janssen T 1977 Symmetry of periodically distorted crystals *Phys. Rev. B* **15** 643–58

[136] van Aalst W, den Holander J, Peterse W J a. M and de Wolff P M 1976 The modulated structure of gamma-Na2CO3 in a harmonic approximation *Acta Crystallogr. Sect. B* **32** 47–58

[137] Petříček V, Eigner V, Dušek M and Cejchan A 2016 Discontinuous modulation functions and their application for analysis of modulated structures with the computing system JANA2006 *Z. Für Krist. - Cryst. Mater.* **231** 301–12

[138] Vernon-Parry K D 2000 Scanning electron microscopy: an introduction *III-Vs Rev.* **13** 40–4

[139] Deepak F L, Mayoral A and Arenal R 2015 *Advanced Transmission Electron Microscopy: Applications to Nanomaterials* (Cham: Springer International Publishing)

[140] Thomas J and Gemming T 2013 *Analytische Transmissionselektronenmikroskopie* (Vienna: Springer Vienna)

[141] Champness P E 1987 Cpnvergent Beam Electron Diffraction *Mineral. Mag.* 33–48

[142] Vincent R and Midgley P A 1994 Double conical beam-rocking system for measurement of integrated electron diffraction intensities *Ultramicroscopy* **53** 271–82

[143] Eggeman A S, White T A and Midgley P A 2010 Is precession electron diffraction kinematical? Part II: A practical method to determine the optimum precession angle *Ultramicroscopy* **110** 771–7

[144] White T A, Eggeman A S and Midgley P A 2010 Is precession electron diffraction kinematical? Part I: Phase scrambling, Multislice simulations *Ultramicroscopy* **110** 763–70

[145] Kolb U, Shankland K, Meshi L, Avilov A and David W I F 2012 *Uniting Electron Crystallography and Powder Diffraction* (Dordrecht: Springer Netherlands)

[146] Fultz B and Howe J 2013 *Transmission Electron Microscopy and Diffractometry of Materials* (Berlin, Heidelberg: Springer Berlin Heidelberg)

[147] Zuo J, Gao M, Tao J, Li B, Twesten R and Petrov I 2004 Coherent Nano-Area Diffraction *Microsc. Res. Tech.* **64** 347–55

[148] Zuo J M and Spence J C H 2017 *Advanced Transmission Electron Microscopy* (New York, NY: Springer)

[149] Biskupek J, Leschner J, Walther P and Kaiser U 2010 Optimization of STEM tomography acquisition - A comparision of convergentbeam and parallel beam STEM tomography *Ultramicroscopy* **110** 1231–7

[150] Ganesh K J, Kawasaki M, Zhou J P and Ferreira P J 2010 D-STEM: A parallel electron diffraction technique applied to nanomaterials *Microsc. Microanal.* **16** 614–21

[151] Pennycook S J and Nellist P D 2011 *Scanning Transmission Electron Microscopy: Imaging and Analysis* (Springer Science & Business Media)

[152] Erni R, Rossell M D, Kisielowski C and Dahmen U 2009 Atomic-resolution imaging with a sub-50-pm electron probe *Phys. Rev. Lett.* **102** 096101

[153] Pinsker Z G, Spink A and Feigl E 1953 *Electron Diffraction* (London: Butterworths)

[154] Vainshtein B K 1956 Kinematic theory of intensities in electron diffraction patterns. Part 2. Patterns from textures and polycrystalline aggregates *Soviel Phys. - Crystallogr.* **1** 117–22

[155] Dorset D L and Hauptman H A 1976 Direct phase determination for quasi-kinematical electron diffraction intensity data from organic microcrystals *Ultramicroscopy* **1** 195–201

[156] Voigt-Martin, Yan D H, Yakimansky A, Schollmeyer D, Gilmore C J and Bricogne G 1995 Structure determination by electron crystallography using both maximum entropy and simulation approaches *Acta Crystallogr. Sect. A* **51** 849–68

[157] Weirich T E, Ramlau R, Simon A, Hovmoller S and Zou X 1996 A crystal structure determined with 0.02 A accuracy by electron microscopy *Nature* **382** 144–6

[158] Gemmi M, Klein H, Rageau A, Strobel P and Le Cras F 2010 Structure solution of the new titanate Li4Ti8Ni3O21 using precession electron diffraction *Acta Crystallogr. Sect. B* **66** 60–8

[159] Weirich T E, Portillo J, Cox G, Hibst H and Nicolopoulos S 2006 Ab initio determination of the framework structure of the heavy-metal oxide CsXNb2.54W2.46O14 from 100kV precession electron diffraction data *Ultramicroscopy* **106** 164–75

[160] Kolb U and Matveeva G N 2009 Electron crystallography on polymorphic organics *Z. Für Krist. - Cryst. Mater.* **218** 259–68

[161] Jiang J 2011 Synthesis and structure determination of the hierarchical meso- microporous zeolite ITQ-43 *Science* **333** 1131–4

[162] Mugnaioli E and Kolb U 2015 Structure Characterization of nanocrystalline porous materials by tomographic electron diffraction *Z. Für Krist. - Cryst. Mater.* **230** 271–88

[163] Gruene T and Mugnaioli E 2021 3D Electron Diffraction for Chemical Analysis: Instrumentation Developments and Innovative Applications *Chem. Rev.* **121** 11823–34

[164] Gemmi M, Campostrini I, Demartin F, Gorelik T E and Gramaccioli C M 2012 Structure of the new mineralsarrabusite, Pb5CuCl4(SeO3)4, solvedby manual electron diffraction tomography *Acta Crystallogr. Sect. B* **68** 15–23

[165] Weirich T E 2011 *Electron Crystallography of Inorganic Materials: Principles, Methods andApplications* (World Scientific)

[166] Schlitt S, Gorelik T E, Stewart A A, Schömer E, Raasch T and Kolb U 2012 Application of clustering techniques to electron-diffraction data: determination of unit-cell parameters *Acta Crystallogr. Sect. A* **68** 536–46

[167] Harker D and Kasper J S 1947 Phases of Fouriser coefficients directly from crystal diffraction data *J. Chem. Phys.* **15** 882–882

[168] Cauchy A L B 1821 Cours d'analyse de l'École Royale Polytechnique

[169] Sayre D 1952 The squaring method: A new method for phase determination *Acta Crystallogr.* **5** 60–5

[170] Yü S H 1942 Determination of absolute from relative x-ray intensity data *Nature* **150** 151–2

[171] Hauptman H and Karle J 1957 A unified algebraic approach to the phase problem. I. space group P-1 *Acta Crystallogr.* **10** 267–70

[172] Giacovazzo C 2011 *Fundamentals of Crystallography* (Oxford, New York: Oxford University Press)

[173] Burla M C, Caliandro R, Carrozzini B, Cascarano G L, Cuocci C, Giacovazzo C, Mallamo M, Mazzone A and Polidori G 2015 Crystal structure determination and refinement via SIR2014 *J. Appl. Crystallogr.* **48** 306–9

[174] Oszlányi G and Sütó A 2004 Ab initio structuresolution by charge flipping *Acta Crystallogr. Sect. A* **60** 134–41

[175] Petříček V, Dušek M and Palatinus L 2014 Crystallographic Computing System JANA2006: General features *Z. Für Krist. - Cryst. Mater.* **229** 345–52

[176] Palatinus L and Chapuis G 2007 *SUPERFLIP* – a computer program for the solution of crystal structures by charge flipping in arbitrary dimensions *J. Appl. Crystallogr.* **40** 786–90

[177] Bragg W L 1930 XXV. The Structure of Silicates *Z. Für Krist. - Cryst. Mater.* **74** 237–305

[178] Berman H 1937 Constitution and classification of the natural silicates *Am. Mineral.* **22** 342–408

[179] Strunz H 1938 Stereochemie der SIlikatmineralien *Zitschrift Für Gesamte Naturwissenschaft* **5** 181–9

[180] Zoltai T 1960 Classification of silicates and other minerals with tetrahedral structures *Am. Mineral.* **45** 960–73

[181] Sudō T 1981 *Electron micrographs of clay minerals* (Tokyo : Amsterdam ; New York: Kodansha ; Elsevier Scientific Pub. Co)

[182] Velde B 1995 *Origin and Mineralogy of Clays* (Berlin, Heidelberg: Springer Berlin Heidelberg)

[183] Pevear D R 1999 Illite and hydrocarbon exploration *Proc. Natl. Acad. Sci.* **96** 3440–6

[184] Galán E and Ferrell R E 2013 Genesis of Clay Minerals *Developments in Clay Science* vol 5 (Elsevier) pp 83–126

[185] Velde B 1977 *Clays and Clay Minerals in Natural and Synthetic Systems* (Amsterdam: Elsevier Scientific Publishing Company)

[186] Bailey S W 1984 Clasification and structures of the micas *Micas* (De Gruyter) pp 1–12

[187] Ferraris G and Ivaldi G 2002 Structural Features of Micas *Rev. Mineral. Geochem.* **46** 117–53

[188] Grim R E, Bray R H and Bradley W F 1937 The mica in argillaceous sediments *Am. Mineral.* **22** 813–29

[189] Reesman A L and Keller W D 1967 Chemical Composition of Illite *SEPM J. Sediment. Res.* **Vol. 37**

[190] Grim R E 1953 *Clay Mineralogy* (New York: McGraw-Hill)

[191] Yoder H S and Eugster H P 1955 Synthetic and natural muscovites *Geochim. Cosmochim. Acta* **8** 225–80

[192] Środoń J and Eberl D D 1984 Illite *Rev. Mineral. Geochem.* **13** 495–544

[193] Drits V A 1997 Mixed-layer minerals *Modular Aspects of Minerals* vol 1, ed S Merlino (European Mineralogical Union) p 0

[194] Meunier A, Velde B and Zalba P 2004 Illite K–Ar dating and crystal growth processes in diagenetic environments: a critical review *Terra Nova* **16** 296–304

[195] Gaudette H E, Eades and Grim 1964 The Nature of Illite *Clays Clay Miner.* **13** 33–48

[196] Palin E J, Dove M T, Hernández-Laguna A and Sainz-Díaz C I 2004 A computational investigation of the Al/Fe/Mg order-disorder behavior in the dioctahedral sheet of phyllosilicates *Am. Mineral.* **89** 164–75

[197] Besson G, Drits V A, Daynyak L G and Smoliar B B 1987 Analysis of cation distribution in dioctahedral micaceous minerals on the basis of IR spectroscopy data *Clay Miner.* **22** 465–78

[198] Sainz-Díaz C I, Palin E J, Dove M T and Hernández-Laguna A 2003 Monte Carlo simulations of ordering of Al, Fe, and Mg cations in the octahedral sheet of smectites and illites *Am. Mineral.* **88** 1033–45

[199] Dong H, Kukkadapu R K, Fredrickson J K, Zachara J M, Kennedy D W and Kostandarithes H M 2003 Microbial Reduction of Structural Fe(III) in Illite and Goethite *Environ. Sci. Technol.* **37** 1268–76

[200] Chen T, Wang H, Li T and Zheng N 2013 New insights into the formation of diagenetic illite from TEM studies *Am. Mineral.* **98** 879–87

[201] Bartier D, Ledésert B, Clauer N, Meunier A, Liewig N, Morvan G and Addad A 2008 Hydrothermal alteration of the Soultz-sous-Forêts granite (Hot Fractured Rock geothermal exchanger) into a tosudite and illite assemblage *Eur. J. Mineral.* **20** 131–42

[202] Kameda J, Miyawaki R, Drits V A and Kogure T 2007 Polytype and morphological analyses of gümbelite, a fibrous Mg-rich illite *Clays Clay Miner.* **55** 453–66

[203] Patrier P, Beaufort D, Laverret E and Bruneton P 2003 High-grade diagenetic dickite and 2M1 illite from the middle proterozoic kombolgie formation (Northern Territory, Australia) *Clays Clay Miner.* **51** 102–16

[204] Güven N 2001 Mica Structure and Fibrous Growth of Illite *Clays Clay Miner.* **49** 189–96

[205] Gill S and Yemane K 1999 Illitization in a Paleozoic, peat-forming environment as evidence for biogenic potassium accumulation *Earth Planet. Sci. Lett.* **170** 327–34

[206] Inoue A, Velde B, Meunier A and Touchard G 1988 Mechanism of illite formation during smectite-to-illite conversion in a hydrothermal system *Am. Mineral.* **73** 1325–34

[207] Dong H and Peacor D R 1996 TEM observations of coherent stacking relations in smectite, I/S, and illite of shales: Evidence for MacEwan crystallites and dominance of 2M1 polytypism *Clays Clay Miner.* **44** 257–74

[208] Bailey S W 1988 X-Ray Diffraction Identification of the Polytypes of Mica, Serpentine, and Chlorite *Clays Clay Miner.* **36** 193–213

[209] Pandey D, Baronnet A and Krishna P 1982 Influence of stacking faults on the spiral growth of polytype structures in mica *Phys. Chem. Miner.* **8** 268–78

[210] Gaillot A-C, Drits V A and Lanson B 2020 Polymorph and polytype identification from individual mica particles using selected area electron diffraction *Clays Clay Miner.* **68** 334–46

[211] Yoder H S 1957 Experimental Studies on Micas: A Synthesis *Clays Clay Miner.* **6** 42–60

[212] Bauluz B, Peacor D R and Ylagan R F 2002 Transmission electron microscopy study of smectite illitization during hydrothermal alteration of a rhyolitic hyaloclastite from Ponza, Italy *Clays Clay Miner.* **50** 157–73

[213] Laverret E, Mas P P, Beaufort D, Kister P, Quirt D, Bruneton P and Clauer N 2006 Mineralogy and Geochemistry of the Host-Rock Alterations Associated with the Shea Creek Unconformity-Type Uranium Deposits (Athabasca Basin, Saskatchewan, Canada). Part 1. Spatial Variation of Illite Properties *Clays Clay Miner.* **54** 275–94

[214] Aldega L and Eberl D D 2005 Detrital illite crystals identified from crystallite thickness measurements in siliciclastic sediments *Am. Mineral.* **90** 1587–96

[215] Weaver C E 1953 A lath shaped non-expanded dioctahedral 2:1 clay mineral

[216] Bauer A, Velde B and Gaupp R 2000 Experimental constraints on illite crystal morphology *Clay Miner. - CLAY Min.* **35** 587–97

[217] Bjørlykke K, Aagaard H, Dypvik D S, Hastings S and Harper A S 1986 Diagenesis and Reservoir Properties of Jurassic Sandstones from the Haltenbanken Area, off-shore Mid Norway *Petroleum Geology of the Northern European Margin* (London: Norwegian Petroleum Society) pp 285–92

[218] Robinson A G, Coleman M L and Gluyas J G 1993 The Age of Illite Cement Growth, Village Fields Area, Southern North Sea: Evidence from K-Ar Ages and 18O/16O Ratios *AAPG Bull.* **77** 68–80

[219] Gaupp R, Matter A, Ramseyer K, Platt J and Walzebuck J 1993 Diagenesis and fluid evolution of deeply buried Permian (Rotliegende) gas reservoirs, Northwest Germany *AAPG Bull. Am. Assoc. Pet. Geol. U. S.* **77** 1111–28

[220] Lander R H, Bloch S, Mehta S and Atkinson C D 1991 Burial diagenesis of Paleosols in the giant Yacheng gas field, People's Republic of China; bearing on illite reaction pathways *J. Sediment. Res.* **61** 256–68

[221] Bjorkum P A and Gjelsvik N 1988 An isochemical model for formation of authigenic kaolinite, K-feldspar and illite in sediments *J. Sediment. Res.* **58** 506–11

[222] Aagaard P, Jahren J S and Egeberg P K 1992 North Sea clastic diagenesis and formation water constraints International symposium on water-rock interaction pp 1147–52

[223] Wilkinson M and Haszeldine R S 2002 Fibrous illite in oilfield sandstones – a nucleation kinetic theory of growth *Terra Nova* **14** 56–60

[224] Macchi L 1987 A review of sandstone illite cements and aspects of their significance to hydrocarbon exploration and development *Geol. J.* **22** 333–45

[225] Lander R H and Bonnell L M 2010 A model for fibrous illite nucleation and growth in sandstones *AAPG Bull.* **94** 1161–87

[226] Schleicher A M, Warr L N, Kober B, Laverret E and Clauer N 2006 Episodic mineralization of hydrothermal illite in the Soultz-sous-Forêts granite (Upper Rhine Graben, France) *Contrib. Mineral. Petrol.* **152** 349–64

[227] Worden R and Morad S 2003 *Clay Mineral Cements in Sandstones* (Wiley-Blackwell)

[228] Fischer C, Dunkl I, Von Eynatten H, Wijbrans J R and Gaupp R 2012 Products and timing of diagenetic processes in Upper Rotliegend sandstones from Bebertal (North German Basin, Parchim Formation, Flechtingen High, Germany) *Geol. Mag.* **149** 827–40

[229] Weibel R, Nielsen M T, Therkelsen J, Jakobsen F C, Bjerager M, Mørk F, Mathiesen A, Hovikoski J, Pedersen S S, Johannessen P N and Dybkjær K 2020 Illite distribution and morphology explaining basinal variations in reservoir properties of Upper Jurassic sandstones, Danish North Sea *Mar. Pet. Geol.* **116** 104290

[230] Hartman P 1972 Structure and morphology *Crystal growth - an introduction* North-Holland series in crystal growth (Amsterdam, New York: North-Holland Pub. Co.; American Elsevier)

[231] Surdam R C, Boese S W and Crossey L J 1984 The Chemistry of Secondary Porosity: Part 2. Aspects of Porosity Modification **59** 127–49

[232] Rex R W 1964 Authigenic Kaolinite and Mica as Evidence for Phase Equilibria at Low Temperatures *Clays Clay Miner.* **13** 95–104

[233] Dana J D 1892 *Descriptive Mineralogy* (New York: J. Wiley and Sons)

[234] Rieder M, Cavazzini G, D'yakonov Y S, Frank-Kamenetskii V A, Gottardi G, Guggenheim S, Koval' P V, Müller G, Neiva A M R, Radoslovich E W, Robert J-L, Sassi F P, Takeda H, Weiss Z and Wones D R 1999 Nomenclature of the micas *Mineral. Mag.* **63** 267–79

[235] Drits V A, Zvyagin B B and Tokmakov P P 1966 Gümbelite - dioctahedral micas 2M2 *Dokl. Acad. Nauk SSSR* **170** 1390–4

[236] Cox S F 1987 Antitaxial crack-seal vein microstructures and their relationship to displacement paths *J. Struct. Geol.* **9** 779–87

[237] Kuwahara Y, Uehara S and Aoki Y 1998 Surface Microtopography of Lath-Shaped Hydrothermal Illite by Tapping-Mode™ and Contact-Mode AFM *Clays Clay Miner.* **46** 574–82

[238] Kuwahara Y, Uehara S and Aoki Y 2001 Atomic Force Microscopy Study of Hydrothermal Illite in Izumiyama Pottery Stone from Arita, Saga Prefecture, Japan *Clays Clay Miner.* **49** 300–9

[239] Taylor W H 1933 The Structure of Sanidine and Other Felspars *Z. Für Krist. - Cryst. Mater.* **85** 425–42

[240] Gering E 1985 *Silizium/Aluminium-Ordnung und Kristallperfektion von Sanidinen* (Karlsruhe: KIT)

[241] Morimoto N 1979 The modulated structures of feldspars *AIP Conference Proceedings* AIP Conference Proceedings Vol. 53 vol 53 (AIP) pp 299–310

[242] Bown M G and Gay P 1958 The reciprocal lattice geometry of the plagioclase felspar structures *Z. Für Krist.* **111** 1–14

[243] Ribbe P H and Gibbs G V 1969 Statistical analysis and discussion of mean Al/Si-0 bond distances and the aluminum content of tetrahedra in feldspars *Am. Mineral.* **54** 85–94

[244] Wenk H R, Joswig W, Tagai T, Korekawa M and Smith B K 1980 The average structure of An 62-66 labradorite *Am. Mineral.* 81–95

[245] Carpenter M A 1991 Mechanisms and kinetics of al-Si ordering in anorthite: I: Incommensurate structure and domain coarsening *Am. Mineral.* **76** 1110–9

[246] Sörum H 1951 Studies on the structures of plagioclase feldspars *Kgl Nor. Vidensk Selsk Skr.* 1–160

[247] Laves F and Chaisson U 1950 An X-Ray Investigation of the "High"-"Low" Albite Relations *J. Geol.* **58** 584–92

[248] McLaren A C and Marshall D B 1974 Transmission electron microscope study of the domain structures associated with the b-, c-, d-, e- and f-reflections in plagioclase feldspars *Contrib. Mineral. Petrol.* **44** 237–49

[249] Carpenter M A 1986 Experimental Delineation of the "e" ." Ii and "e" ." Ci Transformations in Intermediate Plagioclase Feldspars 21

[250] Laves F 1954 The Coexistence of Two Plagioclases in the Oligoclase Compositional Range *J. Geol.* **62** 409–11

[251] Jin S and Xu H 2017 Investigations of the phase relations among *e* 1, *e* 2 and *C* {\bar {\bf 1}} structures of Na-rich plagioclase feldspars: a single-crystal X-ray diffraction study *Acta Crystallogr. Sect. B Struct. Sci. Cryst. Eng. Mater.* **73** 992–1006

[252] Jin S, Xu H, Wang X, Zhang D, Jacobs R and Morgan D 2019 The incommensurately modulated structures of volcanic plagioclase: displacement, ordering and phase transition *Acta Crystallogr. Sect. B Struct. Sci. Cryst. Eng. Mater.* **75** 643–56

[253] Kroll H and Ribbe P H 1983 Lattice parameters, composition and Al,Si order in alkali feldspars

[254] Angel R J, Hazen R M, McCormick T C, Prewitt C T and Smyth J R 1988 Comparative compressibility of end-member feldspars *Phys. Chem. Miner.* **15** 313–8

[255] Megaw H D 1970 Structural relationship between coesite and feldspar *Acta Crystallogr. B* **26** 261–5

[256] Takahashi Y 2002 Practical method of determining plagioclase twinning laws under the microscope. *Bull. Geol. Surv. Jpn.* **53** 795–800

[257] Emmons R C and Gates R M 1943 Plagioclase twinning

[258] Leske N 1778 Abhandlung von einigen isch wandelnden, zum Feldspath gehörigen Steinen aus Labrador *Der Naturforscher* (J.J. Gebauers Witwe und J.J. Gebauer) pp 145–63

[259] Jin S, Xu H, Wang X, Jacobs R and Morgan D 2020 The incommensurately modulated structures of low-temperature labradorite feldspars: a single-crystal X-ray and neutron diffraction study *Acta Crystallogr. Sect. B Struct. Sci. Cryst. Eng. Mater.* **76** 93–107

[260] Bøggild O B 1924 On the labradorization of the feldspars 81

[261] Henn U, Millisenda C C and Stephan T 2020 *Gemmological tables for the identification of gemstones, synthetic stones, artificial products and imitations* (Deutsche Gemmologische Gesellschaft)

[262] Raman C V and Jayaraman A 1950 The structure of labradorite and the origin of its iridescence *Proc. Indian Acad. Sci. - Sect. A* **32** 1

[263] Bolton H C, Bursill L A, McLaren A C and Turner R G 1966 On the origin of the colour of labradorite *Phys. Status Solidi B* **18** 221–30

[264] Miúra Y 1978 Color zoning in labradorite

[265] Hoshi T, Tagai T and Suzuki M 1996 Investigations on Boggild intergrowth of intermediate plagioclase by high resolution transmission electron microscopy

[266] Rayleigh, Lord 1923 Studies of Iridescent Colour and the Structure Producing it. III. The Colours of Labrador Felspar *Proc. R. Soc. Lond. Ser. Contain. Pap. Math. Phys. Character* **103** 34–45

[267] Carpenter M A, McConnell J D C and Navrotsky A 1985 Enthalpies of ordering in the plagioclase feldspar solid solution *Geochim. Cosmochim. Acta* **49** 947–66

[268] Miúra Y, Tomisaka T and Kato T 1975 Labradorescence and the ideal behaviour of thicknesses of alternate lamellae in the Boggild intergrowth 526–41

[269] Christie O H J 1969 Spinodal precipitation in silicates. II. Short survey of theories and some additional remarks on exsolution in feldspar *Lithos* **2** 285–94

[270] Petrishcheva E, Tiede L, Schweinar K, Habler G, Li C, Gault B and Abart R 2020 Spinodal decomposition in alkali feldspar studied by atom probe tomography *Phys. Chem. Miner.* **47** 30

[271] Parsons I, Fitz Gerald J D and Lee M R 2015 Routine characterization and interpretation of complex alkali feldspar intergrowths† *Am. Mineral.* **100** 1277–303

[272] Jin S, Xu H and Lee S 2021 Revisiting the Bøggild Intergrowth in Iridescent Labradorite Feldspars: Ordering, Kinetics, and Phase Equilibria *Minerals* **11** 727

[273] Nissen H-U 1971 End member compositions of the labradorite exsolution *Naturwissenschaften* **58** 454–454

[274] Kalning M, Dorna V, Burandt B, Press W, Kek S and Boysen H 1997 High-Order Supersatellite Reflections in Labradorite. A SynchrotronX-ray Diffraction Study *Acta Crystallogr. A* **53** 632–42

[275] Korekawa M and Jagodzinski H 1967 Die Satellitenreflexe des Labradorits *Schweiz. Mineral. Petrogr. Mitteilungen* **47** 269–78

[276] Boysen H and Kek S 2015 The modulated structure of labradorite *Z. Für Krist. - Cryst. Mater.* **230**

[277] Burandt B, Komorek M, Schnabel B, Press W and Boysen H 1992 High resolution X-ray investigations on the supersatellite reflections of Labradorite *Z. Für Krist.* **200** 141–56

[278] Korekawa M, Horst W, Tagai T, Joswig W and Wenk H R 1979 Structure determination of plagioclase (Labradorite): I. Al/Si distribution in an An66 (neutron diffraction): II. Superstructure of an An54 (X-ray diffraction) *AIP Conference Proceedings* AIP Conference Proceedings Vol. 53 vol 53 (AIP) pp 311–3

[279] Hashimoto H, Nissen H-U, Ono A, Kumao A, Endoh H and Woensdregt C F 1976 High-resolution Electron Microscopy of Labradorite Feldspar *Electron Microscopy in Mineralogy* ed H-R Wenk (Berlin, Heidelberg: Springer Berlin Heidelberg) pp 332–44

[280] Megaw H D 1960 Order and disorder - III. The structure of the intermediate plagioclase felspars *Proc. R. Soc. Lond. Ser. Math. Phys. Sci.* **259** 184–202

[281] Toman K and Frueh A J 1972 Intensity averages of plagioclase satellites: distribution in reciprocal space *Acta Crystallogr. B* **28** 1657–62

[282] de Wolff P M, Janssen T and Janner A 1981 The superspace groups for incommensurate crystal structures with a one-dimensional modulation *Acta Crystallogr. A* **37** 625–36

[283] Yamamoto A, Nakazawa H, Kitamura M and Morimoto N 1984 The modulated structure of intermediate plagioclase feldspar $Ca_xNa_{1-x}Al_{1+x}Si_{3-x}O_8$ *Acta Crystallogr. B* **40** 228–37

[284] Xu H 2015 Direct observation of Ca-Na ordering and structure polarity in Ca-rich intermediate plagioclase feldspar with incommensurate modulated structure *Am. Mineral.* **100** 510–5

[285] Jin S and Xu H 2017 Study on structure variations of incommensurately modulated labradorite feldspars with different cooling histories *Am. Mineral.* **102** 1328–39

[286] Bruce A D, Cowley R A and Murray A F 1978 The theory of structurally incommensurate systems. II. Commensurate-incommensurate phase transitions *J. Phys. C Solid State Phys.* **11** 3591

[287] Heine V and McConnell J D C 1981 Origin of Modulated Incommensurate Phases in Insulators *Phys. Rev. Lett.* **46** 1092–5

[288] Jambor J L and Roberts A C 2004 New mineral names *Am. Mineral.* **89** 249–53

[289] Frost R L, López A, Scholz R, Theiss F L and Romano A W 2015 SEM, EDX, Infrared and Raman spectroscopic characterization of the silicate mineral yuksporite *Spectrochim. Acta. A. Mol. Biomol. Spectrosc.* **137** 607–11

[290] Yakovenchuk V N, Ivanyuk G Y, Pakhomovsky Y A and Men'shikov Y P 1999 *Minerals of the Khibiny massif* (Moscow: Zemyla)

[291] Kramm U and Sindern S 2004 Timing of Kola ultrabasic, carboatite and phoscorites-carbonatite magmatism *Phoscorites and Carbonatites from Mantle to Mine: the Key Example of the Kola Alkaline Province* Mineralogical Scociety Book Series vol 10 (London: Mineralogical Socienty) pp 75–97

[292] Ferraris G 2006 Heterophyllosilicates: prospects of technological applications pp 65–75

[293] Liebau F 1985 *Structural Chemistry of Silicates* (Springer)

[294] Warren B and Bragg W L 1929 XII. The structure of diopside, CaMg(SiO3)2 *Z. Für Krist. - Cryst. Mater.* **69** 168–93

[295] Hesse K-F 1984 Refinement of the crystal structure of wollastonite-2M (parawollastonite) *Z. Für Krist. - Cryst. Mater.* **168** 93–8

[296] Nikitin A V and Belov N V 1962 Crystal structure of batisite Na2BaTi2Si4O14 = Na2BaTiO2[Si4O12] *Dokl. Akad. Nauk SSSR* 1401

[297] Pertlik F and Zahiri R 1999 Rhodonite with a Low Calcium Content: Crystal Structure Determination and Crystal Chemical Calculations *Monatshefte Für Chem.* **130**

[298] Vorma A 1963 Crystal structure of stokesite, CaSnSi3O9·2H2O *Mineral. Mag. J. Mineral. Soc.* **33** 615–7

[299] Krivovichev S V and Burns P C 2004 Crystal structure of synthetic alamosite Pb(SiO3) *Zap. Vseross. Mineral. Obshchestva* 70–6

[300] Cámara F, Sokolova E, Abdu Y and Hawthorne F C 2010 The crystal structures of niobophyllite, kupletskite-(Cs) and Sn-rich astrophyllite: revisions to the crystal chemistry of the astrophyllite-group minerals *Can. Mineral.* **48** 1–16

[301] Oberti R, Hawthorne F C, Ungaretti L and Cnr C 1993 The behaviour of Mn in amphiboles: Mn in richterite *Eur. J. Mineral.* **5** 43–52

[302] Baur W H, Tillmanns E and Hofmeister W 1983 Topological analysis of crystal structures *Acta Crystallogr. B* **39** 669–74

[303] Krivovichev S V 2013 Structural complexity of minerals: information storage and processing in the mineral world *Mineral. Mag.* **77** 275–326

[304] Schwarzmeier J, Bader K, Berger K and Jerz H 1978 Geologische Karte von Bayern 1:25000 - Erläuterungen zum Blatt Nr. 6024 Karlstadt und zum Blatt Nr. 6124 Remlingen

[305] Stober I and Jodocy M 2011 Hydrochemical characteristics of deep seated waters in the Upper Rhine Graben - Basic inforamtion for geothermal energy *Z. Für Geol. Wiss.* **39** 39–57

[306] Frank S, Heinze T, Ribbers M and Wohnlich S 2020 Experimental Reproducibility and Natural Variability of Hydraulic Transport Properties of Fractured Sandstone Samples *Geosciences* **10** 458

[307] Reinhardt M, Jacob A, Sadeghnejad S, Cappuccio F, Arnold P, Frank S, Enzmann F and Kersten M 2022 Benchmarking conventional and machine learning segmentation techniques for digital rock physics analysis of fractured rocks *Environ. Earth Sci.* **81**

[308] Schäffer R, Götz E, Schlatter N, Schubert G, Weinert S, Schmidt S, Kolb U and Sass I 2022 Fluid–Rock Interactions in Geothermal Reservoirs, Germany: Thermal Autoclave Experiments Using Sandstones and Natural Hydrothermal Brines *Aquat. Geochem.* **28**

[309] Frank S, Heinze T and Wohnlich S 2020 Comparison of Surface Roughness and Transport Processes of Sawed, Split and Natural Sandstone Fractures *Water* **12** 2530

[310] Hering D 2020 *Einfluss von Fluidreaktionen auf petrophysikalische Eigenscahften geklüfteter Proben des Remlinger Hartquarzsandsteins* Masterarbeit (Darmstadt: TU Darmstadt)

[311] ESRI 2011 ArcGIS Desktop: Release 10

[312] Momma K and Izumi F 2011 VESTA 3 for three-dimensional visualization of crystal, volumetric and morphology data *J. Appl. Crystallogr.* **44** 1272–6

[313] de la Flor G de la, Orobengoa D, Tasci E, Perez-Mato J M and Aroyo M I 2016 Comparison of structures applying the tools available at the Bilbao Crystallographic Server *J. Appl. Crystallogr.* **49** 653–64

[314] Blatov V A, Shevchenko A P and Proserpio D M 2014 Applied Topological Analysis of Crystal Structures with the Program Package ToposPro *Cryst. Growth Des.* **14** 3576–86

[315] Götz E, Neder R B, Kolb U and Kleebe H-J 2023 The alteration of illite by Bad Nauheim and Gerolstein brine; Implications on fluid permeability in geothermal systems *Appl. Clay Sci.* **243** 107082

[316] Morrow C A, Moore D E and Lockner D A 2001 Permeability reduction in granite under hydrothermal conditions *J. Geophys. Res. Solid Earth* **106** 30551–60

[317] Tenthorey E, Scholz C H, Aharonov E and Léger A 1998 Precipitation sealing and diagenesis: 1. Experimental results *J. Geophys. Res. Solid Earth* **103** 23951–67

[318] Whitney D L and Evans B W 2010 Abbreviations for names of rock-forming minerals *Am. Mineral.* **95** 185–7

[319] de Villiers J P R 1971 Crystal structures of aragonite, strontianite, and witherite *Am. Mineral.* 758–67

[320] Effenberger H, Mereiter K and Zemann J 1981 Crystal structure refinements of magnesite, calcite, rhodochrosite, siderite, smithonite, and dolomite, with discussion of some aspects of the stereochemistry of calcite type carbonates *Z. Für Krist.* 233–43

[321] Grundl T and Delwiche J 1993 Kinetics of ferric oxyhydroxide precipitation *J. Contam. Hydrol.* **14** 71–87

[322] Palatinus L 2013 The charge-flipping algorithm in crystallography *Acta Crystallogr. Sect. B Struct. Sci. Cryst. Eng. Mater.* **69** 1–16

[323] Geatches D L and Wilcox J 2014 Ab initio investigations of dioctahedral interlayer-deficient mica: modelling 1 M polymorphs of illite found within gas shale *Eur. J. Mineral.* **26** 127–44

[324] Götz E, Kleebe H-J and Kolb U 2022 The hierarchical internal structure of labradorite *Eur. J. Mineral.* **34** 393–410

[325] Benna P, Tribaudino M and Bruno E 1995 Al-Si ordering in Sr-feldspar SrAl2Si2O8: IR, TEM and single-crystal XRD evidences *Phys. Chem. Miner.* **22**

[326] Nemeth P, Tribaudino M, Bruno E and Buseck P R 2007 TEM investigation of Ca-rich plagioclase: Structural fluctuations related to the IFormula-PFormula phase transition *Am. Mineral.* **92** 1080–6

[327] Nakada R, Sato M, Ushioda M, Tamura Y and Yamamoto S 2019 Variation of Iron Species in Plagioclase Crystals by X-ray Absorption Fine Structure Analysis *Geochem. Geophys. Geosystems* **20** 5319–33

[328] Nakada R, Sato M, Ushioda M, Tamura Y and Yamamoto S 2020 *Determination on iron species in plagioclase crystals toward the understanding on the magnetite exsolution* (display)

[329] Stokes H T, Campbell B J and van Smaalen S 2011 Generation of $(3 + d)$-dimensional superspace groups for describing the symmetry of modulated crystalline structures *Acta Crystallogr. A* **67** 45–55

[330] Davis B L and Adams L H 1965 Kinetics of the calcite ⇌ aragonite transformation *J. Geophys. Res. 1896-1977* **70** 433–41

[331] Sun W, Jayaraman S, Chen W, Persson K A and Ceder G 2015 Nucleation of metastable aragonite $CaCO_3$ in seawater *Proc. Natl. Acad. Sci.* **112** 3199–204

[332] Kogure T and Drits V A 2010 Structural Change in Celadonite and Cis-Vacant Illite by Electron Radiation in Tem *Clays Clay Miner.* **58** 522–31

[333] Deon F, van Ruitenbeek F, van der Werff H, van der Meijde M and Marcatelli C 2022 Detection of Interlayered Illite/Smectite Clay Minerals with XRD, SEM Analyses and Reflectance Spectroscopy *Sensors* **22** 3602

[334] Hazen R M, Sverjensky D A, Azzolini D, Bish D L, Elmore S C, Hinnov L and Milliken R E 2013 Clay mineral evolution *Am. Mineral.* **98** 2007–29

[335] Hu Y, Ray J R and Jun Y-S 2013 Na^+ , Ca^{2+} , and Mg^{2+} in Brines Affect Supercritical CO_2 –Brine–Biotite Interactions: Ion Exchange, Biotite Dissolution, and Illite Precipitation *Environ. Sci. Technol.* **47** 191–7

[336] Schlabach S 2000 *Auflösungsexperimente von Kaolinit, Montmorillonit, Illit, Serizit und Talk in Batch- und Durchfluss-Reaktoren* (Göttingen: Georg-August-Universität zu Göttingen)

[337] Heydemann A 1966 Über die chemische verwitterung von tonmineralen (experimentelle untersuchungen) *Geochim. Cosmochim. Acta* **30** 995–1035

[338] Feigenbaum S and Shainberg I 1975 Dissolution of Illite—A Possible Mechanism of Potassium Release *Soil Sci. Soc. Am. J.* **39** 985–90

[339] Huggett J M 2005 Sedimentary Rocks - Clays and Their Diagenesis *Encyclopedia of Geology* (Elsevier) pp 62–70

[340] Bjørlykke K, Nedkvitne T, Ramm M and Saigal G C 1992 Diagenetic processes in the Brent Group (Middle Jurassic) reservoirs of the North Sea: an overview *Geology of the Brent Group* vol 61 (London: Geological Society, London, Special Publications) pp 263–87

[341] Le Gallo Y, Bildstein O and Brosse E 1998 Coupled reaction-flow modeling of diagenetic changes in reservoir permeability, porosity and mineral compositions *J. Hydrol.* **209** 366–88

[342] Yund R A 1984 Alkali Feldspar Exsolution: Kinetics and Dependence on Alkali Interdiffusion *Feldspars and Feldspathoids: Structures, Properties and Occurrences* NATO ASI Series ed W L Brown (Dordrecht: Springer Netherlands) pp 281–315

[343] Gordon E K, Samson S and Kamb W B 1966 Crystal Structure of the Zeolite Paulingite *Science* **154** 1004–7

[344] Cámara F, Bellatreccia F, Della Ventura G, Mottana A, Bindi L, Gunter M E and Sebastiani M 2010 Fantappièite, a new mineral of the cancrinite-sodalite group with a 33-layer stacking sequence: Occurrence and crystal structure *Am. Mineral.* **95** 472–80

[345] Vorob'ev E I 2008 Charoite *Charoite* (Novosibirsk: Academy Pubishing "Geo")

[346] Men'shikov Y P 1984 Deniskovite Ca4(K1.4Na0.6)2Si6O16(F,OH)2 - a new mineral from the Khibina massif *Zap. Vsesoyuznogo Mineral. Obshchestva* 718–23

[347] Konev A A, Vorobiev E I, Paradina L F and Sapozhnikov A N 1987 Denisovite from Murunskii Massif - The 2nd find in the world *Dokl. Akad. Nauk SSSR* 196–8

[348] Fersman A E 1923 Minerals of the Khibina and Lovozero tundras *Trans. North. Sci. Econ. Expidition* 16–73

[349] Konev A A, Vorob'ev E I, Sapozhnikov A N, Malyushonok Y U, Paradina L F and Lapides I L 1985 New data on yuksporite *Mineral. Zhurnal* 74–8

[350] Kuznicki S M 1989 Large-pored crystalline titatium molecuar sieve zeolites

[351] Kuznicki S M and Thrush K A 1993 Large-pored molecular sieves with charged octahedral titanium and charged tetrahedral aluminium sites

[352] Spiridonova D V, Britvin S N, Krivovichev S V, Yakovenchuk V N and Armbruster T 2008 Tl-Exchange in Zorite and ETS-4 *Minerals as Advanced Materials I* ed S V Krivovichev (Berlin, Heidelberg: Springer) pp 65–9

[353] Gulati S and Pakzad A 2023 Automated Continuous Diffraction Tomography with Gatan Direct Detection Electron Counting Cameras: Advantages and Best Practices for Data Acquisition *Microsc. Microanal.* **29** 1048–9

[354] Hattne J, Martynowycz M W, Penczek P A and Gonen T 2019 MicroED with the Falcon III direct electron detector *IUCrJ* **6** 921–6

[355] Levin B D A 2021 Direct detectors and their applications in electron microscopy for materials science *J. Phys. Mater.* **4** 042005

[356] Simoncic P, Romeijn E, Hovestreydt E, Steinfeld G, Santiso-Quiñones G and Merkelbach J 2023 Electron crystallography and dedicated electron-diffraction instrumentation *Acta Crystallogr. Sect. E Crystallogr. Commun.* **79** 410–22

[357] Keller W D 1970 Environmental Aspects of Clay Minerals *J. Sediment. Res.* **40**

[358] Bailey S W 1984 Crystal chemistry of the true micas *Micas* (Boston: De Gruyter) pp 13–60

[359] Esquevin J 1958 Les silicates de zinc. Etude de produits de synthèse et des minèraux naturels *Thèse Fac. Sci. Univ. Paris*

[360] Eberl D D 1984 Clay Mineral formation and transformation in rocks an soils *Philos. Trans. R. Soc. Lond. Ser. Math. Phys. Sci.*

[361] Nickling W G 1994 Aeolian sediment transport and deposition *Sediment transport and depositional processes* (Oxford: Blackwell) pp 293–350

[362] Merriman R J 2005 Clay minerals and sedimentary basin history *Eur. J. Mineral.* **17** 7–20

[363] Środoń J, Drits V A, McCarty D K, Hsieh J C C and Eberl D D 2001 Quantitative X-ray diffraction analysis ofclay-bearing rocks from random preparations *Clays Clay Miner.* **49** 514–28

[364] Inoue E 1995 Formation of Clay Minerals in Hydrothermal Environments

[365] White D E 1957 Thermal waters of volcanic origin *GSA Bull.* **68** 1637–58

[366] Burnham C W 1962 Facies and Types of Hydrothermal Alteration 17

[367] Fulignati P 2020 Clay Minerals in Hydrothermal Systems *Minerals* **10** 919

[368] Jiang W-T, Peacor D R, Árkai P, Tóth M and Kim J W 1997 TEM and XRD determination of crystallite size and lattice strain as a function of illite crystallinity in pelitic rocks: Crystallite size and lattice strain of illite *J. Metamorph. Geol.* **15** 267–81

[369] Peters Tj and Hofmann B 1984 Hydrothermal clay mineral formation in a biotite-granite in northern Switzerland *Clay Miner.* **19** 579–90

[370] Clauer N and Chaudhuri S 1995 *Clays in Crustal Environments: Isotope Dating and Tracing* (Springer-Verlag)

[371] Norrish K 1973 Factors in the weathering of mica to vermiculite

[372] Meunier and Velde 2004 The Geology of Illite *Illite*

[373] Hughes R E, Moore D M and Glass H D 1994 Qualitative and Quantitative Analysis of Clay Minerals in Soils *Quantitative Methods in Soil Mineralogy* (John Wiley & Sons, Ltd) pp 330–59

[374] Wilson M J, Bain D C and Duthie D M L 1984 The soil clays of Great Britain: II. Scotland *Clay Miner.* **19** 709–35

[375] Perry E A Jr and Hower J 1972 Late-Stage Dehydration in Deeply Buried Pelitic Sediments1 *AAPG Bull.* **56** 2013–21

[376] Gier S 1998 Burial Diagenetic Processes and Clay Mineral Formation in the Molasse Zone of Upper Austria *Clays Clay Miner.* **46** 658–69

[377] Weaver C E 1979 *Geothermal alteration of clay minerals and shales: diagenesis* (Georgia Inst. of Tech., Atlanta (USA))

[378] Nadeau P H 2011 Earth's energy "Golden Zone": a synthesis from mineralogical research *Clay Miner.* **46** 1–24

[379] Eberl D D 1993 Three Zones for Illite Formation During Burial Diagenesis and Metamorphism *Clays Clay Miner.* **41** 26–37

[380] Ehrenberg S N 1991 Kaolinized, potassium-leached zones at the contacts of the Garn Formation, Haltenbanken, mid-Norwegian continental shelf *Mar. Pet. Geol.* **8** 250–69

[381] Ehrenberg S N, Aagaard P, Wilson M J, Fraser A R and Duthie D M L 1993 Depth-Dependent Transformation of Kaolinite to Dickite In Sandstones of the Norwegian Continental Shelf *Clay Miner.* **28** 325–52

[382] Berger G, Turpault M-P and Meunier A 1992 Dissolution-precipitation processes induced by hot water in a fractured granite. Part 2: Modelling of water-rock interaction *Eur. J. Mineral.* 1477–88

[383] Wang X and Wang H 2021 Structural Analysis of Interstratified Illite-Smectite by the Rietveld Method *Crystals* **11** 244

[384] White N C and Hedenquist J W 1995 Epithermal Gold Deposits: Styles, characteristics andexploration *SEG Discov.* 1–13

[385] Pollastro R M 1985 Mineralogical and Morphological Evidence for the Formation of Illite at the Expense of Illite/Smectite *Clays Clay Miner.* **33** 265–74

[386] Yau Y-C, Peacor D R and McDowell S D 1987 Smectite-to-illite reactions in Salton Sea shales; a transmission and analytical electron microscopy study *J. Sediment. Res.* **57** 335–42

[387] Hower J, Eslinger E V, Hower M E and Perry E A 1976 Mechanism of burial metamorphism of argillaceous sediment: 1. Mineralogical and chemical evidence *GSA Bull.* **87** 725–37

[388] Ahn J H and Peacor D R 1986 Transmission and Analytical Electron Microscopy of the Smectite-To-Illite Transition *Clays Clay Miner.* **34** 165–79

Appendix

Appendix 1: Further information about the classification, transformation and hydrothermal facies of clay minerals.

Classification

There are 56 clay mineral species split into ten groups approved by the International Mineralogical Association (IMA); however, they are not consistent with the nomenclature of the Association Internationale pour l'Étude des Argiles (AIPEA). The ambiguous terminology extends through the entire field of clay mineral science and complicates research [334]. Several parameters are used to differentiate between different clay mineral groups such as: number of tetrahedral and octahedral sheets in one layer, occupancy of the octahedral sheet, type of the interlayer cation and expandability. An overview of the most important groups with their characteristics and representative clay minerals is given in Table A 1. Additionally, there are mixed layer clay minerals. They are structures with intermediate crystallites that often express mineral instability in their randomness [182]. Regular mixed layering, however, seems to portray a stable phase. Mixed layering can most often be seen within illite-smectite (I-S) or chlorite-smectite (C-S).

Table A 1: Most important groups of clay minerals. Characteristics and main representative minerals of the respective groups are listed according to Keller [357], Bailey [358], Velde [182], Darling [72] and Hazen et al. [334].

Group Name	Characteristics	Clay mineral
Kaolin	- 1:1 - 7 Å axis - Dioctahedral - Hexagonal crystals, often stacked as accordion	- **Kaolinite**, **dickite**, **nacrite** $Al_2Si_2O_5(OH)_4$ - **Halloysite**
Serpentine	- 1:1 - 7 Å axis - Trioctahedral - Usually larger than 2 μm	- **Serpentine** $(Mg,Ni,Fe,Mn,Zn,Fe,Al)_3(Al,Fe,Si)_2O_5(OH)_4$
Talk & Pyrophyllite	- 2:1 - 10 Å axis - Di-/trioctahedral - No interlayer cation	- **Talc** $Mg_3Si_4O_{10}(OH)_2$ - **Pyrophyllite** $Al_2Si_4O_{10}(OH)_2$
Smectite & Vermiculite	- 2:1 - 10 Å axis - Di-/trioctahedral - Variable amounts of interlayer cations and H2O - Expandable - Crinkly, cellular morphology	- **Montmorillonite** $(Na,K,Ca)_n(Al,Mg,Fe)_2Si_4O_{10}(OH)_2$ x nH_2O - **Beidellite** $(K,Na,Ca_{0.5})_n(Al,Mg)_2(Si,Al)_4O_{10}(OH)_2$ x nH_2O - **Notronite** $(K,Na,Ca)_n(Fe,Al)_2(Si,Fe)_4O_{10}(OH)_2$ x nH_2O - **Saponite** $(K,Na,Ca)_n(Mg,Al)_{2.5\text{-}3}(Si,Al)_4O_{10}(OH)_2$ x nH_2O - **Vermiculite** $(K,Na,Ca)_n(Mg,Fe,Al)_{<3}(Si,Al)_4O_{10}(OH)_2$ x nH_2O

Illite	- 2:1 - 10 Å axis - Dioctahedral - Non-expandable - Platelets, laths	- **Illite** $(K,H_3O^+)_{0.6\text{-}1}(Al,Mg,Fe)_2(Si,Al)_4O_{10}(OH)_2$ - **Glauconite** $(K,Na,H_2O)_x(Mg,Fe,Al)_2(Al,Si)_4O_{10}(OH)_2$ x nH_2O
Chlorite	- 2:1:1 - 14 Å axis - Both octahedral sheets can be di- or trioctahedral - Plates, rosettes, honeycombs	- **Clinochlore** $Mg_6Si_4O_{10}(OH)_8$ - **Chamosite** $(Fe,Mg,Al,Fe)_6(Si,Al)_4O_{10}(OH)_8$
Sepiolite & Palygorskite	- Clay mineral-like - Chain-structured - Incorporation of two (palygorskite) or three (sepiolite) pyroxene-like chains - Needles	- **Sepiolite** $Mg_4Si6O_{15}(OH)_2$ x $6H_2O$ - **Palygorskite** $(Mg,Al)_2Si_4O_{10}(OH)$ x $4H_2O$

Transformation

There are three different mechanisms for clay mineral formation: inheritance (detrital), neoformation (authigenic) and transformation (diagenetic) [359]. When a clay mineral is inherited, it has only slow reaction rates or is stable at the physical and chemical conditions of the environment that it has been transported into. During neoformation, a clay mineral crystallizes directly from a solution or from previously amorphous material and thus is considered to represent equilibrium conditions [185]. Transformation usually takes place through chemical reactions during weathering or diagenesis of silicates [357]. If a clay mineral transforms into another one it can retain part of its inherited structure. The sequence of the layers or their contents can be modified or only weakly bound ions from the interlayer can be exchanged with the surroundings by means of ion exchange [360].

Clay mineral formation and transformation occurs in different environments: during weathering/soil formation, sedimentation, burial/diagenesis and hydrothermal events (see Figure A 1) [185].

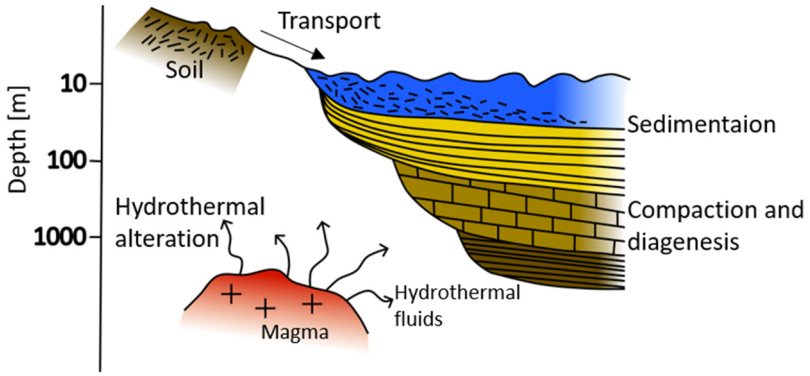

Figure A 1: Schematic illustration of the clay cycle where clay mineral formation or transformation can occur in various environments.

In a weathering environment, the factors that influence clay mineral formation the most are climate (rainfall and temperature), rock type, topography, time and organic matter [184]. The clay minerals present are usually stable under ambient conditions and are formed by incongruent dissolution of unstable silicates. The local water/rock ratio, as well as the chemical composition of the original rock, influence the mineral reactions the most [182]. The possibility of occurrence of organic material and mixed layers in clay minerals and the fact that there are many mobile elements in this environment leads to a great variability in the system [185]. The final assemblage of a fully weathered rock are aluminum- and iron-hydroxides. This situation can only be achieved in tropical environments with high rainfall and therefore a large water/rock ratio, which leads to strong reactions. In environments that are more temperate parent, rocks are transformed into soil with complex mixed layer clay mineral assemblages. In hot and dry environments smectites occur, because the rock composition has a more significant effect on the transformation [182].

Sedimentation leads to mostly detrital clay minerals (90%) with the other part being authigenic [182]. They can be transported by water, wind or ice. In water the largest proportion of clay minerals are transported by rivers as a suspension. When they reach the oceans, they are deposited by settling. Here, alteration of silicate material takes place with a relatively constant composition of seawater [185]. Transport by wind only happens in deserts, semi-arid environments and areas where soil is intensely used for agricultural purposes. Due to their aerodynamic shape as well as strong interparticle forces, particles <80 μm are difficult to lift by the wind and are only swept up into the air upon collision with larger particles [361]. In glacial environments and oceans with seasonal sea-ice, clay minerals can be transported by ice. Sediments resulting from glacial influence are called tills.

During burial and diagenesis, the clay mineral assemblage decreases in diversity with increasing temperature and time [182,184]. In the first 3-5 km, free or weakly bound water is removed. The newly formed minerals are more highly ordered with a larger particle size following the Ostwald step rule [362]. As the porosity decreases with increasing depth, clay mineral formation becomes more dependent on the chemistry of the parent rock [185]. In sedimentary rocks, the most abundant clay minerals are illite, smectite and I-S [363].

Hydrothermal alteration is achieved by the circulation of hot water in a host rock. It is dependent on rock composition, fluid composition, pH, temperature, geotectonic setting and the thermal history of the basin [184]. Hereby the existing mineral assemblage is altered to new minerals, which are stable under hydrothermal conditions. The proceeding reactions are usually temperature zoned and the mineral content can vary strongly over short distances. Ore deposits and geothermal systems often accompany hydrothermal alteration [185]. A hydrothermal solution mainly consists out of meteoric water, which has passed through a cycle of heating in deeper areas and subsequent ascend. Seawater or magmatic fluid can also be part of the hydrothermal solution. This solution is not pure water but contains several additional dissolved substances like salts and gases with the major ions usually being Na^+, K^+ and Cl^- while the Mg^{2+} content is low [364]. In order for it to have a hydrothermal effect on the surrounding rocks, the heated water has to have a temperature, which is significantly higher than the regional geothermal gradient [365]. For this, the presence of a heat source as well as local fracture systems along which the hot water can ascend are crucial. In this environment, new phases mainly consist of hydrous minerals and clay mineral formation can take place from several tens of degrees up until ~300°C.

Facies

Clay minerals are zone markers in hydrothermal alterations and can be of great help identifying the facies. Each facies is characterized by distinct alterations that are dependent on the proximity to the heat source as well as the fluids and rock types present [366]. Minerals of the smectite group are found in the argillic alteration facies. At the expense of silicates, they form at a relatively neutral pH (5.5-7) at temperatures below 160°C from hydrolysis:

$$1.17\ NaAlSi_3O_8 + H^+ = 0.5\ Na_{0.33}Al_{2.33}Si_{3.67}O_{10}(OH)_2 + 1.67\ SiO_2 + Na^+$$

Albite montmorillonite quartz

Sepiolite also occurs in the argillic facies but as alteration product of mafic and ultramafic rocks of the oceanic crust. Kaolin group minerals can be found in the intermediate and advanced argillic facies at temperatures below 150-200°C. Like smectites, they are created by hydrolysis of silicates but at higher H^+ activities:

$$3\ Na_{0.33}Al_{2.33}Si_{3.67}O_{10}(OH)_2 + H^+ + 3.5\ H_2O = 3.5\ Al_2Si_2O_5(OH)_4 + 4\ SiO_2 + Na^+$$

Montmorillonite kaolinite quartz

Pyrophyllitic minerals are present in the advanced argillic facies with acidic hydrothermal fluids (pH 2) and at temperatures between 200-250°C. Illite is common in the phyllic and propylitic facies at temperatures between 22-380°C. In this context, it is created by the alteration of K-feldspar and plagioclase. The composition of illite changes with temperature according to

$$T = 267.95x + 31.50\ [°C] \tag{75}$$

With $x = K + |Fe - Mg|$. Chlorite type minerals and talc are only present in the propylitic facies at temperatures above 220°C in veins and as alteration of mafic minerals like pyroxene or olivine. Serpentine also occurs in the propylitic facies at 250-350°C as reaction products of mafic and ultra-mafic rock alteration by seawater. Biotite occurs in the propylitic and alkali metasomatism facies at temperatures above 320-330°C [367].

Appendix 2: Further information about the use of illite, its formation and illite-smectite mixed layer crystals.

The use of illite

The Kübler index is used to determine the degree of diagenesis in sedimentary basins. This index is not related to the mineral structure, but strictly empirical [193]. With increasing temperature, the 001 reflection in the XRD pattern of illite becomes sharper leading to an increase in "crystallinity". This happens because peak broadening variables decrease with increasing diagenesis: the particle size increases, lattice defects are mended and the amount of smectite layers in I-S is reduced. However, the Kübler index is mainly dependent on the size and the imperfections of a crystal [368]. Care must be taken if the sediments were exposed to a hydrothermal fluid. In this case, the crystallinity can indicate the maximum temperature of the fluid instead of the burial temperature. Furthermore, detrital mica can bias the results leading to an overestimation of the temperature [339]. Because of this, Peters and Hofmann [369] suggested to limit the use of the Kübler index to impermeable clays and shales.

Illite can also be used to determine the age or period of existence of a sediment [194]. Since it contains potassium and has a good Ar retention at temperatures below 175°C, the K/Ar dating method can be applied. It is based on the rate of decay of radioactive ^{40}K to stable ^{40}Ar [370]. Thereby, it is possible to determine the age of authigenic illite and shed light on the burial history of illite-containing rocks [339]. Here, too, mixing with other K-bearing phases may cause contamination and corrupt the age calculations [194].

Illite formation

Illite formation can happen in various environments via different processes and chemical reactions. Under weathering conditions and in soil, mica can be broken into smaller particles until they have reached clay size [371]. Additionally, K^+ leaching can take place to reduce the interlayer charge. Illite can also be formed by the alteration of K-feldspar [372]:

$$\text{K-feldspar} + H^+ + Mg^{2+} \rightarrow \text{illite} + K^+ + Si^{4+}$$

This leads to illite always containing small amounts of Mg. However, illite is often unstable in soils and will be transformed to I-S [373] or vermiculite [374] by a depletion of potassium and other elements [184].

In diagenetic environments, illite can precipitate from solution. Additionally, with increasing temperature pH and K^+/H^+ activity kaolin and smectite minerals become unstable and are replaced by illite [339]. Mainly in shales, smectite is transformed to illite and later muscovite via I-S mixed layering [375]. In order to describe the layer stacking sequence in mixed layered materials, the Reichweite index R is used. R = 0 indicates random layering with 0-60% illite content, R = 1 and R = 3 ordered layering with 65-85% and 85-100% illitic layers, respectively. For the smectite to illite transformation, the series looks as follows [184]:

$$\text{Smectite} \rightarrow \text{I-S (R = 0)} \rightarrow \text{I-S (R = 1)} \rightarrow \text{I-S (R = 3)} \rightarrow 1M_d \text{ illite} \rightarrow 2M_2 \text{ muscovite}$$

The degree of crystallinity increases with decreasing smectite content [195]. The gradual illitization of I-S is mirrored in an increase in K^+ and Al^{3+}, which can be produced by the dissolution of K-feldspar [376].

$$\text{Smectite} + K^+ + Al^{3+} \rightarrow \text{illite} + Si^{4+} + Fe^{3+} + Na^+ + Mg^{2+}$$

Alternatively, a reaction can occur that conserves aluminum, but in exchange causes smectite to dissolve [339]:

$$\text{Smectite} + K^+ \rightarrow \text{illite} + Si^{4+} + Fe^{3+} + Na^+ + Mg^{2+}$$

There is a correlation between the smectite content and the depth of oil reservoirs [377]. The illitization of smectite takes place between 60-120°C, which is the "golden zone" for oil occurrence [378].

Eberl [379] suggested three zones for illite formation during diagenesis. In the first 1.85-3 km, smectite is transformed to illite by K^+ ion exchange. In the following kilometer, organic acids dissolve K-bearing phases and smectite leading to a neoformation of illite. At depths >4 km Ostwald ripening happens through recrystallization from less stable illite crystals.

In sandstones, kaolinite is usually formed by the alteration of K-feldspar by the following reaction:

$$2\ KAlSi_3O_8 + 2H^+ + 9H_2O \rightarrow Al_2Si_2O_5(OH)_4 + 4\ H_4SiO_4 + 2\ K^+ \quad <120°C$$

K-feldspar kaolinite

At temperatures above 120°C kaolinite and K-feldspar react together to form illite:

$$2\ KAlSi_3O_8 + Al_2Si_2O_5(OH)_4 \rightarrow KAl_3Si_3O_{10}(OH)_2 + SiO_2\ (aq) + H_2O$$

K-feldspar kaolinite illite

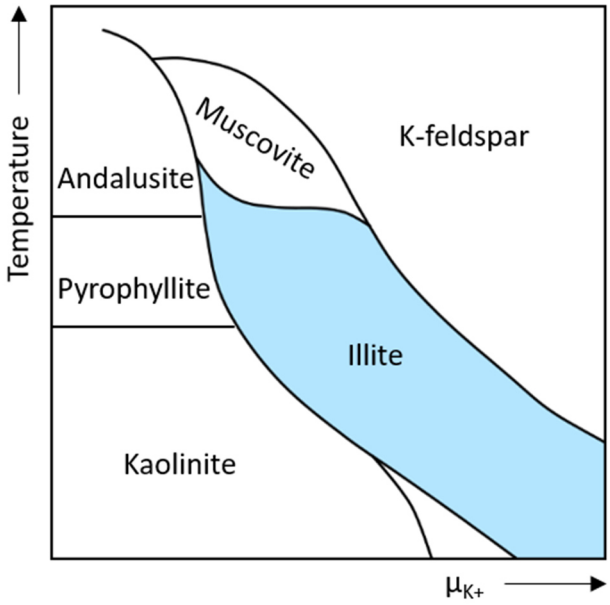

Figure A 2: The stability of illite depicted in a temperature vs. μ_{K+} diagram. The lower the temperature, the higher the K^+/H^+ activity ratio has to be for illite to be formed.

In this case illitized sandstones should have no remaining kaolinite and K-feldspar [372], except the opposite has been observed [380]. In addition, illite was detected at lower temperatures of 90-95°C [381]. Below 120°C, the K^+/H^+ activity ratio, which is controlled by the solubility of K-feldspar, is not high enough to overcome the energy barrier for illite formation [339,382]. This means that for illitization to occur at lower temperatures, the fluid must be highly oversaturated in K^+ (see Figure A 2). However, this also results in a high degree of

oversaturation with regard to K-feldspar, which can no longer be dissolved. Therefore, an external source of K^+ or an increase in pH is required [372]:

$$3\ Al_2Si_2O_5(OH)_4 + 2\ K^+ \rightarrow 2\ KAl_3Si_3O_{10}(OH)_2 + 2\ H^+ + 3\ H_2O$$

Kaolinite illite

Illite smectite mixed layer

Illite-smectite mixed layer clay minerals are 2:1 phyllosilicates with non-expandable illite and expandable smectite layers [383]. This interstratification occurs in different proportions. The dominating layers have an impact on geo-engineering projects and mineral or geothermal exploration [384]. The proportion of illite in I-S increases with increasing temperature, time and burial depth [385]. The transformation can either be discontinuous with discrete phases, which must be formed via dissolution and neocrystallization of illite [207]. Hydrothermal fluids can transport the reactants [386]. On the other hand, continuous layer sequences could occur by successive replacement of individual layers, which is a solid-state reaction [387] or by a mixture of the two [388].

Spinodal decomposition is an important mechanism for the segregation of solid solutions between two end-members with the same structure and, accordingly, with a continuous free energy curve (ΔG_{mix}) [87]. It is based on the concept of uphill diffusion [269]. No nucleation is needed for this, but the solid solution segregates continuously. The composition range in which this is possible is defined in the free energy curve by two inflection points [88] (see Figure A 3A)). In nucleation, there is a local fluctuation in composition with a high amplitude. In contrast, spinodal segregation has a large fluctuation in composition with a low amplitude. The spatial concentration varies with a sinusoidal shape. The diffusion coefficient is proportional to d^2G/dx^2, which is negative between the two inflection points on the free energy curve. In the initial stages, the solid solution remains a single phase. To increase the amplitude of the phase distribution, driven by reduction of the free energy, Na^+, for example, must diffuse up the concentration gradient [88]. With increasing chemical segregation, the amplitudes increase until a bimodal composition is reached which is in equilibrium (see Figure A 3B)). Distinguishing spinodal segregation from nucleation is possible only in the very early stages from maturation [87] (see Figure A 3: Spinodal decomposition. A) The $\triangle G_{mix}$ curve has two inflection points for a solid solution in-between which the free energy will be reduced for an exsolution of an average composition of c_2. Fluctuations between c_2^+ and c_2^- lead to a reduction in free energy of $\triangle G_2$. Outside of the inflection points (c_1) fluctuations lead to an increase in free energy. The positions of the inflection points at certain temperatures are determined by the spinodal curve. The solvus is defined by the tangents of the minima of the free energy curve. B) shows the progression of spinodal decomposition while C) shows nucleation and growth. C_0 is the starting composition of the solid solution. C_1 and c_2 are the equilibrium compositions of the segregated phases. In the end the lamellar intergrowths cannot be distinguished anymore.Figure A 3C)). At low temperatures and slow diffusion rates, there is a possibility that even over long periods of time the process will not progress beyond the spinodal stage. The chemical fluctuations are periodic and can be described as sinusoidal modulations in composition. Their wavelength is usually between 50 and 500 Å. The interfaces are oriented perpendicular to the direction with the largest chemically induced eigenstrain leading to a minimization in elastic strain energy [270].

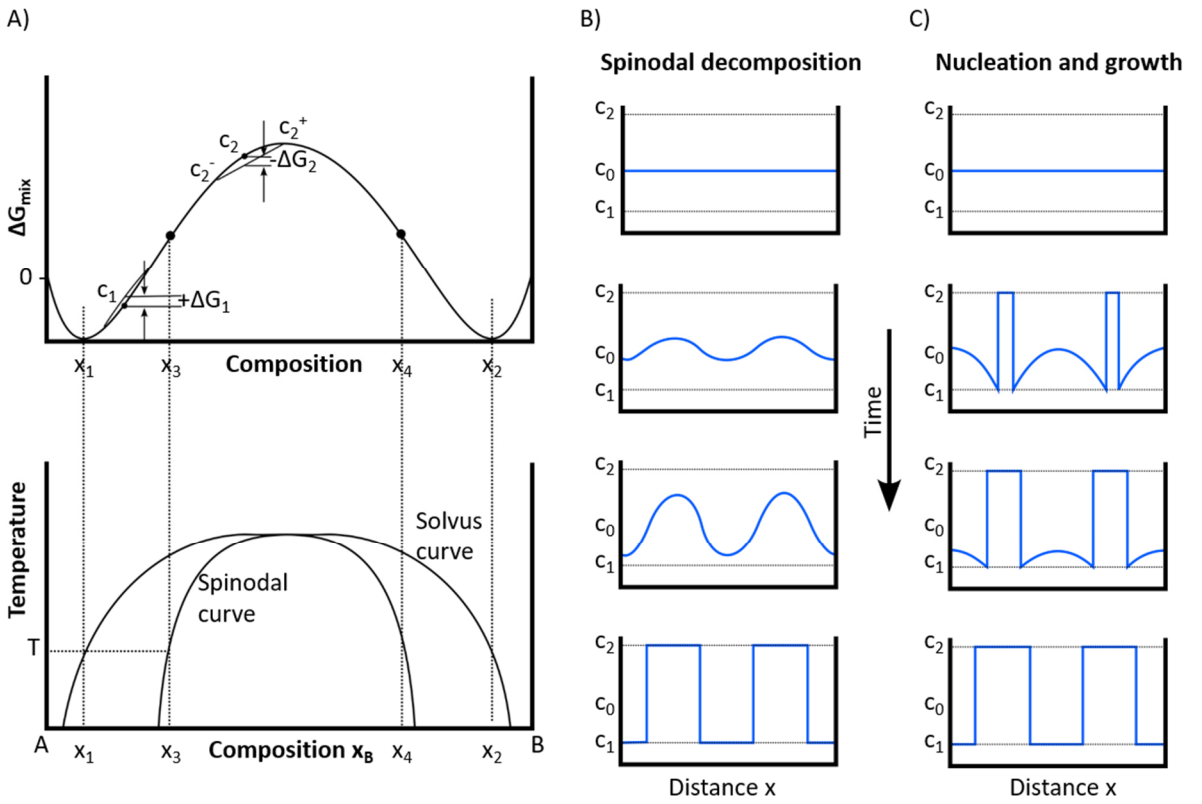

Figure A 3: Spinodal decomposition. A) The ΔG_{mix} curve has two inflection points for a solid solution in-between which the free energy will be reduced for an exsolution of an average composition of c_2. Fluctuations between c_2^+ and c_2^- lead to a reduction in free energy of ΔG_2. Outside of the inflection points (c_1) fluctuations lead to an increase in free energy. The positions of the inflection points at certain temperatures are determined by the spinodal curve. The solvus is defined by the tangents of the minima of the free energy curve. B) shows the progression of spinodal decomposition while C) shows nucleation and growth. C_0 is the starting composition of the solid solution. C_1 and c_2 are the equilibrium compositions of the segregated phases. In the end the lamellar intergrowths cannot be distinguished anymore.

Appendix 4: Determination of crystal morphologies of barite precipitates based on NaCl and inhibitor addition.

Barite crystals obtained from crystallization experiments performed by Philipp Zuber were investigated. These crystals were prepared following TEM standards, allowing for characterization of the crystals using TEM imaging and diffraction modes, was well as EDS analysis. Additionally, the orientation matrix within the crystals was measured using Fast-ADT data to determine the preferred or inhibited growth directions. In three-dimensional reciprocal space, the unit cell of barite was found to be: a = 8.88 Å, b = 5.46 Å, c = 7.16 Å, with $\alpha = \beta = \gamma = 90°$ (2/m 2/m 2/m; orthorhombic-dipyramidal). Due to the presence of preferred orientations in the barite crystals, the diffraction patterns could be indexed at a tilt angle of 0° in the three-dimensional reconstructed reciprocal space and the orientation matrix in this position was determined. Three different crystallization series were analyzed: (i) variation of NaCl content at room temperature, (ii) variation of NaCl content at 90°C and (iii) addition of an inhibitor along with NaCl.

In the crystallization series (i), involving a variation of NaCl content at room temperature, a preferential orientation along the [100] direction was observed. The facets of the barite crystals undergo changes in their size ratio as the NaCl content increases from 0 mol/L to 1 mol/L. The addition of NaCl significantly inhibits growth along the [001] direction, while favoring growth along the [010] direction. Consequently, the (001) facet enlarges, while the (010) facet drastically reduces in size (see Figure A 4). However, the preferential orientation remains the same for all four investigated single crystals of barite.

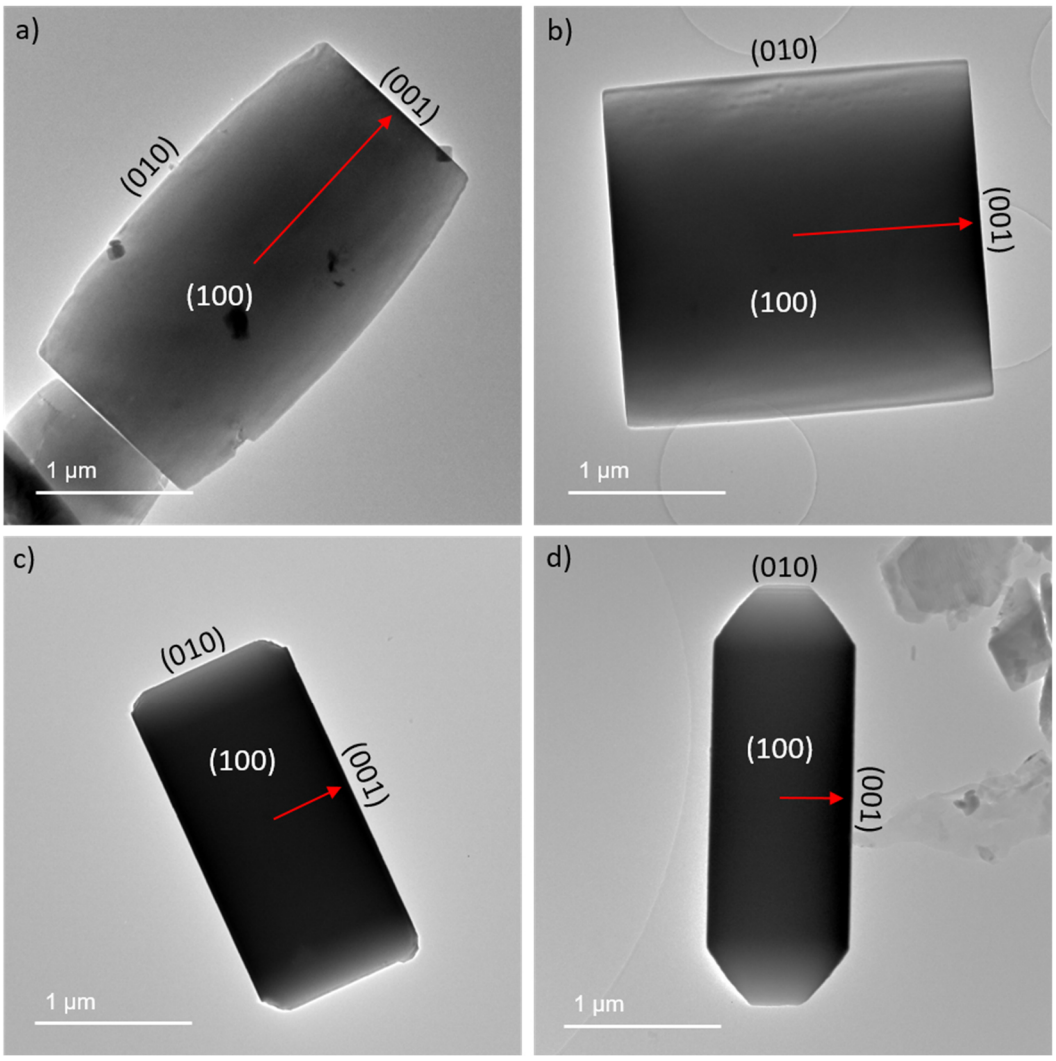

Figure A 4: Crystallization series (i) of barite at room temperature with increasing NaCl content: a) 0 mol/L, b) 0.1 mol/L, c) 0.5 mol/L and d) 1 mol/L. The growth along the [001] direction (red arrow) is inhibited by the addition of NaCl, while the [010] direction is strongly favored.

In crystallization series (ii), varying the NaCl content at 90°C, an initial preference for the [100] orientation is observed. However, at moderate NaCl concentrations ranging from 0.25 to 0.75 mol/L, the crystals become more isometric. Growth along the [100] direction is favored in this range. For high NaCl concentrations (5 mol/L), this direction is strongly inhibited again. The [010] direction experiences accelerated growth due to the addition of NaCl. Unlike the experiments at room temperature, growth along the [001] direction is also favored here, resulting in a significant reduction of the (001) facet size (see Figure A 5).

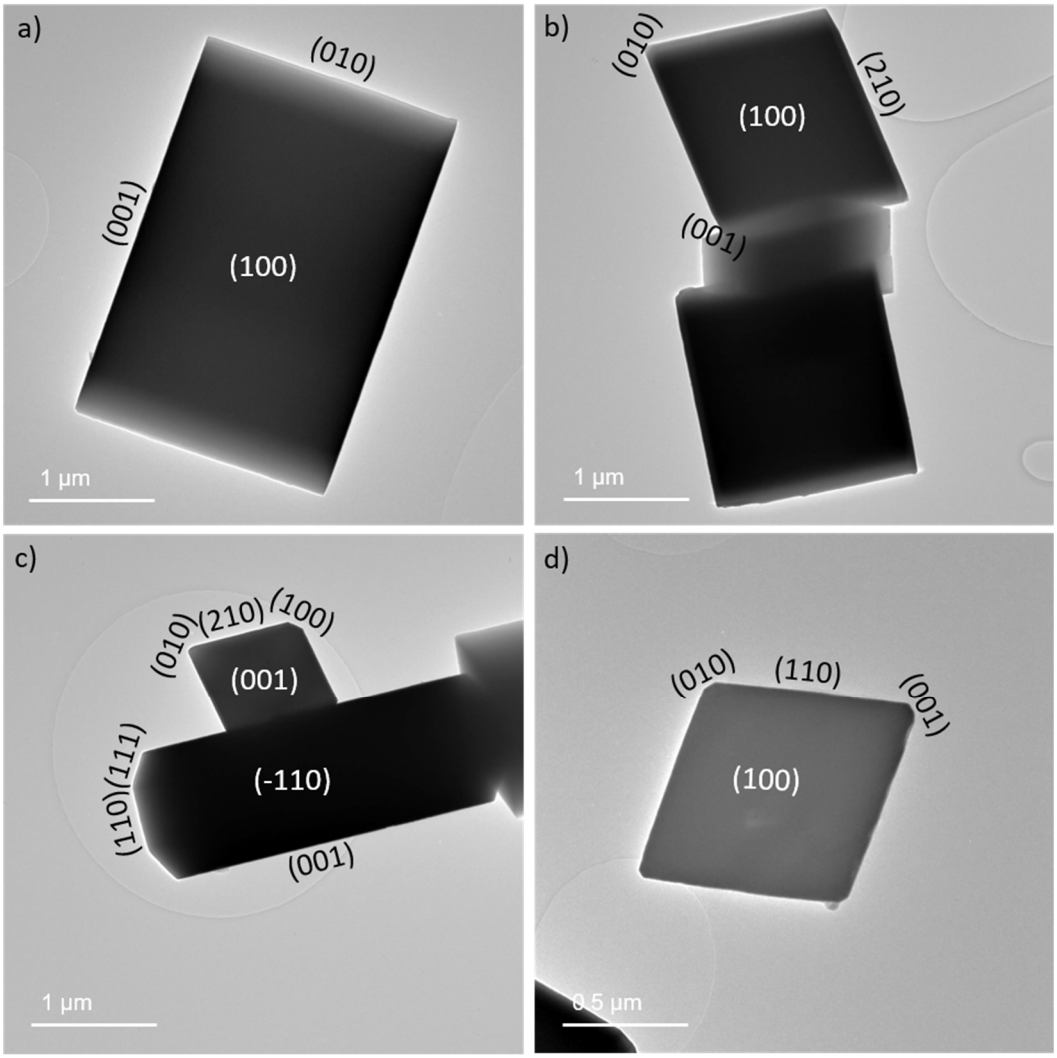

Figure A 5: In crystallization series (ii) of barite at 90°C with increasing NaCl content, a) 0.1 mol/L, b) 0.25 mol/L, c) 0.75 mol/L and d) 5 mol/L, the growth along the [100] direction is inhibited by the addition of NaCl, while the [010] and [001] directions facets.

Diethylentriaminepentamethylenephosphonic acid (DTPMP) is used as an inhibitor for the crystallization of barite in geothermal plants. The addition of DTPMP alters the surface energies of the individual facets. Crystal formation is not completely inhibited, the morphology changes only slightly compared to the crystallization series without inhibitor addition. It is noticeable that smooth facets are no longer formed (see Figure A 6). Instead, the facets are rounded and indentations can be observed in the crystal surface. Increasing the inhibitor concentration from 1 mol/L to 10 mol/L inhibits the growth direction along [001], resulting in elongated crystals. Interestingly, the addition of 1 mol/L NaCl to 1 mol/L DTPMP has a similar effect. However, when a smaller amount of NaCl (0.1 mol/L) is added, the (001) facet is smooth again. Additionally, the crystals are split into smaller domains. The orientation remains similar, allowing the main zones to still be observed in the diffraction pattern of the entire crystal (see Figure A 6E)). This splitting into smaller domains occurs independently of the morphology of the barite crystal and always happens in the direction perpendicular to the (100) plane, namely along [100]. It is particularly pronounced when adding 0.1 mol/L NaCl and 1 mol/L DTPMP.

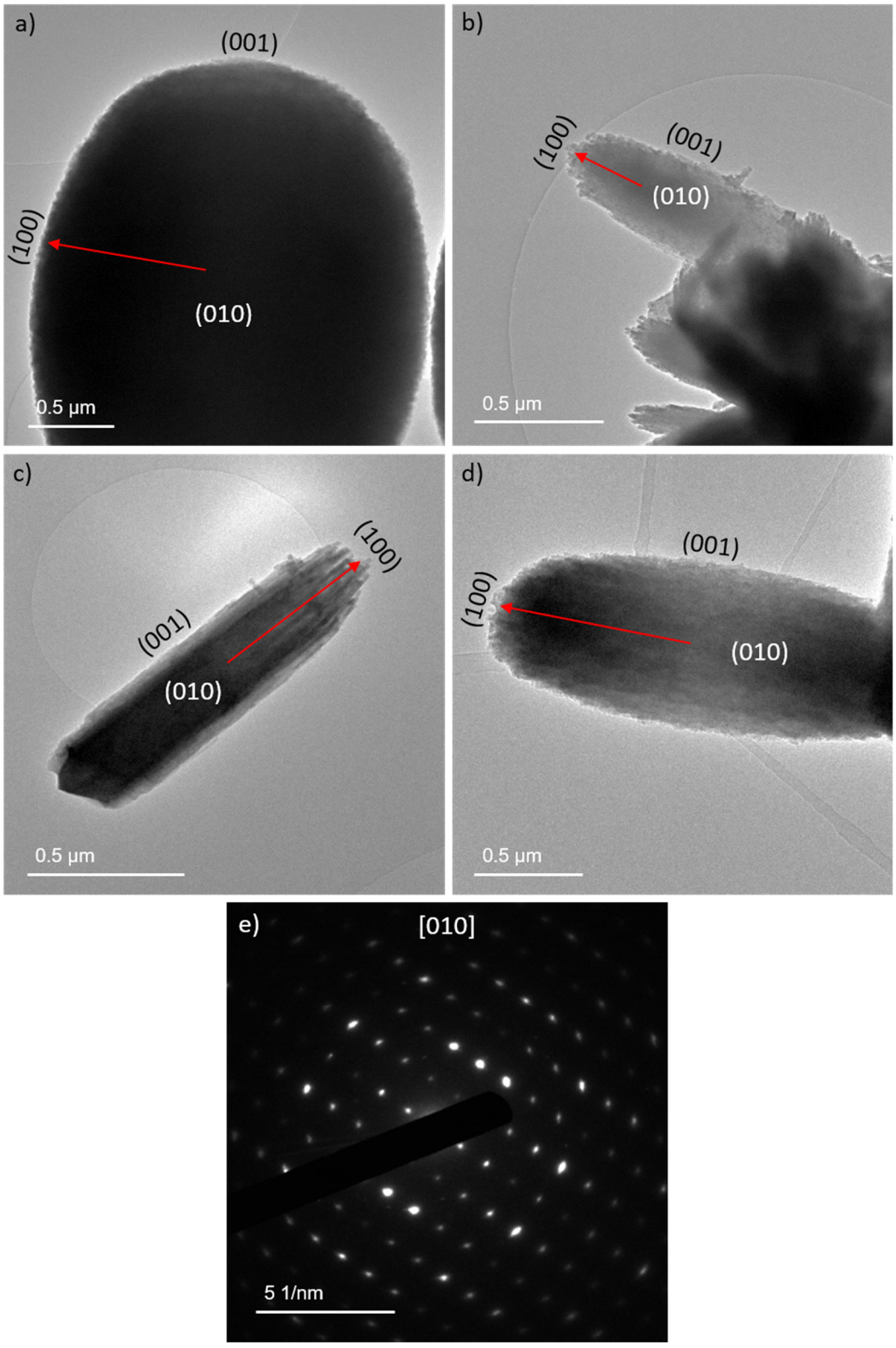

Figure A 6: Crystallization series (iii) of barite with inhibitor DTPMP: a) 1 mol/L DTPMP, b) 10 mol/L DTPMP, c) 1 mol/L DTPMP and 0.1 mol/L NaCl and d) 1 mol/L DTPMP and 1 mol/L NaCl. Along the [100] direction (red arrow), elongated nanocrystals form, which exhibit a similar orientation and merge into a larger crystal. E) Diffraction pattern of the barite crystal depicted in b). The diffraction spots are slightly blurred. Despite the splitting of the crystal into smaller domains, it displays a relatively uniform diffraction pattern.

To investigate the nanocrystallites in more detail and detect possible inhibitor adsorption, HRTEM examinations were conducted. Figure A 7 exemplifies this for barite crystals exposed to 10 mol/L DTPMP. For clarification of the morphology, Figure A 7A) displays a SEM SE image

of the crystals. The DTPMP adsorption was observed as an amorphous boundary on certain surfaces of the nanocrystals, although not all facets were equally covered. This suggests a preferential adsorption of the inhibitor on specific growth facets. Since the barite nucleus crystallizes directly from the solution containing DTPMP, it is likely that DTPMP attaches to the surfaces of the barite nanocrystallites immediately after their nucleation. Additional nanocrystallites can grow on this newly generated surface, which are again enveloped by DTPMP. As the inhibitor referentially adsorbs on certain facets, there is a degree of freedom in the orientation of newly growing crystals. This results in the barite crystal exhibiting slightly different local orientations but displaying a relatively uniform diffraction pattern when considered as a whole crystal (see Figure A 6E)).

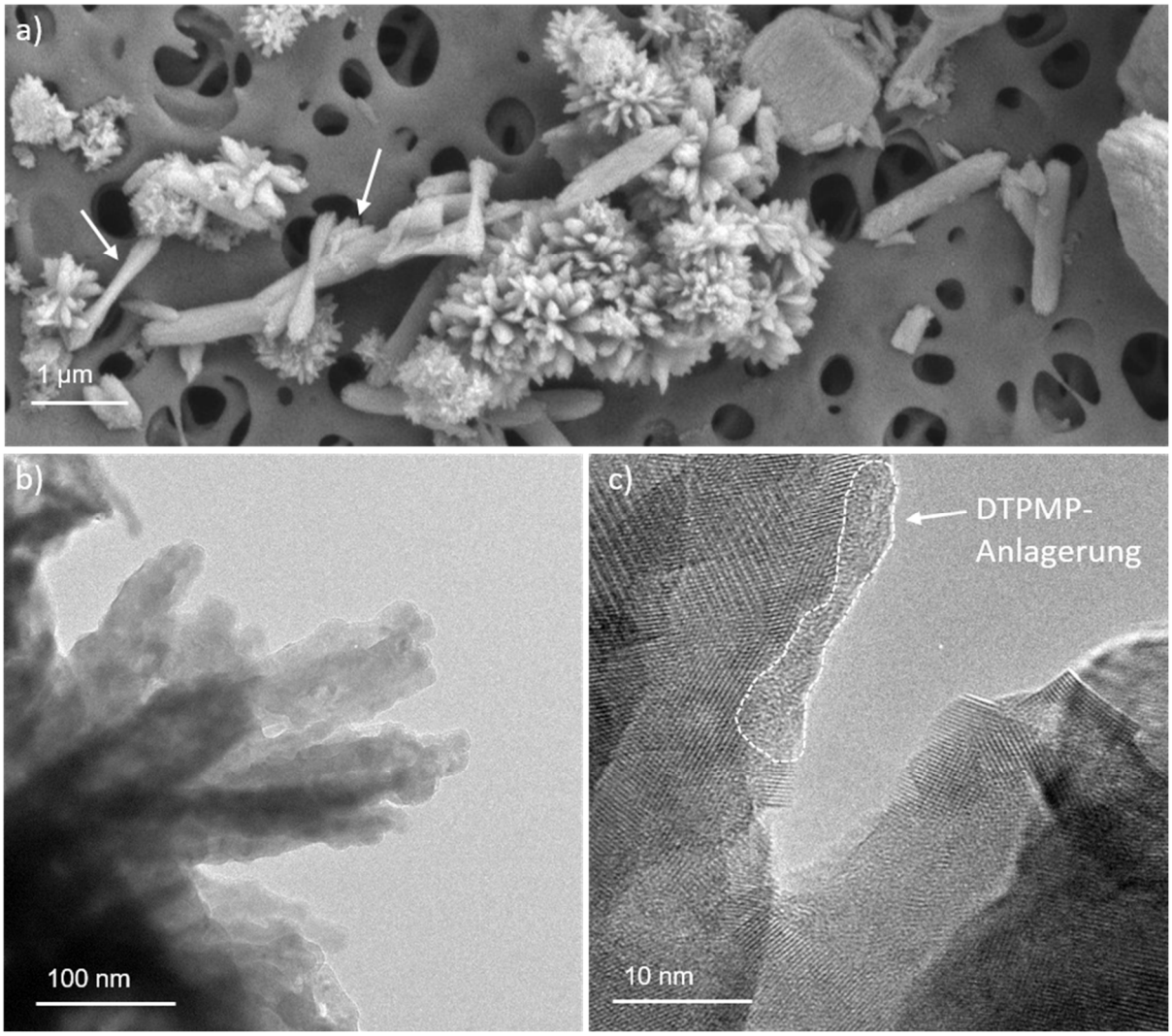

Figure A 7: Barite crystals with 10 mol/L DTPMP. a) SEM SE image of the barite crystals. The arrows highlight exemplary crystals shown in b) and c) in bright-field TEM imaging. In b), the nanocrystallites can be observed. c) HRTEM image of the nanocrystallites displaying different orientations. On the left edge, an attachment of amorphous DTPMP is visible (indicated by a white dashed line), while no attachment occurred on the opposite edge. (SEM image by Philipp Zuber)

The morphology of barite crystals in the crystallization experiments undergoes significant changes upon the addition of NaCl and/or DTPMP. These added substances affect the surface energies on specific facets of the crystals or attach to them, thereby inhibiting growth in that direction and altering the crystal morphology. Such changes in morphology, particularly the observed branching into small nanocrystals, influence the transport properties of barite crystals

and their impact on pore system clogging in rocks. Elongated or branched agglomerates of barite certainly contribute significantly to a reduction in rock permeability.

Appendix 5: All acquired ADT datasets of illite, labradorite and eveslogite with descriptions of the measurements and the cell parameters.

Sample	Crystal	Microscope	Tilt range [°]	Tilt angle [°]	Beam size [nm]	Exposure time [s]	Binning	Precession 1°	Tilt axis	Cell parameters [Å] [°]	Axes in dataset	Remarks
20210531 Illite_D7	Cry2	JEOL 2100	-50 - +50	1	75	1	1	Yes	-152.6	a = 5.11 b = 8.84 c = 10.19 α = 89.58 β = 101.09 γ = 89.22	a, b	1M polytype Two crystals
20210531 Illite_D7	Cry4	JEOL 2100	-60 - +45	1	75	0.5	1	Yes	-152.4	a = 5.13 b = 8.85 c = 9.81 α = 90.00 β = 101.28 γ = 91.36	b	1M polytype
20210531 Illite_D7	Cry8	JEOL 2100	-50 - +60	1	75	1	1	Yes	-153.4	a = 5.18 b = 8.72 c = 10.19 α = 90.53	a, b	1M polytype Diffuse streaks

										β = 100.55 γ = 89.64		
20211029 Illite_D7	Cry2	JEOL 2100	-50 - +35	1	80	1	1	Yes	-152.6	a = 5.19 b = 8.81 c = 9.79 α = 90.31 β = 100.87 γ = 91.18	a, b	1M polytype
20211029 Illite_D7	Cry2	JEOL 2100	-50 - +35	1	80	0.5	1	Yes	-153.2	a = 5.19 b = 8.79 c = 9.64 α = 90.71 β = 100.50 γ = 90.85	a, b	Polycrystalline
20211029 Illite_D7	Cry3	JEOL 2100	-60 - +50	1	80	1	1	Yes	-151.8	a = 5.18 b = 8.93 c = 9.92 α = 89.56 β = 101.38 γ = 91.48	a, b	

20211029 Illite_D7	Cry5	JEOL 2100	-50 - +45	1	80	0.5	1	Yes	-153.4	a = 5.13 b = 8.78 c = 9.76 α = 89.56 β = 100.57 γ = 91.50	a, b	Slightly diffuse
20211106 Illite_D7	Cry3	JEOL 2100	50 - +6	1	80	1	1	Yes		a = b = c = α = β = γ =		Lost crystal
20211106 Illite_D7	Cry6	JEOL 2100	-60 - +60	1	80	1	1	Yes	-152.4	a = 5.06 b = 9.03 c = 9.84 α = 89.80 β = 100.94 γ = 90.91	b	
20211109 Illite_D7	Cry7	JEOL 2100	-60 - +3	1	80	1	1	Yes		a = b =		Lost crystal

										c = α = β = γ =		
20211109 Illite_D7	Cry3	JEOL 2100	-55 - +60	1	100	1	1	Yes	-152.2	a = 5.17 b = 8.70 c = 9.87 α = 89.30 β = 101.56 γ = 90.23	a, b	Used for structure solution
20211109 Illite_D7	Cry4	JEOL 2100	-55 - +60	1	100	1	1	Yes	-152.4	a = 5.17 b = 8.74 c = 9.90 α = 90.17 β = 101. 00 γ = 90.53	a, b	Used for structure solution
20220519 Illite_unalt	Cry3	JEOL 2100	-45 - +60	1	100	0.5	1	Yes	-153.2	a = b = c = α =		Bad dataset

										β = γ =		
20220519 Illite_unalt	Cry7	JEOL 2100	-50 - +60	1	100	0.5	1	Yes	-150.6	a = 5.06 b = 8.94 c = 9.89 α = 89.97 β = 100.90 γ = 90.60	a, b	
20220519 Illite_unalt	Cry10	JEOL 2100	-60 - +60	1	100	0.5	1	Yes	-152.0	a = 5.19 b = 8.75 c = 9.86 α = 90.52 β = 100.91 γ = 90.15	a, b	Beam not always on the crystal
20220617 Illite_E30	Cry2	JEOL 2100	-60 - +60	1	100	0.5	1	Yes	-152.4	a = 5.18 b = 8.95 c = 9.89 α = 90.28 β = 101.93 γ = 91.45	a, b	Slightly diffuse

20220617 Illite_E30	Cry3	JEOL 2100	-60 - +60	1	100	0.5	1	Yes	-152.2	a = 5.12 b = 9.07 c = 9.86 α = 90.81 β = 101.44 γ = 89.96	a, b	Slightly diffuse
20220617 Illite_E30	Cry8	JEOL 2100	-60 - +60	1	100	0.5	1	Yes		a = b = c = α = β = γ =		Polycrystalline
20220617 Illite_E30	Cry9	JEOL 2100	-60 - +60	1	100	0.5	1	Yes	-151.8	a = 5.06 b = 9.03 c = 10.04 α = 89.48 β = 100.64 γ = 90.06	a, b	
20220617 Illite_unalt	Cry3	JEOL 2100	-50 - +50	1	100	0.5	1	Yes	-152.6	a = 5.10 b = 8.95	a, b	twinned

										c = 10.05 α = 89.69 β = 101.75 γ = 89.02		
20220617 Illite_unalt	Cry4	JEOL 2100	-50 - +60	1	100	0.5	1	Yes	-151.2	a = 5.13 b = 9.00 c = 9.82 α = 89.62 β = 101.63 γ = 90.87	a, b	
20220617 Illite_unalt	Cry6	JEOL 2100	-60 - +60	1	100	0.5	1	Yes	-153.6	a = 5.11 b = 9.00 c = 10.18 α = 89.88 β = 99.16 γ = 90.93	a, b	
20220617 Illite_unalt	Cry7	JEOL 2100	-50 - +50	1	100	0.5	1	Yes	-151.4	a = 5.05 b = 9.01 c = 10.05 α = 90.17	a, b	

										β = 101.37 γ = 89.64		
20220622 Illite_E30	Cry1	FEI F30	-60 - +60	0.1	200	0.5	4	No	44	a = 5.25 b = 8.94 c = 10.21 α = 89.61 β = 101.58 γ = 90.23	a, b	Twinned Doubled c axis
20221006 Illite_D7	Cry8	JEOL 2100	-50 - +50	0.2	200	0.1	2	No	-151.8	a = 5.23 b = 8.78 c = 9.87 α = 89.61 β = 100.77 γ = 90.46	a, b	Measured at the very tip Diffuse streaks
20221006 Illite_D7	Cry8	JEOL 2100	-50 - +50	0.2	200	0.1	2	No	-151.6	a = 5.21 b = 8.76 c = 9.87 α = 89.31 β = 100.76 γ = 90.23	a, b	Slightly polycrystalline Diffuse streaks

20221006 Illite_D7	Cry8	JEOL 2100	-50 - +50	0.2	200	0.2	2	No	-151.8	a = 5.23 b = 8.78 c = 9.87 α = 89.62 β = 100.77 γ = 90.46	a, b	Diffuse streaks
20221006 Illite_D7	Cry8	JEOL 2100	-50 - +50	0.2	200	0.1	4	No	-151.6	a = 5.22 b = 8.79 c = 9.79 α = 89.37 β = 100.09 γ = 90.48	a, b	Diffuse streaks
20220928 Illite_D7	Cry1	FEI F30	-60 - +35	0.1	200	0.2		No	47	a = 3.78 b = 6.59 c = 8.45 α = 92.3 β = 100.9 γ = 90.4	a, b	Polycrystalline
20220928 Illite_D7	Cry2	FEI F30	-60 - +60	0.1	200	0.2		No	47	a = b =		Polycrystalline, cell not found

										c = α = β = γ =		
20220928 Illite_D7	Cry3	FEI F30	-60 - +60	0.1	200	0.2		No	48	a = 3.88 b = 6.66 c = 7.90 α = 91.00 β = 101.14 γ = 90.85	a, b	Polycrystalline Diffuse scattering

Sample	Crystal	Microscope	Tilt range [°]	Tilt angle [°]	Beamsize [nm]	Exposure time [s]	Binning	Precession 1°	Tilt axis	Cell parameters [Å] [°]	Axes in dataset	Remarks
20191017 Labradorite_3	Cry1	FEI F30	-60 - +60	1	185	0.4	2	Yes	43.8	a = 8.52 b = 13.52 c = 7.36 α = 93.18 β = 116.09	a, c	

										γ = 90.29		
20191017 Labradorite_3	Cry1	FEI F30	-60 - +60	1	185	0.4	2	Yes	42.8	a = 8.47 b = 13.57 c = 7.37 α = 94.72 β = 116.03 γ = 89.03	a, c	90° rotated
20191017 Labradorite_3	Cry2	FEI F30	-60 - +60	1	185	0.4	2	Yes	43.0	a = b = c = α = β = γ =		Polycrystalline, cell not found
20191017 Labradorite_3	Cry3	FEI F30	-60 - +60	1	185	0.4	2	Yes	43.8	a = 8.46 b = 13.36 c = 7.38 α = 93.47 β = 115.81 γ = 89.58	a, c	

20191017 Labradorite_3	Cry4	FEI F30	-60 - +60	1	185	0.2	2	Yes	43.6	a = 8.46 b = 13.36 c = 7.35 α = 93.76 β = 115.80 γ = 89.80	a, c	
20200128 Labradorite_3	Cry1	JEOL 2100	-60 - +60	1	90		1	Yes		a = b = c = α = β = γ =		Polycrystalline, cell not found
20200128 Labradorite_3	Cry3	JEOL 2100	-60 - +60	1	90		1	Yes		a = b = c = α = β = γ =		Polycrystalline, cell not found
20200204 Labradorite_3	Cry5	FEI F30	-60 - +60	1	150	0.5	2	Yes	43.2	a = 7.79 b = 12.25	a, c	

										c = 6.76 α = 93.64 β = 116.69 γ = 89.98		
20200204 Labradorite_3	Cry5	FEI F30	-60 - +60	1	150	0.5	2	Yes	43.8	a = 7.76 b = 12.21 c = 6.82 α = 93.34 β = 116.44 γ = 89.72	a, c	90° rotated
20200204 Labradorite_3	Cry5	FEI F30	-60 - +60	1	150	0.25	2	Yes	43.4	a = 7.77 b = 12.25 c = 6.75 α = 93.65 β = 116.49 γ = 89.98	a, c	
20200204 Labradorite_3	Cry5	FEI F30	-60 - +60	1	150	0.25	2	Yes	43.6	a = 7.75 b = 12.21 c = 6.77 α = 93.33	a, c	90° rotated

										β = 116.54 γ = 89.72		
20200204 Labradorite_3	Cry5_in	FEI F30	-60 - +60	1	150	0.5	2	Yes	43.8	a = 7.74 b = 12.24 c = 6.71 α = 93.62 β = 116.06 γ = 89.40	a, c	
20200204 Labradorite_3	Cry5_in	FEI F30	-60 - +60	1	150	0.5	2	Yes	43.8	a = 7.75 b = 12.23 c = 6.78 α = 94.14 β = 116.64 γ = 89.98	a, c	90° rotated
20200210 Labradorite_3	Cry1	FEI F30	-60 - +60	1	150	0.5	2	Yes	43.8	a = 7.73 b = 12.20 c = 6.80 α = 93.99 β = 116.06 γ =89.04	a, c	

20200210 Labradorite_3	Cry1_2	FEI F30	-60 - +60	1	150	0.5	2	Yes	43.6	a = 7.79 b = 12.20 c = 6.82 α = 93.81 β = 116.25 γ = 89.82	a, c	
20200210 Labradorite_2	Cry2	FEI F30	-60 - +60	1	150	0.5	2	Yes	43.6	a = 7.73 b = 12.20 c = 6.65 α = 93.23 β = 115.24 γ = 90.77	a, b	On one lamella
20200210 Labradorite_2	Cry3	FEI F30	-60 - +60	1	200	0.5	2	Yes		a = b = c = α = β = γ =		On several lamellae, lost crystal
20200211 Labradorite_2	Cry1	FEI F30	-60 - +60	0.5	150	0.25	2	Yes	43	a = 7.83 b = 12.13	a, b	

										c = 6.74 α = 93.40 β = 115.50 γ = 90.12		
20200211 Labradorite_2	Cry2	FEI F30	-60 - +60	0.25	150	0.25	2	Yes	44	a = 7.76 b = 12.20 c = 6.70 α = 92.62 β = 114.88 γ = 89.66	a, b	Smeared reflections
20200211 Labradorite_2	Cry3	FEI F30	-60 - +60	1	150	0.25	2	Yes		a = b = c = α = β = γ =		Bad dataset
20210217 Labradorite_3	Cry3	JEOL 2100	-50 - +50	1	70	1.5	1	Yes	-152.8	a = 8.00 b = 12.72 c = 6.92 α = 93.17	a, b	Bad dataset

										β = 116.77 γ = 91.5		
20210311 Labradorite_P	Cry1	JEOL 2100	-50 - +50	1	75	1.5	1	Yes	-152.6	a = 7.87 b = 12.69 c = 7.04 α = 93.76 β = 115.62 γ =90.02	a	Bad dataset
20210311 Labradorite_P	Cry2	JEOL 2100	-40 - +35	1	75	1.5	1	Yes	-152.2	a = 7.80 b = 12.59 c = 7.00 α = 93.57 β = 116.02 γ = 90.00	a, b	
20210311 Labradorite_P	Cry2	JEOL 2100	-40 - +35	1	75	0.5	1	Yes	-152.2	a = 7.73 b = 12.75 c = 6.95 α = 94.20 β = 116.10 γ = 89.45	a,c	

20210421 Labradorite_2	Cry1	JEOL 2100	-20 - +20	1	150	0.5	1	Yes	-152.2	a = b =. c = α = β = γ =		Pericline boundary
20210421 Labradorite_2	Cry2	JEOL 2100	-20 - +20	1	150	0.5	1	Yes	-152.0	a = 7.75 b = 12.77 c = 6.97 α = 94.70 β = 115.32 γ = 91.21		Pericline matrix
20210421 Labradorite_2	Cry3	JEOL 2100	-20 - +20	1	150	0.5	1	Yes	-153.0	a = 7.75 b = 12.71 c = 6.95 α = 92.32 β = 115.56 γ = 89.23		Pericline twin
20210518 Labradorite_3	Cry2	JEOL 2100	-60 - +60	1	75	0.5	1	Yes	-152.6	a = 8.03 b = 12.70	a, b	

										c = 6.90 α = 92.41 β = 116.55 γ = 91.62		
20210518 Labradorite_3	Cry2_2	JEOL 2100	-60 - +60	1	75	0.5	1	Yes	-153.2	a = 7.99 b = 12.70 c = 6.91 α = 93.36 β = 115.95 γ = 90.95	a, b	
20210518 Labradorite_3	Cry2_3	JEOL 2100	-60 - +60	1	75	0.5	1	Yes	-153	a = 7.99 b = 12.70 c = 6.92 α = 93.17 β = 116.15 γ = 91.16	a, b	
20210518 Labradorite_3	Cry3	JEOL 2100	-60 - +60	1	75	0.5	1	Yes	-152.6	a = 7.99 b = 12.70 c = 6.91 α = 92.84	a, b	

										β = 115.88 γ = 91.21		
20210518 Labradorite_3	Cry3_2	JEOL 2100	-60 - +60	1	75	0.5	1	Yes	-152.8	a = 7.99 b = 12.69 c = 6.90 α = 92.48 β = 115.90 γ = 91.21	a, b	
20211214 Labradorite_P	Cry5	JEOL 2100	-60 - +60	1	100	1	1	Yes	-152.4	a = 8.04 b = 12.64 c = 6.88 α = 94.47 β = 116.58 γ = 87.69	b	
20211214 Labradorite_P	Cry5	JEOL 2100	-60 - +60	1	100	0.5	1	Yes	-152.4	a = 8.02 b = 12.63 c = 6.88 α = 93.84 β = 116.70 γ = 88.02	b	

20211214 Labradorite_P	Cry6	JEOL 2100	-60 - +60	1	100	1	1	Yes	-152.4	a = 8.00 b = 12.46 c = 6.90 α = 93.50 β = 114.48 γ = 89.45	a, c	
20211214 Labradorite_P	Cry6	JEOL 2100	-60 - +60	1	100	0.5	1	Yes	-152.2	a = 7.92 b = 12.56 c = 6.99 α = 94.12 β = 115.34 γ = 90.23	a, b	
20211214 Labradorite_P	Cry7	JEOL 2100	-60 - +60	1	100	1	1	Yes	-152.0	a = 8.04 b = 12.60 c = 7.07 α = 93.18 β = 117.85 γ = 89.66	a, c	
20211214 Labradorite_P	Cry7	JEOL 2100	-60 - +60	1	100	0.5	1	Yes	-152.2	a = 7.99 b = 12.60	b	

										c = 6.89 α = 93.94 β = 115.34 γ = 89.78		
20211214 Labradorite_P	Cry10	JEOL 2100	-55 - +60	1	100	1	1	Yes	-152.8	a = 7.94 b = 12.66 c = 6.95 α = 95.23 β = 117.31 γ = 88.99	b	
20211214 Labradorite_P	Cry10	JEOL 2100	-55 - +60	1	100	0.5	1	Yes	-152.2	a = 7.95 b = 12.77 c = 6.98 α = 93.25 β = 117.21 γ = 89.20	c	

Sample	Crystal	Microscope	Tilt range [°]	Tilt angle [°]	Beamsize [nm]	Exposure time [s]	Binning	Precession 1°	Tilt axis	Cell parameters [Å] [°]	Axes in dataset	Remarks
20200304 Eveslogite_II_lamellae_flat	Cry1	FEI F30	-50 - +50	1	120	1	2	Yes	43.8	a = 14.86 b = 46.34 c = 16.60 α = 90.07 β = 109.57 γ = 90.15		
20200304 Eveslogite_II_lamellae_flat	Cry2	FEI F30	-45 - +45	1	120	1	2	Yes	43.8	a = 14.92 b = 46.77 c = 16.69 α = 90.12 β = 109.55 γ = 89.98		
20200320 Eveslogite_P	Cry5	FEI F30	-60 - +50	1	120	1	2	Yes	45.0	a = 14.80 b = 46.21 c = 16.34 α = 90.29 β = 110.02		

										γ = 90.85		
20200320 Eveslogite_P	Cry6_1	FEI F30	-60 - +38	1	120	1	2	Yes		a = b = c = α = β = γ =		Lost crystal
20200320 Eveslogite_P	Cry6_2	FEI F30	-60 - +60	1	120	1	2	Yes	45.4	a = 14.93 b = 46.30 c = 16.58 α = 90.20 β = 109.52 γ = 90.31		
20200320 Eveslogite_P	Cry7_1	FEI F30	-60 - +50	1	120	1	2	Yes		a = b = c = α = β = γ =		Polycrystalline Lost crystal

20200320 Eveslogite_P	Cry7_2	FEI F30	-60 - +50	1	120	1	2	Yes		a = b = c = α = β = γ =		Polycrystalline Lost crystal
20200320 Eveslogite_P	Cry14	FEI F30	-60 - +60	1	120	1	2	Yes	44.8	a = 14.97 b = 46.25 c = 16.68 α = 90.03 β = 109.59 γ = 90.25		
20200320 Eveslogite_P	Cry15	FEI F30	-60 - +60	1	120	1	2	Yes		a = b = c = α = β = γ =		Lost crystal
20200320 Eveslogite_P	Cry16	FEI F30	-50 - +50	1	120	1	2	Yes		a = b =		Lost crystal

										c = α = β = γ =		
20200320 Eveslogite_P	Cry17_1	FEI F30	-50 - +50	1	120	1	2	Yes	44.6	a = 14.96 b = 46.26 c = 16.65 α = 90.01 β = 109.58 γ = 90.26		
20200320 Eveslogite_P	Cry17_2	FEI F30	-50 - +50	1	120	1	2	Yes	45.0	a = 14.96 b = 46.26 c = 16.65 α = 90.01 β = 109.58 γ = 90.26		
20200320 Eveslogite_P	Cry18	FEI F30	-60 - +60	1	120	1	2	Yes	44.0	a = 14.82 b = 46.23 c = 16.73 α = 90.10		

										β = 109.79 γ = 90.50		
20200318 Eveslogite_hochkant	Cry8	FEI F30	-60 - +60	1	120	1	2	Yes	43.8	a = 14.95 b = 46.54 c = 16.62 α = 90.07 β = 109.77 γ = 90.48		

Appendix 6: Individual and average bond lengths of the single cell of labradorite.

T	O	Single cell		
		kinematical	dynamical	
		Distance [Å]	Distance [Å]	Average [Å]
T2o	O2	1.66(2)	1.677(8)	1.652(7)
	O3	1.637(13)	1.633(5)	
	O4	1.610(17)	1.650(7)	
	O7	1.649(18)	1.646(7)	
T1o	O1	1.67(2)	1.653(9)	1.678(7)
	O6	1.700(17)	1.675(6)	
	O7	1.665(17)	1.686(7)	
	O8	1.668(14)	1.697(6)	
T1m	O3	1.620(13)	1.635(5)	1.646(8)
	O4	1.72(2)	1.671(10)	
	O5	1.650(19)	1.614(7)	
	O6	1.656(18)	1.664(7)	
T2m	O1	1.640(19)	1.649(7)	1.655(7)
	O2	1.68(2)	1.680(8)	
	O5	1.60(2)	1.641(7)	
	O8	1.664(13)	1.648(5)	
M1	O1	3.21(4)	3.651(18)	
	O2	2.34(2)	2.352(13)	
	O3	2.91(4)	3.570(18)	
	O4	3.12(4)	2.671(17)	
	O5	3.42(4)	2.730(16)	
	O6	2.48(4)	2.378(16)	
	O7	2.49(4)	2.422(16)	
	O8	2.40(4)	2.544(16)	
	M2	0.67(6)	0.78(2)	
M2	O1	3.60(4)	3.127(16)	
	O2	2.31(3)	2.310(10)	
	O3	3.58(5)	2.823(15)	
	O4	2.67(4)	3.190(17)	
	O5	2.79(4)	3.472(15)	
	O6	2.44(4)	2.470(13)	
	O7	2.42(4)	2.482(12)	
	O8	2.59(5)	2.405(15)	

Appendix 7: Atom positions in the labradorite structure (x, y, z) of the single cell with their occupancies (occ) and their anisotropic temperature factor (U(aniso); U11, U22, U33, U12, U13, U23) after kinematical refinement.

	x	y	z	occ	U(aniso) [Å]
M1Ca	-0.237(3)	0.492(4)	0.150(4)	0.32	-0.012(8) 0.29(5) 0.032(15)
M1Na				0.33	-0.032(17) 0.003(9) -0.14(2)
M1K				0.03	
M2Ca	-0.225(4)	0.528(3)	0.091(5)	0.32	0.001(14) 0.03(2) 0.025(19)
T_{1o}Si	0.0081(10)	0.1634(10)	0.2191(12)	0.46	-0.017(4) 0.030(9) -0.018(4)
T_{1o}Al				0.54	-0.004(4) -0.008(3) 0.001(4)
T_{1m}Si	0.0042(10)	0.8200(9)	0.2333(11)	0.69	-0.009(4) 0.015(8) -0.020(4)
T_{1m}Al				0.31	0.007(4) -0.004(3) 0.000(4)
T_{2o}Si	0.1854(9)	0.6094(8)	0.3166(12)	0.64	-0.020(4) 0.009(8) -0.014(4)
T_{2o}Al				0.36	0.000(4) -0.007(3) -0.005(4)
T_{2m}Si	0.1811(9)	0.3789(9)	0.3547(12)	0.62	-0.023(4) 0.039(10) -0.016(4)
T_{2m}Al				0.38	-0.001(4) -0.006(3) -0.004(4)
O1	0.0142(19)	0.2915(14)	0.2762(19)	1	0.013(7) 0.004(13) -0.009(6) -0.004(6) -0.004(5) 0.001(6)
O2	0.0815(16)	0.4933(15)	0.2747(19)	1	-0.008(6) 0.033(15) -0.006(6) 0.001(6) -0.007(5) 0.007(7)
O3	0.3102(18)	0.6347(14)	0.5693(19)	1	0.007(7) 0.012(13) -0.013(7) 0.003(6) -0.012(5) -0.003(6)
O4	0.0170(15)	0.6867(15)	0.2181(18)	1	-0.012(6) 0.051(15) -0.016(6) 0.015(7) -0.015(5) -0.022(7)
O5	0.3148(17)	0.3506(17)	0.251(2)	1	-0.007(6) 0.066(17) 0.010(8) 0.005(7) 0.009(6) -0.014(8)
O6	-0.0012(18)	0.8685(15)	0.0202(17)	1	0.018(8) 0.051(15) -0.018(6) 0.009(8) 0.015(6) 0.014(7)
O7	0.3133(16)	0.6086(15)	0.1905(19)	1	-0.012(6) 0.043(15) -0.007(6) -0.025(7) -0.005(5) -0.009(7)
O8	0.3009(16)	0.3913(13)	0.6152(18)	1	-0.001(6) 0.001(12) -0.011(7) 0.000(6) -0.011(5) 0.004(6)

Appendix 8: Atom positions in the labradorite structure (x, y, z) of the single cell with their occupancies (occ) and their anisotropic temperature factor (U(aniso); U11, U22, U33, U12, U13, U23) after dynamical refinement.

	x	y	z	occ	U(aniso) [Å]
M1Ca	-0.2313(12)	0.4862(13)	0.1598(13)	0.32	0.027(3) 0.116(18) 0.051(6)
M1Na				0.33	0.000(6) 0.016(4) -0.036(6)
M1K				0.03	
M2Ca	-0.2291(16)	0.5306(14)	0.0918(17)	0.32	0.013(4) 0.011(10) 0.013(5)
$T_{1o}Si$	0.0062(4)	0.1642(4)	0.2141(4)	0.46	0.007(1) 0.016(4) 0.0087(16)
$T_{1o}Al$				0.54	-0.005(2) 0.002(1) -0.001(2)
$T_{1m}Si$	0.0030(4)	0.8191(4)	0.2333(4)	0.69	0.007(1) 0.008(4) 0.0092(15)
$T_{1m}Al$				0.31	0.0084(17) 0.003(1) 0.001(2)
$T_{2o}Si$	0.1860(3)	0.6094(3)	0.3163(4)	0.64	0.008(1) 0.000(4) 0.0089(15)
$T_{2o}Al$				0.36	0.005(2) 0.003(1) 0.0015(16)
$T_{2m}Si$	0.1827(3)	0.3787(3)	0.3581(4)	0.62	0.007(1) 0.008(4) 0.0086(15)
$T_{2m}Al$				0.38	-0.0008(17) 0.002(1) 0.003(2)
O1	0.0147(6)	0.2908(6)	0.2767(7)	1	0.020(2) 0.045(8) 0.021(3)
					-0.010(3) 0.007(2) 0.003(3)
O2	0.0818(5)	0.4925(5)	0.2783(7)	1	0.015(2) 0.009(6) 0.019(2)
					-0.004(3) 0.0055(17) 0.001(3)
O3	0.3111(6)	0.6328(6)	0.5689(7)	1	0.019(2) 0.042(7) 0.014(2)
					0.006(3) 0.0004(18) -0.003(3)
O4	0.0142(6)	0.6892(7)	0.2170(7)	1	0.021(2) 0.039(8) 0.022(3)
					0.014(3) -0.0001(19) 0.000(3)
O5	0.3168(6)	0.3522(7)	0.2454(8)	1	0.024(2) 0.037(7) 0.041(3)
					0.006(3) 0.020(2) -0.002(3)
O6	-0.0036(6)	0.8685(6)	0.0192(7)	1	0.028(2) 0.044(7) 0.013(2)
					-0.001(3) 0.0101(19) 0.004(3)
O7	0.3131(6)	0.6051(6)	0.1896(7)	1	0.022(2) 0.021(6) 0.023(2)
					-0.006(3) 0.0115(19) 0.002(3)
O8	0.3021(6)	0.3929(6)	0.6158(6)	1	0.020(2) 0.031(7) 0.013(2)
					-0.002(3) -0.001(2) 0.006(3)

Appendix 9: Position modulation waves of the kinematically refined labradorite structure.

	Position modulation		x	y	z
M1	Wave 1	cos	-0.005(2)	0.0266(17)	-0.0190(13)
		sin	-0.0342(18)	-0.0062(16)	0.0077(13)
	Wave 2	cos	0.001(2)	-0.0229(18)	0.0099(16)
		sin	0.010(2)	0.003(2)	0.0191(15)
M2	Wave 1	cos	-0.004(2)	0.009(2)	-0.0016(16)
		sin	0.014(4)	0.041(4)	-0.006(3)
	Wave2	cos	-0.020(4)	0.019(3)	-0.011(2)
		sin	-0.015(4)	0.012(3)	0.015(2)
T_{1o}	Wave 1	cos	0.0013(14)	0.0071(12)	-0.0021(9)
		sin	0.0103(13)	0.0003(11)	0.0047(9)
	Wave 2	cos	-0.0009(14)	-0.0047(12)	0.0034(9)
		sin	0.0131(14)	0.0173(12)	0.0174(9)
T_{1m}	Wave 1	cos	-0.0006(14)	-0.0017(12)	0.0015(9)
		sin	-0.0004(14)	0.0034(12)	-0.0030(9)
	Wave 2	cos	-0.0019(14)	0.0030(12)	0.0017(9)
		sin	-0.0104(14)	0.0085(12)	0.0116(9)
T_{2o}	Wave 1	cos	-0.0020(13)	-0.0055(12)	0.0020(9)
		sin	0.0007(14)	0.0050(12)	0.0006(9)
	Wave 2	cos	0.0014(14)	-0.0078(12)	0.0034(9)
		sin	0.0067(14)	0.0159(12)	0.0195(9)
T_{2m}	Wave 1	cos	-0.0003(14)	0.0033(12)	0.0007(10)
		sin	0.0037(15)	-0.0043(12)	0.0016(10)
	Wave 2	cos	-0.0068(15)	0.0038(13)	-0.0021(10)
		sin	0.0126(15)	0.0161(13)	0.0199(10)
O1	Wave 1	cos	-0.0018(19)	-0.0121(13)	-0.0034(13)
		sin	-0.0027(19)	-0.0075(15)	0.0028(12)
	Wave 2	cos	0.0300(19)	0.0043(16)	0.0072(13)
		sin	0.0065(19)	0.0061(15)	0.0225(12)
O2	Wave 1	cos	0.001(2)	0.0004(19)	-0.0005(15)
		sin	0.011(2)	0.0023(19)	0.0075(14)
	Wave 2	cos	-0.006(2)	-0.003(2)	-0.0003(15)
		sin	0.014(2)	0.0176(19)	0.0204(15)
O3	Wave 1	cos	-0.002(2)	0.0083(18)	-0.0001(15)
		sin	0.004(2)	-0.0033(17)	-0.0011(15)
	Wave 2	cos	-0.027(2)	0.0094(18)	-0.0109(15)
		sin	0.006(2)	0.0053(17)	0.0262(14)
O4	Wave 1	cos	-0.0060(18)	-0.0007(16)	0.0053(13)
		sin	0.0012(17)	0.0055(15)	-0.0022(13)

	Wave 2	cos	0.0006(17)	-0.0139(16)	0.0107(13)
		sin	-0.0092(17)	-0.0070(15)	0.0213(12)
O5	Wave 1	cos	0.001(2)	0.0131(19)	-0.0109(15)
		sin	0.004(2)	-0.001(2)	0.0015(15)
	Wave 2	cos	-0.013(2)	0.000(2)	-0.0022(17)
		sin	0.013(2)	0.017(2)	0.0195(16)
O6	Wave 1	cos	-0.002(2)	-0.0070(19)	-0.0035(16)
		sin	0.005(2)	-0.0041(19)	-0.0035(15)
	Wave 2	cos	0.007(2)	0.000(2)	0.0026(17)
		sin	0.026(2)	0.0158(19)	0.0259(16)
O7	Wave 1	cos	0.001(2)	-0.0117(18)	-0.0019(14)
		sin	0.000(2)	0.0073(18)	0.0026(14)
	Wave 2	cos	-0.020(2)	-0.0051(19)	0.0024(14)
		sin	-0.009(2)	0.0076(19)	0.0141(14)
O8	Wave 1	cos	0.003(2)	0.0026(19)	0.0028(15)
		sin	0.013(2)	-0.0030(19)	0.0057(15)
	Wave 2	cos	-0.002(2)	-0.003(2)	-0.0082(16)
		sin	0.019(2)	0.0231(19)	0.0229(15)

Appendix 10: Occupancy modulation waves of the kinematically refined labradorite structure.

	Occupancy	Wave 1		Wave 2	
		ocos	osin	ocos	osin
M1Ca	0.32	-0.085(13)	0.114(11)	0.12(4)	0.29(2)
M1Na	0.33	0.085(13)	-0.114(11)	-0.12(4)	-0.29(2)
M1K	0.03	0.085(13)	-0.114(11)	-0.12(4)	-0.29(2)
M2Ca	0.32	-0.048(16)	-0.003(17)	0.19(2)	0.075(19)
T_{2o}Si	0.64	0.096(13)	-0.106(12)	-0.06(4)	-0.31(2)
T_{2o}Al	0.36	-0.096(13)	0.106(12)	0.06(4)	0.31(2)
T_{1o}Si	0.46	0.081(13)	-0.117(11)	-0.14(4)	-0.29(2)
T_{1o}Al	0.54	-0.08(13)	0.117(11)	0.14(4)	0.29(2)
T_{1m}Si	0.69	0.100(3)	-0.101(12)	-0.03(4)	-0.32(2)
T_{1m}Al	0.31	-0.100(3)	0.101(12)	0.03(4)	0.32(2)
T_{2m}Si	0.62	0.086(13)	-0.114(11)	-0.11(4)	-0.30(2)
T_{2m}Al	0.38	-0.086(13)	0.114(11)	0.11(4)	0.30(2)

Appendix 11: Atom positions (x, y, z), occupancy (occ) and isotropic displacement factors (U(iso)) for the average structure of the dynamically refined incommensurately modulated labradorite cell.

	x	y	z	occ	U(iso) [Å]
M1Ca	-0.2261(17)	0.4816(17)	0.0839(12)	0.32	-0.0106
M1Na				0.33	
M1K				0.03	
M2Ca	-0.222(3)	0.514(4)	0.021(2)	0.32	-0.0219
T_{1o}Si	0.0064(7)	0.1639(7)	0.1072(5)	0.46	-0.0076
T_{1o}Al				0.54	
T_{1m}Si	0.0034(6)	0.8191(8)	0.1167(4)	0.69	-0.0011
T_{1m}Al				0.31	
T_{2o}Si	0.1863(6)	0.6099(7)	0.1602(5)	0.64	-0.0072
T_{2o}Al				0.36	
T_{2m}Si	0.1852(7)	0.3786(7)	0.1803(4)	0.62	-0.0007
T_{2m}Al				0.38	
O1	0.0166(10)	0.2894(11)	0.1383(6)	1	-0.0144
O2	0.0799(10)	0.4943(11)	0.1401(6)	1	0.0041
O3	0.3021(11)	0.6294(12)	0.2818(7)	1	-0.0054
O4	0.0146(10)	0.6889(11)	0.1070(6)	1	-0.0148
O5	0.3089(11)	0.3517(13)	0.1200(8)	1	0.0086
O6	-0.0037(10)	0.8672(12)	0.0094(7)	1	0.0042
O7	0.3067(11)	0.6075(12)	0.0955(6)	1	0.0011
O8	0.2980(10)	0.3922(12)	0.3059(7)	1	0.0013

Appendix 12: Average, minimum and maximum bond lengths for the dynamically refined labradorite structure.

T	O	Average distance [Å]	Min. distance [Å]	Max. distance [Å]
T_{2o}	O2	1.69(7)	1.55(8)	1.83(8)
	O3	1.59(4)	1.40(5)	1.80(5)
	O4	1.67(5)	1.54(6)	1.84(6)
	O7	1.63(6)	1.32(6)	1.88(6)
T_{1o}	O1	1.61(7)	1.39(7)	1.99(7)
	O6	1.68(6)	1.58(6)	1.78(6)
	O7	1.72(6)	1.35(6)	2.15(6)
	O8	1.75(5)	1.55(6)	1.94(6)
T_{1m}	O3	1.71(4)	1.49(5)	1.98(5)
	O4	1.68(7)	1.58(8)	1.87(8)
	O5	1.67(6)	1.48(7)	1.86(7)
	O6	1.68(6)	1.61(7)	1.79(7)
T_{2m}	O1	1.63(6)	1.26(6)	1.87(6)
	O2	1.74(7)	1.47(8)	2.00(8)
	O5	1.60(7)	1.42(7)	1.80(7)
	O8	1.58(5)	1.32(5)	1.94(5)
M1	O1	3.28(8)	3.01(8)	3.43(8)
	O2	2.27(6)	2.03(7)	2.53(7)
	O3	2.60(8)	2.00(9)	3.63(9)
	O4	3.25(8)	2.46(9)	3.99(9)
	O5	3.36(9)	2.79(10)	3.97(10)
	O6	2.48(7)	2.18(8)	2.97(8)
	O7	2.62(7)	2.18(8)	2.90(8)
	O8	2.52(9)	2.20(9)	2.80(9)
	M2	1.37(12)	0.70(13)	1.78(13)
M2	O1	3.62(9)	2.71(10)	4.39(10)
	O2	3.23(10)	2.26(12)	3.76(12)
	O3	3.52(10)	2.94(10)	3.95(10)
	O4	2.81(10)	2.42(12)	3.22(12)
	O5	2.65(11)	1.90(13)	3.25(13)
	O6	2.50(9)	1.78(11)	3.55(11)
	O7	2.30(10)	1.73(12)	2.61(12)
	O8	2.84(11)	2.46(11)	3.69(11)

Appendix 13: Position modulation waves of the dynamically refined labradorite structure.

	Position modulation		x	y	z
M1	Wave 1	cos	-0.001(2)	0.004(3)	-0.0198(18)
		sin	-0.026(2)	-0.008(2)	0.0055(16)
	Wave 2	cos	-0.016(3)	-0.018(3)	0.011(2)
		sin	0.037(2)	-0.020(3)	0.0399(15)
M2	Wave 1	cos	-0.005(3)	0.018(3)	0.002(3)
		sin	0.021(4)	-0.001(4)	-0.012(3)
	Wave2	cos	-0.024(3)	0.039(4)	0.014(3)
		sin	0.018(3)	-0.013(4)	0.056(2)
T_{1o}	Wave 1	cos	-0.0041(18)	0.0069(18)	-0.0019(12)
		sin	0.0021(17)	-0.0016(16)	-0.0020(11)
	Wave 2	cos	0.0187(14)	-0.0012(19)	0.0022(11)
		sin	0.0060(12)	-0.0078(14)	0.0221(6)
T_{1m}	Wave 1	cos	0.0022(17)	-0.0068(17)	0.0005(11)
		sin	0.0006(18)	-0.0013(17)	-0.0014(11)
	Wave 2	cos	0.0102(16)	0.005(2)	0.0052(10)
		sin	-0.0052(13)	-0.0114(15)	0.0160(7)
T_{2o}	Wave 1	cos	-0.0111(14)	-0.0022(17)	-0.0001(11)
		sin	-0.0039(17)	0.0033(17)	-0.0029(11)
	Wave 2	cos	0.0044(15)	-0.0120(18)	0.0036(11)
		sin	-0.0001(12)	-0.0016(13)	0.0223(6)
T_{2m}	Wave 1	cos	0.0132(15)	0.0068(16)	0.0016(11)
		sin	0.0024(18)	-0.0037(17)	0.0002(11)
	Wave 2	cos	0.0122(17)	-0.004(2)	0.0040(11)
		sin	0.0139(14)	-0.0035(16)	0.0189(7)
O1	Wave 1	cos	0.002(3)	-0.014(2)	-0.0005(15)
		sin	0.001(3)	-0.008(2)	-0.0003(16)
	Wave 2	cos	0.0281(18)	0.0033(19)	-0.0053(13)
		sin	0.0284(17)	-0.0014(19)	0.0239(8)
O2	Wave 1	cos	-0.003(3)	-0.013(2)	-0.0036(17)
		sin	0.003(3)	0.006(3)	0.0045(17)
	Wave 2	cos	-0.023(2)	-0.003(3)	-0.0027(15)
		sin	0.018(2)	-0.001(3)	0.0158(12)
O3	Wave 1	cos	0.007(3)	0.011(2)	0.0003(17)
		sin	-0.004(3)	-0.005(2)	-0.0068(16)
	Wave 2	cos	-0.0343(17)	-0.004(2)	-0.0040(15)
		sin	0.014(2)	-0.009(2)	0.0243(9)
O4	Wave 1	cos	-0.003(2)	-0.012(2)	0.0011(15)
		sin	0.000(2)	0.009(2)	-0.0029(15)

	Wave 2	cos	0.0317(15)	0.009(2)	0.0105(12)
		sin	-0.0126(18)	-0.0099(18)	0.0217(9)
O5	Wave 1	cos	-0.002(3)	0.011(3)	-0.004(2)
		sin	0.005(3)	0.008(3)	0.0011(18)
	Wave 2	cos	-0.019(2)	0.000(3)	-0.0048(19)
		sin	0.019(2)	-0.007(2)	0.0259(11)
O6	Wave 1	cos	0.011(2)	0.005(3)	0.0027(17)
		sin	0.009(3)	-0.004(3)	-0.0018(18)
	Wave 2	cos	-0.015(2)	0.012(3)	-0.0033(17)
		sin	0.017(2)	0.001(2)	0.0221(10)
O7	Wave 1	cos	-0.001(3)	-0.012(2)	0.0005(17)
		sin	0.000(3)	0.005(3)	0.0032(17)
	Wave 2	cos	-0.0353(16)	-0.003(2)	-0.0058(14)
		sin	0.004(2)	0.006(2)	0.0163(11)
O8	Wave 1	cos	-0.004(3)	0.000(3)	-0.0007(18)
		sin	0.015(2)	0.002(3)	0.0007(17)
	Wave 2	cos	-0.015(2)	-0.021(2)	-0.0133(14)
		sin	0.018(2)	-0.006(3)	0.0182(13)

Appendix 14: Occupancy modulation waves of the dynamically refined labradorite structure.

	Occupancy	Wave 1		Wave 2	
		ocos	osin	ocos	osin
M1Ca	0.32	-0.026(14)	-0.047(14)	0.141(14)	0.545(13)
M1Na	0.33	0.026(14)	0.047(14)	-0.141(14)	0.545(13)
M1K	0.03	0.026(14)	0.047(14)	-0.141(14)	0.545(13)
M2Ca	0.32	-0.068(18)	0.07(2)	0.37(3)	0.41(3)
T_{2o}Si	0.64	0.021(14)	0.049(14)	-0.034(14)	-0.562(13)
T_{2o}Al	0.36	-0.021(14)	-0.049(14)	0.034(14)	0.562(13)
T_{1o}Si	0.46	0.027(14)	0.046(14)	-0.177(14)	-0.535(13)
T_{1o}Al	0.54	-0.027(14)	-0.046(14)	0.177(14)	0.535(13)
T_{1m}Si	0.69	0.019(14)	0.050(14)	0.016(14)	-0.563(13)
T_{1m}Al	0.31	-0.019(14)	0.050(14)	0.016(14)	-0.563(13)
T_{2m}Si	0.62	0.025(14)	0.047(14)	-0.134(14)	-0.547(13)
T_{2m}Al	0.38	-0.025(14)	0.047(14)	0.134(14)	0.547(13)

Appendix 15: Atom positions in the eveslogite structure (x, y, z) with their occupancies (occ) and their isotropic temperature factor (U(iso)) after kinematical refinement.

Atomlabel	Species	x	y	z	occ	U(iso)
Ba1	Ba	0.34392(18)	0.14859(13)	0.25320(15)	0.60(2)	0.0173(4)
Sr1	Sr				0.40(2)	
Ba2	Ba	0.22423(19)	0.21968(13)	0.93450(17)	0.55(2)	
Sr2	Sr				0.45(2)	
Ba3	Ba	0.16363(18)	0.14493(13)	0.77281(16)	0.43(2)	
Sr3	Sr				0.57(2)	
Ba4	Ba	0.7089(2)	0.56999(14)	0.89290(19)	0.26(2)	
Sr4	Sr				0.74(2)	
K1	K	0.1492(4)	0.3393(2)	0.3948(4)	1	0.0223(3)
K2	K	0.6460(4)	0.3389(2)	0.4007(4)		
K3	K	0.6695(4)	0.0275(2)	0.7825(4)		
K4	K	0.8299(4)	0.5289(2)	1.2182(4)		
K5	K	0.6316(4)	0.4604(2)	0.3594(4)		
K6	K	0.2529(4)	0.3984(2)	0.7029(4)		
K7	K	0.1346(4)	0.4598(2)	0.3574(4)		
K8	K	0.3501(4)	0.2681(2)	0.2622(4)		
K9	K	0.8481(4)	0.2678(2)	1.2607(4)		
K10	K	0.7556(4)	0.3966(2)	0.7047(4)		
K11	K	0.8462(4)	0.1458(2)	1.2695(4)		
K12	K	0.7963(4)	0.0603(2)	1.1219(4)		
K13	K	0.6480(4)	0.1455(2)	0.7411(3)		
K14	K	0.7119(4)	0.2165(2)	0.9265(4)		
K15	K	0.4286(8)	0.0831(3)	0.8916(7)	0.5	
K16	K	0.9681(8)	0.0825(3)	0.9004(7)		
K17	K	1.0664(8)	0.2097(4)	1.1431(7)		
K18	K	0.5363(8)	0.2092(3)	1.1489(7)		
K19	K	0.2134(8)	0.0951(3)	0.9121(7)		
K20	K	0.4066(9)	0.3881(4)	0.5123(8)		
K21	K	0.8988(8)	0.3891(3)	0.5123(8)		
Ca1	Ca	0.7057(3)	0.17990(16)	0.5449(3)	0.83(3)	0.0056(6)
Na1	Na				0.17(3)	
Ca2	Ca	0.2016(3)	0.17958(17)	0.5474(3)	0.82(3)	
Na2	Na				0.18(3)	
Ca3	Ca	0.3053(4)	0.11327(18)	0.4849(3)	0.58(3)	
Na3	Na				0.42(3)	
Ca4	Ca	0.8073(4)	0.11436(18)	0.4853(3)	0.53(3)	
Na4	Na				0.47(3)	
Ca5	Ca				0.71(3)	

Na5	Na	0.9578(3)	0.17751(17)	0.5515(3)	0.29(3)	
Ca6	Ca	0.5541(4)	0.11465(17)	0.4824(3)	0.68(3)	
Na6	Na				0.32(3)	
Ca7	Ca	0.0533(4)	0.11504(19)	0.4851(4)	0.42(3)	
Na7	Na				0.58(3)	
Ca8	Ca	0.5283(4)	0.27949(19)	0.7510(4)	0.45(3)	
Na8	Na				0.55(3)	
Ca9	Ca	0.0303(4)	0.27997(19)	0.7540(4)	0.41(3)	
Na9	Na				0.59(3)	
Ca10	Ca	0.4520(4)	0.1781(2)	0.5467(4)	0.24(3)	
Na10	Na				0.76(3)	
Ca11	Ca	0.7846(4)	0.27886(18)	0.7533(3)	0.56(3)	
Na11	Na				0.44(3)	
Ca12	Ca	0.2834(4)	0.27909(18)	0.7579(3)	0.56(3)	
Na12	Na				0.44(3)	
Ca13	Ca	0.5226(5)	0.5117(2)	0.7134(5)	0.03(2)	
Na13	Na				0.97(2)	
Ca14	Ca	0.7652(4)	0.5088(2)	0.7199(4)	0.26(2)	
Na14	Na				0.74(2)	
Ca15	Ca	0.0235(5)	0.5093(2)	0.7137(5)	0.01	
Na15	Na				0.99	
Ca16	Ca	0.2656(5)	0.5077(2)	0.7236(5)	0.01	
Na16	Na				0.99	
Ca17	Ca	0.3194(3)	0.54303(16)	0.5229(3)	0.91(3)	
Na17	Na				0.09(3)	
Ca18	Ca	0.9086(3)	0.34863(16)	1.0920(3)	0.85(3)	
Na18	Na				0.15(3)	
Ca19	Ca	0.0665(3)	0.54354(17)	0.5157(3)	0.85(2)	
Na19	Na				0.15(2)	
Ca20	Ca	0.5675(3)	0.54282(16)	0.5165(3)	0.99	
Na20	Na				0.01	
Ca21	Ca	0.8998(3)	0.43873(16)	1.0696(3)	0.99	
Na21	Na				0.01	
Ca22	Ca	0.7190(4)	0.32104(18)	0.9093(3)	0.57(3)	
Na22	Na				0.43(3)	
Ca23	Ca	0.9716(3)	0.31786(17)	0.9168(3)	0.78(3)	
Na23	Na				0.22(3)	
Ca24	Ca	0.8193(3)	0.54394(17)	1.5247(3)	0.77(3)	
Na24	Na				0.23(3)	
Ca25	Ca	0.1601(3)	0.34942(16)	1.0930(3)	0.99	
Na25	Na				0.01	

Ca26	Ca	0.3332(3)	0.25071(16)	0.5539(3)	0.99	
Na26	Na				0.01	
Ca27	Ca	0.4085(3)	0.34866(16)	1.0926(3)	0.93(3)	
Na27	Na				0.07(3)	
Ca28	Ca	0.4704(3)	0.31846(17)	0.9180(3)	0.78(3)	
Na28	Na				0.22(3)	
Ca29	Ca	0.5803(3)	0.25077(16)	0.5528(3)	0.99	
Na29	Na				0.01	
Ca30	Ca	0.8331(3)	0.24968(16)	0.5533(3)	0.99	
Na30	Na				0.01	
Ca31	Ca	0.6464(3)	0.43823(17)	1.0728(3)	0.69(3)	
Na31	Na				0.31(3)	
Ca32	Ca	0.0800(3)	0.25103(16)	0.5498(3)	0.99	
Na32	Na				0.01	
Ca33	Ca	0.6608(3)	0.34926(16)	1.0922(3)	0.99	
Na33	Na				0.01	
Ca34	Ca	1.1485(3)	0.43905(17)	1.0724(3)	0.79(3)	
Na34	Na				0.21(3)	
Ca35	Ca	0.2201(4)	0.3196(2)	0.9117(4)	0.32(3)	
Na35	Na				0.68(3)	
Ca36	Ca	0.3992(3)	0.43884(16)	1.0710(3)	0.99	
Na36	Na				0.01	
Ca37	Ca	0.1979(3)	0.46296(16)	0.8675(3)	0.99	
Na37	Na				0.01	
Ca38	Ca	0.6975(3)	0.46427(16)	0.8699(3)	0.99	
Na38	Na				0.01	
Ca39	Ca	0.9492(3)	0.46264(16)	0.8734(3)	0.86(2)	
Na39	Na				0.14(2)	
Ca40	Ca	0.4482(3)	0.46310(16)	0.8725(3)	0.99	
Na40	Na				0.01	
M1	Ti	0.5539(3)	0.05037(13)	0.1355(2)	0.7396	0.0046(2)
	Nb				0.0479	
	Fe				0.1337	
	Mn				0.0787	
M2	Ti	0.9641(3)	0.23818(14)	0.9070(2)	0.7396	
	Nb				0.0479	
	Fe				0.1337	
	Mn				0.0787	
M3	Ti	0.8897(2)	0.14624(15)	0.7172(2)	0.7396	
	Nb				0.0479	
	Fe				0.1337	

	Mn				0.0787	
M4	Ti	0.0493(3)	0.050855	0.1363(2)	0.7396	
	Nb				0.0479	
	Fe				0.1337	
	Mn				0.0787	
M5	Ti	0.1158(2)	0.14656(14)	0.3144(2)	0.7396	
	Nb				0.0479	
	Fe				0.1337	
	Mn				0.0787	
M6	Ti	0.4666(3)	0.23791(14)	0.9065(2)	0.7396	
	Nb				0.0479	
	Fe				0.1337	
	Mn				0.0787	
M7	Ti	0.3953(2)	0.14741(15)	0.7165(2)	0.7396	
	Nb				0.0479	
	Fe				0.1337	
	Mn				0.0787	
M8	Ti	0.6214(2)	0.14562(15)	0.3139(2)	0.7396	
	Nb				0.0479	
	Fe				0.1337	
	Mn				0.0787	
Ti9	Ti	0.5285(2)	0.36412(13)	0.75639(18)	0.351	
Nb9	Nb				0.649	
Ti10	Ti	1.0299(2)	0.36453(13)	0.75704(18)	0.432	
Nb10	Nb				0.568	
Fep	Fe	0.2594(2)	0.15106(14)	0.02301(19)	0.63	
Mnp	Mn				0.37	
Si1	Si	-0.0244(4)	0.08107(19)	0.3034(4)	1	0.00566(18)
Si2	Si	0.2349(4)	0.08847(19)	0.6641(4)		
Si3	Si	0.8836(4)	0.2739(2)	1.0540(4)		
Si4	Si	0.3472(4)	0.44693(19)	1.2656(4)		
Si5	Si	0.4717(4)	0.08141(19)	0.3034(4)		
Si6	Si	0.7080(4)	0.39728(19)	1.2654(4)		
Si7	Si	0.7509(4)	0.08171(19)	0.3020(4)		
Si8	Si	0.2664(4)	0.58757(19)	0.3368(4)		
Si9	Si	0.4206(4)	0.31092(19)	0.4649(4)		
Si10	Si	0.1379(4)	0.25511(19)	0.3589(4)		
Si11	Si	0.8479(4)	0.44566(19)	1.2665(4)		
Si12	Si	0.9224(4)	0.30992(19)	0.4679(4)		
Si13	Si	0.4316(4)	0.16522(19)	0.9343(3)		
Si14	Si	0.6357(4)	0.2550(2)	0.3574(4)		

Si15	Si	1.0129(4)	0.08805(19)	0.6691(4)		
Si16	Si	0.3559(4)	0.34711(19)	1.2872(4)		
Si17	Si	1.0576(4)	0.49852(19)	1.1523(4)		
Si18	Si	0.4934(4)	0.12715(19)	0.1060(3)		
Si19	Si	0.1162(4)	0.3236(2)	0.6169(4)		
Si20	Si	0.3805(4)	0.2754(2)	1.0543(4)		
Si21	Si	0.4967(4)	0.20482(19)	0.3696(4)		
Si22	Si	0.4906(4)	0.39795(19)	1.2646(4)		
Si23	Si	0.7586(4)	0.2105(2)	0.7276(4)		
Si24	Si	1.0135(4)	0.16315(19)	0.9331(3)		
Si25	Si	0.2593(4)	0.2096(2)	0.7283(4)		
Si26	Si	0.2365(4)	0.38953(19)	0.9340(4)		
Si27	Si	0.9897(4)	0.39714(19)	1.2648(4)		
Si28	Si	0.5039(4)	0.43761(19)	0.6796(4)		
Si29	Si	0.5546(4)	0.49852(19)	1.1528(4)		
Si30	Si	1.2083(4)	0.39747(19)	1.2667(4)		
Si31	Si	0.5675(4)	0.29262(19)	1.1916(4)		
Si32	Si	1.0034(4)	0.43763(19)	0.6791(4)		
Si33	Si	0.6182(4)	0.32375(19)	0.6166(4)		
Si34	Si	0.5149(4)	0.0895(2)	0.6681(4)		
Si35	Si	0.8230(4)	0.47111(19)	0.5701(4)		
Si36	Si	-0.0020(4)	0.20622(19)	0.3687(4)		
Si37	Si	0.7349(4)	0.39005(19)	0.9317(4)		
Si38	Si	0.2528(4)	0.08114(19)	0.3023(4)		
Si39	Si	0.8558(4)	0.34716(19)	1.2874(4)		
Si40	Si	0.0318(4)	0.2107(2)	0.7277(4)		
Si41	Si	0.9581(4)	0.38952(19)	0.9271(4)		
Si42	Si	0.1176(4)	0.53798(19)	0.3229(4)		
Si43	Si	0.3358(4)	0.32513(19)	0.6131(4)		
Si44	Si	0.8366(4)	0.3246(2)	0.6104(4)		
Si45	Si	0.3224(4)	0.47109(19)	0.5708(4)		
Si46	Si	0.5370(4)	0.2112(2)	0.7300(4)		
Si47	Si	1.0742(4)	0.2925(2)	1.1910(4)		
Si48	Si	0.6589(4)	0.27381(19)	1.0503(4)		
Si49	Si	0.4573(4)	0.3891(2)	0.9289(4)		
Si50	Si	0.6171(4)	0.53805(19)	1.3232(4)		
Si51	Si	0.7770(4)	0.2059(2)	0.3663(4)		
Si52	Si	1.1430(4)	0.51294(19)	1.0096(4)		
Si53	Si	0.1057(4)	0.47186(19)	0.5619(4)		
Si54	Si	0.2769(4)	0.20553(19)	0.3678(4)		
Si55	Si	1.1538(4)	0.2750(2)	1.0503(4)		

Si56	Si	0.6421(4)	0.51296(19)	1.0077(4)		
Si57	Si	0.6029(4)	0.47155(19)	0.5639(4)		
Si58	Si	0.0840(4)	0.12659(19)	0.1041(3)		
Si59	Si	0.4099(4)	0.48755(19)	0.4253(4)		
Si60	Si	0.6401(4)	0.01320(19)	0.9950(4)		
Si61	Si	0.8641(4)	0.51202(19)	1.0055(4)		
Si62	Si	-0.0881(4)	0.48850(19)	0.4251(4)		
F1	F	0.5989(6)	0.1522(3)	0.5884(5)	1	0.0046
F2	F	0.4055(6)	0.1388(2)	0.4264(5)		
F3	F	0.9096(6)	0.1422(3)	0.4314(5)		
F4	F	0.2941(6)	0.4553(3)	0.7823(5)		
F5	F	0.7900(6)	0.4562(3)	0.7798(5)		
O1	O	0.3327(7)	0.2281(3)	0.8178(6)	1	0.01089(17)
O2	O	0.8316(7)	0.2281(3)	0.8147(6)		
O3	O	0.4519(7)	0.4280(3)	1.2986(6)		
O4	O	0.0673(7)	0.0103(3)	0.1837(6)		
O5	O	0.5767(7)	0.0108(3)	0.1838(6)		
O6	O	0.9555(7)	0.4282(3)	1.2994(6)		
O7	O	0.6113(7)	0.2861(3)	0.2972(6)		
O8	O	0.0156(7)	0.5569(3)	0.2937(6)		
O9	O	0.1126(7)	0.2854(3)	0.2938(6)		
O10	O	0.3725(7)	0.3071(3)	1.0030(6)		
O11	O	0.4284(7)	0.2757(3)	0.4791(6)		
O12	O	0.5197(7)	0.5586(3)	1.2948(6)		
O13	O	-0.0729(7)	0.2752(3)	0.4802(6)		
O14	O	0.8803(7)	0.3058(3)	1.0032(6)		
O15	O	0.2722(7)	0.3674(3)	1.3133(6)		
O16	O	0.8721(7)	0.4781(3)	1.3183(6)		
O17	O	1.1483(7)	0.2786(3)	1.1506(6)		
O18	O	0.0163(7)	0.1155(3)	0.3123(6)		
O19	O	0.5520(7)	0.2050(3)	0.4758(6)		
O20	O	0.0536(7)	0.2041(3)	0.4775(6)		
O21	O	0.6999(7)	0.5579(3)	1.2968(6)		
O22	O	0.3726(7)	0.4776(3)	1.3244(6)		
O23	O	0.8669(7)	0.2920(3)	0.6521(6)		
O24	O	0.4769(7)	0.0603(3)	0.2204(6)		
O25	O	0.7738(7)	0.3682(3)	1.3108(6)		
O26	O	0.2935(7)	0.1169(3)	0.7121(6)		
O27	O	0.6485(7)	0.2774(3)	1.1471(6)		
O28	O	0.7066(6)	0.4602(3)	0.5505(6)		
O29	O	0.7965(7)	0.1781(3)	0.7073(6)		

O30	O	0.3910(7)	0.4443(3)	0.6268(6)		
O31	O	0.3537(6)	0.0860(3)	0.2786(6)		
O32	O	0.7956(7)	0.1166(3)	0.7121(6)		
O33	O	0.3688(6)	0.5845(3)	0.3079(6)		
O34	O	0.2206(6)	0.3339(3)	0.5987(6)		
O35	O	0.8427(7)	0.5024(3)	0.6160(6)		
O36	O	0.2026(7)	0.5575(3)	0.2970(6)		
O37	O	-0.0112(7)	0.0614(3)	0.2262(6)		
O38	O	0.4620(7)	0.2758(3)	1.1532(6)		
O39	O	0.2086(6)	0.4613(3)	0.5503(6)		
O40	O	0.8325(7)	0.4736(3)	0.4708(6)		
O41	O	1.1210(7)	0.3070(3)	1.0008(6)		
O42	O	0.6231(7)	0.3063(3)	0.9978(6)		
O43	O	1.0510(7)	0.4639(3)	1.1451(6)		
O44	O	0.2174(7)	0.2366(3)	0.3227(6)		
O45	O	0.3701(7)	0.2914(3)	0.6515(6)		
O46	O	0.5402(7)	0.3284(3)	0.8168(6)		
O47	O	0.4952(7)	0.1172(3)	0.7238(6)		
O48	O	0.9957(7)	0.1174(3)	0.7229(6)		
O49	O	0.4568(7)	0.3682(3)	1.3146(6)		
O50	O	0.2997(7)	0.1780(3)	0.7115(6)		
O51	O	0.1736(7)	0.3960(3)	1.1596(6)		
O52	O	0.3428(7)	0.1479(3)	0.5844(6)		
O53	O	0.3056(7)	0.2054(3)	0.4746(6)		
O54	O	1.1004(7)	0.5091(3)	1.2561(6)		
O55	O	0.8487(7)	0.1479(3)	0.5857(6)		
O56	O	0.9954(7)	0.4222(3)	0.9707(6)		
O57	O	0.7194(7)	0.1151(3)	0.3111(6)		
O58	O	0.4452(7)	0.3941(3)	1.1551(6)		
O59	O	0.5157(7)	0.1152(3)	0.3171(6)		
O60	O	0.4901(7)	0.1788(3)	0.7083(6)		
O61	O	0.8921(6)	0.4439(3)	0.6214(6)		
O62	O	0.0118(6)	0.4721(3)	0.4667(6)		
O63	O	0.9562(7)	0.3681(3)	1.3146(6)		
O64	O	0.4862(7)	0.4199(3)	0.9711(6)		
O65	O	0.6313(7)	0.5159(3)	1.1084(6)		
O66	O	1.1127(6)	0.3978(3)	1.2967(6)		
O67	O	0.6708(7)	0.3958(3)	1.1618(6)		
O68	O	0.2198(7)	0.1151(3)	0.3083(6)		
O69	O	0.0796(7)	0.4459(3)	0.6236(6)		
O70	O	0.8320(6)	0.3917(3)	0.8963(6)		

O71	O	0.9453(7)	0.3955(3)	1.1555(6)		
O72	O	-0.1491(6)	0.0852(3)	0.2797(6)		
O73	O	0.2325(7)	0.2301(3)	0.6397(6)		
O74	O	0.1572(7)	0.5315(3)	0.4250(6)		
O75	O	0.8462(7)	0.3259(3)	0.5092(6)		
O76	O	0.6150(7)	0.5043(3)	0.6098(6)		
O77	O	0.1118(7)	0.5031(3)	0.6111(6)		
O78	O	0.9657(6)	0.2764(3)	1.1540(6)		
O79	O	0.9929(7)	0.1774(3)	0.7139(6)		
O80	O	0.5835(7)	0.4430(3)	0.6232(6)		
O81	O	0.0415(7)	0.0924(3)	0.0999(6)		
O82	O	0.3469(7)	0.5018(3)	0.6139(6)		
O83	O	0.2920(7)	0.5905(3)	0.4388(6)		
O84	O	0.5520(7)	0.4626(3)	1.1457(6)		
O85	O	0.5973(7)	0.5082(3)	1.2622(6)		
O86	O	1.1316(6)	0.0865(3)	0.6880(6)		
O87	O	0.3149(7)	0.3346(3)	1.1897(6)		
O88	O	1.0058(7)	0.4015(3)	0.6850(6)		
O89	O	0.0718(7)	0.1432(3)	0.1863(6)		
O90	O	0.6136(7)	0.4808(3)	0.9667(6)		
O91	O	0.6092(6)	0.3986(3)	1.2940(6)		
O92	O	0.1779(7)	0.5093(3)	0.8142(6)		
O93	O	0.1729(7)	0.2645(3)	0.4586(6)		
O94	O	1.1276(7)	0.5163(3)	1.1050(6)		
O95	O	0.0997(7)	0.1479(3)	0.5933(6)		
O96	O	0.9492(7)	0.5150(3)	1.1109(6)		
O97	O	0.8074(7)	0.2057(3)	0.4744(6)		
O98	O	0.2087(7)	0.0888(3)	0.5633(6)		
O99	O	0.3353(7)	0.4723(3)	0.4708(6)		
O100	O	0.3114(7)	0.4549(3)	1.1569(6)		
O101	O	0.3285(7)	0.3270(3)	0.8343(6)		
O102	O	0.7120(7)	0.2361(3)	0.3263(6)		
O103	O	0.3152(6)	0.1640(3)	0.9292(6)		
O104	O	0.5627(7)	0.1458(3)	0.1865(6)		
O105	O	0.6777(7)	0.5106(3)	0.8169(6)		
O106	O	0.2701(6)	0.2694(3)	1.0568(6)		
O107	O	1.0413(7)	0.3300(3)	0.8202(6)		
O108	O	0.8320(7)	0.3265(3)	0.8337(6)		
O109	O	0.3495(7)	0.3262(3)	0.5110(6)		
O110	O	0.1238(7)	0.2909(3)	0.6537(6)		
O111	O	0.2671(7)	0.4286(3)	1.2993(6)		

O112	O	0.3744(6)	0.2086(3)	0.3319(6)		
O113	O	1.0907(7)	0.2466(3)	0.9987(6)		
O114	O	0.4970(7)	0.1453(3)	0.0136(6)		
O115	O	0.7229(6)	0.3336(3)	0.5987(6)		
O116	O	0.6530(7)	0.5290(3)	1.4242(6)		
O117	O	0.6252(7)	0.2900(3)	0.6566(6)		
O118	O	0.2120(7)	0.1784(3)	0.3080(6)		
O119	O	0.4483(7)	0.2747(3)	0.8638(6)		
O120	O	0.5149(6)	0.4716(3)	0.4661(6)		
O121	O	0.7729(6)	0.2726(3)	1.0618(6)		
O122	O	0.8936(7)	0.2447(3)	0.9976(6)		
O123	O	0.1865(7)	0.0624(3)	0.2231(6)		
O124	O	0.5328(7)	0.2358(3)	0.3278(6)		
O125	O	0.3770(6)	0.1217(3)	0.0870(6)		
O126	O	1.1142(7)	0.4798(3)	0.9642(6)		
O127	O	-0.0883(7)	0.5237(3)	0.4459(6)		
O128	O	0.7667(7)	0.4280(3)	1.3003(6)		
O129	O	0.6536(6)	0.2048(3)	0.7530(6)		
O130	O	0.5967(7)	0.3480(3)	0.6749(6)		
O131	O	0.4492(7)	0.5153(3)	1.1057(6)		
O132	O	0.6787(7)	0.0622(3)	0.2249(6)		
O133	O	-0.0114(7)	0.2329(3)	0.6387(6)		
O134	O	0.2177(7)	0.4226(3)	0.9682(6)		
O135	O	0.1543(6)	0.2067(3)	0.7538(6)		
O136	O	0.4166(7)	0.5232(3)	0.4491(6)		
O137	O	0.7217(7)	0.4229(3)	0.9743(6)		
O138	O	0.9482(7)	0.1454(3)	0.8509(6)		
O139	O	0.1931(6)	0.1265(3)	0.0933(6)		
O140	O	0.0139(7)	0.1764(3)	0.3181(6)		
O141	O	0.4491(7)	0.3844(3)	0.8245(6)		
O142	O	0.7157(7)	0.1790(3)	0.3001(6)		
O143	O	0.1596(7)	0.1437(3)	0.4333(6)		
O144	O	0.5005(7)	0.4010(3)	0.6863(6)		
O145	O	0.7533(7)	0.3643(3)	1.0037(6)		
O146	O	0.6911(7)	0.2776(3)	0.8513(6)		
O147	O	0.4027(7)	0.2467(3)	1.0003(6)		
O148	O	0.7426(7)	0.2319(3)	0.6405(6)		
O149	O	0.8903(7)	0.3199(3)	0.3579(6)		
O150	O	0.3838(7)	0.3209(3)	0.3624(6)		
O151	O	0.6647(7)	0.1432(3)	0.4312(6)		
O152	O	0.5418(7)	0.0946(3)	0.1042(6)		

O153	O	0.5346(7)	0.2272(3)	0.8231(6)		
O154	O	0.4414(7)	0.1482(3)	0.8492(6)		
O155	O	0.9808(7)	0.1953(3)	0.9548(6)		
O156	O	0.3991(7)	0.3510(3)	0.6678(6)		
O157	O	0.5222(7)	0.1785(3)	0.3141(6)		
O158	O	0.3295(6)	0.3921(3)	0.8946(6)		
O159	O	0.0324(7)	0.2361(3)	0.3295(6)		
O160	O	1.0024(7)	0.1414(3)	1.0142(6)		
O161	O	0.6696(7)	0.2635(3)	0.4588(6)		
O162	O	0.0950(7)	0.3496(3)	0.6758(6)		
O163	O	0.0226(7)	0.0668(3)	0.4061(6)		
O164	O	0.5659(7)	0.3284(3)	1.1734(6)		
O165	O	0.8991(7)	0.3510(3)	0.6696(6)		
O166	O	0.9508(7)	0.2795(3)	0.8633(6)		
O167	O	0.2740(7)	0.0657(3)	0.3959(6)		
O168	O	1.0293(7)	0.3255(3)	0.5177(6)		
O169	O	0.8854(7)	0.5403(3)	0.9544(6)		
O170	O	0.5227(7)	0.0662(3)	0.4015(6)		
O171	O	0.0337(7)	0.2266(3)	0.8191(6)		
O172	O	0.9452(7)	0.3841(3)	0.8263(6)		
O173	O	1.0652(7)	0.3277(3)	1.1775(6)		
O174	O	0.6158(7)	0.0397(3)	1.0504(6)		
O175	O	1.0796(7)	0.5411(3)	0.9539(6)		
O176	O	0.8179(7)	0.3342(3)	1.1887(6)		
O177	O	0.4941(7)	0.2339(3)	0.6459(6)		
O178	O	0.8165(7)	0.4520(3)	1.1609(6)		
O179	O	1.0408(7)	0.4558(3)	0.7754(6)		
O180	O	0.7825(7)	0.0674(3)	0.3978(6)		
O181	O	0.5923(7)	0.2470(3)	0.9908(6)		
O182	O	0.4940(7)	0.3588(3)	0.9851(6)		
O183	O	0.9581(7)	0.0895(3)	0.5654(6)		
O184	O	0.5801(7)	0.5405(3)	0.9506(6)		
O185	O	0.1947(7)	0.2740(3)	0.8538(6)		
O186	O	0.4697(7)	0.1977(3)	0.9527(6)		
O187	O	0.6619(7)	0.3807(3)	0.8374(6)		
O188	O	0.5444(7)	0.4561(3)	0.7760(6)		
O189	O	0.2977(6)	0.1972(3)	0.1114(6)		
O190	O	1.1292(6)	0.1631(3)	0.9327(6)		
O191	O	0.7613(6)	0.5198(3)	1.0247(6)		
O192	O	0.6348(7)	-0.0194(3)	1.0334(6)		
O193	O	0.8730(6)	0.2072(3)	0.3316(6)		

O194	O	0.2514(7)	0.3619(3)	1.0031(6)		
O195	O	0.5287(6)	0.3266(3)	0.5176(6)		
O196	O	0.8685(7)	0.4794(3)	0.9735(6)		
O197	O	0.9976(7)	0.3594(3)	0.9863(6)		
O198	O	0.1564(7)	0.3818(3)	0.8369(6)		
O199	O	0.7388(6)	0.0220(3)	0.9719(6)		
O200	O	0.4652(7)	0.0902(3)	0.5686(6)		
H1o189	H	0.368712	0.199852	0.135152	1	0.0131
H2o189	H	0.248801	0.200205	0.139905		

Appendix 16: Bond lengths of the atoms in the eveslogite structure.

Atom1	Atom2	Distance	Atom1	Atom2	Distance	Atom1	Atom2	Distance
Ba/Sr1	O31	2.832(14)	Ba/Sr3	O135	2.783(14)	K3	O22	2.751(14)
	O59	2.753(11)		O190	2.865(11)		O33	2.892(15)
	O68	2.680(12)	Ba/Sr4	O24	2.688(9)		O36	2.874(14)
	O112	2.936(14)		O31	2.668(10)		O94	2.884(10)
	O118	2.678(12)		O105	2.894(14)		O131	2.889(13)
	O125	3.082(11)		O123	2.753(12)		O199	2.848(11)
	O139	2.896(9)		O125	2.692(13)	K4	O8	2.805(11)
	O157	2.742(11)		O139	2.864(13)		O16	2.727(14)
	O189	3.043(12)		O169	2.718(11)		O21	2.869(14)
	F2	2.632(8)		O184	2.661(12)		O65	2.839(10)
Ba/Sr2	O1	2.812(12)		O191	2.993(13)		O86	2.940(15)
	O103	2.826(13)	K1	O9	2.850(14)		O96	2.853(13)
	O106	2.885(13)		O15	2.802(14)		O191	2.928(11)
	O113	2.724(12)		O34	3.065(11)	K5	O3	2.812(12)
	O135	2.769(10)		O63	2.913(11)		O28	2.863(11)
	O147	2.688(10)		O66	3.006(15)		O40	2.875(10)
	O171	2.733(9)		O109	2.889(10)		O84	3.202(11)
	O185	2.718(14)		O168	3.061(13)		O85	2.591(14)
	O189	2.837(10)		O173	3.295(11)		O91	2.937(15)
	O190	2.871(13)	K2	O7	2.828(14)		O116	3.225(16)
Ba/Sr3	O26	2.671(12)		O25	2.972(14)		O120	2.791(13)
	O48	2.569(11)		O49	2.894(11)		O128	2.812(14)
	O50	2.858(12)		O75	2.851(10)	K6	O34	3.291(15)
	O79	2.716(11)		O91	3.118(15)		O69	3.179(13)
	O86	2.911(14)		O115	2.976(11)		O141	2.880(10)
	O95	2.692(9)		O195	2.938(13)		O156	3.154(14)
	O103	2.822(8)	K3	O12	2.913(12)		O158	2.886(11)
K6	O162	3.062(14)	K10	O70	2.880(11)	K14	O2	2.894(13)
	F4	2.816(14)		O80	3.142(13)		O121	3.232(14)
	O198	2.992(13)		O115	3.243(15)		O122	2.756(12)
K7	O6	2.788(12)		O130	3.061(14)		O129	2.654(11)
	O39	2.891(11)		O165	3.070(14)		O146	2.961(15)
	O43	3.185(11)		O172	2.798(10)		O153	2.553(10)
	O54	2.680(14)		O187	2.939(13)		O181	2.643(14)
	O62	2.903(13)		F5	2.899(14)	K15	O21	3.148(14)
	O66	2.923(16)	K11	O18	2.656(12)		O26	3.233(15)
	O99	2.876(10)		O57	2.527(14)		O65	3.13(2)
	O111	2.746(14)		O72	2.718(16)		O152	3.261(14)
	O11	3.267(11)		O140	2.634(12)		O154	3.02(2)

	O17	2.863(10)		O142	2.552(14)		O184	3.187(17)
	O38	2.743(13)		F3	2.430(9)	K16	O81	3.021(14)
	O44	2.776(14)		O193	2.905(15)		O94	3.251(19)
K8	O87	3.174(15)	K12	O37	2.684(10)		O96	3.27(2)
	O106	3.078(11)		O72	2.617(12)		O138	2.92(2)
	O112	2.866(15)		O92	2.479(15)		O160	3.145(18)
	O124	2.851(12)		O132	2.710(13)		O169	3.165(15)
	O150	2.803(14)		O174	2.605(11)		O175	3.213(18)
K9	O13	3.306(11)		O175	2.596(13)	K17	O17	3.29(2)
	O27	2.841(10)		O199	2.826(13)		O44	3.179(14)
	O78	2.782(13)	K13	O29	2.768(13)		O89	3.06(2)
	O102	2.866(14)		O32	2.641(13)		O113	2.944(18)
	O121	2.987(11)		O33	2.832(16)		O118	3.080(14)
	O149	2.754(14)		O47	2.453(13)		O122	3.168(15)
	O159	2.858(12)		O60	2.600(13)		O155	2.902(14)
	O176	3.167(15)		F1	2.309(9)	K18	O38	3.18(2)
	O193	2.916(15)		O129	2.660(16)		O102	3.306(13)
K18	O104	2.90(2)	Ca/Na2	O53	2.454(13)	Ca/Na7	O98	2.444(12)
	O124	3.099(17)		O95	2.317(13)		O143	2.336(14)
	O142	3.163(14)		O143	2.347(13)		O163	2.465(14)
	O147	3.000(15)	Ca/Na3	O52	2.152(13)		O183	2.438(14)
	O157	3.033(17)		O98	2.410(13)		F3	2.284(11)
	O186	2.986(15)		O143	2.386(12)	Ca/Na8	O45	2.338(10)
	O189	3.289(15)		F2	2.258(12)		O46	2.411(15)
K19	O125	3.199(13)		O167	2.517(14)		O117	2.403(13)
	O139	3.307(16)		O200	2.446(11)		O119	2.435(13)
K20	O15	3.235(14)	Ca/Na4	O55	2.128(13)		O146	2.331(10)
	O30	3.163(19)		O83	2.399(14)		O153	2.598(15)
	O109	2.89(2)		O151	2.314(12)		O177	2.582(14)
	O144	2.701(15)		O180	2.483(14)	Ca/Na9	O23	2.407(10)
	O156	3.012(18)		O183	2.372(11)		O107	2.458(15)
	O195	3.243(19)		F3	2.292(12)		O110	2.446(14)
K21	O25	3.237(15)	Ca/Na5	O20	2.396(13)		O166	2.373(13)
	O61	3.027(19)		O55	2.244(13)		O171	2.602(15)
	O75	2.93(2)		O79	2.460(11)		O185	2.360(10)
	O88	2.713(14)		O95	2.320(12)	Ca/Na10	O19	2.416(14)
	O165	3.027(18)		O97	2.434(11)		O52	2.287(14)
Ca/Na1	O19	2.376(11)		F3	2.397(11)		O53	2.357(12)
	O29	2.470(10)	Ca/Na6	O59	2.498(11)		O60	2.442(12)
	O55	2.394(12)		F1	2.316(12)		F1	2.285(11)
	F1	2.245(11)		O83	2.387(11)		F2	2.519(12)

	O97	2.406(13)		O151	2.374(13)	Ca/Na11	O2	2.476(14)
	O151	2.369(13)		F2	2.274(10)		O23	2.364(13)
Ca/Na2	O20	2.303(11)		O170	2.485(14)		O108	2.463(14)
	O50	2.513(10)		O200	2.420(13)		O117	2.327(10)
	O52	2.368(12)	Ca/Na7	O95	2.192(13)		O146	2.368(13)
Ca/Na11	O166	2.424(9)	Ca/Na16	O132	2.612(16)	Ca/Na21	O137	2.578(10)
Ca/Na12	O1	2.483(14)		F4	2.512(15)		O178	2.242(12)
	O45	2.469(13)	Ca/Na17	O74	2.368(9)		O196	2.324(13)
	O101	2.445(14)		O82	2.297(13)	Ca/Na22	O14	2.379(10)
	O110	2.378(10)		O83	2.473(14)		O42	2.360(13)
	O119	2.393(9)		O136	2.275(13)		O46	2.496(10)
	O185	2.296(13)		O170	2.400(11)		O108	2.323(13)
Ca/Na13	O5	2.497(14)		O180	2.474(13)		O145	2.400(14)
	O24	2.419(16)	Ca/Na18	O14	2.336(13)		O146	2.136(15)
	O76	2.453(14)		O71	2.314(14)	Ca/Na23	O14	2.252(13)
	O82	2.508(11)		O145	2.294(10)		O41	2.154(10)
	O105	2.269(10)		O173	2.379(10)		O107	2.161(13)
	O188	2.664(16)		O176	2.407(13)		O108	2.020(10)
Ca/Na14	O4	2.363(10)		O197	2.469(13)		O166	1.898(14)
	O35	2.293(14)	Ca/Na19	O74	2.301(13)		O197	2.132(14)
	O76	2.272(10)		O77	2.313(13)	Ca/Na24	O35	2.314(13)
	O105	2.286(14)		O127	2.288(11)		O98	2.407(14)
	O123	2.576(15)		O163	2.302(13)		O116	2.463(10)
	F5	2.525(14)		O180	2.380(11)		O127	2.288(13)
Ca/Na15	O4	2.399(14)		O183	2.395(14)		O163	2.379(11)
	O35	2.539(11)	Ca/Na20	O76	2.229(13)		O167	2.332(13)
	O37	2.550(16)		O116	2.286(12)	Ca/Na25	O41	2.351(13)
	O77	2.387(14)		O136	2.233(11)		O51	2.321(14)
	O92	2.241(10)		O167	2.443(10)		O87	2.320(10)
	O179	2.574(16)		O170	2.363(13)		O173	2.408(13)
Ca/Na16	O5	2.236(11)		O200	2.475(14)		O194	2.301(13)
	O77	2.324(10)	Ca/Na21	O43	2.369(11)		O197	2.406(9)
	O82	2.411(14)		O56	2.514(13)	Ca/Na26	O11	2.364(13)
	O92	2.203(15)		O71	2.332(13)		O45	2.338(13)
Ca/Na26	O53	2.354(14)	Ca/Na31	O67	2.327(14)	Ca/Na36	O58	2.376(13)
	O73	2.468(13)		O84	2.322(13)		O64	2.471(13)
	O93	2.359(10)		O90	2.486(13)		O84	2.352(11)
	O177	2.388(10)		O137	2.281(13)		O100	2.258(12)
Ca/Na27	O10	2.297(13)		O178	2.433(10)		O134	2.653(10)
	O58	2.250(14)	Ca/Na32	O13	2.348(11)		O192	2.440(13)
	O87	2.437(13)		O20	2.367(14)		O92	2.223(15)

	O164	2.359(10)		O73	2.355(10)		O126	2.364(13)
	O182	2.452(13)		O93	2.348(13)		O134	2.369(13)
	O194	2.288(10)		O110	2.372(13)	Ca/Na37	O179	2.247(9)
Ca/Na28	O10	2.302(13)		O133	2.364(13)		F4	2.253(11)
	O42	2.185(10)	Ca/Na33	O42	2.388(13)		O192	2.500(10)
	O46	2.204(13)		O67	2.343(14)	Ca/Na38	O90	2.363(13)
	O101	2.048(10)		O145	2.328(13)		O105	2.225(15)
	O119	2.125(15)		O164	2.355(13)		O137	2.437(13)
	O182	2.068(14)		O176	2.347(10)		O188	2.219(9)
Ca/Na29	O11	2.365(11)		O182	2.449(9)		F5	2.278(11)
	O19	2.353(14)	Ca/Na34	O43	2.364(13)		O196	2.531(10)
	O117	2.347(13)		O51	2.331(14)	Ca/Na39	O4	2.304(15)
	O148	2.415(10)		O56	2.359(10)		O56	2.330(13)
	O161	2.336(13)		O100	2.366(10)		O126	2.432(10)
	O177	2.342(13)		O126	2.443(13)		O179	2.364(12)
Ca/Na30	O13	2.346(13)		O134	2.315(13)		F5	2.273(8)
	O23	2.407(13)	Ca/Na35	O10	2.239(10)		O196	2.377(13)
	O97	2.297(14)		O41	2.380(14)	Ca/Na40	O5	2.298(15)
	O133	2.301(10)		O101	2.299(14)		O64	2.436(13)
	O148	2.327(13)		O107	2.515(10)		O90	2.459(10)
	O161	2.389(10)		O185	2.222(15)		O188	2.397(12)
Ca/Na31	O64	2.451(10)		O194	2.337(14)		F4	2.208(8)
Ca/Na40	O192	2.331(13)	M5	O140	1.987(13)	Ti/Nb10	O165	2.007(9)
M1	O5	1.917(14)		O143	1.786(10)		O172	2.081(12)
	O24	2.054(12)	M6	O1	2.002(9)		O198	1.979(10)
	O132	1.939(9)		O119	1.768(14)	Fep/Mnp	O103	1.998(11)
	O152	2.037(14)		O147	2.031(12)		O125	2.102(11)
	O174	1.909(12)		O153	1.946(12)		O139	2.016(12)
	O184	1.989(9)		O181	1.884(9)		O189	2.455(13)
M2	O2	2.013(9)		O186	1.941(13)		O190	1.999(8)
	O113	1.938(9)	M7	O26	1.978(13)	Si1	O18	1.639(15)
	O122	2.034(12)		O47	1.939(13)		O37	1.574(13)
	O155	2.052(13)		O50	1.916(13)		O72	1.697(11)
	O166	1.964(14)		O52	1.979(10)		O163	1.670(11)
	O171	2.035(12)		O60	1.985(13)	Si2	O21	1.654(13)
M3	O29	1.920(13)		O154	1.990(9)		O26	1.572(14)
	O32	1.870(13)	M8	O57	1.963(13)		O86	1.641(12)
	O48	1.967(12)		O59	2.044(13)		O98	1.518(11)
	O55	1.975(10)		O104	1.915(9)	Si3	O14	1.636(15)
	O79	2.041(13)		O142	2.071(13)		O78	1.631(9)
	O138	2.007(9)		O151	1.761(10)		O121	1.622(12)

M4	O4	1.950(13)		O157	2.041(13)		O122	1.621(14)
	O37	1.959(12)	Ti/Nb9	O46	1.845(13)	Si4	O3	1.639(12)
	O81	1.944(12)		O130	1.998(12)		O22	1.633(14)
	O123	2.043(9)		O141	2.027(12)		O100	1.669(11)
	O169	2.018(12)		O144	1.960(12)		O111	1.636(14)
	O175	1.961(9)		O156	1.995(9)	Si5	O24	1.644(13)
M5	O18	1.978(13)		O187	2.044(9)		O31	1.603(11)
	O68	2.070(13)	Ti/Nb10	O88	1.979(12)		O59	1.626(15)
	O89	1.926(9)		O107	1.824(13)		O170	1.632(11)
	O118	2.003(13)		O162	1.944(12)	Si6	O25	1.625(13)
Si6	O67	1.553(11)	Si13	O154	1.599(13)	Si20	O147	1.637(14)
	O91	1.618(12)		O186	1.547(14)	Si21	O19	1.605(10)
	O128	1.609(14)	Si14	O7	1.662(14)		O112	1.649(10)
Si7	O57	1.585(15)		O102	1.580(14)		O124	1.692(14)
	O72	1.585(12)		O124	1.626(12)		O157	1.588(14)
	O132	1.573(12)		O161	1.567(11)	Si22	O3	1.617(14)
	O180	1.574(12)	Si15	O8	1.620(14)		O49	1.704(14)
Si8	O32	1.616(13)		O48	1.630(15)		O58	1.650(11)
	O33	1.676(12)		O86	1.616(11)		O91	1.594(10)
	O36	1.630(13)		O183	1.571(10)	Si23	O2	1.629(11)
	O83	1.543(11)	Si16	O15	1.658(14)		O29	1.618(15)
Si9	O11	1.592(15)		O49	1.650(12)		O129	1.695(12)
	O109	1.591(14)		O87	1.565(11)		O148	1.638(13)
	O150	1.600(11)		O150	1.628(13)	Si24	O138	1.545(11)
	O195	1.644(11)	Si17	O43	1.556(15)		O155	1.587(15)
Si10	O9	1.670(14)		O54	1.625(11)		O160	1.667(13)
	O44	1.654(13)		O94	1.644(14)		O190	1.649(11)
	O93	1.553(11)		O96	1.635(11)	Si25	O1	1.676(11)
	O159	1.652(12)	Si18	O104	1.569(11)		O50	1.584(15)
Si11	O6	1.642(12)		O114	1.695(12)		O73	1.617(13)
	O16	1.651(14)		O125	1.599(10)		O135	1.679(12)
	O128	1.633(14)		O152	1.618(15)	Si26	O134	1.632(15)
	O178	1.612(11)	Si19	O34	1.672(12)		O158	1.650(13)
Si12	O13	1.566(15)		O110	1.566(15)		O194	1.622(14)
	O75	1.614(14)		O162	1.589(14)		O198	1.619(10)
	O149	1.712(11)		O168	1.647(9)	Si27	O6	1.630(14)
	O168	1.617(11)	Si20	O10	1.620(15)		O63	1.675(14)
Si13	O103	1.633(11)		O38	1.611(9)		O66	1.652(10)
	O114	1.571(11)		O106	1.608(12)		O71	1.640(11)
Si28	O30	1.573(10)	Si35	O35	1.565(14)	Si42	O54	1.642(14)
	O80	1.682(13)		O40	1.633(12)		O74	1.557(11)

	O144	1.644(15)		O61	1.607(13)	Si43	O34	1.626(11)
	O188	1.665(12)	Si36	O20	1.646(10)		O45	1.642(14)
Si29	O65	1.677(14)		O140	1.617(14)		O109	1.700(12)
	O84	1.615(15)		O159	1.620(14)		O156	1.544(13)
	O85	1.695(11)		O193	1.676(10)	Si44	O23	1.601(14)
	O131	1.619(11)	Si37	O70	1.660(13)		O75	1.660(12)
Si30	O15	1.657(13)		O137	1.656(15)		O115	1.616(11)
	O51	1.608(11)		O145	1.584(14)		O165	1.587(13)
	O66	1.587(12)		O187	1.567(10)	Si45	O30	1.612(13)
	O111	1.619(14)	Si38	O31	1.618(12)		O39	1.602(11)
Si31	O7	1.610(11)		O68	1.606(15)		O82	1.527(14)
	O27	1.687(13)		O123	1.544(12)		O99	1.661(12)
	O38	1.605(12)		O167	1.577(12)	Si46	O60	1.586(14)
	O164	1.627(15)	Si39	O25	1.638(14)		O129	1.601(11)
Si32	O61	1.567(10)		O63	1.641(12)		O153	1.656(13)
	O69	1.653(13)		O149	1.619(13)		O177	1.628(13)
	O88	1.621(15)		O176	1.590(11)	Si47	O9	1.574(11)
	O179	1.657(12)	Si40	O79	1.580(15)		O17	1.540(14)
Si33	O115	1.669(12)		O133	1.669(12)		O78	1.625(11)
	O117	1.633(15)		O135	1.662(11)		O173	1.592(15)
	O130	1.525(14)		O171	1.611(13)	Si48	O27	1.603(12)
	O195	1.664(9)	Si41	O56	1.631(14)		O42	1.672(14)
Si34	O12	1.643(14)		O70	1.698(10)		O121	1.572(11)
	O33	1.585(11)		O172	1.570(12)		O181	1.624(13)
	O47	1.604(14)		O197	1.634(14)	Si49	O64	1.529(14)
	O200	1.502(10)	Si42	O8	1.609(12)		O141	1.638(12)
Si35	O28	1.655(11)		O36	1.654(13)		O158	1.719(10)
Si49	O182	1.615(14)	Si57	O28	1.641(12)			
Si50	O12	1.598(12)		O76	1.621(14)			
	O21	1.640(13)		O80	1.666(14)			
	O85	1.622(14)		O120	1.637(9)			
	O16	1.567(11)	Si58	O81	1.639(15)			
Si51	O97	1.626(11)		O89	1.563(13)			
	O102	1.642(14)		O139	1.619(11)			
	O142	1.645(13)		O160	1.647(10)			
	O193	1.639(13)	Si59	O22	1.576(11)			
Si52	O94	1.612(12)		O99	1.624(14)			
	O126	1.643(14)		O120	1.585(11)			
	O175	1.630(13)		O136	1.637(15)			
	O199	1.658(11)	Si60	O131	1.679(9)			
	O39	1.608(12)		O174	1.583(14)			

Si53	O62	1.649(9)		O192	1.598(15)
	O69	1.645(14)		O199	1.616(13)
	O77	1.591(14)	Si61	O96	1.712(9)
Si54	O44	1.664(13)		O169	1.588(14)
	O53	1.607(11)		O191	1.630(12)
	O112	1.674(13)		O196	1.556(15)
	O118	1.628(13)	Si62	O16	1.666(11)
Si55	O17	1.631(12)		O40	1.675(13)
	O41	1.627(14)		O62	1.539(11)
	O106	1.643(11)		O127	1.612(15)
	O113	1.611(13)	H1o189	O189	0.96
Si56	O65	1.665(12)	H2o189	O189	0.96
	O90	1.577(14)			
	O184	1.610(13)			
	O191	1.654(11)			

Appendix 17: Results of TEM-EDS measurements of different grains of eveslogite. Some grains additionally contained 0.1 at% Ta and Grain7 and Grain8 contained 1.0 at% As, which were both counted as impurities and are thus not listed in the table. The elemental composition is shown in at% for all elements excluding oxygen.

	Ca	Ba	Sr	K	Na	Ti	Nb	Fe	Mn	Si	Al	Cl	F
Grain1	19.8	1.2	1.8	11.3	7.8	5.1	2.3	1.1	0.9	42.1	0.6	0.6	5.2
Grain2	20.1	2.2	2.3	11.1	7.8	3.9	0.6	1.2	0.8	48.8	0.3	0.7	0.1
Grain3	21.8	1.5	2.1	10.7	7.6	4.9	1.1	1.2	0.7	46.5	0.6	1.0	0.0
Grain4	22.3	1.7	2.2	12.6	13.2	4.9	1.4	1.5	0.9	36.6	0.8	1.5	0.1
Grain5	22.3	1.3	1.5	11.9	9.5	5.6	1.2	1.2	0.7	43.1	0.8	0.8	0.0
Grain6	21.6	0.8	1.5	10.8	10.0	6.2	0.5	1.1	0.9	45.0	0.6	1.0	0.0
Grain7	19.3	1.5	1.7	11.5	10.7	3.9	1.6	1.1	0.6	38.5	0.5	1.0	7.0
Grain8	18.6	1.5	2.0	11.9	13.4	4.1	1.1	1.2	0.9	43.2	0.7	0.0	0.0
Grain9	17.4	1.0	1.7	10.9	8.5	5.4	1.2	0.9	0.7	43.9	0.5	0.6	7.2
Grain10	21.1	2.1	2.2	10.2	8.2	5.6	0.7	1.1	0.8	48.5	0.3	0.7	0.1
Grain11	20.4	0.7	1.6	11.4	8.2	5.6	0.7	1.1	0.8	48.5	0.3	0.7	0.1
Grain12	20.4	1.9	1.3	9.9	8.0	4.0	1.2	1.2	0.9	50.1	0.4	0.6	0.0

Acknowledgements

I extend my deepest gratitude to my supervisors, Prof. Dr. Hans-Joachim Kleebe and especially Prof. Dr. Ute Kolb, who has been by my side since my master's thesis, for their guidance and expertise throughout this dissertation. The support and feedback have been invaluable.

I thank Dr. Yasar Krysiak and, particularly, Dr. Sergi Plana Ruiz for their invaluable assistance from early on in my academic journey and for patiently teaching me intricate concepts and techniques.

I appreciate Dr. Stefan Lauterbach for his technical assistance.

I express sincere gratitude to Prof. Dr. Reinhard Neder, Dr. Rafael Schäffer and Nils Schlatter for their collaboration on illite and other ReSalt projects.

I am deeply thankful to Dr. Wulf Depmeier, Dr. Michael Czank, Dr. Mariana Klementova, Dr. Lukas Palatinus, Dr. Marko Schowalter and Dr. Sergey Krivovichev for their assistance, knowledge and additional measurements on eveslogite.

Special recognition goes to the members of AK Kolb for their invaluable moral support and collaborative spirit.

To my family and Anne Burger, thank you for the moral support and meticulous proof reading.

Lastly, I am indebted to my fiancé, Joa, for his unwavering support, understanding and patience throughout this journey.